Carbonatite-Related Rare-Earth Mineralization in the Bear Lodge Alkaline Complex, Wyoming: Paragenesis, Geochemical and Isotopic Characteristics

by

Meghan Moore

A Thesis Submitted to the Faculty of Graduate Studies of
The University of Manitoba
in partial fulfillment of the requirements of the degree of

MASTER OF SCIENCE

Department of Geological Sciences
University of Manitoba
Winnipeg

Abstract

The Bear Lodge alkaline complex in northeastern Wyoming (USA) is host to potentially economic rare-earth mineralization in carbonatite and carbonatite-related veins and dikes that intrude heterolithic diatreme breccias in the Bull Hill area of the Bear Lodge Mountains. The deposit is zoned and consists of pervasively oxidized material at and near the surface, which passes through a thin transitional zone at a depth of ~120-183m, and grades into unaltered carbonatites at depths greater than ~183-190m. Carbonatites in the unoxidized zone consist of coarse and fine-grained calcite that is Sr-, Mn- and inclusion-rich and are characterized by the presence of primary burbankite, early-stage parisite and synchysite with minor bastnäsite that have high $(La/Nd)_{cn}$ and $(La/Ce)_{cn}$ values. The early minerals are replaced with polycrystalline pseudomorphs consisting of secondary rare-earth fluorocarbonates and ancylite with minor monazite. Different secondary parageneses can be distinguished on the basis of the relative abundances and composition of individual minerals. Variations in key element ratios, such as $(La/Nd)_{cn}$, and chondrite-normalized profiles of the rare-earth minerals and calcite record multiple stages of hydrothermal deposition involving fluids of different chemistry. A single sample of primary calcite shows mantle-like $\delta^{18}O_{V\text{-}SMOW}$ and $\delta^{13}C_{V\text{-}PDB}$ values, whereas most other samples are somewhat depleted in ^{13}C ($\delta^{13}C_{V\text{-}PDB} \approx -8$ to $-10‰$) and show a small positive shift in $\delta^{18}O_{V\text{-}SMOW}$ due to degassing and wall-rock interaction. Isotopic re-equilibration is more pronounced in the transitional and oxidized zones; large shifts in $\delta^{18}O_{V\text{-}SMOW}$ (to ~ 18‰) reflect input of meteoric water during pervasive hydrothermal and supergene oxidation. The textural relations, mineral chemistry, and C and O stable-isotopic variations record a polygenetic sequence of rare-earth mineralization in the deposit. With the exception of one Pb-poor sample showing an appreciable positive shift in $^{208}Pb/^{204}Pb$ value (~39.2), the Bear Lodge carbonatites are remarkably uniform in their Nd, Sr and Pb isotopic composition: $(^{143}\mathrm{Nd}/^{144}\mathrm{Nd})_i=0.512591$-0.512608; $\varepsilon\mathrm{Nd}=0.2$-0.6; $(^{87}\mathrm{Sr}/^{86}\mathrm{Sr})_i=0.704555$-0.704639; $\varepsilon\mathrm{Sr}=-1.5$-2.7; $(^{206}\mathrm{Pb}/^{204}\mathrm{Pb})_i=18.071$-18.320; $(^{207}\mathrm{Pb}/^{204}\mathrm{Pb})_i=15.543$-15.593; $(^{208}\mathrm{Pb}/^{204}\mathrm{Pb})_i=38.045$-39.165. These isotopic characteristics indicate that the source of the carbonatitic magma was in the subcontinental lithospheric mantle, and modified by subduction-related metasomatism. Carbonatites are interpreted to be generated from small degrees of partial melt that may have been produced via interaction of upwelling asthenosphere giving a small depleted MORB component, with an EM1 component likely derived from subducted Farallon crust.

Acknowledgements

First of all, I would like to thank my advisor, Dr. Anton Chakhmouradian, for your encouragement, patience and guidance. I have learned so much from you in the field, in the lab, and in the classroom. Thank you for your time and energy, and for sharing your expertise of not only carbonatites, but also of writing and culture, she-she. Thanks to my family and friends for encouraging me to finish, when it would have been easier to give up. I am especially thankful for the unconditional love and support of my husband, Jonathan, for providing a platform in which I could pursue this goal. Thank you for all you are to me and our family. Thank you to my children, Jonah and Sophie, who unknowingly have provided me with endless inspiration. Thank you for forgiving the time I have dedicated to this work, for your laughter and love, and the ever-present reminder of what is really important in life. Thank you to my Dad for your constant emphasis of how important it is to finish what I started, and to do it well. I would like to thank Dr. Tony Mariano for sharing your passion, and for many field excursions and conversations involving wine, poetry, birds and rocks. You are a constant inspiration, chiend-an. I would like to thank Clint Cox for investing in my future. Thank you for your time, advice and patience. I hope to one day repay your kindness. I would like to thank all the folks from Rare Element Resources, particularly Jim Clark and John Ray, for giving me the opportunity to study the Bull Hill deposit. I am grateful for the conversations and questions we have shared. I would like to acknowledge Ravi Sidhu for all your time and patience in the EMPA lab. My data would not be of the caliber it is without your help. Thank you to Panseok Yang, Misuk Yun and Lizzie Ann Spencer for your guidance in collecting the data on which this thesis is built. Finally, I would like to acknowledge the University of Manitoba for funding through the UMGF.

Dedication

I am proud to dedicate this thesis to the memory of my mother, Mary Ann Marsters, who taught me to “be the best I can be.” I wish you were here to celebrate this moment in time, but I know that you are celebrating where you are now. Thanks for teaching me the value of education, a good work ethic, how to take care of myself, how to smile in the face of adversity, and the innumerable things that simply cannot be described with words. Sometimes life takes you on a different route than you had planned on the path to follow your dreams, you showed me how to take it all in stride and keep going, never giving up but sometimes taking a necessary reprieve. There were days when I relied on the memory of the sound of your voice telling me that I can do anything I set my mind to. I did it, Mom.

Table of Contents

List of Tables

List of Figures

Chapter 1. Introduction

1.1 Introduction to Rare Earth Elements

The term “rare earth elements” (REE) refers to fifteen f-transition elements that make up the lanthanide series of the periodic table (Fig. 1.1), including lanthanum (La), cerium (Ce), praseodymium (Pr), neodymium (Nd), promethium (Pm), samarium (Sm), europium (Eu), gadolinium (Gd), terbium (Tb), dysprosium (Dy), holmium (Ho), erbium (Er), thulium (Tm), ytterbium (Yb) and lutetium (Lu). Yttrium (Y) is usually included in this category due to its similar chemical properties and almost identical ionic radius to holmium. Scandium (Sc) is typically not included among the REE by geochemists owing to its much smaller ionic radius. It is notable that promethium (Pm) is not found in nature because its isotopes are very short-lived products of α-decay of ^{151}Eu and fission of ^{238}U. The discovery and separation of the individual lanthanides took over 150 years, attesting to the difficulty of isolating and separating the REE *from* one another, as well as their similarity *to* one another (Habashi, 1990; Gupta and Krishnamurthy, 2005).

The REE are naturally subdivided into groups on the basis of their atomic mass, ionic radius and chemical properties. The Cerium group consists of light rare-earth elements (LREE), including La, Ce, Pr, Nd, Sm and Eu, whereas the Yttrium group consists of Y and the heavy rare-earth elements (HREE), i.e. Gd, Tb, Dy, Ho, Er, Tm, Yb and Lu. Note that the division between LREE and HREE is completely arbitrary and some authors consider Eu part of the HREE group, whereas others place Gd in the LREE group. Geological processes may cause fractionation of the LREE from HREE, which is driven by the differences in their basicity, ionic size and affinity for a specific cation coordination (Henderson, 1984; Gupta and Krishnamurthy, 2005). Some authors also distinguish the middle rare-earth elements (MREE) as a separate group consisting of Sm, Eu, Gd and Tb (although Nd and Dy may also be included in this category).

1.1.1 Chemical properties of the REE

In order to understand how the REE behave in Geological systems, it is necessary to have an understanding of their (geo)chemical properties. These elements are lithophile and most commonly occur in the 3+ oxidation state. The common trivalent state of the REE and their broadly similar ionic radii explain their simultaneous occurrence within one mineral (Castor and Hedrick, 2006) and the fact that these elements occur as a group rather than as isolated elements (Henderson, 1984). In natural systems, Eu can attain an oxidation state of 2+ under reducing conditions, whereas Ce can be oxidized to Ce^{4+}in the surficial environment. Divalent Eu readily substitutes for Ca^{2+} in plagioclase, and Ce^{4+} easily bonds with oxygen to form the mineral cerianite, CeO_2, leading to the use of these two elements as a redox proxy (Mariano, 1989a).

The electron configuration of the lanthanides is most notable for variable occupancy of the 4f subshell, i.e. La has 0 electrons in the 4f block, and each subsequent element gains one electron in the 4f subshell, leading to 14 electrons and a filled 4f subshell in Lu. This is important because the 4f subshell is two quantum levels below the valence shell (the 5d shell) hence, the inner shell is filled rather than a new shell being added (Fig. 1.1). This leads to a progressive decrease of the ionic radius with increasing atomic number (Henderson, 1984; Fig. 1.2), which is one reason the LREE naturally fractionate from the HREE (Samson and Wood, 2004). Many of the unique properties exhibited by the REE are a result of the poor shielding of the 4f electrons by $5s^2$ and $5p^6$ electrons (Henderson, 1996).

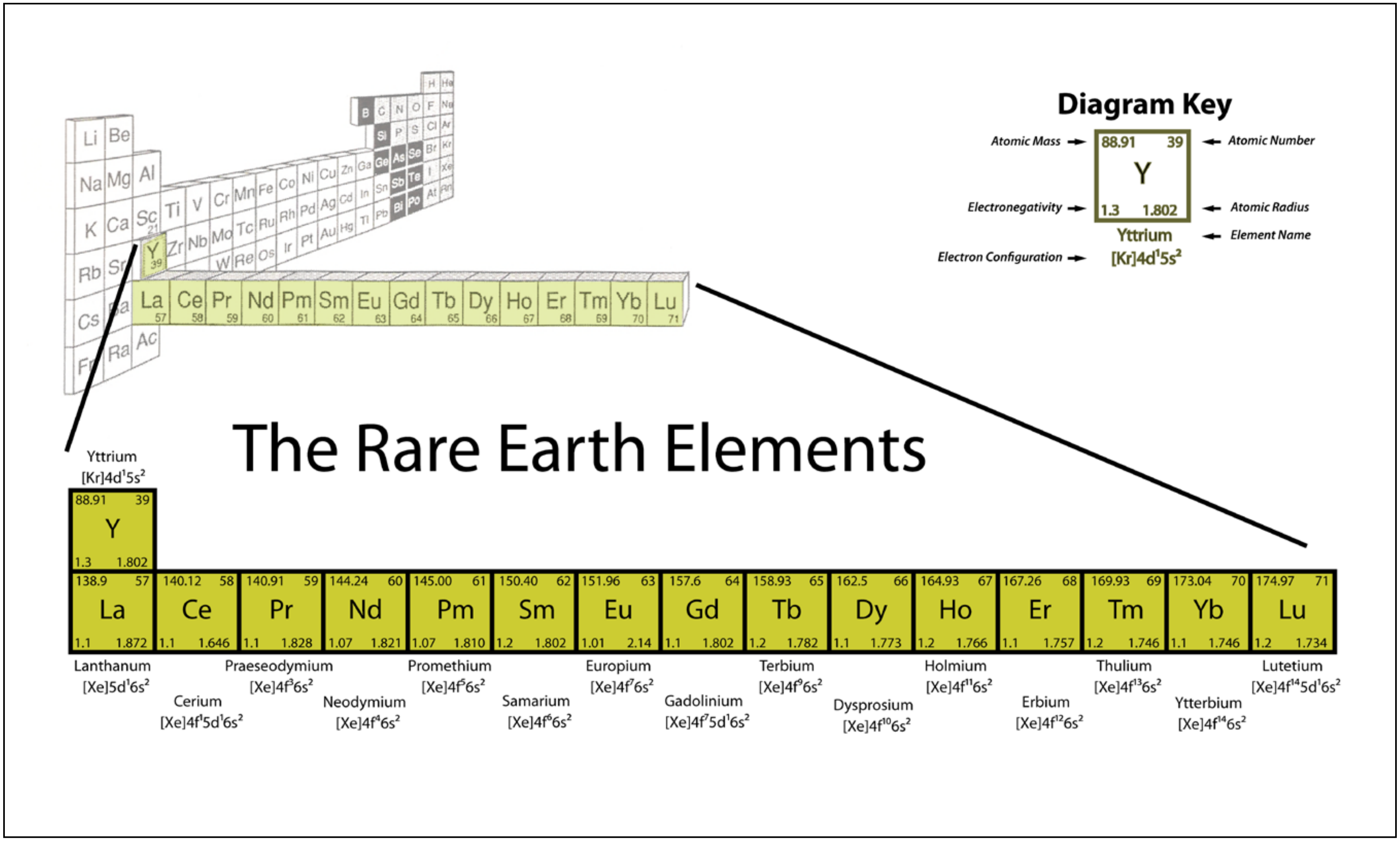

Figure 1.1. Periodic table showing location of the lanthanides and the atomic mass, electronegativity and electron configuration of each. Diagram of background periodic table (in upper left corner) from Habashi (1990).

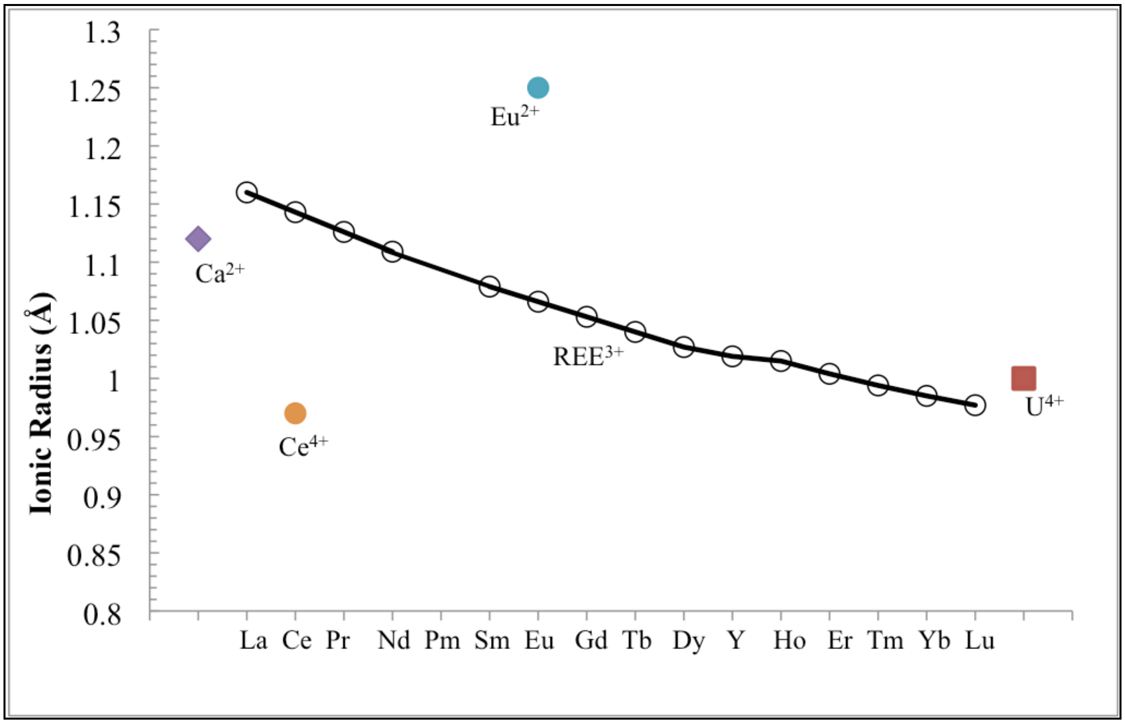

Figure 1.2. Variation in ionic radius (for CN = 8) across the lanthanide series.

It should be noted that ionic radius is a function of valence (oxidation state) and coordination number (CN) in specific minerals, and thus is slightly variable. In general, the rare-earths have large ionic radii that make it unlikely for isomorphous substitutions to occur in many common silicate minerals, which is one reason why the REE are generally considered incompatible elements in most silicate systems (Henderson, 1996). The ionic radii of the Cerium group elements are most similar to those of Ca^{2+}, whereas the Yttrium group elements have radii close to U^{4+} or Mn^{2+}. This allows for isomorphous substitution of REE in Ca, U-Th minerals and ferromagnesian silicates (Burt, 1989, Fig. 1.2). Bonding characteristics of the rare earth cations with anions or anionic groups are largely ionic due to the 3+ oxidation state and the preferential filling of the inner 4f orbital (Henderson, 1984).

A wide range of possible coordination numbers (CN) is observed in the structure of minerals containing the REE. The coordination number of a cation is a reflection of its ionic radius relative to the specific anion or anionic group forming its nearest coordination sphere. The HREE and LREE tend to have different CN due to a decrease in ionic radius across the lanthanide series. The HREE have a CN of 6-9 in most crystal structures, whereas the LREE typically have a higher CN ranging from 7 to 12 (Burt, 1989; Mariano, 1989b; Miyawaki and Nakai, 1996).The most common CN for the REE is eight (Miyawaki and Nakai, 1996). Coordination of bonding sites is one expression of fractionation between the LREE or HREE groups (Burt, 1989). If the CN is between 7 and 9, elements from either group can be incorporated in the crystal structure (Clark, 1989). Coordination polyhedra incorporating rare-earth cations are often distorted due to deviation of the shape of molecular orbitals and bond angles from the ideal parameters in polyhedra with an odd CN (e.g., 7 or 9; Miyawaki and Nakai, 1996).

1.1.2 Partitioning of the REE

A detailed discussion of REE partitioning is beyond the scope of this thesis. However, a brief overview is in order to provide a basis for the understanding of how and why different REE are concentrated in different igneous systems. Partitioning is a term that is used in geology to quantitatively describe the compatibility of an element relative to coexisting phases at equilibrium. The partition coefficient (D) is an experimentally or empirically derived measurable parameter that, in igneous systems, describes the distribution of an element between a melt and minerals crystallizing from that melt ($D^{\text{sol/liq}}$), between two immiscible melts ($D^{\text{liq1/liq2}}$), or between a melt and a vapor ($D^{\text{liq/vap}}$). In a simple two-phase system, $D^{\text{sol/liq}}$ is equal to the ratio of the concentration of element i in the mineral (solid phase) to the concentration of the same element in the melt (liquid phase), i.e. $D_i^{sol/liq} = C_i^{sol}/C_i^{liq}$. The value of $D_i^{sol/liq}$ determines whether element i will be preferentially partitioned into the crystal or the melt and depends on the structure and composition of both mineral and melt, energetic constraints, and intensive properties (especially temperature and pressure; McKay, 1989; Wood and Blundy, 2002; Blundy and Wood, 2003). For small values of $D_i^{sol/liq}$ (<< 1), the element is effectively retained in the melt and for large values (≥ 1), the element will be preferentially incorporated in the solid phase. Partition coefficients are determined empirically for *specific minerals* in *specific systems* under *specific P-T conditions*. When partition coefficients are applied to systems significantly different from those in which they were measured, serious error is inevitable (Samson and Wood, 2004). The concept of partitioning is important with respect to REE geochemistry because it describes how readily a specific member of that group can substitute for major elements in common rock-forming minerals (for example, how likely La will substitute for Ca in apatite). Additionally, partitioning data show how efficiently individual REE fractionate from one another in different minerals and crystallization environments.

1.1.3 Natural abundances of the REE

The distribution of REE in natural systems exhibits the pronounced Oddo-Harkins effect, i.e. the elements with an even atomic number (Ce, Nd, Sm, Gd, Dy, Er and Yb) have more stable nuclei and thus are more abundant than their odd-numbered neighbors (La, Pr, Eu, Tb, Ho, Tm and Lu) (Henderson, 1984; Burt, 1989; Fig.1.3A). This effect taken into account, there is a general trend of decreasing abundance with increasing atomic number; Ce is the most abundant and Tm is the least abundant members of the series in the Earth's crust (Henderson, 1984; Gupta and Krishnamurthy 2005). Several estimates of the relative crustal abundances of REE have been compiled (Table 1.1). When crustal abundances of the REE are compared to crustal abundances of other elements, it does not appear that the REE are really that “rare” (Fig. 1.4). They are, however, rarely concentrated to levels amenable to economically profitable mining and metallurgical recovery.

During partial melting of mantle rocks, the LREE are more incompatible relative to the HREE and Y due to their larger ionic radius and thus will partition into the melt phase. The process of crust formation over 4.5 billion years (e.g., Jacobsen, 1988) has produced enrichment of the LREE in the crust and depletion of these elements in the upper mantle (Hollings and Wyman, 2004; Workman and Hart, 2004).

To eliminate the Oddo-Harkins effect, the abundances of REE in Geological materials are typically normalized to those in the mean CI chondrite thought to represent the undifferentiated solar system material (e.g., Table 1.2 and references therein, Fig. 1.3B). In addition to chondrite-normalized REE diagrams, it is common to use the REE concentrations in the primitive mantle (PM) as a basis for normalization. Table1.2 lists the concentration of REE in these and other commonly used reference materials.

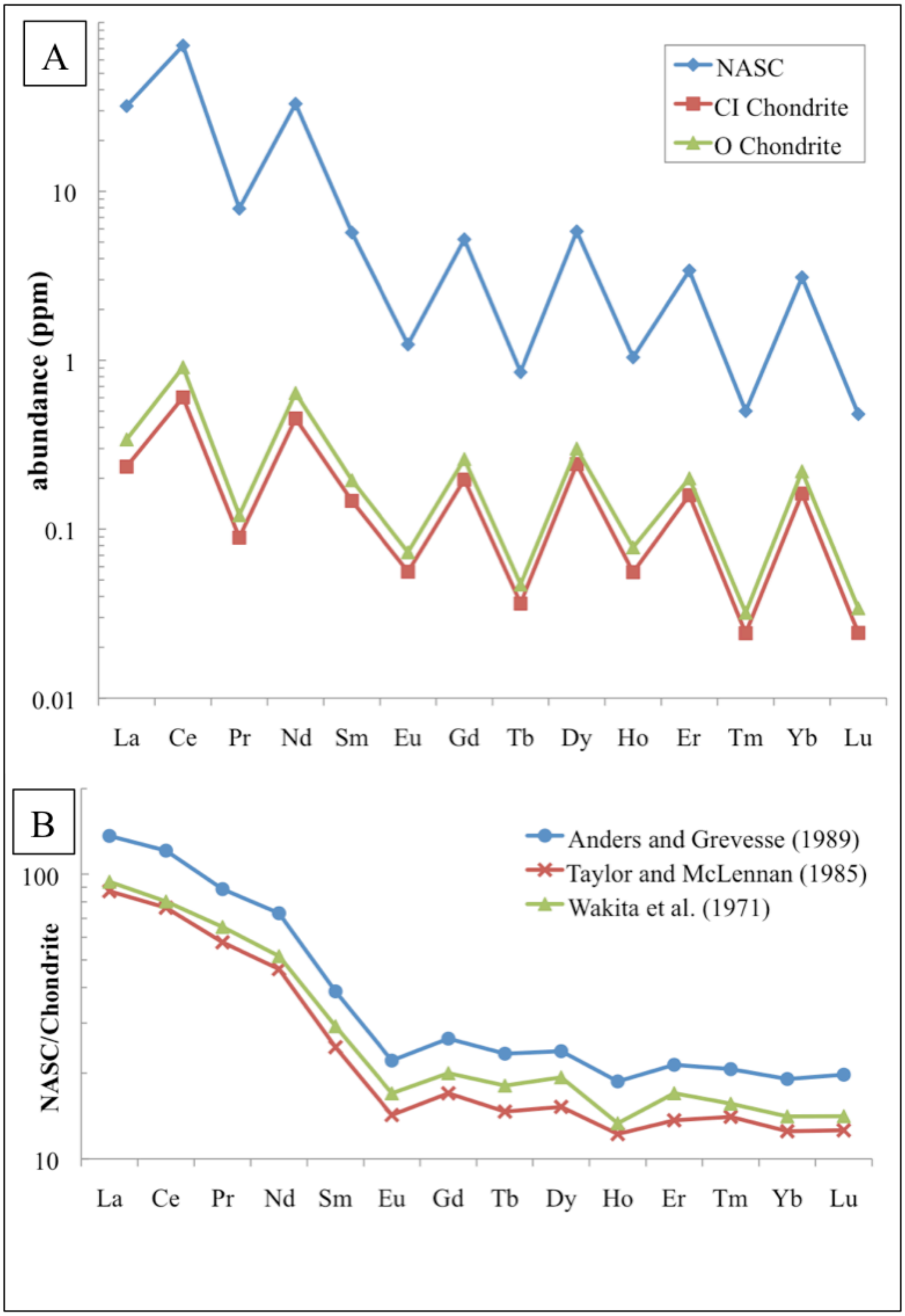

Figure 1.3. (A) Variation in abundance of the REE in chondrite meteorites and North American Shales Composite (NASC), illustrating the Oddo-Harkins effect. (B) REE abundances in NASC normalized to those in chondrite. Chondrite normalization values differ according to different authors but follow the same general trend.

Table 1.1. Relative crustal abundances (in ppm) of REE.

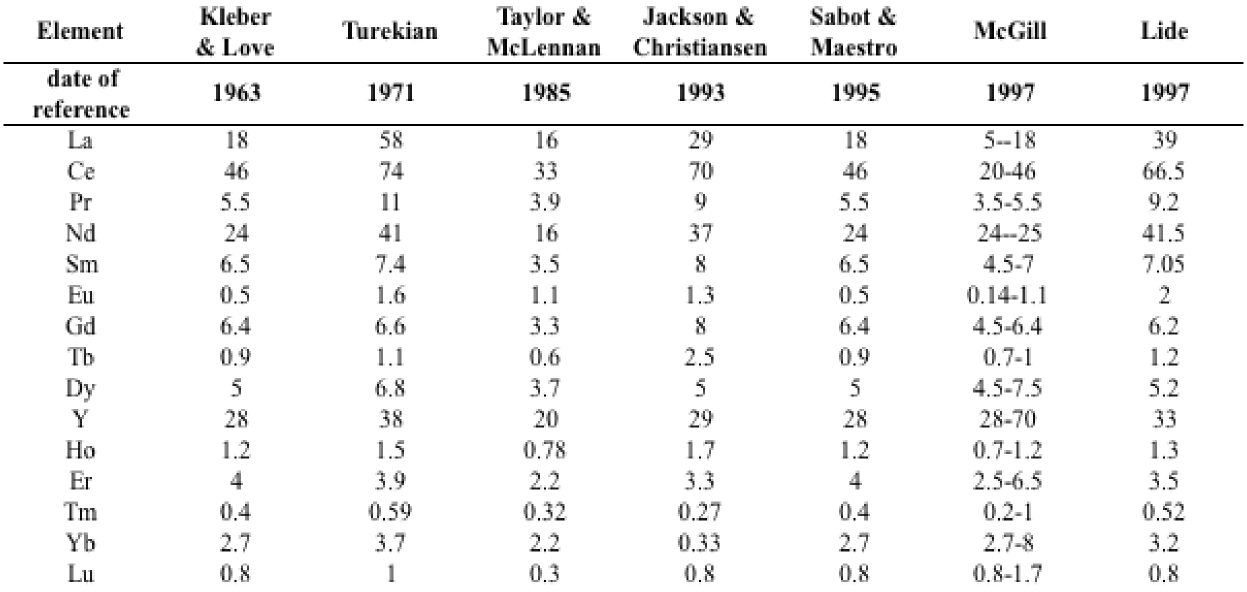

Element	**Kleber & Love**	**Turekian**	**Taylor & McLennan**	**Jackson & Christiansen**	**Sabot & Maestro**	**McGill**	**Lide**
date of reference	**1963**	**1971**	**1985**	**1993**	**1995**	**1997**	**1997**
La	18	58	16	29	18	5--18	39
Ce	46	74	33	70	46	20-46	66.5
Pr	5.5	11	3.9	9	5.5	3.5-5.5	9.2
Nd	24	41	16	37	24	24--25	41.5
Sm	6.5	7.4	3.5	8	6.5	4.5-7	7.05
Eu	0.5	1.6	1.1	1.3	0.5	0.14-1.1	2
Gd	6.4	6.6	3.3	8	6.4	4.5-6.4	6.2
Tb	0.9	1.1	0.6	2.5	0.9	0.7-1	1.2
Dy	5	6.8	3.7	5	5	4.5-7.5	5.2
Y	28	38	20	29	28	28-70	33
Ho	1.2	1.5	0.78	1.7	1.2	0.7-1.2	1.3
Er	4	3.9	2.2	3.3	4	2.5-6.5	3.5
Tm	0.4	0.59	0.32	0.27	0.4	0.2-1	0.52
Yb	2.7	3.7	2.2	0.33	2.7	2.7-8	3.2
Lu	0.8	1	0.3	0.8	0.8	0.8-1.7	0.8

The REE abundances of CI chondrites serve as a good proxy for the abundances of these elements in the silicate Earth and thus, variations in the relative proportion of specific REE within the series (e.g., degree of HREE-LREE fractionation) can be used to track different petrogenetic processes (such as partial melting, fractional crystallization, magma mixing, etc.) in the mantle and crust (Henderson, 1996). For example, the REE abundances in undifferentiated materials are proportional to those in the CI reservoir (McKay, 1989), providing the basis for estimating how the Earth's asthenosphere, suboceanic and subcontinental lithosphere and crust have evolved through time. This is one reason why these elements are used as *source* tracers for different igneous rocks. The degree of fractionation can be measured using the ratio of chondrite (cn), or Primitive Mantle (PM) normalized concentrations of a Ce-group to an Y-group element, typically La/Yb or La/Lu (Samson and Wood, 2004).

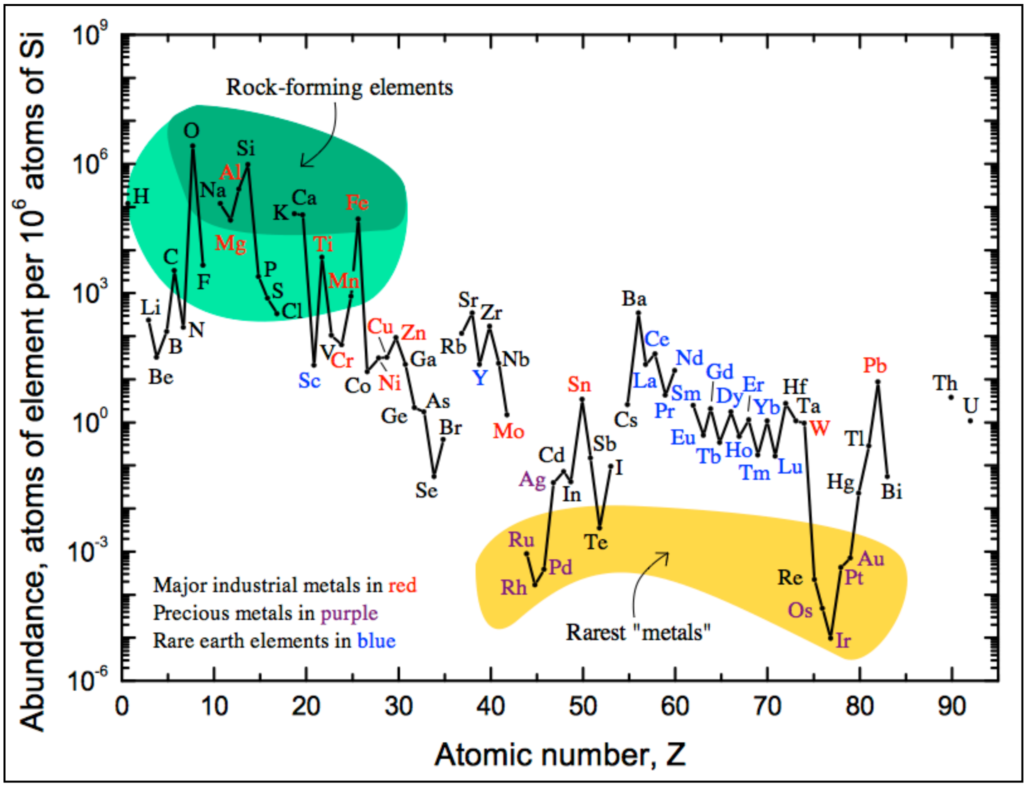

Figure 1.4. Comparison of the relative abundances of REE and other elements (normalized to 10^6 atoms of Si) in the upper continental crust. Image courtesy of the United States Geological Survey (Haxel et al., 2002).

Table 1.2. Abundance in ppm of REE in reference materials commonly used in geochemical analysis. NASC — North American shale composite.

Reference material	**Ordinary Chondrite**	**CI Chondrite**	**CI* Chondrite**	**CI Chondrite**	**CI Chondrite**	**Primitive mantle**	**Shales (NASC)**
reference	**Wakita et al.**	**Evensen et al.**	**Taylor and McLennan**	**Anders and Grevesse**	**McDonough and Sun**	**Sun and McDonough**	**Gromet et al.**
date of reference	**1971**	**1978**	**1985**	**1989**	**1995**	**1989**	**1984**
element							
La	0.34	0.24	0.37	0.23	0.24	0.69	32
Ce	0.91	0.64	0.96	0.60	0.61	1.78	73
Pr	0.12	0.10	0.14	0.09	0.09	0.28	7.9
Nd	0.64	0.47	0.71	0.45	0.46	1.35	33
Sm	0.20	0.15	0.23	0.15	0.15	0.44	5.7
Eu	0.07	0.06	0.09	0.06	0.06	0.17	1.24
Gd	0.26	0.20	0.31	0.20	0.20	0.60	5.2
Tb	0.05	0.04	0.06	0.04	0.04	0.11	0.85
Dy	0.30	0.25	0.38	0.24	0.25	0.74	5.8
Ho	0.08	0.06	0.09	0.06	0.05	0.16	1.04
Er	0.20	0.17	0.25	0.16	0.16	0.48	3.4
Tm	0.03	0.03	0.04	0.02	0.02	0.07	0.5
Yb	0.22	0.17	0.25	0.16	0.16	0.49	3.1
Lu	0.03	0.03	0.04	0.02	0.02	0.07	0.48

* = Normalized to a volitile free chondrite: C1 chondrite of Evensen et al. * 1.5

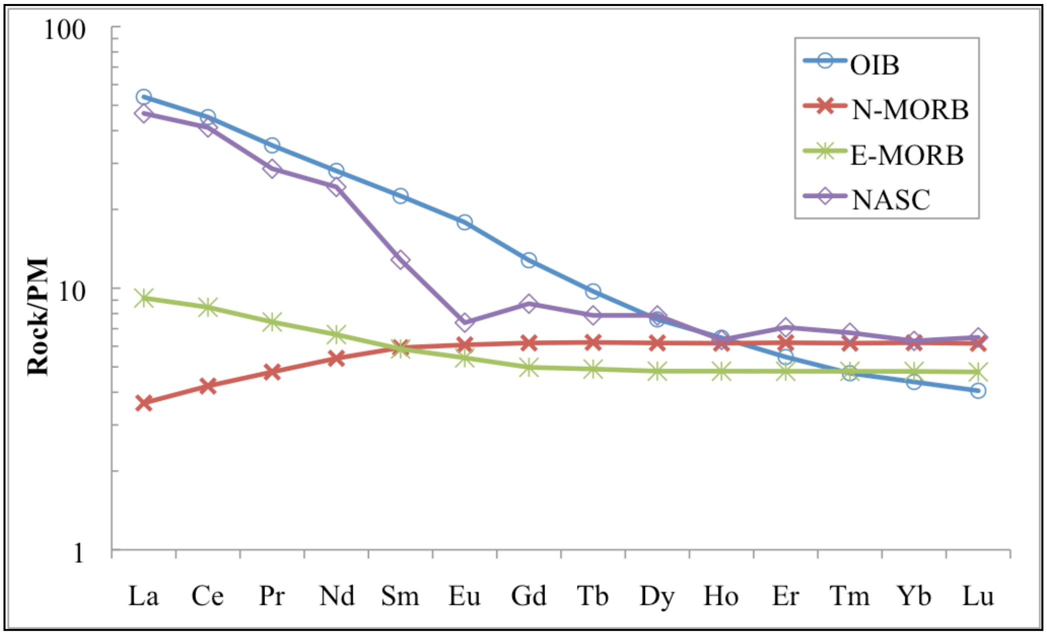

Figure 1.5. PM-normalized REE distributions of different crustal rocks. N-MORB = normal mid-ocean ridge basalt, E-MORB = enriched mid-ocean ridge basalt, OIB = ocean island basalt. Data and the PM normalization values are from Sun and McDonough (1989).

1.2 Uses of the REE

The REE are used in a variety of applications, each element having its own specific practically valuable properties. A comprehensive list of these properties was compiled by Gupta and Krishnamurthy (2005). Some of the more notable uses include (Haxel et al., 2002; Castor and Hedrick, 2006; Cox, 2009; Hatch, 2012): Ce in glass polishing and automotive catalytic converters; La-rich REE compounds in fuel cracking catalysts; Y, Eu, Gd, and Tb in phosphors; Sm and Nd in rare-earth magnets used in hybrid and electric vehicles, wind turbines, computer disc drives, cellular phones, etc.; and La in nickel-metal-hydride batteries. Currently, an adequate substitute is not available for most of these elements in the applications listed.

The USGS distinguishes the two principal types of end-use markets for REE (Goonan, 2011): well-established mature markets (catalysts, metallurgy, glassmaking and lighting), and those markets that are still being developed (such as permanent magnets, battery alloys and ceramics). Mature markets used about 59% of total rare earth oxides (REO) produced in 2008 with Ce, La and Y (in order of decreasing importance) comprising the bulk of the REE used. Developing markets used the remaining 41% of REO, with Nd being the dominant element used, followed by La, Ce, Pr, Y, Dy, Gd and Sm (ibid.). Because new technologies are constantly being developed and 25% of these new technologies require REE, the demand for these elements (and especially HREE) is predicted to increase in the future. The main focus areas of technological development are in the fields of REE magnets, superconductors, luminescent materials, catalysts, hydrogen storage, biological and agricultural uses (ICRE, 2010). The science and development of new materials involving rare earths are exciting and innovative, many new ideas are being explored and their potential impact on the future of energy, communication and other technologies is very promising. For more detailed information regarding the end-uses of the REE, please refer to the references cited above.

1.3 Geological Environments that Concentrate Rare Earth Elements

Concentrated occurrences of REE are found in a wide range of tectonic settings, and can form via igneous, hydrothermal and weathering processes. Even a cursory description of all the deposit types is well beyond the scope of this thesis. The following is a brief introduction to igneous and hydrothermal environments. For a recent synopsis of the various REE systems and related deposits, refer to Chakhmouradian and Wall (2012), Chakhmouradian and Zaitsev (2012), Kynicky et al. (2012), and Mariano and Mariano (2012).

Igneous systems that are known to host elevated levels of the REE most commonly form in anorogenic, typically rift-related tectonic settings where fractionated mantle-derived rocks are emplaced in structural lineaments (Chakhmouradian and Wall, 2012). Carbonatites and associated alkaline rocks in the Kola Peninsula of Russia, the Pan American Rift in Brazil and the East African Rift are notable examples. Post-orogenic and orogenic settings also host potentially economic REE concentrations. Most notable concentrations of REE occur in, or are accompanied by, carbonatites and/or alkaline silicate igneous rocks (Castor and Hedrick, 2006).

Primary igneous processes that can concentrate the REE include partial melting, fractional crystallization and equilibrium liquid immiscibility, and generally require a source enriched in REE (Chakhmouradian and Zaitsev, 2012). Examples of primary igneous deposits include the Mountain Pass carbonatite, USA and syenite at Kipawa, Canada. Incompatibility of the REE is expressed by their occurrence in the most fractionated rocks forming at late stages of petrogenesis (Mariano, 1989b). Owing to bulk partition coefficients, the LREE are generally enriched in highly fractionated silica-undersaturated rock types such as carbonatites, whereas the HREE are concentrated in acidic rocks such as peraluminous to peralkaline granites and pegmatites of the NYF family (Mariano, 1989c; Chakhmouradian and Wall, 2012; Chakhmouradian and Zaitsev, 2012; Kynicky et al., 2012; Mariano and Mariano, 2012). In most cases, it is a combination of igneous and late-stage processes (such as hydrothermal alteration or supergene enrichment) that produces economically viable REE deposits. Examples of these geologically complex systems include a carbonatite-hosted hydrothermal deposit at Kangankunde, Malawi (Wall and Mariano, 1996), the carbonatite-hosted deposits in the Mianning district of China (Hou et al., 2009), the Thor Lake alkaline complex in Canada (Sheard et al., 2012), and the carbonatite-hosted deposit in the Bear Lodge Mountains, USA (this work).

In some instances, it is unclear what deposit type is the most fitting model for mineralization. A good example of this is the world-class and well-studied Bayan Obo Fe-Nb-REE mine in Inner Mongolia, China. In this unique case, metasomatism and hydrothermal activity undoubtedly reworked the metasediments that host REE mineralization but the source of these elements has not been definitively constrained to date (Smith et al., 2014).

1.4 Objectives and Purpose of the Present Work

Carbonatite-related rare-earth mineralization was identified at the Bear Lodge alkaline complex (BLAC) in northeastern Wyoming, USA (see below), and is currently the focus of a mine development program by Rare Element Resources, Inc. (discussed in detail in Chapter 2). Most previous research was unpublished in the form of confidential reports for mining companies (Mariano, 1978b; 1981; 1988b) that focused on description and economic evaluation of select samples. Previously published research was either limited in sample size and scope, and not detailed enough to make definitive interpretations about the genesis of REE mineralization in the deposit (e.g., Mariano, 1989c; Mariano and Mariano, 2012; Wall and Zaitsev, 2004), or was focused primarily on preliminary mapping and description of geoligical units and mineralization types in the Bear Lodge Mountains (e.g., Staatz, 1983). Although previous research provided an excellent background, this work is the first to adequately address the genesis of the deposit.

This thesis is focused on detailed petrographic and geochemical characterization of different carbonatite units and mineralized parageneses based on a careful study of drill core and surface samples. The textural interrelations, compositional variation, and stable C-O isotopic characteristics of the major and accessory minerals, determined with modern analytical techniques, aid in the recognition of a paragenetic sequence, and in the identification of primary, hydrothermal, and supergene REE mineralization types. Stable-isotopic (C-O) characteristics of different carbonate phases are used to constrain the relative contribution of hypogene and supergene sources into the fluid reservoir. Radiogenic isotopic compositions (Sr, Nd and Pb) of whole-rock samples are used to elucidate the source characteristics of the Bear Lodge carbonatites. The main purposes of this research are to improve the current understanding of the sources and processes responsible for the formation of the Bear Lodge REE deposit, and to improve the existing model of REE mineralization in carbonatite petrogenesis.

1.5 Sample Collection and Selection

The author collected representative rock samples from various surface occurrences and drill core between May and September of 2009. One-hundred fifty-three drill core samples were collected from three holes drilled by Rare Element Resources (RER), including RES04-2, RES07-2 and RES08-4 in the Bull Hill SW target area (see Chapter 2). Holes RES04-2 and RES07-2 both carry high to low-grade mineralization, but were drilled at different azimuth and inclinations. Hole RES08-4 was drilled into the west side of the Bull Hill fault.

The samples were chosen to reflect the diversity of rock types, minerals and textures observed at the deposit in order to accurately characterize the different carbonatite units and allow for study of the relationships among them. The drill core was sampled to cover the scope of both high- and low-grade mineralization to allow correlation of individual carbonatite units and mineral assemblages with assay data. All drill core samples were cut in half with a diamond-bladed saw on site at the RER drill core storage facility. Each sample was subjected to further detailed analysis and can be easily matched to the split core retained in the RER facility on the basis of its sample number, which reflects the hole number and sampling depth.

Eleven additional samples and some accompanying data were collected earlier and loaned for the present project by Dr. Anthony N. Mariano, whose collection incorporates material acquired by him during the previous exploration work at Bear Lodge. These samples are rock slabs cut from drill core WP-2 and WP-6, both obtained by Hecla Mining Company in 1987.

The samples were then carefully inspected and narrowed down to a suite of 48 samples for further detailed analysis. A complete list of the selected research material and the types of analysis performed for each of the samples can be found in Appendix A.

Chapter 2. Geological Setting

The Bear Lodge Alkaline Complex (discussed in Chapter 3) is part of the northern Black Hills intrusive belt, which is the easternmost exposure of alkaline magmatism related to the Laramide orogeny. The Bear Lodge Mountains are located within the Archean Wyoming Province near the boundary with Proterozoic crust generated in the Trans-Hudson orogeny (Lisenbee, 1985).

2.1 Archean Wyoming Province

The Archean Wyoming Craton is a geological province that consists of three distinct subprovinces that formed and became amalgamated between 3.0 and 2.5 Ga, as interpreted from multiple phases of deformation and metamorphism (Dudás and Harlan, 1999; Mirnejad and Bell, 2008 and references therein). Shallow marine carbonate and clastic sedimentary rocks ranging from Cambrian to Cretaceous in age were subsequently deposited on the basement crust (Snoke, 1993; Feeley, 2003).

Exposures of Archean rocks consist of metamorphic core complexes that crop out as far east as the Black Hills, north as southern Alberta, and west as the Idaho-Oregon border (Fig. 2.1; Dudás, 1991; Buhlmann et al., 2000; Feeley, 2003). Isotopic and geochemical evidence obtained from xenoliths of mafic igneous rocks (or their metamorphosed equivalents) entrained in predominately Eocene mantle-derived igneous rocks in the Wyoming Province provides constraints on the composition and formation of the Wyoming sub-continental lithospheric mantle (SCLM) and asthenosphere. Pyroxene xenocrysts from the Haymond School dike in Montana indicate temperatures of magma generation around ~1200 °C at a pressure of 5 GPa in the SCLM beneath the Crazy Mountains Basin (Dudás and Harlan, 1999). Granulite pyroxenite xenoliths from the Leucite Hills in southern Wyoming record temperatures > 800 °C and pressures of ~1.1-1.3 GPa (Dudás and Harlan, 1999; Mirnejad and Bell, 2008). This evidence indicates granulitic conditions in the SCLM beneath the Wyoming Province (ibid.). Garnet peridotite xenoliths from Eocene diatremes of the Missouri Breaks region (Montana) indicate that the Archean SCLM extends to depths > 150 km below Montana (Dudás, 1991).

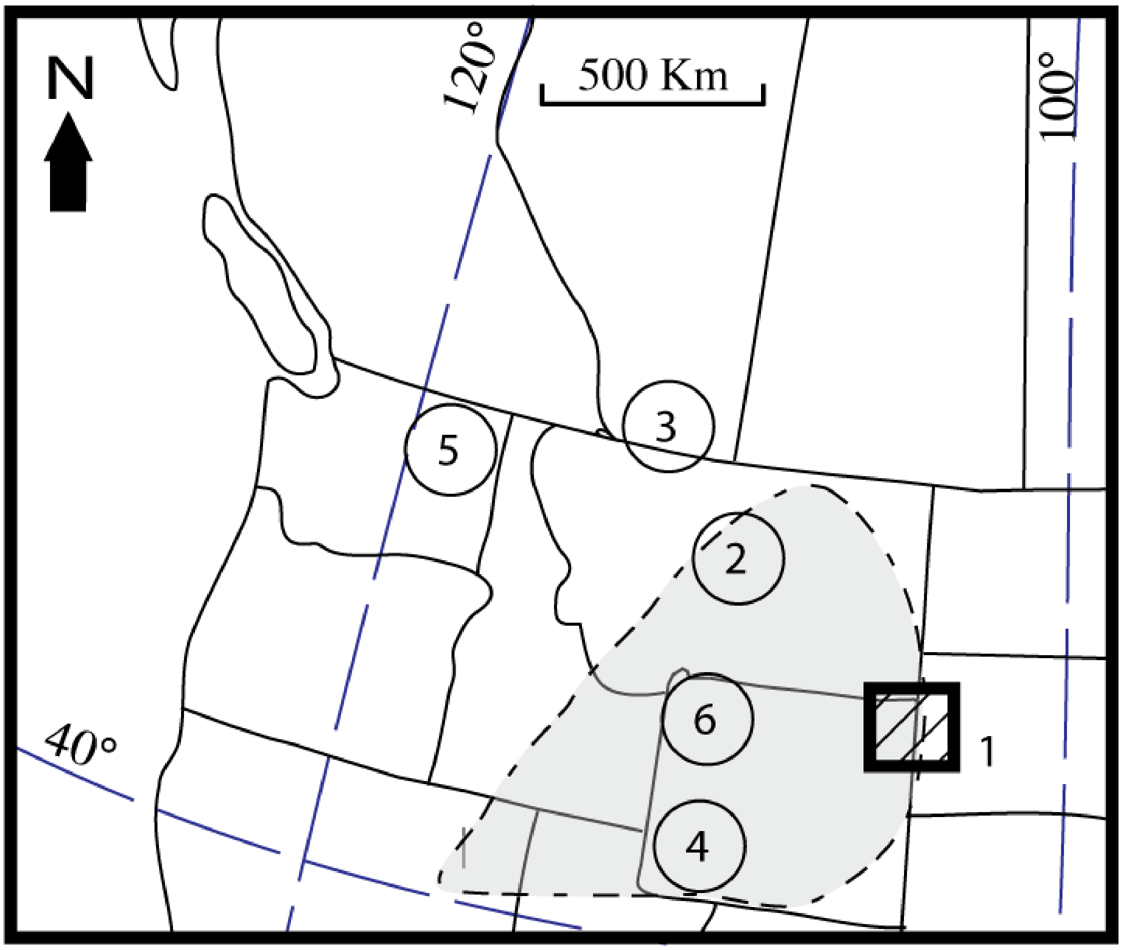

Figure 2.1. Generalized location map showing the Wyoming Craton (shaded area) with respect to other localities discussed in text: (1) Black Hills (diagonally ruled box shows boundaries of Black Hills map; Fig. 2.3); (2) Montana alkaline province; (3) Milk River minettes, Alberta; (4) Leucite Hills; (5) Colville igneous complex; (6) Absaroka volcanic province (circles marking individual provinces are not to scale, and are intended for location purposes only). Wyoming Archean Craton is shaded. After Buhlmann et al. (2000); Feeley (2003).

Geochemical characteristics of the Wyoming Province include depletion of high field strength elements (HFSE) such as Nb and Zr, coupled with enrichment in large-ion lithophile elements (LILE), especially Ba (Buhlmann et al., 2000; Feeley, 2003). Radiogenic Pb isotopic data provide evidence for subduction-related partial melting in the Montana metasedimentary subprovince and Beartooth—Bighorn magmatic zone (Mirnejad and Bell, 2008 and references therein). The enrichment in LILE, together with low εNd values, are interpreted to indicate depletion of the SCLM in HFSE and HREE in the Paleoproterozoic (2.2 to 2.0 Ga), followed by early Neoproterozoic (~0.95 Ga) metasomatic enrichment in LREE and LILE (Buhlmann et al., 2000; Feeley, 2003; Mirnejad and Bell, 2008). Dudás (1991) suggested that subduction lasted from 1.9 to 1.6 Ga. In some cases (Milk River minettes, Alberta; Highwood Mountains, Montana), lack of correlation between $^{87}Sr/^{86}Sr$ with $^{87}Rb/^{86}Sr$ ratios may indicate a much younger LILE enrichment event associated with late Cretaceous-Eocene, rather than Precambrian, subduction (Buhlmann et al., 2000; Feeley, 2003). However, pyroxenite xenoliths entrained in 3.0-0.9 Ma lamproites in the Leucite Hills (Wyoming) are interpreted as derived from a ~2.6 Ga mantle source showing a LILE-enriched, HFSE-depleted geochemical signature typical of calc-alkaline subduction-related arc magmas (Bell and Mirnejad, 2008). The above evidence indicates that the Archean Wyoming Craton was assembled via subduction and amalgamation of magmatic arcs. Subduction-induced metasomatism of the SCLM was the principal process responsible for its HFSE-depleted and LILE-enriched geochemical signature.

2.2 Cordilleran Tectonics

Together, the Laramide and Sevier orogenies are part of the greater Cordilleran orogeny that formed the Rocky Mountains along the west coast of North America, but they are distinct events recognized by different styles and mechanisms of deformation. The Sevier deformation is manifested as a thin-skinned fold and thrust belt, whereas the Laramide deformation involved basement rocks and produced core complexes juxtaposed along steep reverse or thrust faults against younger basins (Fig. 2.2; Snoke, 1993; Bird, 1998; Wells and Hoisch, 2008). Some overlap occurs between the Sevier and Laramide orogenic events, i.e. Late Cretaceous to Early Eocene deformation in the Sevier belt of the Cordillera is consanguineous with shortening in the Laramide foreland (Wells and Hoisch, 2008).

The tectonic plate arrangements changed during the transition from Sevier (moderate slab dip) to Laramide (low-angle to horizontal slab dip) subduction, as inferred from observations of different deformational styles (Wells and Hoisch, 2008 and references therein). It was also suggested that the subducting plates were segmented and had different dips and orientations: shallow to horizontal under the Laramide front in the central part of the orogenic belt, with a steeper dip to the south (Wells and Hoisch, 2008). These differences resulted in variable timing of the transition from the Sevier to Laramide stage of deformation along the orogenic belt (ibid.).

2.2.1 Sevier tectonics

The Sevier orogeny was active from the Middle Jurassic to Early Eocene (Bird, 1998; Wells and Hoisch, 2008). Compressional stress in the Sevier belt was transmitted through the over-thickened and weakened Cordilleran crust (Bird, 1998). Shortening in the Sevier hinterland occurred in the Mid- to Late Jurassic and Late Cretaceous, while shortening in the foreland is evidenced by a thin-skinned fold and thrust belt that formed during the Early Cretaceous to Eocene (Wells and Hoisch, 2008). The last major shortening in the Sevier belt occurred ~70 Ma (Bird, 1998).

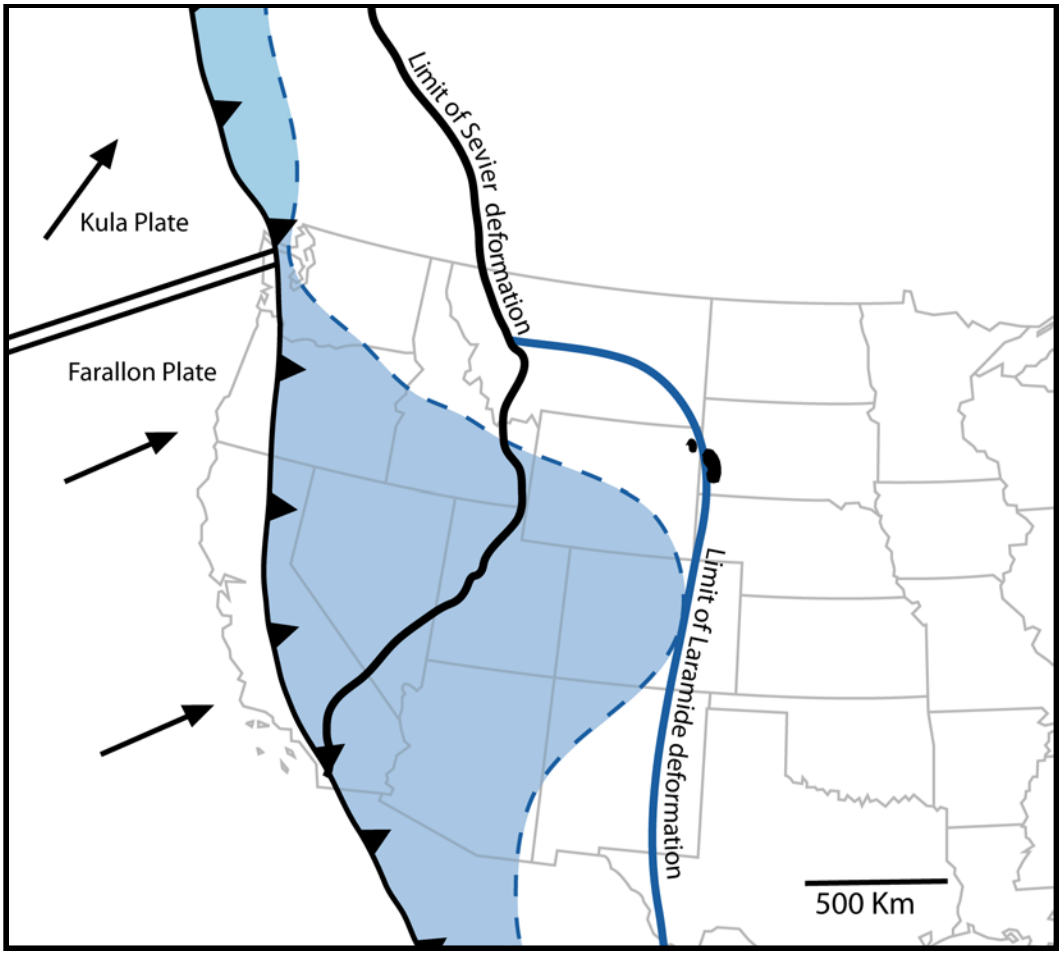

Figure 2.2. Map of the United States showing limits of deformation of the Laramide and Sevier Orogenies and proposed location of the paleotrench. Blue area shows proposed contact of horizontal Farallon Plate with the North American crust. Modified from Bird (1998), Bunge and Grand (2000) and DeCelles and Coogan (2004).

The Sevier fold and thrust belt is a classic example of intraplate deformation that has been very well studied in western Wyoming, southeastern Idaho and northern Utah (Snoke, 1993). Exposures of the Sevier belt in this area are metamorphic rocks that record deep burial and exhumation (Wells and Hoisch, 2008). In southwestern California and Arizona, exposures are composed of Precambrian rocks thrust over Paleozoic and Mesozoic rocks that were proximal to the magmatic arc and are plastically deformed (Snoke, 1993). Exposures of exhumed metamorphic core complexes associated with peraluminous granites of Late Cretaceous

(Sevier) age in the Mojave Desert and Great Basin were interpreted by Wells and Hoisch (2008) as products of partial melting of the over-thickened crust.

2.2.2 Laramide tectonics

The east-northeast and west-southwest convergence of the North American plate with the Kula and Farallon plates, and all the spatially and temporally related magmatism and deformation have been the focus of research for over a century. However, there is no single model that successfully integrates and reconciles all available geological and geophysical evidence. The mechanism is yet to be identified that would explain deformation associated with broadly coeval, widespread alkaline magmatism far inland of the subduction zone in western North America.

Timing estimates

Basement-cored uplifts in the eastern Rocky Mountains that occurred from the Late Cretaceous through Mid-Eocene are generally accepted as an expression of the Laramide orogeny (Snoke, 1993). Laramide-style deformation began ca. ~75-70 Ma in western Wyoming, where thrusting is concentrated in the Teton and Wind River ranges, and expanded east to the Black Hills of South Dakota by ~55 Ma (Bird, 1998). The rate of convergence is estimated to have ranged from 1 to 1.5 mm/yr, peaking at 60-55 Ma. The rate of subduction decreased ~ 58 Ma, or between 50 and 45 Ma (Bird, 1998; Dudás and Harlan, 1999; Wells and Hoisch, 2008). A triple-junction between the Kula, Farallon and Pacific Plates formed ~54 million years ago (Duke, 2005). A change in the direction of compression in the Late Paleozoic – early Eocene gave rise to exhumation of metamorphic core complexes in Idaho, Washington and British Columbia between 55 and 48 Ma (Dudás, 1991). The Laramide orogeny was diachronous. It ended ~51 Ma in Wyoming, but lasted until ~40-35 Ma in Colorado and New Mexico (Snoke, 1993).

The transition to an extensional regime began in the southern portion of the orogenic belt (Mojave Desert area) and occurred during the period of rapid convergence (~75-67 Ma), but much later (~49-40) Ma in the central parts of the orogen and in Wyoming (Bird, 1984, 1998; Wells and Hoisch, 2008). Extensional tectonics continued to affect the Rocky Mountain foreland after ~29 Ma, whereas the last major phase of compression occurred ~40 Ma in Utah (Bird, 1998).

Deformation

Crustal deformation related to the Laramide orogeny is manifested in deep-rooted reverse and thrust faults that resulted in 5-10% crustal shortening and thickening to over 55 km in the eastern Wyoming part of the Cordilleran orogenic belt (Snoke, 1993; Bird, 1998). Laramide structures are traditionally recognized by a northwest-trending fabric of Precambrian basement uplifts (metamorphic core complexes associated with basins) in the northern part of the orogen (Colville Igneous Complex, Montana) and northwest-trending monoclines (Comb Ridge, San Miguel Swell, Black Hills) in its southern portion. Bird (1998) used inverse tectonic modeling and estimated plate velocities to interpret that the subducting plates moved ~4900 km landward with respect to the North American plate.

Magmatism

Paleocene-Eocene alkaline magmatism was widespread. It occurred throughout western North America, including the Rocky Mountain Alkaline Province (RMAP), which encompasses the Montana and Great Plains Alkaline Provinces, Colorado Mineral Belt, and isolated centers of igneous activity in Arizona, Utah, New Mexico, California and Texas (Jensen, 2003). In the northern part of the RMAP, Eocene igneous activity occurred over an area of 250 by 400 km wide (British Columbia and Yukon) and expanded to a ~1,000 km wide area south of Lat. 42° N (Dudás, 1991). The Black Hills intrusive belt is located ~1,200 to 1,500 km from the inferred location of the Kula-Farallon trench (Fig. 2.2; Lisenbee, 1985; Dudás, 1991).

Eocene magmatic activity in the Canadian Cordillera was confined to a continental arc of calc-alkaline composition formed between ~52 and ~48 Ma (Dudás and Harlan, 1999). Alkaline Eocene igneous rocks in Montana range from 54 to 48 Ma (ibid.). Volcanic rocks in the Challis complex (Idaho) are as young as ~45 Ma, whereas volcanic rocks in the Absaroka complex (Wyoming-Montana) range from 53 to 48 Ma (ibid). Magmatism in the Black Hills occurred at ~60-46 Ma (Lisenbee, and DeWitt, 1993; Duke, 2005). Many Eocene alkaline rocks in the RMAP also cluster around 50 Ma. The northern portion (> 50° N) of magmatic activity is up to 10 Ma younger than the southern portion (Dudás, 1991). Dudás and Harlan (1999) suggested that a transition from alkaline to calc-alkaline magmatism along the northwestern margin of the Wyoming Craton occurred after 48 Ma. Alkaline silicate rocks associated with carbonatites in the Rattlesnake Hills of Wyoming are ~44-45 Ma old (Duke and Frost, 2013) and carbonatite dikes in the Bear Lodge mountains (the focus of the present work) are ~51 Ma old (Anderson, 2013a). Alkaline rocks (lamproites) in the Leucite Hills (Wyoming) are much younger than the majority of igneous rocks in the RMAP (~3.0-0.9 Ma) and appear to be related to back-arc spreading or plume activity (Mirnejad and Bell, 2006). Snoke (1993) postulated two distinct major episodes of alkaline magmatism: a Laramide-related episode associated with subduction between ca. 80 and 55 Ma, and younger events (Absaroka-Gallatin and Challis-Kamloops volcanism), generally localized north of Lat. 42° N and associated with post-orogenic crustal extension. Based on the available age constraints, magmatism in the Black Hills is probably related to the syn-Laramide subduction (Snoke, 1993).

Syn-Laramide igneous rocks range in composition from potassic-alkaline to sodic-alkaline and calc-alkaline, and include syenite, trachyte, latite, phonolite, comendite, tephrite, malignite, aillikite, alnöite, melnoite, benmoreite, lamproite, kimberlite and carbonatite (Thorkelson and Taylor, 1989; Hole, et al., 1991; Dudás and Harlan, 1999; Breisprecher, et al., 2003; Duke, 2005, 2009). Note the above rocks were classified according to different classification schemes and by different authors over time. Xenoliths of mafic igneous and metamorphic protolith rocks in the RMAP have high Ba and LREE contents, which is consistent with subduction in a continental arc setting. These characteristics, along with depletion of HFSE and variation in ^{87}Rb/^{86}Sr ratios, are also present in Eocene rocks from the RMAP. The geochemical signature of the Eocene rocks could either be inherited from the ancient (based on Pb-Pb pseudoisochron ages), metasomaticaly enriched lithosphere of the Wyoming craton, or derived from Paleocene to Eocene subduction-induced metasomatism in the mantle wedge (Irving et al., 1989; Dudás, 1991; Dudas and Harlan, 1999; Morris and Hooper, 1997; Buhlmann et al., 2000; Feeley, 2003; Mirnejad and Bell, 2008; Wells and Hoisch, 2008).

The SCLM below the Wyoming craton is interpreted to influence the geochemical composition of Eocene alkaline igneous complexes in the northwestern United States (Dudás, 1991; Norman and Mertzman, 1991; O'Brien et al., 1995; Dudás and Harlan, 1999; Buhlmann et al., 2000; Feeley, 2003). In addition to the trace-element variations discussed previously in this section, the presence of both kimberlites (Missouri Breaks) and carbonatites (Bearpaw Mountains, Montana; Rattlesnake Hills and Bear Lodge, Wyoming) indicates the existence of CO_2-rich mantle sources in this part of the SCLM (Dudás, 1991; Duke and Frost, 2013).

2.3 Tectonic Models

Several different models have been proposed to explain the temporal and spatial correlation between subduction, extension, deformation and magmatism during and after the Laramide orogeny based on evidence from a large number of igneous localities. However, there is no single model that successfully accounts for all of the available evidence from different occurrences of Eocene magmatism (Dudás, 1991). Most models for the Laramide orogeny invoke upwelling of hot asthenosphere close to the base of the crust to generate melting.

The temporal distribution of alkaline magmatism and complex variations in geochemical and isotopic compositions, often in the same complex, indicate that this magmatism did not occur in a uniform geodynamic regime. Magmas tapping geochemically similar sources were generated in different tectonic environments (Dudás, 1991). One problem is that published interpretations are often based on trace-element criteria alone, making it hard to differentiate between Precambrian and Eocene metasomatism without radiogenic isotopic data (Feeley, 2003).

2.3.1 Flat-slab subduction

The shallow slab or “flat-slab” hypothesis has been the most popular and widely accepted model to explain the features of Laramide tectonics for many years. Subduction-related models invoke a very shallow to horizontally dipping slab based on geophysical (e.g., tomographic imaging of the inferred subducted plates) and structural evidence (e.g., crustal deformation as far inland as the Black Hills and the presence of a “magmatic gap”). The “gap” indicates the lack of magmatism near the paleotrench, with the large volume of temporally close magmatism occurring far inland, due to the proximity of the subducting slab to the overriding plate. The shallow or flat-slab model involves sub-horizontal subduction, owing to shear coupling between the subducting and overriding plates, or to viscous stresses in the mantle (Bird, 1984; 1998).

Most flat-slab models include removal of the SCLM by either delamination or thermal erosion (Bird, 1988; Dudás, 1991).

Early versions of this hypothesis postulate that compressive stress applied through horizontal subduction increased the area of contact between the overriding and subducting plates from ca. 80-75 to ~55 Ma, when subduction of a transform fault changed the velocity and azimuth of velocity of the subducting slab (Bird, 1998). This change resulted in lesser contact between the subducting and overriding plates, which led to voluminous magmatism in response to inflow of asthenospheric material and melting of the metasomatized mantle. A slightly different version of the above model suggests that magmatism occurred above a flexure in the slab, where the angle of subduction steepened, and perhaps the hinge line on the slab moved west during a decrease in convergence rate (Bird, 1988b) to allow for asthenospheric melting (Dudás, 1991; Bird, 1984).

Another model involving shallow slab subduction is based on interpretations of the Absaroka volcanic suite (Dudás and Harlan, 1999; Feeley, 2003). According to this model, metasomatism of enriched SCLM and asthenosphere by compositionally variable fluids derived from the subducted Farallon plate was followed by detachment and foundering of the downgoing plate, an increase in slab dip and onset of extension contemporaneously with the upwelling of hot asthenosphere (Dudás and Harlan, 1999; Feeley, 2003**).** Recent data do not support this hypothesis, at least for latitudes between 30° and 50° N, owing to the lack of (1) continuous magmatism, (2) recognizable forearc and backarc zones, (3) age progression of magmatism expected from a constant rate of subduction, and (4) also because of conflicting interpretations of geochemical data (Dudás, 1991). However, there is evidence for the change in the rate of convergence at those latitudes (Bird, 1988; O'Brien et al, 1995; Dudás and Harlan, 1999; Wells and Hoisch, 2008).

One hypothesis suggests that subduction of the Farallon slab changed from a steep to shallow dip from north to south between the Sevier and Laramide orogenies. A steeper dip is recognized in the Great Plains, whereas shallow angles were reported for the Basin and Range province (Bird, 1998; Wells and Hoisch, 2008). Evidence for shallow slab subduction in the southern part of the orogen (Great Basin) is present in the form of high-pressure Franciscan-type metamorphic rocks in tectonic contact beneath Mesozoic arc rock exposures in windows in the Sevier belt in the Mojave area, and transverse ranges in southern Arizona (Wells and Hoisch, 2008). Exposures of these rocks are interpreted to be remnants of underplating oceanic sediments produced during low-angle subduction (ibid.).

Bird (1988) created a quantitative model that successfully predicts some physical effects of horizontal subduction, including displacement, thickness and temperature variations of the crust through time. His model has several inconsistencies with the present-day geology, but overall supports the idea that horizontal subduction caused the Laramide orogeny.

2.3.2 Mantle upwelling

A model based on evidence from the Crazy Mountains of Montana (Dudás, 1991) involves heating of a lithospheric source by upwelling mantle, which tapped a deep, CO_2-rich reservoir. As the rate of subduction decreased at ~58 Ma, the subducted plate foundered and sank, providing an avenue for hot asthenosphere to flow into the mantle wedge (O'Brien et al, 1995; Dudás and Harlan, 1999). Chemical input from subduction of the Farallon plate was not recognized in the Crazy Mountains. The upwelling mantle probably caused thermal erosion of the SCLM and crustal uplift (Dudás, 1991).

2.3.3 Post-orogenic collapse and extension related to lithospheric delamination

Exhumation of metamorphic core complexes and voluminous magmatism that occurred in a compressional tectonic regime could indicate that the traditional interpretation of "Laramide" complexes as being related to the subduction of the Farallon Plate beneath North America is not correct (Norman and Mertzman, 1991; Morris and Hooper, 1997; Feeley, 2003). Post-Laramide extension in the Colville igneous complex in the northern portion of the orogen (Washington), and in the Mojave Desert in its southern portion, may be related to collapse of the orogenic system. The postulated collapse facilitated the exhumation of metamorphic core complexes and gave rise to decompression-induced crustal melting.

A model for the Colville complex involves removal of the SCLM and lower crust after subduction, whereas an alternative model for the Mojave and Basin and Range province proposes that the SCLM was removed after the Sevier orogeny, but before the Laramide orogeny, and may have facilitated the previously mentioned shallow dip of the slab (Wells and Hoisch, 2008). Yet another hypothesis interprets the removal of the SCLM by mechanical erosion involving a shallow-subducting slab (Bird, 1998).

All models invoking lithospheric delamination by some mechanism suggest that the influx of hot asthenospheric material occurred during extension in order to generate heat and aid decompressional crustal melting. The loss of lithospheric mantle led to the transition from a compressional to an extensional regime, and the exhumation of metamorphic core complexes along low-angle normal faults associated with magmatism, as in the Basin and Range province (ibid). Removal of the lower crust additionally facilitated isostatic uplift and accounts for present-day elevations, as well as the onset of extension in that province (ibid.).

In the Colville igneous complex, metamorphic core complexes are associated with graben faults and volcanic centers in the grabens (Morris and Hooper, 1997 and references therein). Low-HFSE and high-LILE geochemical signatures in the volcanic centers are interpreted from Sr-Nd isotopic evidence to be inherited from different crustal sources, where a Proterozoic subduction-related signature was preserved (Morris and Hooper, 2003). In the Mojave Desert, Late Cretaceous peraluminous granites were emplaced in an extensional environment following the Sevier Orogeny ~75 to ~67 Ma (Wells and Hoisch, 2008). The granites are derived from mid-crustal levels with juvenile geochemical components (ibid.). Pressure-temperature-time paths indicate that exhumation of metamorphic core complexes was contemporaneous with magmatism in the Mojave Desert, Great Basin, and the southern Cordillera magmatic arc (ibid).

The mantle delamination hypothesis may not be valid in certain locations because a SCLM-like component is interpreted to have been present in the sources of melts and xenoliths from many igneous occurrences. Young basalts of the Snake River plain (Idaho) and lamproites of Smoky Butte (Montana) contain geochemical and isotopic evidence of an ancient mantle component, virtually invalidating the hypothesis of lithospheric delamination in these cases (Dudás, 1991). Barometric studies of mantle xenoliths indicate that the Archean lithosphere beneath the Wyoming Province was present to depths > 110 km up to at least 42 Ma (Dudás and Harlan, 1999).

2.3.4 Slab window hypothesis

The hypothesis that subduction of the Kula-Farallon spreading ridge led to the formation of a slab window into the asthenosphere was proposed and supported by Hole et al. (1991), Thorkelson and Taylor (1989), Breisprecher (2003), and Duke (2005, 2009). According to this hypothesis, the mid-ocean ridge continued to spread apart after subduction, leading to the upwelling of asthenospheric material and its interaction with, and melting of, the overlying mantle wedge, subducting plate and SCLM (Hole, et al. 1991; Thorkelson and Taylor, 1989). This interaction may explain the wide variations in geochemical and isotopic compositions reported for the Eocene magmas, and deformation that cannot be explained by subduction alone (Hole et al., 1991; Thorkelson and Taylor, 1989; Russo et al., 2010). The slab window hypothesis was proposed to explain the geological complexity of the western United States and southwestern Canada. This type of tectonic environment is also recognized in Antarctica, India, China, Indonesia, and South America (Hole et al., 1991; Russo et al., 2010).

Evidence for slab window tectonics includes the change in geochemical compositions of temporally related magmatism from an arc-like (calc-alkaline) character to intraplate or ocean-island basalt affinity, which involves an increase in alkalinity (Hole et al., 1991; Breisprecher et al., 2003; Dostal et al., 2003). Trace element characteristics of slab window environments have highly fractionated REE distributions (expressed in high LREE/HREE ratios), show enrichment in HFSE, LREE and LILE in comparison with the primitive mantle (Breisprecher et al., 2003), and enrichment in LREE and LILE in comparison with mid-ocean-ridge basalts (MORB). All these features are observed in alkaline complexes interpreted to be confined to the slab window, including the Challis, Absaroka and Kamloops volcanic series, and the Montana alkaline province. The presence of adakites (andesitic to dacitic magmas with presumed derivation from subducted crust) in the Princeton and Kamloops volcanic fields of southern British Columbia is consistent with the interpretation that the edge of the slab window is located beneath this area (Breisprecher et al., 2003).

Several estimates are proposed for the location of the Kula-Farallon spreading ridge when it reached the North American trench and formed a triple junction prior to subduction. However, there is an uncertainty of > 3,000 km in the location of the Kula-Farallon plate boundary (Bunge and Grand, 2000). Change in the strike of the subducted slab from northwest-southeast north or the Great Lakes to north-south south of the Great Lakes is observed in seismic images, perhaps indicating the current location of the Kula-Farallon spreading ridge (ibid.).

2.4 Black Hills

2.4.1 Structure and timing

The following description of the Black Hills area is based on the work of Lisenbee and DeWitt (1993). The Black Hills uplift is a northwest-trending, doubly plunging anticline that is made up of several north- and northwest-trending west-vergent monoclines (ibid.). Steep, west-facing monoclines border the uplift on its western margin adjacent to the Powder River Basin to the southwest. On the eastern margin, a gentler, broad arch bounds the uplift where it abuts the Williston Basin to the northeast. It is estimated that 2,700 m of differential uplift occurred between the Black Hills and the adjacent basins. The uplift is separated into two blocks east and west of the Fanny Peak Monocline. The western block plunges to the north, and the eastern block plunges to the south and is uplifted ~335 m relative to the western block. The Precambrian core of the uplift is exposed in the eastern block. Reverse faults are interpreted to be present under the monoclines in the western part of the uplift (ibid.).

The sedimentary record in both the Powder River and Williston Basins indicates that the Black Hills uplift formed initially during the Laramide orogeny, beginning around 65 Ma. Vertical movements occurred again in the Late Paleocene or Early Eocene, as evidenced by an angular unconformity between sedimentary rocks deposited in the Powder River Basin. The size and orientation of this uplift are similar to other Laramide-related uplifts in the western United States. However, the large distance of the Black Hills uplift from the trench makes it difficult to explain its relationship to other Laramide complexes. One hypothesis is that the crustal boundary between the Archean Wyoming Province to the west and the Trans-Hudson Province to the east may have played a key role in concentrating stress and inducing deformation.

2.4.2 Igneous rocks

The northern Black Hills intrusive belt consists of a linear, west- to northwest-trending suite of dominantly alkaline rocks that straddle the boundary between the Archean Wyoming Craton to the west and the Proterozoic Trans-Hudson crust to the east (Fig. 2.3). The Black Hills belt includes from east to west:

1) Bear Butte;
2) Black Hills intrusive complex, host of the Homestake Au deposit at Lead;
3) Tinton mining district, located on the Wyoming-South Dakota border;
4) Bear Lodge Mountains;
5) Devils Tower;
6) Missouri Buttes;
7) Barlow Canyon Laccolith;
8) Many smaller laccoliths, dikes and sills, both exposed and buried.

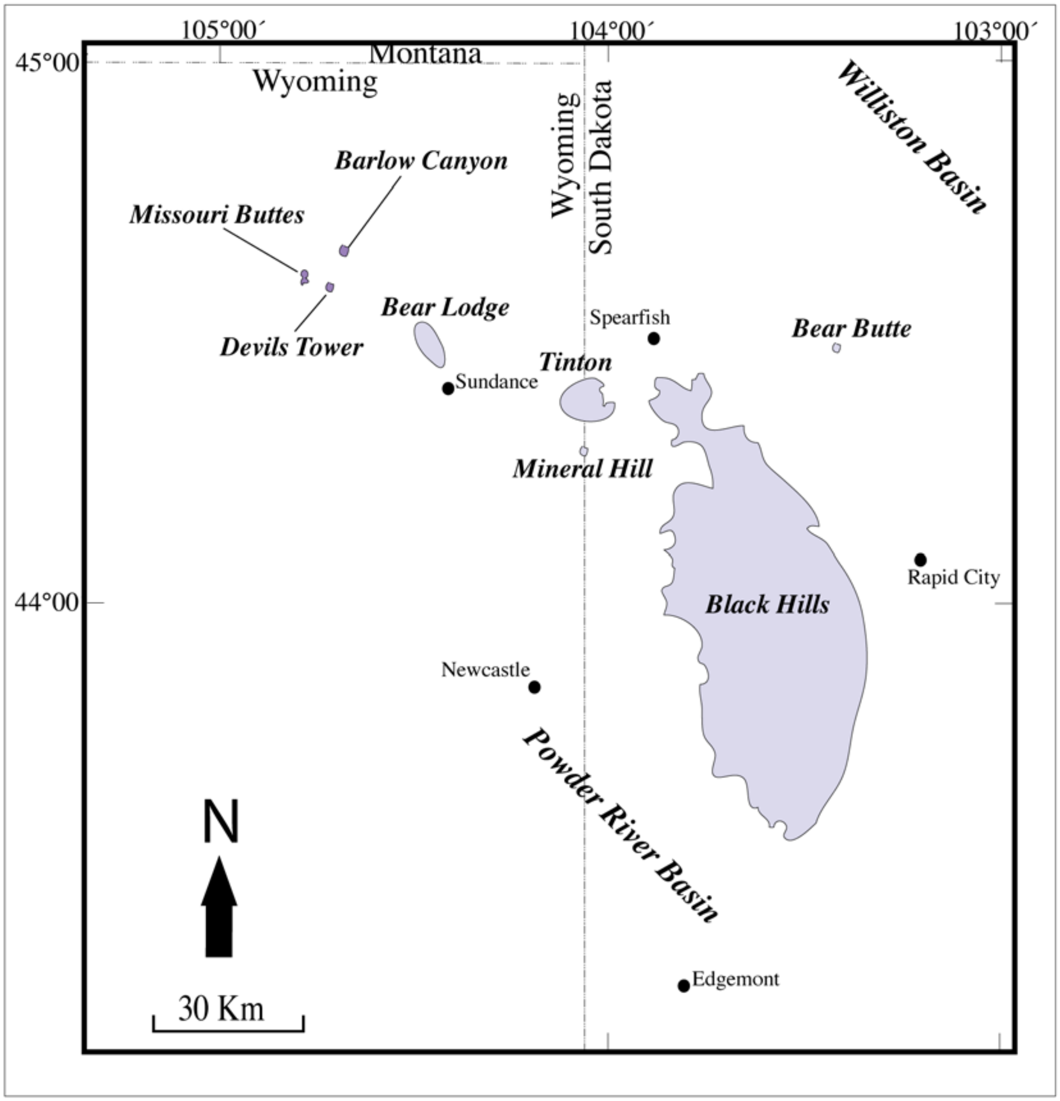

Figure 2.3. Location map of the northern Black Hills intrusive suite discussed in text. Municipal localities shown for reference.

The igneous rocks decrease in age from ~62 to ~48 Ma and in their degree of silica saturation to the northwest (Snoke, 1993). The eastern igneous bodies, from Tinton to Bear Butte, are dominantly calc-alkaline to subalkaline in composition (granite and rhyolite), whereas the western half of the belt, from Lead (located ~20 km southeast of Spearfish) to Barlow Canyon, comprises dominantly alkaline rocks: essexite, ijolite, syenite and nepheline syenite, with subordinate quartz monzonite and granite. However, there are some exceptions to this distribution. For example, carbonatite was reported in the Tinton dome by Lisenbee and DeWitt (1993). Geochemically, rocks from the northern Black Hills igneous belt are largely iron-rich and metaluminous to slightly peraluminous (Lisenbee and DeWitt, 1993). Snoke (1993) postulated that the shallow-level intrusions were emplaced along a Precambrian zone of crustal weakness. The temporal relationship between uplift (see above) and magmatism is not well understood (Lisenbee and DeWitt, 1993).

Chapter 3. Bear Lodge Alkaline Complex (BLAC)

3.1 History of Exploration and Previous Work

The following is a brief account of those who have made notable contributions to the Geological understanding of the BLAC (for further references, see Staatz, 1983; Noble et al., 2009 and Noble, 2013). The first reference to rocks in the Bear Lodge Mountains was made by the explorer Lieutenant G.K. Warren, who led an expedition to the area in 1857 (Staatz, 1983). With gold fever ensuing in the Black Hills in the mid- to late 1800's, the search inevitably reached the Bear Lodge Mountains. This culminated in the short-lived Bock Mine and a small milling operation in 1880. Prospecting for gold continued in the 1880's. Newton and Jenny first noted Th- and REE-rich veins in their account of the area (Staatz, 1983). The first geological map including the Bear Lodge Mountains was compiled in the early 1900's by Darton and O'Hara, who mapped the 30' Devils Tower, Sundance and Aladdin quadrangles at the 1:125,000 scale (ibid.). Darton summarized the contemporary understanding of the geology of the Bear Lodge Mountains in 1909.

The USGS and United States Bureau of Mines (USBM) were primarily interested in the U and Th potential of the area following the Atomic Energy Act of 1946 and subsequent creation of the United States Atomic Energy Commission (AEC). The USBM explored the Bear Lodge Mountains in 1944 for fluorite and in 1949 for REE- and Th-rich veins that were studied by Wilmarth and Johnson of the USGS (Staatz, 1983; Noble et al., 2009). In 1950, the USBM delineated an area with an average total content of REE above 2000 ppm, and they drilled and sampled the veins in 1951. The search for U in the Black Hills and Bear Lodge Mountains, stimulated by the AEC, continued through the 1950's.

In 1983, Staatz with the USGS, published a detailed study of the geology of the BLAC, with particular emphasis on the Th and REE deposits. In the process of compiling USGS Professional Paper 1049-D, Staatz completed petrographic and geochemical analyses, a radiometric survey, an extensive sampling program and a larger scale (1:24,000) geological map of the area, with corresponding radioactivity and element contour maps. In this publication, Staatz wrote: "The Bear Lodge disseminated deposits have one of the largest resources of both total rare earths and thorium in the United States, and although the grade of both commodities is lower than some other deposits, their large size and relative cheapness of mining make them an important future resource" (p. D1).

Following the decline of interest by the USBM in the 1950's, different mining companies acquired claims and conducted exploration programs focused on several different commodities in the Bear Lodge District. In 1972, the Duval Corporation identified Cu, low-grade Au and REE mineralization, and initiated a drilling and exploration program focused on porphyry Cu-Mo type mineralization using the carbonatite-related Palabora deposit in South Africa as a model. The rare earth mineralization was significant enough for Duval Corporation to engage Molycorp as a joint venture partner in 1978. Molycorp was already involved with REE mining and production at its Mountain Pass mine in California. Molycorp conducted a drilling program specifically focused on the REE mineralization in the Bear Lodge Mountains between 1978 and 1980. They also completed geological mapping and soil geochemical, ground magnetic, radiometric, induced polarization-resistivity, and transient electromagnetic surveys. This work resulted in an estimated resource of 8.3 million tonnes of total rare earth oxides (REO) grading ~1.71% in two areas and one body with 6.2 million tonnes grading ~1.25% REO (unpublished data). In 1980, Molycorp was absorbed by UNOCAL and pulled out of the joint venture. Duval Corporation continued exploration at decreased levels, completing two drill holes, a gravity survey, and trenching until 1984, when the property was discarded with the formation of Battle Mountain Gold from Duval Corporation. Western Nuclear Incorporated investigated the potential for radioactive minerals with a small drill program in 1984-1985.

Between 1986 and 1991, Hecla Mining Company focused on exploration for rare-earth mineralization in the Bear Lodge Mountains with the acquisition of a core property from Newmont and a large block of adjacent claims. Hecla's exploration program identified a "geological" resource of 7.7 million tonnes at a grade of 3.0% REO, including 3.9 million tonnes grading 3.8% REO in three carbonatite dikes. Hecla's interest shifted from REE to Au mineralization in the Bear Lodge Mountains in 1991. Also in 1991, the USBM re-evaluated the drilling results from their work in 1951, defining a stockwork-type deposit with 1.5% REO in 10 of 20 holes (unpublished data).

Many other companies invested in Au exploration in the Bear Lodge Mountains through drilling, geophysical and geochemical programs. The list of companies includes: FMC Corporation (1982-1986), International Curator Resources (1987-1988), Newmont Exploration (1986-1988; 2003-2010), Cocoa Mines (1990-1991), Hecla (see above) and Phelps Dodge (1994-1996). The American Copper and Nickel Corporation explored the area for its Au potential, completing their work between 1988 and 1989. For detailed further information regarding the amount and extent of exploration conducted by these companies, refer to Noble et al. (2009).

3.2 Current Exploration and Research

Rare Element Resources (RER) has been conducting exploration in the Bear Lodge Mountains since 2004 with a focus on REE mineralization and definition of a viable economic resource. Drilling programs were conducted in 2004-2005 and 2007-2013. In 2006, a joint venture was established between Newmont Mining Corporation and Paso Rico (USA), a subsidiary of RER, for further exploration focused on both gold (by Newmont) and rare earth elements (by RER). Newmont pulled out of the joint venture in 2010 after compiling an extensive database, including detailed geological mapping and geochemical (soil and rock chip) and geophysical surveys. The geophysical work included gravity, IP-resistivity, radiometric and controlled source audio-magnetotelluric surveys.

The current rare-earth exploration program by RER and previous results from the Hecla program indicate that the most significant REE resource occurs in a zone of carbonatite and carbonatite-related dikes that cut the Bull Hill diatreme and adjacent trachyte-phonolite host rocks along the southwestern flank of Bull Hill. The 2011 exploration program identified three additional targets that contain significant REE mineralization in the Whitetail Ridge, Carbon Hill and East Taylor Ridge locations. The latter three targets have higher abundances of HREE than Bull Hill.

A preliminary economic assessment (John T. Boyd Company, 2010) and preliminary feasibility study (PFS; Roche Engineering, 2011) were completed for the Bear Lodge project, and an updated PFS is scheduled for release in 2014. The objective of the project is the development of an open-pit mine, physical upgrading plant and hydrometallurgical plant. Both cited studies issued NI 43-101 compliant reports that indicate that the Bear Lodge project is economically and technically viable. The PFS by Roche Engineering (2011) indicates that, provided favorable market conditions, the mine will come on-stream in 2015, with a projected life of at least 19 years. The current updated measured plus indicated resource is 15.71 million tonnes at a grade of 3.11% REO. Only the near-surface oxide and oxide-carbonate (see Section

3.3 below) subzones are included in the mine plan. At the time of this writing, the project is moving from the exploration to development stage.

These recent developments provided previously unavailable opportunities and ample research material for in-depth studies of the BLAC and related mineralization. Olinger (2012) completed an M.Sc. thesis focused on the whole-rock geochemistry of carbonatites and their host rocks with an emphasis on calcite textures and parageneses. Felsman (2009) completed an M.Sc. thesis focused on Au mineralization in the Carbon Hill and Taylor Ridge areas of the Bear Lodge Mountains. This study included a detailed analysis of lithologic units, structural geology and host rock alteration. Duke (2005, 2009) published on the regional geology, including the Bear Lodge Mountains, Black Hills and nearby alkaline complexes that probably formed in the same tectonic environment. Her work focused on the Sr-Nd isotopic variation, whole-rock geochemical characteristics and geochronology of individual igneous occurrences in the Great Plains Alkaline Province. Jensen (2003) completed a Ph.D. dissertation on the Cripple Creek deposit in Colorado, which is hosted in alkaline rocks. He compiled data on similar alkaline magmatism and related ore deposits elsewhere, including the Bear Lodge Mountains. Since 1977, Dr. Anthony N. Mariano has been involved in REE exploration in the Bear Lodge Mountains for several companies, including Molycorp, Hecla, and RER. He has contributed much important geological and mineralogical knowledge to their exploration efforts. Dr. James Clark was involved in REE exploration for both Hecla in the late 1980’s, and currently for RER. He has also made many contributions to the understanding of this deposit. Dr. Mariano and Dr. Clark, along with John Ray (currently Chief Geologist for RER) were consulted on multiple occasions during the preparation of the present thesis. Their contributions were mostly through personal and e-mail communications, but they also gave access to unpublished technical reports.

3.3 Local Geological Setting

The BLAC is a dome with dimensions of ~13 km NW-SE by 10 km NE-SW, consisting of multiple intrusions that were subjected to polyphase hydrothermal and metasomatic activity. Porphyritic to aphanitic textures indicate a sharp thermal gradient between the intrusions and their country rock, and given the young age of magmatism, imply shallow emplacement. The presence of minor volcanic rocks broadly contemporaneous with the intrusions suggests that the complex was part of a larger volcano-plutonic system.

Staatz (1983) reported (K/Ar) radiometric ages of sanidine crystals that ranged from 50.5 to 38.3 Ma and concluded that the Eocene igneous activity in the Bear Lodge Mountains was long-lived. Lisenbee and DeWitt (1993) interpreted the younger ages as spurious, based on regional geochronological data. Five pulses of magmatism were recognized by Duke et al. (2002), including three regional pulses occurring at ~58 Ma, 55-54 Ma and 50-46 Ma, and two younger undated events (Duke et al., 2002). The ages of late-magmatic phases in the BLAC (latite and trachyte whole-rocks), determined with the ^{40}Ar/^{39}Ar incremental heating technique, are 47.3 ± 0.20 and 46.0 ± 0.30 Ma (errors are 2θ), respectively (Duke et al., 2002). ^{40}Ar/^{39}Ar age determinations of biotite and orthoclase hosted in altered carbonatites range from 51 ± 0.04 to 52 ± 0.20 Ma (Anderson, 2013a). The most recent Geological map with the location of units of the Bear Lodge complex was compiled by Newmont and RER geologists (Fig. 3.1).

3.3.1 Igneous rocks

Precambrian granite, subjected to variable degrees of fenitization, consists of alkali feldspar, biotite and locally quartz, with accessory magnetite, apatite, zircon and monazite. This rock is preserved as rafts in the southern part of the complex and represents the only igneous unit in the BLAC not directly associated with Eocene magmatism. This unit is modified in some areas by fenitic alteration involving the dissolution of quartz, similar to the “bug hole” granites associated with fenitization at the Cripple Creek Gold deposit, Colorado (Jensen, 2003).

Eocene igneous rocks consist of a central intrusive body with subordinate plugs, sills, dikes, laccoliths and diatremes (Fig. 3.1). Geophysical data indicate the presence of satellite intrusions at depth (Ray, 2009, 2013 personal communications; Clark, 2009 personal communications). Igneous units are described below based on the NI-43-101 technical report of Noble et al. (2009), confidential reports by Mariano (1978b, 1981, 1988) and personal communications by Ray (2009). Silicate rock units were not investigated in the present work.

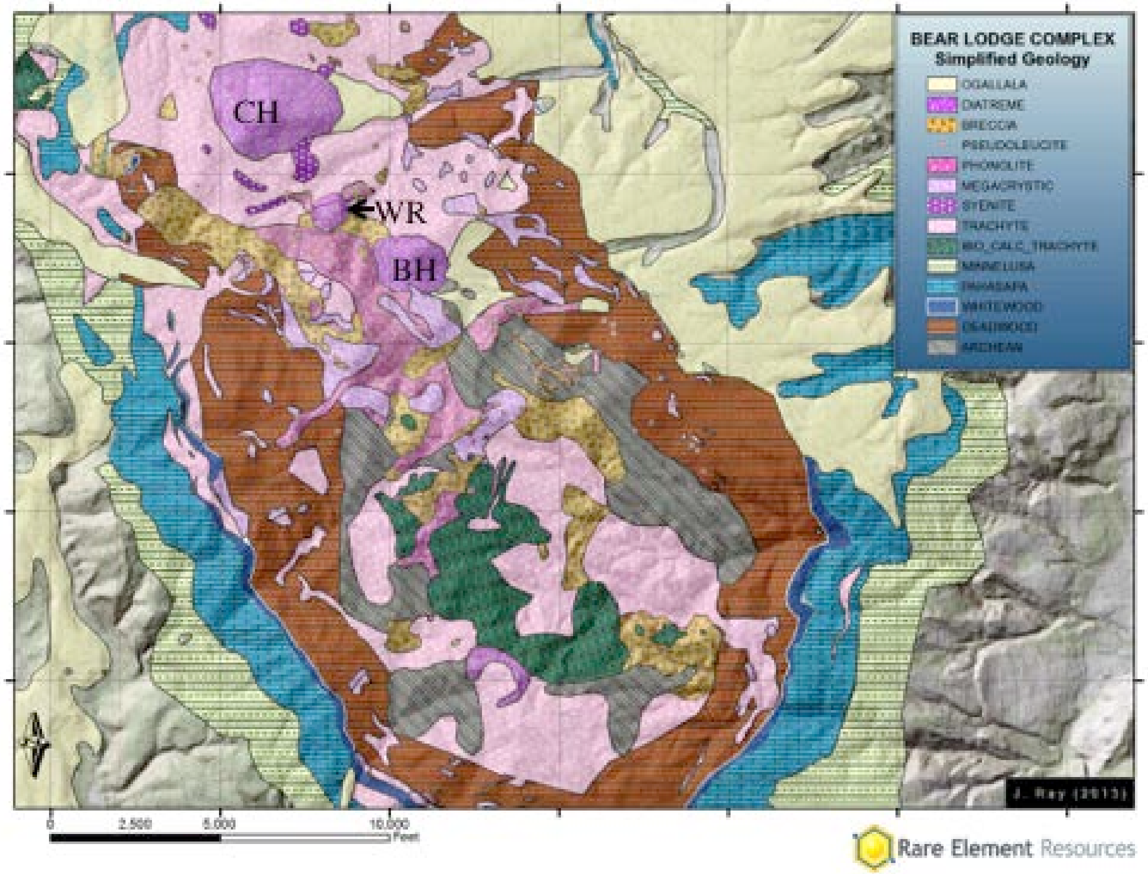

Figure 3.1. Simplified Geological map of the BLAC courtesy of RER, showing locations discussed in text. BH = Bull Hill, CH = Carbon Hill and WR = Whitetail Ridge.

Stocks and sills of trachyte and phonolite are the largest units by volume and are located in the central part of the complex. These units occur both pre- and post-carbonatite emplacement. Syenite is also present in the north-central part of the complex. A gradational boundary between trachyte and syenite was observed in some areas by Felsman (2009). Small volumes of trachyte or phonolite flows are present around the periphery of the dome.

Phonolite and trachyte units are named in the field according to the presence or absence of feldspathoid (dominantly nepheline) phenocrysts. Felsman (2009) identified four different trachyte units, based on texture, turbidity of groundmass feldspars, groundmass and phenocryst feldspar compositions and phenocryst abundance. Specific units, including those described by Felsman (2009) and Noble et al. (2009), include megacrystic sanidine trachyte porphyry, hornblende trachyte porphyry, carbonate-bearing trachyte, trachyte porphyry, trachyte and phonolite porphyry. Trachytoid (sub-parallel alignment of feldspar phenocrysts; Le Maitre, 2002) and flow textures are observed in drill core (e.g., Molycorp DDH #6, 627' intercept; Mariano, 1978b). These rocks generally consist of phenocrysts or megacrysts of sanidine and/or nepheline, with lesser biotite and clinopyroxene phenocrysts, in an aphanitic groundmass of sodic or potassic feldspar, devitrified glass, biotite, nepheline and/or sodalite, alkali amphibole, augite and accessory pyrite. Carbonate minerals (dominantly calcite) occur in association with pyrite. Small veinlets of potassium feldspar are minor in abundance, which indicates incipient fenitization affected these rocks (Mariano, 1978b; Felsman, 2009). The structural relations and petrographic mineralogical and textural variations among these different units provide evidence of multiple episodes of trachyte emplacement both prior to, and following, fenitization (Felsman, 2009).

Syenite, microsyenite and nepheline syenite are grouped under the name “syenite”. These rocks have variable textures and consist of alkali feldspar of sodic or potassic or mixed compositions ± nepheline, biotite, clinopyroxene and amphibole. Olivine, titanite, magnetite and pyrite occur in accessory amounts, whereas allanite, apatite, pyrrhotite and ilmenite are very scarce. Syenite clasts are found within diatremes, indicating that some syenite intrusion predated the diatreme emplacement. Fenite alteration is also observed in the syenites (Mariano, 1978b).

Dikes of late-stage pseudoleucite porphyry crosscut the trachyte, phonolite and diatreme breccias, and also form clasts in the diatremes. Pseudoleucite refers to replacement products of leucite, often comprising several complexly integrown minerals (e.g., nepheline + analcime), or a monomineralic aggregate of potassium feldspar. Other constituents in the porphyry include sanidine ± andradite phenocrysts in an aphanitic groundmass of devitrified glass, nepheline, potassium feldspar, biotite and pyroxene, with accessory sulfide minerals.

Mariano (1978b) described distinct textural and mineralogical variations in the igneous rock units he observed in specific intervals of Molycorp holes DDH#5 and #6. In the 83-92 m interval of DDH#5, malignite consists of nepheline, augite and potassium feldspar, with accessory apatite and titanite. Augite is replaced by andradite, biotite and calcite in some areas; calcite also infills microfractures. The 265 m intercept is slightly different and is classified as a juvite-malignite. Here, some of the nepheline appears to be a product of incipient fenitization. Minor amounts of pyrite are also present, along with ~20 vol. % calcite. In hole DDH#6, augite, biotite, apatite, and calcite occur as inclusions in andradite; and primary calcite makes up ~20 vol. % of the rock (Mariano, 1978b).

Lamprophyres, classified based on their textural features and mineralogy, occur both early and late in the intrusive sequence. These rocks were not studied in this work; the following descriptions are from Noble et al. (2009). The rocks are dark grey to black and fine-grained, with mafic minerals composing ≥ 50 vol. %. Pyroxene, biotite, nepheline, potassium feldspar and pyrite are rock-forming minerals, whereas magnetite, apatite and carbonate are accessory phases. These rocks are spatially and temporally associated with trachyte and the diatreme units.

At least two different breccia units are identified in the BLAC; these units contain clasts of variable composition, size and morphology. Intrus*ion* breccia (note the spelling) occurs along the southern and northeastern contacts of the Bull Hill diatreme. Clasts in this unit are dominantly monolithic trachyte or phonolite in a trachytic or phonolitic matrix. Intrus*ive* breccia with heterolithic clasts occurs as pipes or bodies that form the Whitetail Ridge, Carbon Hill and Bull Hill diatremes. This breccia type is volumetrically larger than the previously mentioned intrusion breccia and is more phonolitic in composition. The Carbon Hill diatreme is very different in appearance from the Bull Hill diatreme, and these diatremes may represent two or more distinct events in the evolution of the BLAC. The Carbon Hill intrusion breccia is matrix-supported with clasts of syenite and microsyenite in a porphyritic microcrystalline matrix of syenitic composition.

The Bull Hill diatreme is composed of a heterolithic, matrix- and locally clast-supported breccia. Variably altered clasts are composed of carbonatite, syenite trachyte, pyroxenite and lamprophyre. Three zones, differing in the extent of alteration of precursor rocks and REE potential, are recognized within the diatreme: an oxidized zone, which has a variable thickness and locally extends to depths of more than 100 m below the surface. The oxidized portion of the mineralized body is divided into two subzones in this work, referred to below as “FMR”-type (for the abundance of Fe, Mn and REE minerals in this unit) and “Ox-Ca” subzone (oxides + carbonate minerals). The latter is distinguished from the more intensely altered “FMR”-type by the presence of some relict carbonate and sulfide material. The “Ox-Ca” subzone generally underlies the “FMR”-type, but in some areas, is exposed at the surface. The “Ox-Ca” subzone grades into the transitional zone at depths ranging from ~150 to 180 m below the surface. In the transitional zone, some (but not all) sulfides are oxidized and maintain their relict crystal form. The transitional zone overlies the unoxidized zone, where sulfides are not affected by oxidation. The unoxidized igneous material generally occurs at depths in excess of 180 to 190 m below the surface. Further details on mineral relations in these different units are provided below and in Chapter 5.

Carbonatites occur as microveinlets, veins, and dikes that crosscut the Bull Hill diatreme in a structurally controlled, dominantly northwestern orientation, and with a steep northeast-southwest dip. A small carbonatite dike cutting the Carbon Hill diatreme is exposed at the surface, whereas carbonatites in the Bull Hill diatreme are only encountered in sub-surface samples from drill core or trenches. The textural and mineralogical characteristics of the carbonatites are extremely variable. Detailed petrographic descriptions are given in Chapter 5. Mineralogical and geochemical data are presented in Chapters 6 and 7.

The most recent geochronological data indicate that the carbonatites in the BLAC were emplaced after the voluminous 46-50 Ma magmatism, but prior to the emplacement of late-stage trachytes and phonolite dikes at 38-40 Ma (Duke, 2005; 2009; Clark; 2009; Felsman, 2009). The work of Anderson (2013a) indicates the presence of primary biotite and potassium feldspar in the carbonatites that are older than the associated silicate rocks. This discrepancy can be explained by the ambiguity of crosscutting relationships between the carbonate and silicate rocks. Carbonatites both crosscut the Bull Hill diatreme as dikes and occur as clasts within the diatreme breccia. Notably, the carbonatite clasts are invariably barren of REE mineralization and may represent an early carbonatite intrusive event (Clark, 2014, personal communication). Thus, we conclude that carbonatitic activity was nearly contemporaneous with, but outlasted the emplacement of the diatreme.

3.3.2 Structural geology

The BLAC is a dome comprising two lobes. The southern lobe was uplifted relative to the northern lobe (Felsman, 2009). Gravity and magnetic anomalies show that the root of the dome is a deep cylindrical mass that plunges to the northeast (Ray, 2013). Radial fractures associated with the uplift facilitated the emplacement of dike swarms and veins within the dome. Earlier-emplaced dikes generally have a northwest or northeast strike, whereas younger dikes strike north-northwest in response to regional Laramide-related compression superimposed on the stress field that was developed locally around the dome (Felsman, 2009). Faults and folds in the BLAC are intimately associated with and likely facilitated the intrusion of the igneous units (Staatz, 1983). The Bull Hill diatreme is located in the ENE trending Redwater Creek Graben (Ray, 2009, personal communications). The Whitetail Ridge, Carbon Hill and Bull Hill diatremes have a general northwest alignment.

3.3.3 Alteration

Several types of alteration occur within the Bear Lodge alkaline complex, including supergene oxidation, fenitization (i.e., metasomatism by alkali-rich oxidizing fluids), and hydrothermal carbonate alteration associated with REE mineralization in the Bull Hill diatreme. Alteration of potassium feldspar and pyrite, sulfidation, fenitization, and oxidation along with minor argillic alteration, sericitization and silicification are associated with Au mineralization within the same exploration area (Felsman, 2009; Noble et al., 2009). This section will consider exclusively the alteration associated with REE mineralization.

Fenitization is a complex style of alteration that is not always readily identified or recognized (Jensen, 2003). Alkali metasomatism, via oxidizing fluids associated with carbonatitic, alkaline, or peralkaline magmatism, stabilizes Fe in the ferric (Fe^{3+}) state (Mariano, 1978a). This allows for small amounts of Fe^{3+} substitution for Al^{3+} in feldspars, particularly potassium feldspar. This substitution enhances feldspar luminescence and is most easily recognized with cathodoluminescence imaging techniques. In the BLAC, fenitization is widespread and ranges from incipient to massive. Some trachyte samples consist almost entirely of metasomatic potassium feldspar (Felsman, 2009). Fenitization is more pervasive in the Carbon Hill diatreme than in the Bull Hill diatreme. During fenitization, biotite and pyrite form at the expense of primary mafic minerals and are eventually altered to clay and iron oxides. Rare-earth mineralization is also associated locally with fenitization.

Fenitization recognition criteria include (Felsman, 2009):

- the presence of turbid potassium feldspar that commonly shows red luminescence and is associated with biotite and pyrite;
- potassium feldspar veinlets;
- replacement of plagioclase and groundmass minerals with potassium feldspar;
- the removal of silica (manifested by the absence of quartz in some areas of the Precambrian granite);
- the remobilization of sodium in the system to form aegirine and aegirine-augite;
- bleaching;
- development of glimmerite or hydrothermal biotite veinlets;
- formation of green-luminescent “pinprick” fluorite;
- orange-luminescent hydrothermal apatite rims around primary apatite;

- destruction of magnetite.

Oxidation overprints fenitization, early silicification, and argillization throughout the district. It is most pervasive in the Bull Hill diatreme, where oxidation can permeate to depths of more than ~230 m below the surface. Oxidation is also present below this level, but is structurally controlled (Felsman, 2009). In the oxidized zone of the Bull Hill diatreme, Fe and Mn oxides and hydroxides (such as goethite, hematite and ramsdellite) are present as amorphous, cryptocrystalline, or botryoidal coatings on fracture surfaces and in vugs. They replace early mafic minerals and calcite to produce a gossanous cap over the fresh or incipiently altered diatreme material below. The presence of cerianite (CeO_2), found together with bastnäsite and other minerals depleted in Ce, attests to a high O_2 activity at this alteration stage. In the Taylor Ridge area, it is noteworthy that goethite is the most common secondary Fe mineral, whereas hematite dominates at Carbon Hill (Felsman, 2009). This indicates variable H_2O activity in the oxidation profile.

Carbonate alteration, resulting in replacement of minerals by calcite and development of calcite veining, may or may not be associated with carbonatite magmatism. Mariano (1978b) determined that calcite veining in malignite is not associated with REE mineralization, suggesting no genetic link to the carbonatites. Overall, it is difficult to establish definitively which types of alteration are related to the emplacement of carbonatite dikes and veins. In this work, only glimmerite zones along the selvage of some veins could be conclusively identified as a product of interaction between carbonatite and its silicate wallrock.

Chapter 4. Methodology

All applicable instrumental standards and set-up parameters are listed in Appendix B as Tables B.1 –B.6.

4.1 Microscopy

Slabs from the representative samples were cut by the author manually with the goal of capturing the minerals and textures of interest while preserving an adequate amount of material for other types of analysis. These slabs were cut into conventional (26 × 46 × 0.03 mm) polished thin sections and thick sections (26 × 46 × 0.1-0.2 mm) by Vancouver Petrographics. Thick sections were made predominantly for samples consisting of opaque minerals from the oxidized zone. Preliminary petrographic characterization (mineral identification and investigation of textural relationships) of all polished sections was conducted in transmitted and reflected light, using a binocular Nikon polarizing microscope and attached Nikon camera for sample imaging and mapping.

4.2 Cathodoluminescence

Cathodoluminesence (CL) imaging is a petrographic technique that has been widely applied to the characterization and recognition of REE minerals, fenitization and other purposes, where polarizing microscopy is not adequate (e.g., Mariano, 1978a, 1988a, 1989d; Marshall, 1988; Mason and Mariano, 1990). The CL techniques involve bombardment of a sample (usually a thin polished section, polished slab or grain mount) with a beam of accelerated electrons generated by a cathode gun. The electron bombardment causes excitation of electrons in the sample to a higher-energy level, followed by their stepwise return to the initial (ground) state, which involves emission of visible photons from elements that behave as cathodoluminescence “activators” (ibid.*)*. Typical activators include cations characterized by electron transitions in their inner orbitals shielded by outer orbitals, such as REE^{3+} (Mariano, 1978a; 1989d), as well as elements with unfilled outer orbitals, such as Mn^{2+} (Marshall, 1988). Activators generally occur as minor substituents in minerals (e.g., Mn^{2+} in calcite). Crystal-field effects are responsible for variations in CL color of the same activator in different minerals. An example of this effect is orange Mn^{2+}-induced luminescence in calcite and red Mn^{2+}-induced luminescence in dolomite. Thus, the emission wavelength is distinct for each activator-mineral combination (Marshall, 1988).

It is noteworthy that, if an activator is present in high concentrations, it may “quench” luminescence, which is known as concentration quenching (Marshall, 1988; Mariano, 1989d; Mason and Mariano, 1990). For example, minerals containing REE as major elements (e.g., ancylite) tend not to show any cathodoluminescence. In some cases, elements present at trace levels (e.g., Fe^{2+} in carbonates) can also act as “quenchers” by absorbing photon emissions (Mariano, 1978a; Marshall, 1988; Mason and Mariano, 1990).

Cathodoluminescence imaging is a powerful observational tool for qualitative assessment of the presence of trace elements in a mineral (Marshall, 1988; Mariano, 1989d). Because CL imaging has high sensitivity to some trace elements that occur in amounts below the detection limits of other standard techniques (e.g., back-scattered electron imaging, electron-microprobe analysis), it is indispensable for the detection of fine-scale zonation in minerals containing activator cations (Mariano, 1978a; Marshall, 1988). For further information about this technique, refer to Marshall (1988). In the present study, the CL imaging technique was used to select samples and areas for further analysis. All CL images were acquired with a Technosyn cold-cathode system attached to a Nikon binocular petrographic microscope. Instrumental conditions were optimized for each sample, but generally the beam current was set at ~15kV and 220-630 μA.

4.3 Electron-microprobe Analysis

Electron-microprobe analysis (EMPA) is well suited for the quantitative characterization of geological materials because this technique is generally non-destructive (but see below), capable of in situ analysis of small samples (a few μm across), and has a detection limit on the order of $n \times 10^2$ ppm for many elements. Additionally, a variety of imaging capabilities is typically available in modern electron-microprobe instruments. These techniques involve bombarding the sample with a beam of electrons generated by a tungsten filament and accelerated by an anode. When the electron beam interacts with the sample, electrons in atoms at the surface are excited and emit X-ray photons when they return to their ground state. This type of emission can be detected and quantified with different types of spectrometers. An energy-dispersive spectrometer is designed to measure the energy of the photons. It is utilized in energy-dispersive spectrometry (EDS) used primarily for the identification of major and minor elements present in the sample (covering the range from F to U). A wavelength-dispersive spectrometer (WDS) is tuned to a specific wavelength of X-ray emission and is used to convert the number of registered photons to the concentration of a specific element in the sample.

4.3.1 EMPA instrumental parameters

All electron microprobe analyses for this thesis were conducted at the University of Manitoba on a Cameca SX100 electron microprobe equipped with a Windows-based operating system and a PGT EDS and five WDS spectrometers. The specific acquisition information and spectrometer setups for analysis of REE minerals are listed in Table B.1; Table B.2 lists the analytical setups for apatite and carbonate minerals. Although most of the minerals analyzed are rare-earth carbonates or fluorocarbonates, and thus not thermally stable under the high-energy electron beam, the small grain size precluded using beam diameters > 10 μm. Count times were 20s on peak and 10s on background positions, with the exception of F, for which these parameters were 30s and 15s, respectively. Fluorine was first in the acquisition sequence, followed by Na to avoid their loss to volatilization or diffusion. Matrix corrections were conducted using a ϕρz model with the Cameca software. Peak-overlaps were corrected by manually resetting background locations on either side of the peak or, when not possible due to overlaps, calculating a slope and using peak height analysis program (Table B.1). Minerals that were characterized using EMPA include bastnäsite, parisite, synchysite, ancylite, monazite, cerianite, apatite, strontianite and calcite. Back-scattered electron (BSE) images were used in conjunction with petrography to investigate textural and temporal relationships. Nineteen elements were included in the analysis of REE minerals (Table B.1). The rare-earth orthophosphate standards (Table B.3**)** were used to calibrate the instrument for the REE.

4.4 Mass Spectrometry

Mass spectrometry (MS) is used in a variety of geological applications, including quantification of mineral chemistry and isotopic analysis of whole rock and mineral samples. There are different MS instruments that vary with respect to resolution, sample introduction, ion source, ion separator (mass analyzer), and ion detector (collector). The MS techniques are best suited for the quantification of (ultra-)trace elements or isotopes. Minimal interference problems and a low background of mass spectra, in addition to the variety of available instrumentation, make these techniques readily tunable to a specific sample type or research goal.

After introduction of the sample into the instrument, different elements are atomized and then ionized. The ions are transported via different mediums (depending on the instrument) to a mass analyzer, where they are separated based on the flight paths of different ionic species in an electromagnetic field. The mass analyzer focuses the ions into a collector, which measures the mass-to-charge ratio of the elements or isotopes selected for analysis, and counts the number of different ionic species. Mass spectrometry is a destructive technique that has quantitative detection limits in the 0.1 to 1 ppb range, depending on the resolution and sensitivity of a particular instrument.

Three different mass spectrometers were used in this work: a laser-ablation inductively-coupled-plasma mass spectrometer (LA-ICP-MS) for determination of trace elements in calcite, strontianite, fluorite, ancylite, apatite, monazite and rare-earth fluorocarbonates; a thermal ionization mass spectrometer (TIMS) for determination of Sr, Nd and Pb radiogenic isotopic compositions of whole-rock samples; and a gas-bench isotope-ratio mass spectrometer (GB-IRMS) for determination of stable C and O isotopic compositions of calcite (Table B.4).

4.4.1 Laser-ablation inductively-coupled-plasma mass spectrometry

The LA-ICP-MS technique begins with the introduction of a solid sample, in this case a polished thick-section, which is then ablated with a laser in a He atmosphere into a very fine aerosol that is atomized and ionized in a high-temperature plasma torch and coupled with Ar gas that carries the ions to the mass spectrometer. Mass fractionation, contamination and interference issues associated with complex ions can be problematic, but are generally avoided and corrected for using instrumental software. For the purposes of trace element determinations, one element (usually a major element) is independently quantified as an internal standard in order to convert the number of raw counts measured by the MS detector into concentrations of the unknown elements.

All trace-element analyses for this work were conducted at the University of Manitoba on a Thermo-Finnigan Element 2 high-resolution sector-field ICP-MS attached to a UV 213 nm nano-second laser-ablation system. The instrument was calibrated using the NIST610 glass standard at the beginning and end of every sequence of analyses to account and correct for instrumental drift. The BCR standard was analyzed at the end of each sequence in order to determine the precision of the analytical data. The laser-ablation instrumental settings were as follows: a 30 µm beam diameter was used for both spot and transect analyses; laser power was set at 80% with a repetition rate of 10Hz for measurements of the standard and reduced to 5 Hz for measurements of the sample at a fluence of 8.02 J/cm^2. A laser warm-up time was 30 s, followed by 43 runs in a 60 s ablation window for spot analyses. Transects were run at 5 µm/s and a repetition rate of 20 Hz. The number of runs and repeats varied with the transect length. Minerals were first analyzed with EPMA to quantify the abundance of an internal standard (Sr for strontianite and Ca for all other minerals). Approximately 5 min were allowed between two successive measurements in order for the background level to come down. The calcite and fluorite analyses wer conducted under lowered laser power because they did not ablate well and gave a week signal. The system was also purged for longer intervals between analyses of these minerals in order to eliminate the so-called “memory effect”, where residue from earlier analyses contaminates later measurements.

The Glitter online interactive data reduction software (van Achterbergh et al., 2001) was used for spot analyses, and an unpublished program created by Panseok Yang at the University of Manitoba was used for transect analyses. In all cases, accuracy was estimated to be better than 20%, and precision varied between 5 and 10%.

4.4.2 Thermal ionization mass spectrometry

Thermal ionization mass spectrometry (TIMS) is used exclusively for measuring isotopic abundances in geochronological, geochemical and cosmochemical research. In the present work, Pb, Sr and Nd isotopic compositions were measured using this technique to investigate source characteristics of the Bear Lodge carbonatites and the extent of their interaction with crustal rocks and fluids. Samples were chosen from different parageneses in the unoxidized and transitional zones of the deposit, and consisted of pulps from previously acquired whole-rock geochemical analyses.

All radiogenic isotopic data were collected by a ThermoFinnigan Triton TI TIMS at the Isotope Geochemistry and Geochronology research Centre at Carleton University, Ottawa, Canada. The samples were first dissolved in 6N HCl to extract the carbonate. Because the elements of interest (Pb, Sr and Nd) are not trace elements in carbonatites, the samples were then diluted so their Nd contents were ~3 µg/l to avoid possible contamination of the instrument. Conventional resin column chromatography was then used to separate the elements of interest (see http://iggrc.carleton.ca for details). The elements of interested were dried onto a rhenium filament and loaded on a magazine, which was placed under vaccuum. The instrument uses a current to heat the filament to a specific temperature to ionize the sample. Ions are then focused via high-voltage electrostatic extraction and condenser source plates, where they are transported in a vacuum and separated via deflection around a magnet. Nine faraday cups collect the individual isotopes, which are amplified and recorded by the instrumental software. Table B.6 lists typical instrumental conditions used for TIMS analysis. Some samples needed to be run using the total evaporation (TE) method at a higher current in order for all ions to be collected. In this mode, the entire sample is burned off the filament and 5,000 cycles are run at 0.13 s/cycle.

4.4.3 Gas-bench isotope-ratio mass spectrometry

The GB-IRMS technique was used to measure stable C and O isotopic ratios of samples from different parageneses and zones of the deposit. Grains were handpicked from 17 calcite and one strontianite sample and digested in H_3PO_4 at 70 °C for 2 to 3 h to generate CO_2 gas, in which the isotopic ratios were quantified using the mass spectrometer. All analyses were conducted at the University of Manitoba using a Thermo Finnigan GasBench II connected to a Thermo Finnigan Delta V Plus Isotope Ratio Mass Spectrometer. The sample gases were transferred through two water traps to remove water and a gas chromatograph to separate CO_2 from other species. Sample CO_2 gas was injected ten times into the mass spectrometer, and the signal acquisition time was ~800 s.

The instrument was calibrated at the beginning, middle and end of each run using calcite standards NBS 18 and NBS 19. A calibration curve was constructed using the known and measured values of these standards. As a quality check, calibrated internal calcite standards CHI and Exp50 were run as unknowns. Precision is ± 0.2 ‰ for $\delta^{13}C$ and ± 0.1 ‰ for $\delta^{18}O$.

4.5 Whole-rock Geochemistry

Geochemical analyses of whole-rock pulverized samples were conducted by Acme Labs using lithium borate fusion digestion. The pulverized sample was mixed with a $LiBO_2/LiB_4O_7$ flux, fused in a furnace and digested in HNO_3. The liquid sample was then analyzed by atomic emission spectrometry for major elements, and by ICP-MS for trace elements. Fluorine was determined by titration. The AES method detects elements via photons that are emitted at specific wavelengths for each element. The intensity of photon emission is proportional to the concentration of the element. A complete suite of major and trace elements were analyzed (see Chapter 7). The coarse-grained sulfide fraction was removed from the samples before sending them in for analysis in order to evaluate them with respect to the primary carbonatite compositions.

4.6 Raman Microspectroscopy

Raman techniques use inelastic scattering of light by molecules, which undergo different forms of molecular vibration when irradiated with monochromatic laser light. These vibrations can be detected and quantitatively characterized as Raman spectra, which provide means for fast and generally non-destructive identification of minerals in micro-samples. This method is particularly useful in identifying minerals that contain water, hydroxyl, carbonate or any other molecular groups and radicals which cannot be detected or measured by other conventional techniques, such as EMPA or LA-ICP-MS. Raman spectroscopy is also very helpful in distinguishing between different minerals of similar chemistry (e.g., polymorphs or ion-deficient variants of the same structure). Raman measurements can be conducted in situ on mineral grains ~1 µm in diameter.

In this study, Raman measurements were conducted on thin sections using a LabRam Aramis Horiba Jobin Yvon instrument at the University of Manitoba. The spectra were collected with a 532-nm laser, a 100-µm confocal hole and 100-µm slit. In all cases, the chemical composition of the sample was first checked by EDS, and Raman spectroscopy was used to verify the identity of certain REE-bearing minerals.

Chapter 5. Petrography of Carbonatites and their Alteration Products

Petrographic descriptions of carbonatites and their alteration products from the different zones of the deposit are presented below. Parageneses are defined by the presence of characteristic mineral assemblages that appear to be in equilibrium. The descriptions below encompass the range of abundance, size and morphology of minerals in the sample set (e.g., not all minerals listed are present in every sample). Mineral abundances were estimated visually and are approximate, whereas grain sizes were approximated using BSE imaging and polarized-light microscopy. Unless noted otherwise, measurements stand for an overall variation in grain size.

5.1 Unoxidized Zone

Thirty-two samples from the unoxidized zone were chosen for detailed study. These samples consist of white carbonatite veins that crosscut heterolithic breccias, trachyte and fenite. Based on observations from the drill core, the veins range from a few mm to several m in thickness. Five different parageneses were identified in the unoxidized carbonatite veins:

1) Burbankite paragenesis;

2) REE fluorocarbonate paragenesis;

3) REE fluorocarbonate-fluorite paragenesis;

4) Ancylite paragenesis;

5) Ancylite-REE fluorocarbonate paragenesis.

With the exception of the burbankite and REE fluorocarbonate parageneses (see below), rare-earth minerals in the unoxidized zone dominantly occur in polycrystalline aggregates that developed pseudomorphically after a precursor mineral with hexagonal morphology. The pseudomorphs are vuggy, and host microscopic crystals lining the cavities.

5.1.1 Burbankite paragenesis

Three samples from this study contain burbankite-group minerals. Sample T-684-L is a white burbankite carbonatite, provided by A.N. Mariano from his work Hecla drill hole WP-2. This is the only sample from drill hole WP-2 examined in this study. Sample BL71 contains carbocernaite, as well as relict burbankite in pseudomorphs, and sample BL70 contains carbocernaite in pseudomorphs.

Phenocrysts in sample T-684-L make up ~30 vol.% of the rock and consist of anhedral to subhedral biotite crystals (0.01 to 0.25 mm, ~5 to 15 vol.%) and anhedral, embayed 0.2 to 1 mm burbankite crystals (5-15 vol. %). The burbankite crystals are zoned with respect to Sr and Ba (Fig. 5.1). Subhedral 10 to 50 µm ancylite and strontianite grains are present in fractures and at the edges of the burbankite, and appear to have developed at the expense of burbankite (Fig. 5.2). Euhedral pyrite cubes (0.25 to 5 mm) locally make up ~15 to 20 vol.% of the carbonatite. Prismatic strontianite and biotite (0.12 to 0.5 mm, ~5-7 vol.%) are associated with burbankite and pyrite (Fig. 5.3). Prismatic rutile (150 to 200 µm, <5 vol.%) occurs at the contact between areas containing burbankite and associated minerals and the carbonatite groundmass.

The carbonatite groundmass consists of 0.2 to 1 mm heterogranular, anhedral to subhedral calcite. The smaller grains tend to be associated with burbankite and its associated minerals, whereas the larger size fraction makes up the bulk of the groundmass also containing minor biotite and small burbankite crystals. Numerous cryptocrystalline inclusions are present in the calcite, particularly in the coarser-grained variety.

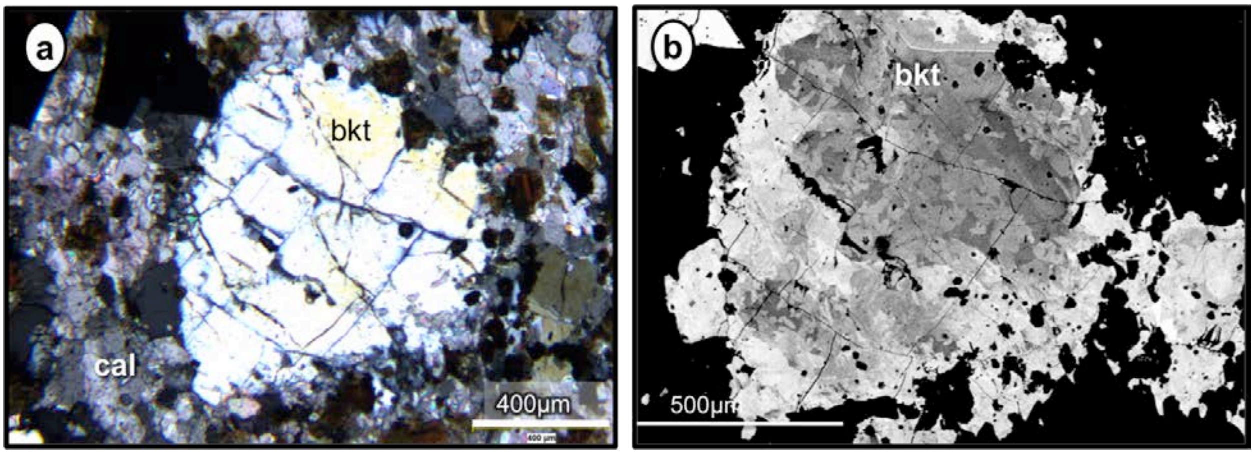

Figure 5.1. A large fractured burbankite crystal (bkt) in calcite groundmass (cal), sample T-684-L (burbankite paragenesis). a) Thin section image in cross-polarized light (XPL). b) BSE image showing irregular zonation of the burbankite.

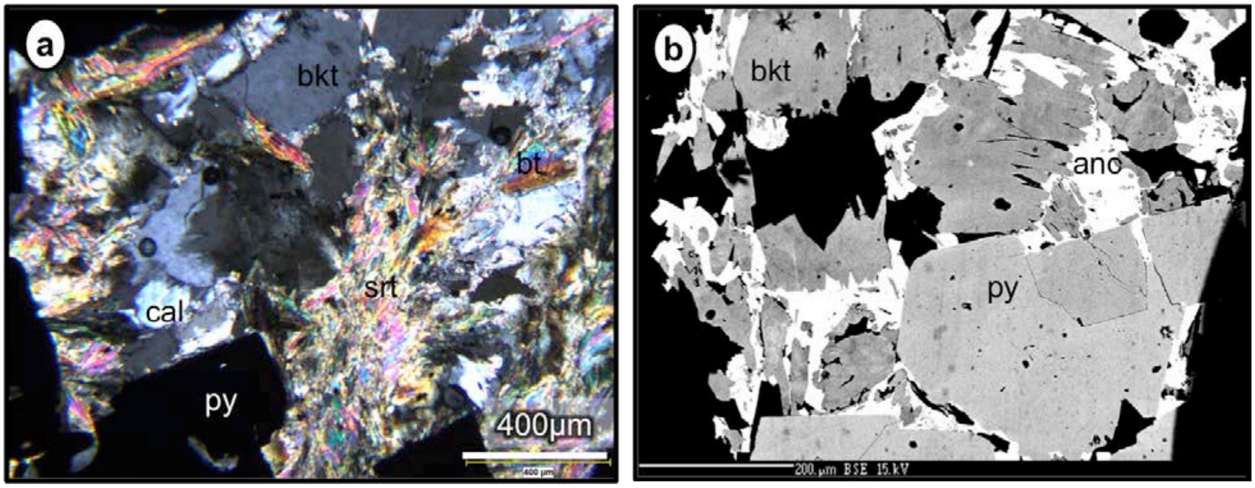

Figure 5.2. Images of sample T-684-L from the burbankite paragenesis. a) Burbankite (bkt) phenocryst with an overgrowth of strontianite (srt) in calcite (cal) groundmass. Thin section image (XPL). b) Ancylite (anc) growing in fractures in burbankite, BSE image. In both cases, burbankite is associated with pyrite (py).

Sample BL71 is a vuggy white ancylite-, strontianite-, burbankite- and carbocernaite-bearing carbonatite (Figs. 5.3 and 5.4). Cavities (~2.5 cm, ~18 vol.%) are lined with light yellow-green 0.1-0.3 mm rhombohedral prisms identified as carbocernaite based on its Raman spectra (see below). The mineral is complexly zoned and contains a low-AZ core (AZ = average atomic number) enriched in Ca and Sr, and a high-AZ oscillatory rim enriched in Na, REE and Th (Fig. 5.4a). Hexagonal and subrounded polycrystalline pseudomorphs are also present (~6 vol.%) and may or may not contain relict burbankite. The pseudomorphs consist of subhedral to pitted ancylite (0.05-0.6 mm, 15-100 vol.% of the pseudomorph), strontianite (0-85 vol.%) and subhedral barite (2-50 vol.%).

Other minerals in the pseudomorphs include subhedral to euhedral pyrite (~10 vol.%) and galena (2-3 vol.%). The groundmass consists of coarse-grained (1-3 mm) calcite with serrated grain boundaries. Some grains are zoned with Mn-enriched cores and Sr-rich rims and contain microcrystalline inclusions of apatite. Fine-grained, turbid calcite occurs around burbankite-bearing vugs (Fig. 5.3).

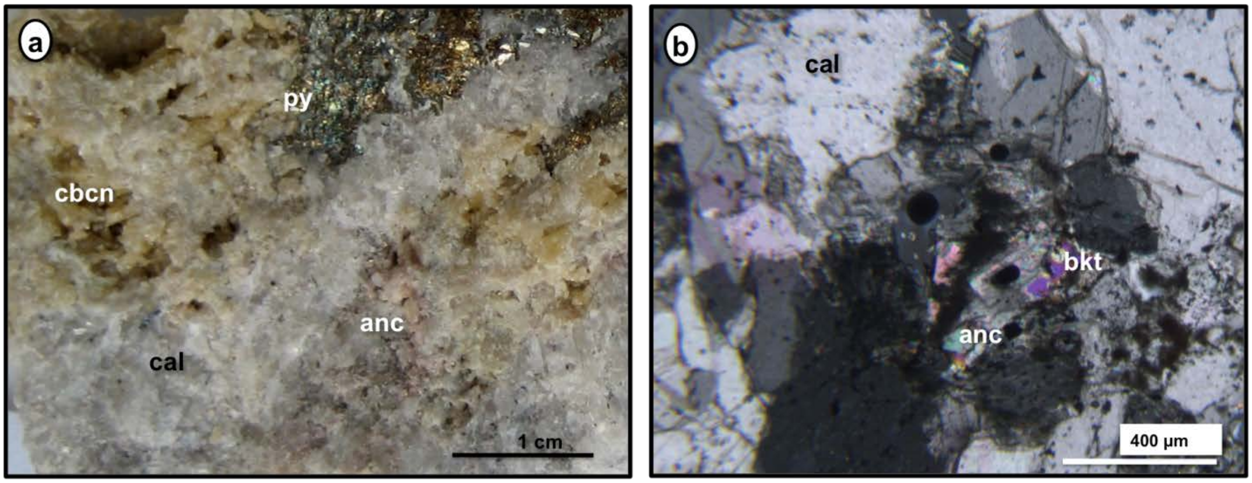

Figure 5.3. Images of sample BL71 (burbankite paragenesis). a) Hand specimen photograph showing a vug lined with yellow carbocernaite (cbcn). b) Thin section photograph (XPL) showing relict burbankite (bkt) in a pseudomorph composed predominantly of ancylite (anc); other abbreviations: py, pyrite; cal, calcite.

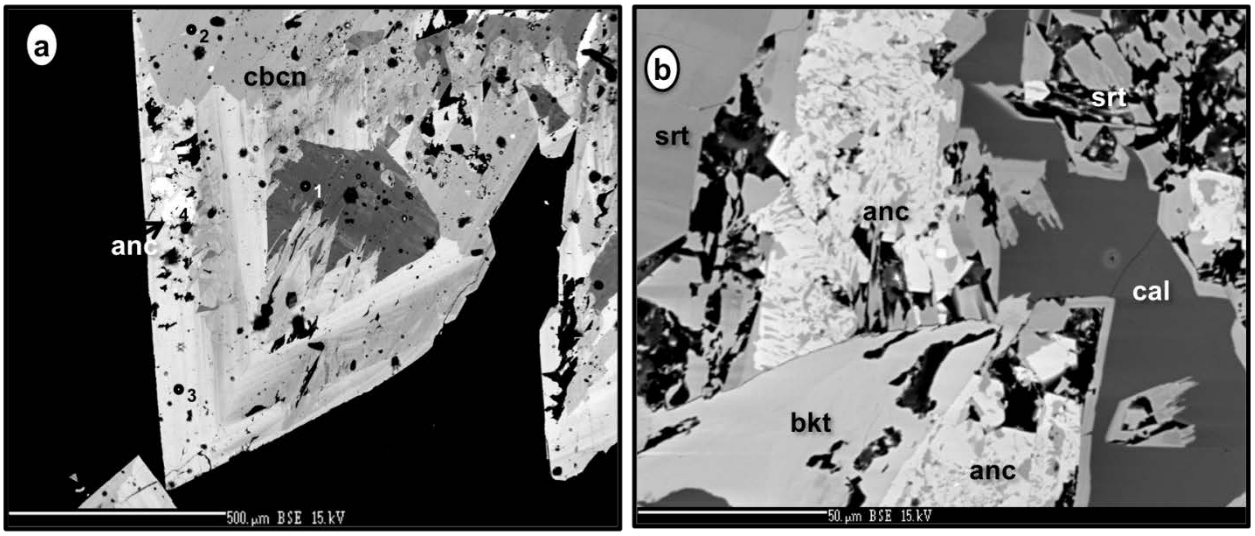

Figure 5.4. Images of sample BL71 (burbankite paragenesis). a) Sector-zoned carbocernaite crystal (cbcn) from the vuggy area in Figure 5.3a (BSE image).Points 1-3 indicate individual spot analyses of carbocernaite of different composition. Point 4 corresponds to ancylite (anc) replacing carbocernaite. b) BSE image showing a symplectitic intergrowth of ancylite and strontianite (srt) and skeletal strontianite replacing burbankite with of calcite (cal) in vuggy open spaces (black).

Sample BL70 (Fig. 5.5) is a white carbonatite containing polycrystalline pseudomorphs (~0.4-2 mm, ~21 vol.% of the rock) that consist of sub- to euhedral ancylite (~0.1 mm, ~26 vol.% of the pseudomorph), acicular REE fluorocarbonates (10-100 µm, ~8 vol.%), anhedral carbocernaite (1-3 mm, ~5 vol.%) and Mn-enriched calcite (~61 vol.%). The carbonatite groundmass is composed of fine- to medium-grained sub- to euhedral calcite (up to 50 vol.% of the rock), fine- to medium- grained prismatic to subhedral strontianite (40-50 vol.%), heterogranular potassium feldspar (~ 22 vol.%) and ~7 vol.% of sub- to euhedral pyrite and rutile. Carbocernaite is partially replaced with ancylite (Fig. 5.5).

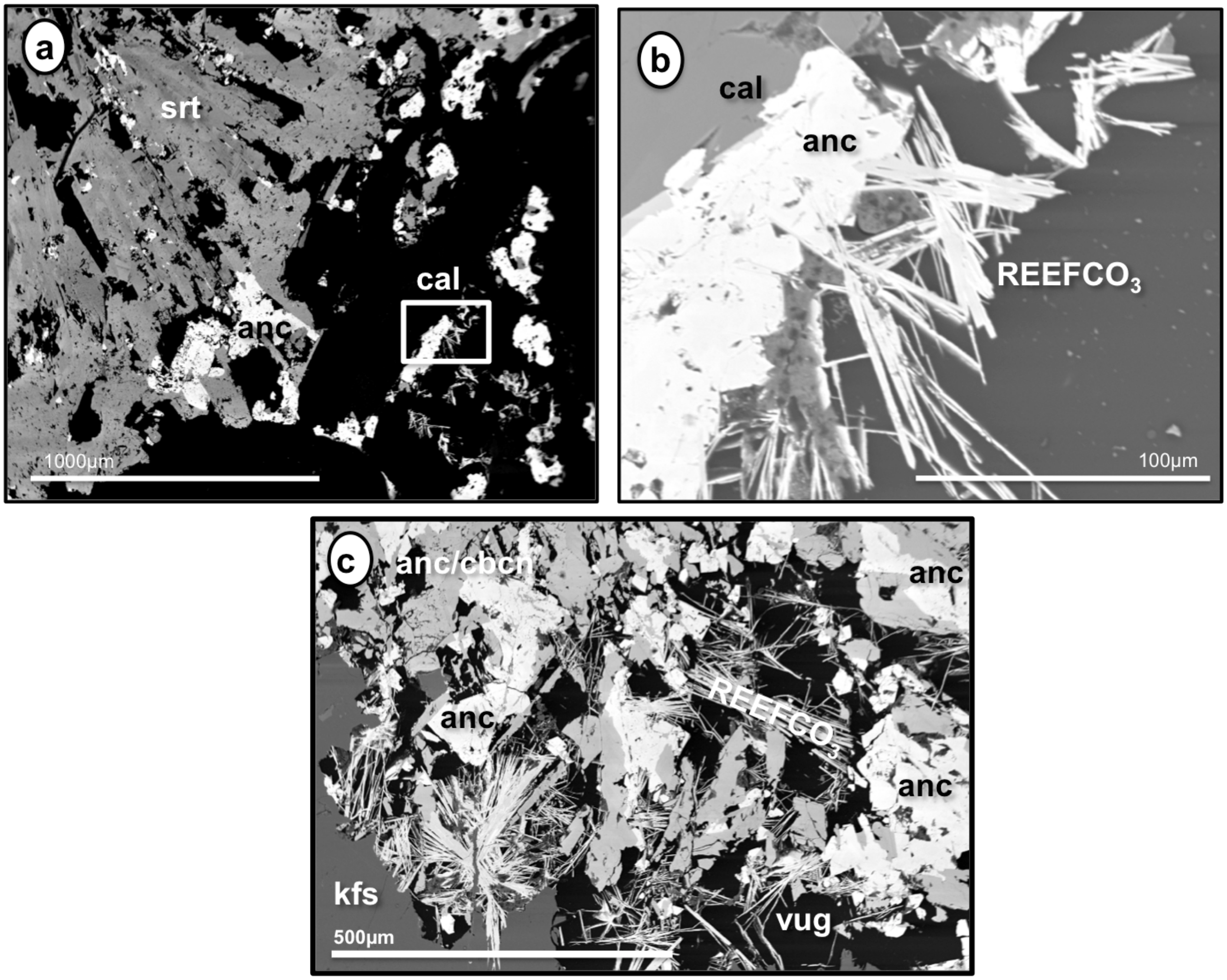

Figure 5.5. BSE images of sample BL70 from the burbankite paragenesis. a) Strontianite (srt) and ancylite (anc) with calcite (cal). b) A close-up image of the area outlined by the white rectangle in a) showing acicular REE fluorocarbonates (REEFCO$_3$) forming encrustations on ancylite grains lining a vug in calcite. c) REE fluorocarbonates associated with intergrown ancylite and carbocernaite (cbcn) in a vug; kfs = potassium feldspar.

5.1.2 Rare-earth fluorocarbonate paragenesis

Rare-earth fluorocarbonates (parisite, synchysite and bastnäsite) occurring in association with strontianite, barite and pyrite are characteristic of the REE fluorocarbonate paragenesis. Only one sample, BL7, was observed to comprise exclusively this paragenesis (Fig. 5.6). The REE fluorocarbonate paragenesis was also identified in sample BL81 (Figs. 5.7 and 5.8), which contains multiple carbonatite veins. In this sample, veins hosting the REE fluorocarbonate paragenesis crosscut fenitized trachyte, and in turn, are crosscut by carbonatite veins hosting the ancylite paragenesis. The carbonatite veins are white, vuggy and host REE fluorocarbonates in the cavities (Figs. 5.6a and 5.7a**)**. The groundmass consists of heterogranular to allotriomorphic calcite ranging from 10 µm to 0.5 cm in size and containing many microcrystalline inclusions. The calcite is dominantly subhedral with embayed grain boundaries. The smaller grains are generally associated with the REE fluorocarbonates, whereas the larger size fraction forms the bulk of the groundmass.

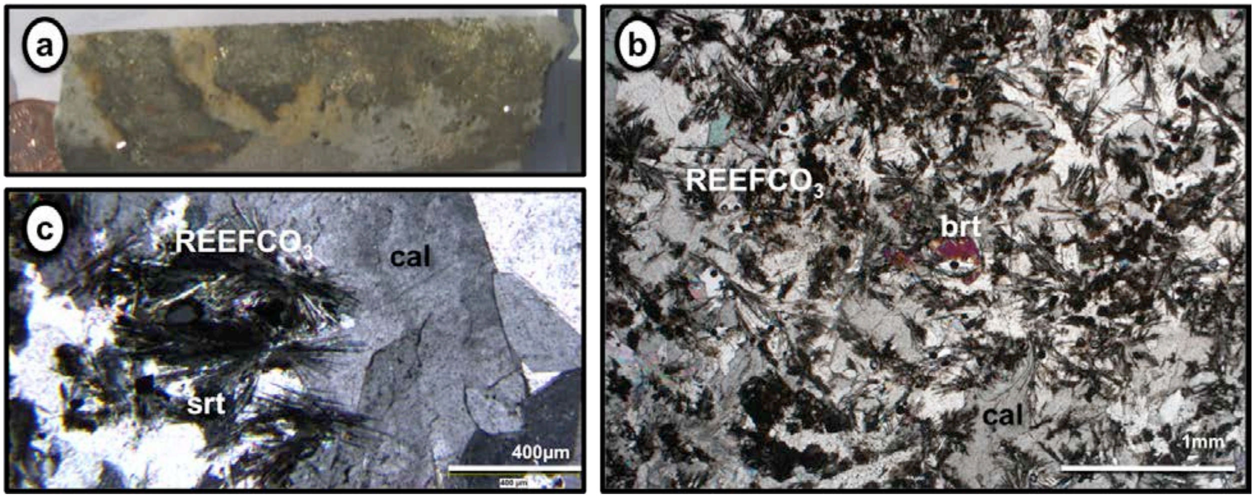

Figure 5.6. Images of sample BL7 from the REE fluorocarbonate paragenesis. a) Core sample consisting of white carbonatite with microscopic REE fluorocarbonates associated with pyrite; b) and c) photomicrographs in XPL showing syntaxial intergrowths of REE fluorocarbonates (REEFCO$_3$) associated with barite (brt) and strontianite (srt), respectively, in calcite groundmass (cal). Note the lack of hexagonal pseudomorphs.

Sample BL7 contains anhedral strontianite (~0.5 mm, 10-20 vol.%) and subhedral barite crystals (0.5 mm, ~5-7 vol.%) spatially associated with the REE fluorocarbonates. Both BL7 and BL81 contain centimeter-sized veins of subhedral pyrite (~25-50 vol.%), where individual pyrite crystals range from 4 mm to 1 cm across and are spatially associated with the REE fluorocarbonates (Fig. 5.8). The latter comprise syntaxially intergrown fasciate bundles of parisite and synchysite (~0.5-0.8 mm in length, 0.02-0.05 mm in width, 25-50 vol.%). This is the most typical habit of REE fluorocarbonates in the unoxidized and transitional zones. It is difficult to estimate the relative abundance of parisite and synchysite in these intergrowths due to their intimate association and extremely fine grain size. Bastnäsite is also present in some of the intergrowths, but is volumetrically subordinate with respect to the other two minerals.

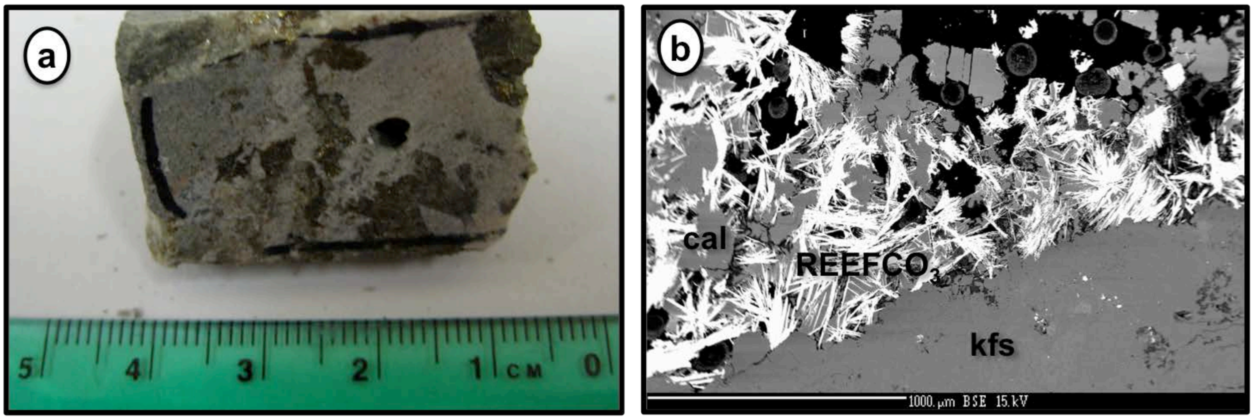

Figure 5.7. Images of sample BL81 containing the REE fluorocarbonate paragenesis. a) Hand specimen, note vugs. b) BSE image of xenocrystic potassium feldspar (kfs) from fenite in carbonatite composed of REE fluorocarbonates ($REEFCO_3$) and calcite (cal).

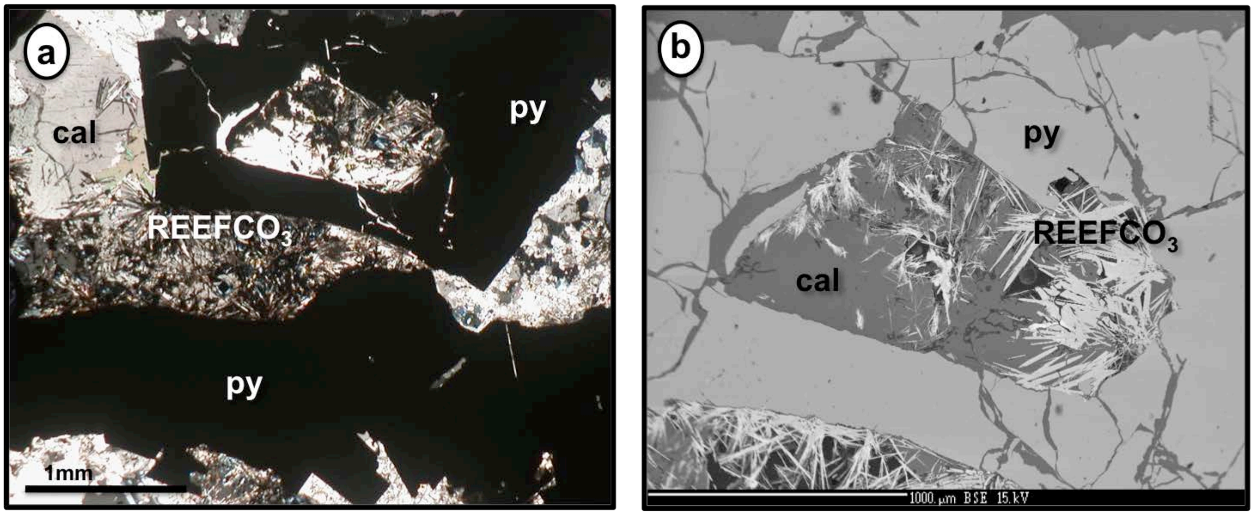

Figure 5.8. Images of sample BL81 containing the REE fluorocarbonate paragenesis. a) Photomicrograph in XPL showing fasciate bundles of REE fluorocarbonates ($REEFCO_3$) associated with pyrite (py) in calcite carbonatite groundmass (cal); b) detail of a); BSE image.

5.1.3 REE fluorocarbonate-fluorite paragenesis

Sample BL87 is the only sample from this work that contains fluorite (Fig. 5.9). The fluorite (up to 8 mm; ~5-10 vol.%) is anhedral; its cleavage planes are partially infilled with calcite. Complex polymineralic pseudomorphs are abundant (0.5-5 mm, 30-40 vol.%) and contain acicular bundles of REE fluorocarbonates (up to 0.5 mm length; 10-15 vol.%), anhedral barite (0.15-0.35 mm; 10-15 vol.%), web-like poikilitic strontianite (0.07-0.35 mm; 50-60 vol.%), subhedral ankerite (~0.2 mm; < 2 vol.%) and small (~20 µm; < 2 vol.%) euhedral pyrite (Fig. 5.10). Open space in the pseudomorphs and elsewhere in the matrix makes up to 25 vol.% of the rock. Rare-earth fluorocarbonates and barite are typically associated with this open space. Strontianite has a "spongy", skeletal texture and in many cases, overgrows barite and REE fluorocarbonates in the pseudomorphs. One pseudomorph was observed in a vug in fluorite.

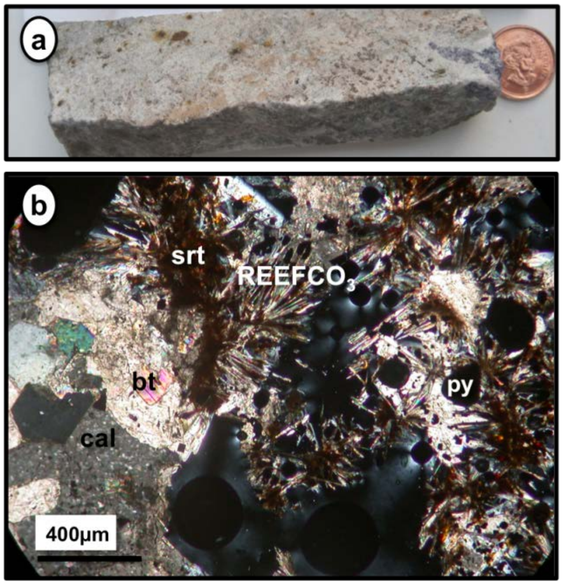

Figure 5.9. Images of sample BL87 containing the REE fluorocarbonate-fluorite paragenesis. a) Hand specimen, note purple fluorite at right. b) Photomicrograph in XPL showing REE fluorocarbonates (REEFCO$_3$) and strontianite (srt) in a vuggy pseudomorph in calcite groundmass (cal); py, pyrite; bt, biotite.

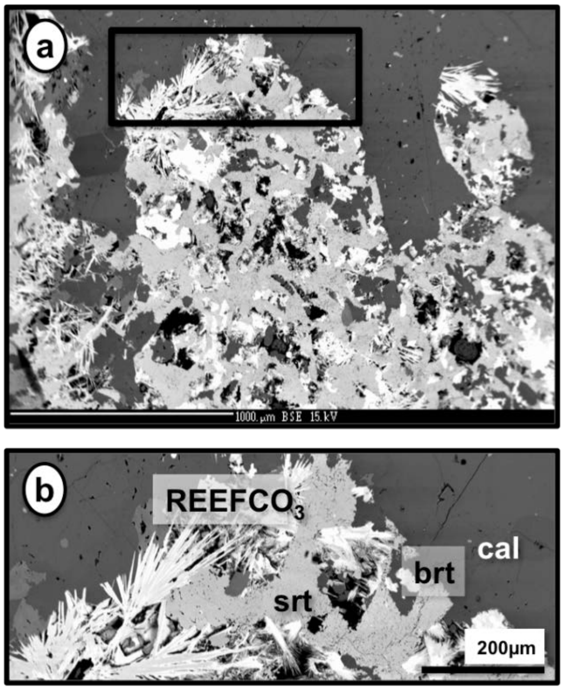

Figure 5.10. BSE images of sample BL87 containing the REE fluorocarbonate-fluorite paragenesis. a) Hexagonal pseudomorphs in calcite groundmass. b) Detail of a) showing intimate association of REE fluorocarbonates (REEFCO$_3$) with strontianite (srt) and barite (brt); cal, calcite. Note skeletal texture of strontianite.

The carbonatite groundmass is very similar to that in the REE fluorocarbonate paragenesis. Altered subhedral to euhedral pyrite (~3 vol.%, 0.25-1mm) occurs in the groundmass, but not as veins described above for BL7 and BL81. Biotite, associated with altered pyrite, is present in very minor proportions (< 2 vol.%).

5.1.4 Ancylite paragenesis

Ancylite and strontianite are both characteristic of the ancylite paragenesis, which is observed in 12 samples. Carbonatites that host the ancylite paragenesis are generally white, inequigranular, porphyritic-phaneritic to porphyritic-aphanitic vuggy rocks (Fig. 5.11). The carbonatite groundmass consists dominantly of calcite (0.1-4 mm, 70-100 vol.%), which shows appreciable variations in Sr and Mn contents, as inferred from its EDS spectra. Cathodoluminescence imaging combined with EDS shows fine-scale zonation with respect to both major and trace elements in the calcite grains (Fig. 5.12). Minor ankerite is intergrown with calcite in two of the samples. Euhedral pyrrhotite, pyrite and galena (≤ 40 µm, 2-15 vol.%) are disseminated throughout the groundmass. Pyrite is associated with hexagonal pseudomorphs and biotite. Potassium feldspar occurs both as xenocrysts entrained in the carbonatite and as contact zones between the carbonatite veins and their host rocks (Fig. 5.13a). One of the samples (BL127) contains a zone of fine-grained aegirine grading into glimmerite at the contact of the carbonatite with its silicate wall-rock (heterolithic breccia).

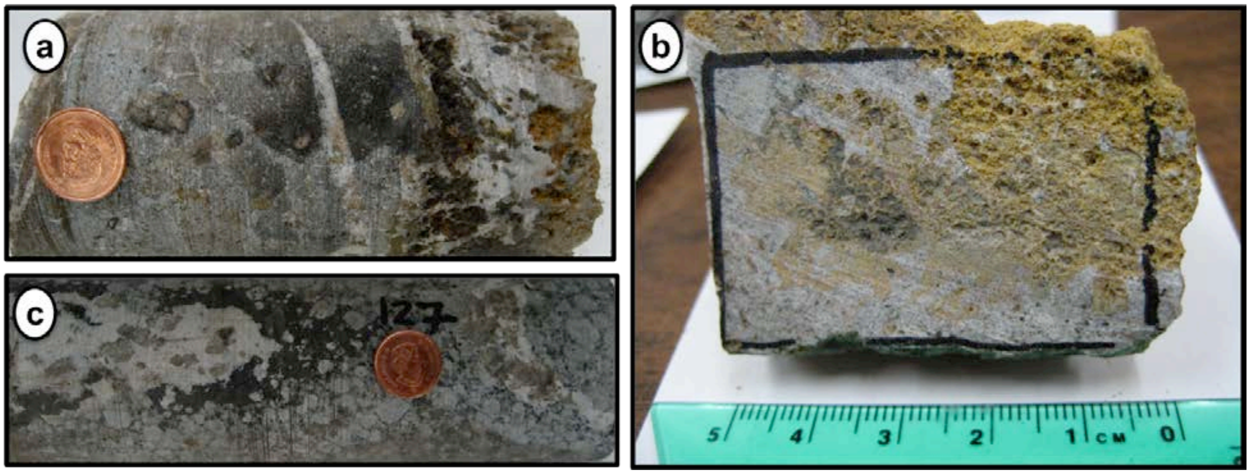

Figure 5.11. Images of carbonatite hand specimens hosting the ancylite paragenesis. a) Carbonatite veins with orange to brown pseudomorphs crosscutting heterolithic breccia (sample BL131). b) Abundant brown, vuggy pseudomorphs in carbonatite vein (sample BL125). c) Black aegirine zone at the contact between carbonatite and heterolithic breccia; note abundant hexagonal pseudomorphs in carbonatite (sample BL127).

The carbonatite veins contain relatively large polymineralic pseudomorphs of hexagonal morphology (~0.2-15 mm, 13-80 vol.%), subhedral to euhedral biotite (0.08-3 mm, 2-7 vol.%), euhedral prismatic strontianite (1-3 mm in length, 3-5 vol.%), and apatite of various morphology. Some apatite is euhedral and occurs as veinlets (~7mm in width, Fig. 5.14b), clusters or individual crystals (~50-250 µm) associated with, or enclosed by the pseudomorphs (Fig. 5.13c).

Some apatite grains exhibit a hopper habit (Fig. 5.14c). In CL images, apatite crystals generally have dull purple cores and brightly luminescent lemon-yellow rims (Fig. 5.14d).

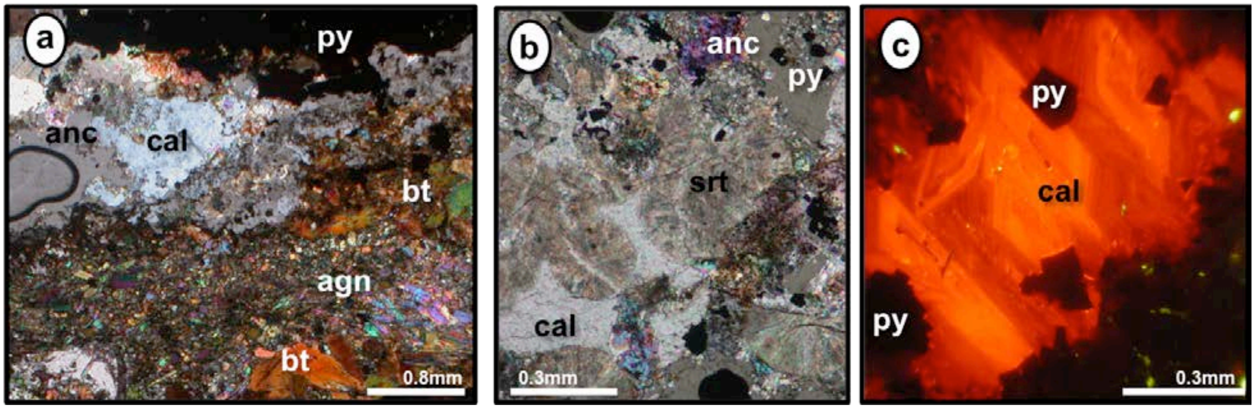

Figure 5.12. Microphotographs of sample BL123A containing the ancylite paragenesis. a) A zone of fine-grained aegirine (agn) grading into glimmerite composed predominantly of biotite (bt) at the contact between carbonatite and its wall-rock; XPL. b) Ancylite (anc) associated with radiating strontianite (srt) in carbonatite; XPL. c) Fine-scale zonation of calcite (cal) in carbonatite; CL image. Abbreviation: py, pyrite.

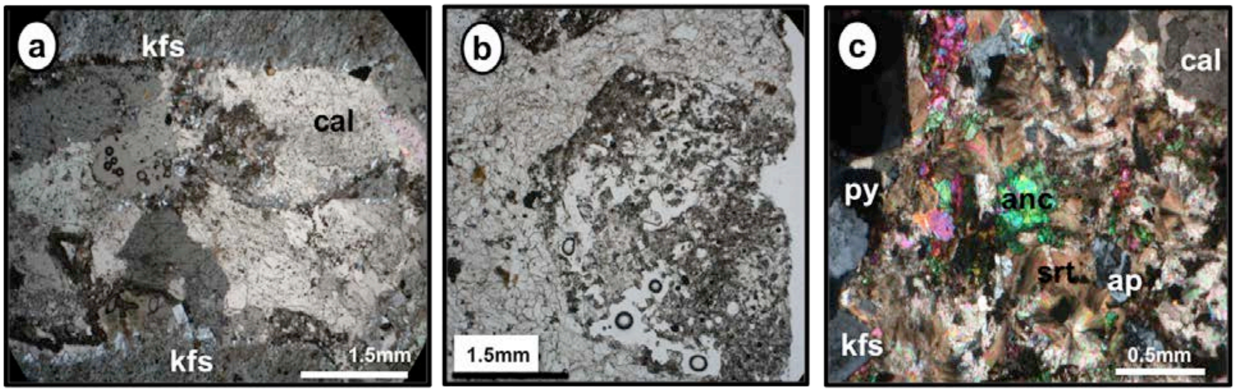

Figure 5.13. Photomicrographs of the ancylite paragenesis (XPL). a) Calcite carbonatite (cal) crosscutting optically turbid fenitized trachyte or breccia; note potassium feldspar (kfs) developed at the contact between the two rock, sample BL85. b) Vuggy hexagonal pseudomorph in carbonatite groundmasss, sample BL4. c) Typical mineral assemblage composing hexagonal pseudomorphs, sample BL131: ancylite (anc), strontianite (srt) and apatite (ap); py, pyrite.

The pseudomorphs are morphologically similar to those in the REE fluorocarbonate-fluorite and ancylite-REE fluorocarbonate parageneses (Fig. 5.12b). Ancylite (0.01-6 mm, 2-100 vol.% of the pseudomorph) is subhedral to euhedral and occasionally exhibits curved crystal faces. Some ancylite has a “spongy” texture. Other minerals in the pseudomorphs include (percent values are with respect to the total volume of a pseudomorph): web-like or radiating strontianite (0.3-0.5 mm, 0-85 vol.%), anhedral to euhedral barite (~0.4 mm, 0-15 vol.%), subhedral to euhedral pyrite or pyrrhotite (0-10 vol.%), anhedral granular, locally Mn-rich calcite (0.05-2 mm, 10-40 vol.%), and subhedral to euhedral biotite (0-30 vol.%). Minor fine-grained monazite occurs interstitially with respect to the other minerals in one of the samples. All pseudomorphs are vuggy (Figs. 5.13 and 5.14) and some extremely so (up to 50 vol.% of open space). Ancylite is almost always associated with strontianite and usually with barite (Fig. 5.14a). Lozenge-shaped ancylite crystals are enclosed in barite, whereas barite is developed in ancylite in the same sample (BL123A, Fig. 5.14f). One of the samples hosts symplectitic intergrowths of ancylite and strontianite similar to that shown in Fig. 5.4 (burbankite paragenesis).

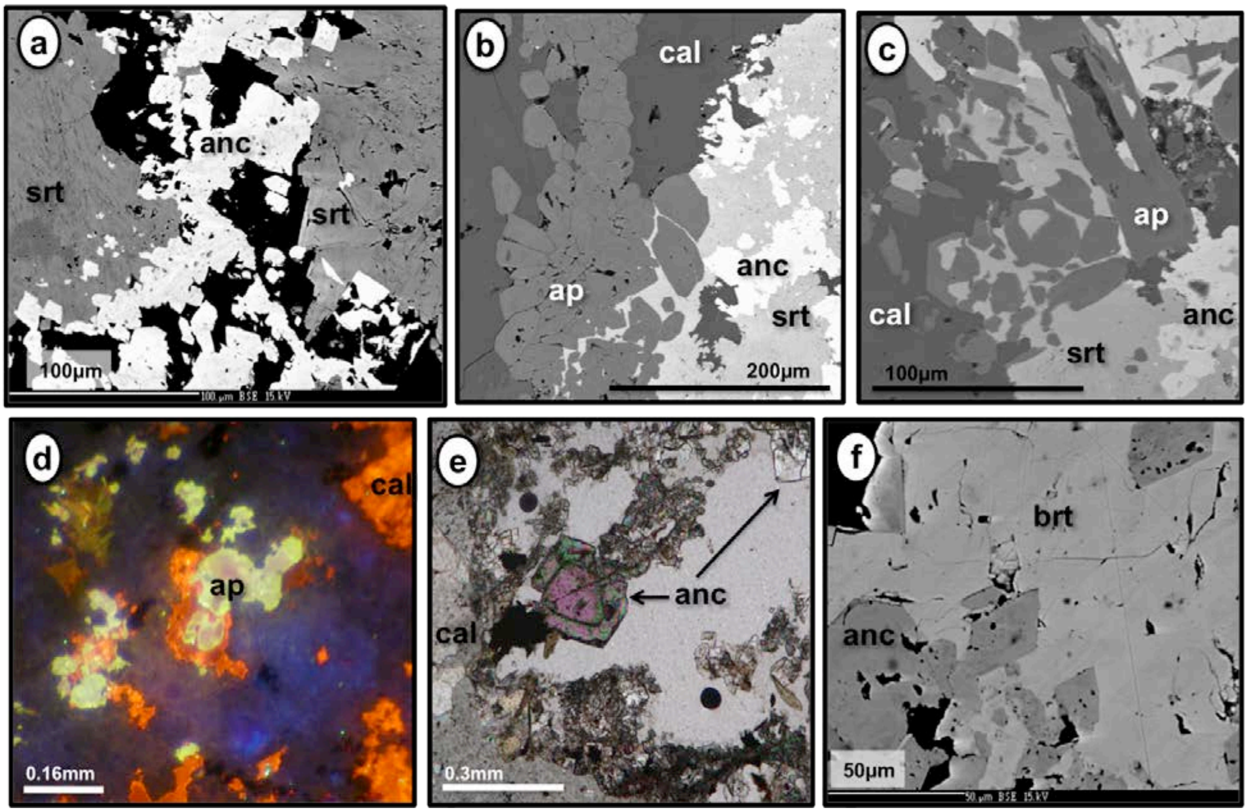

Figure 5.14. Textural characteristics of the ancylite paragenesis. a) Typical relationship between ancylite (anc) and strontianite (srt) in vuggy pseudomorph, black is open space (BSE image, sample BL125). b) Late apatite (ap) veinlet in calcite (cal) carbonatite containing ancylite-strontianite pseudomorphs (BSE image, sample BL125). c) Inclusions of early hopper apatite in vuggy strontianite-ancylite pseudomorph (BSE image, sample BL125). d) Apatite with purple-luminescent cores and yellow rims in calcite and potassium feldspar (blue) groundmass (CL image, sample BL4). e) Euhedral ancylite crystals in vuggy pseudomorph (thin section image, XPL, sample BL131). f) Lozenge-shaped ancylite crystals in barite (brt) (BSE image, sample BL123A).

5.1.5 Ancylite-REE fluorocarbonate paragenesis

The ancylite-REE fluorocarbonate paragenesis is the most common paragenesis among the samples of unoxidized carbonatites examined in the present work (13 out of the 32 samples). The carbonatite veins that host the ancylite-REE fluorocarbonate paragenesis are generally white, inequigranular porphyritic-phaneritic to porphyritic-aphanitic, rocks with abundant cavities similar to the veins previously described (Fig. 5.15). The carbonatite groundmass consists of allotriomorphic-granular to hypidiomorphic-heterogranular calcite and strontianite

(67-100 vol.% of the rock). In some cases, the carbonate groundmass is turbid and contains micro- to cryptocrystalline (2-20 µm) inclusions. Abundant disseminated grains of pyrite are present (< 5 vol.%), accompanied by lesser quantities of chalcopyrite and pyrrhotite, and very minor sphalerite and galena. Larger crystals of subhedral to euhedral pyrite also occur (3-5 vol.%). Fine-grained, euhedral biotite and anhedral, turbid xenocrysts of potassium feldspar are entrained in some carbonatite veins. Some of the feldspar crystals are fractured (Fig. 5.16b). Pyrite is often oxidized along the rim. Rutile is present at the contact of the carbonatite and its fenitized wallrock in sample BL63.

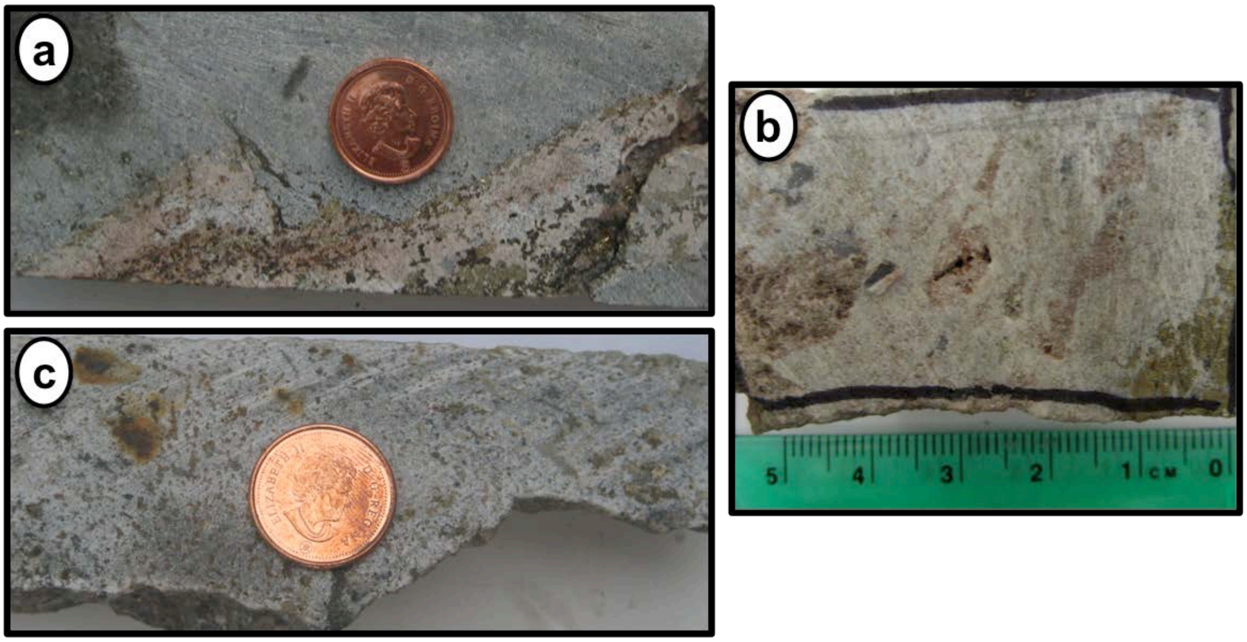

Figure 5.15. Hand specimen photos of carbonatites containing the ancylite-REE fluorocarbonate paragenesis. a) Pink and white carbonatite vein crosscutting fenitized trachyte. Note abundant pyrite developed at the contact between the two rocks (sample BL78). b) White carbonatite with pink pseudomorphs of hexagonal morphology (sample BL5). c) White carbonatite vein with abundant small pseudomorphs (sample BL97).

Coarse grains in the carbonatite comprise polymineralic pseudomorphs (0.1-20 mm, ~5-21 vol.% of the rock) and euhedral biotite crystals (0.25-5 mm, ~7-30 vol.%) commonly aggregated as books. Pyrite sometimes occurs along biotite cleavage planes. The pseudomorphs are similar to those already described, but contain both ancylite and REE fluorocarbonates (Figs. 5.16, 5.17). Subhedral to euhedral ancylite crystals (20-500 µm, 7-40 vol.% of the pseudomorph) predominate volumetrically over smaller crystals of rare-earth fluorocarbonates (1.2-4 µm in width by 11-200 µm in length, 1-8 vol.% of the pseudomorph). The morphology of ancylite and REE fluorocarbonates is the same as those described previously for the ancylite and REE fluorocarbonate parageneses (compare Figs. 5.7, 5.9, 5.12-5.17). The majority of the pseudomorphs also contain (percent values are relative to the volume of a pseudomorph): subhedral to euhedral prismatic strontianite and Sr-rich calcite (~200 µm, 25-52 vol.%), anhedral Sr-poor and Mn-rich calcite (0.2-1 mm, 10-60 vol.%), subhedral to anhedral barite (10-80 µm, 8-10 vol.%), and anhedral to euhedral biotite (~50 µm, 1-10 vol.%). Minor proportions of anhedral apatite (1-10 vol.%), monazite (~6 vol.%), ankerite (8-15 vol.%) and celestine (trace) were also observed in one or more samples (e.g., Fig. 5.16e). As in the other parageneses, the pseudomorphs comprise as much as 30 vol.% of open space.

In some cases, ancylite appears to develop at the expense of earlier formed REE fluorocarbonates. In other cases, the fluorocarbonates clearly formed later than ancylite (Figs. 5.17b, c). However, ancylite is invariably associated with strontianite in the pseudomorphs, whereas the REE fluorocarbonates are generally associated with pyrite and other opaque minerals. The REE fluorocarbonates commonly occur outside of the pseudomorphs, but are still confined to cavities. Manganese-rich calcite is interstitial with respect to all other minerals in the pseudomorphs. Ankerite has a radiating habit and is associated with calcite, pyrite and synchysite. Strontianite exhibits a skeletal (web-like) or radiating habit (Fig. 5.16d), contains variable levels of Ca, and hosts inclusions of calcite and ancylite in some cases. In thin section, strontianite is brown, turbid and appears to be interstitial with respect to most other minerals (Figs. 5.16c, 5.17a). Monazite grains are perched on ancylite and ankerite crystals. Biotite and pyrite often occur at the contact between carbonatite veins and the wallrock, forming a thin glimmerite selvage (Fig. 5.15). Apatite inclusions occur in calcite, both in the carbonatite groundmass and within the pseudomorphs. Some apatite grains contain minute (≤ 5 µm) inclusions of burbankite and ancylite (~11 µm), identified on the basis of EDS spectra. The small size of these inclusions precludes their accurate analysis by WDS.

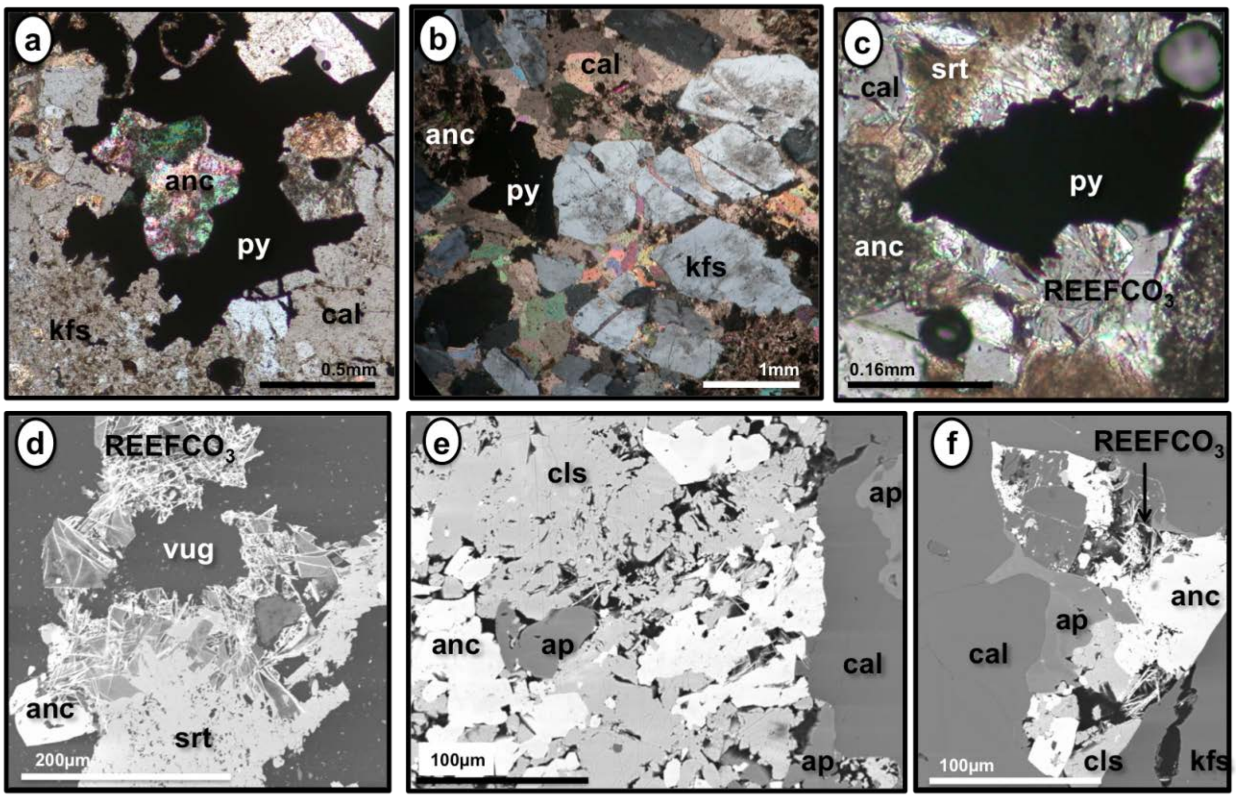

Figure 5.16. Images of the ancylite-REE fluorocarbonate paragenesis. a) Photomicrograph (in XPL) showing ancylite (anc) enclosed in pyrite (py) at the contact between calcite carbonatite (cal) and fenitized rock containing abundant potassium feldspar (kfs), sample BL62. b) Fractured potassium feldspar xenocrysts or phenocrysts (?) entrained in calcite carbonatite, sample BL70 (XPL). c) Pseudomorph containing calcite, strontianite (srt), ancylite, pyrite and rare-earth fluorocarbonates ($REEFCO_3$); note anhedral form of ancylite and open space surrounding the rare-earth fluorocarbonates, sample BL62 (XPL). d) to f) are BSE images showing ancylite and associated minerals in pseudomorphs: d) ancylite and strontianite overprinting early rare-earth fluorocarbonates, sample BL117; e) celestine (cls) and ancylite associated with apatite (ap), sample BL97; f) ancylite intergrown with celestine, rare-earth fluorocarbonates and apatite in vug, sample BL97.

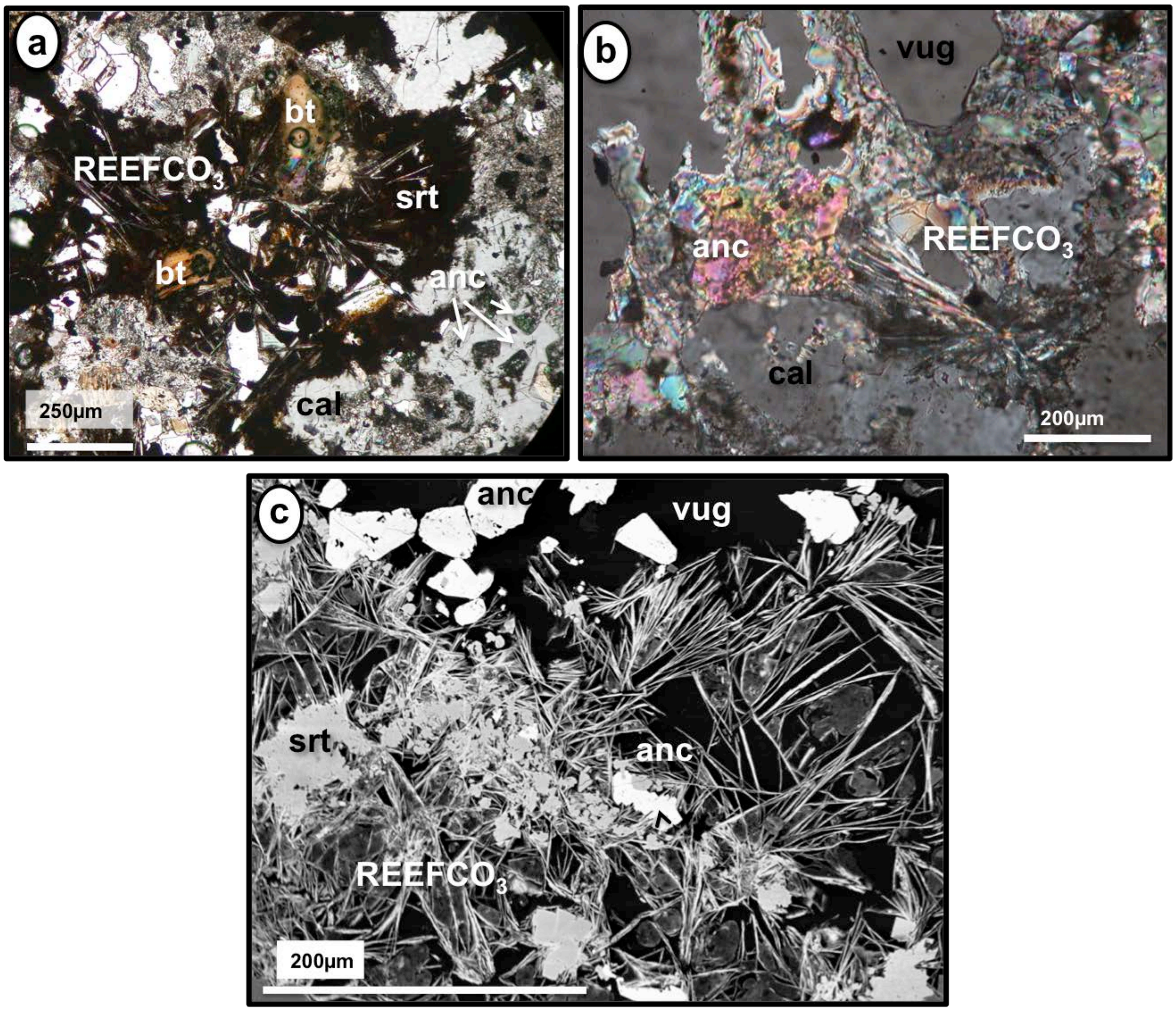

Figure 5.17. Photomicrographs of textural relationships of the ancylite-REE fluorocarbonate paragenesis; a) vuggy pseudomorph with REE fluorocarbonates (REEFCO3) overgrown by strontianite (srt, brown cloudy material) and biotite (bt), surrounded by web-like calcite (cal) and ancylite (anc)(XPL) (sample BL78); b) ancylite co-existing with rare-earth fluorocarbonates and calcite in open space (XPL);c) ancylite crystals perched on fasciate bundles of REE fluorocarbonates with late-stage strontianite (BSE) (sample BL63).

5.2 Transitional Zone

Eleven samples from the transitional zone were studied in detail. In this zone, carbonatites show incipient stages of oxidation; i.e., the carbonate groundmass of these rocks is visibly altered, but not completely replaced with oxide minerals (Fig. 5.18). The color of carbonatite ranges from white to black depending on the degree of alteration, which is extremely variable even on a hand-specimen scale.

Carbonatite mineral assemblages are variable in this zone and include monazite-REE fluorocarbonate-bearing ancylite-rich carbonatite, cerianite-ancylite-parisite-bearing carbonatite, biotite-bearing carbonatite, and monazite-ancylite-REE fluorocarbonate-bearing carbonatite. All these varieties are described together, owing to the limited number of samples from this zone and their variable degree of alteration. The carbonatites range in texture from allotriomorphic-heterogranular to inequigranular porphyritic-phaneritic or -aphanitic vuggy rocks containing recognizable pseudomorphs similar to those described from the unoxidized zone. Rare-earth minerals occur both as discrete crystals in the carbonatite groundmass and inthe pseudomorphs.

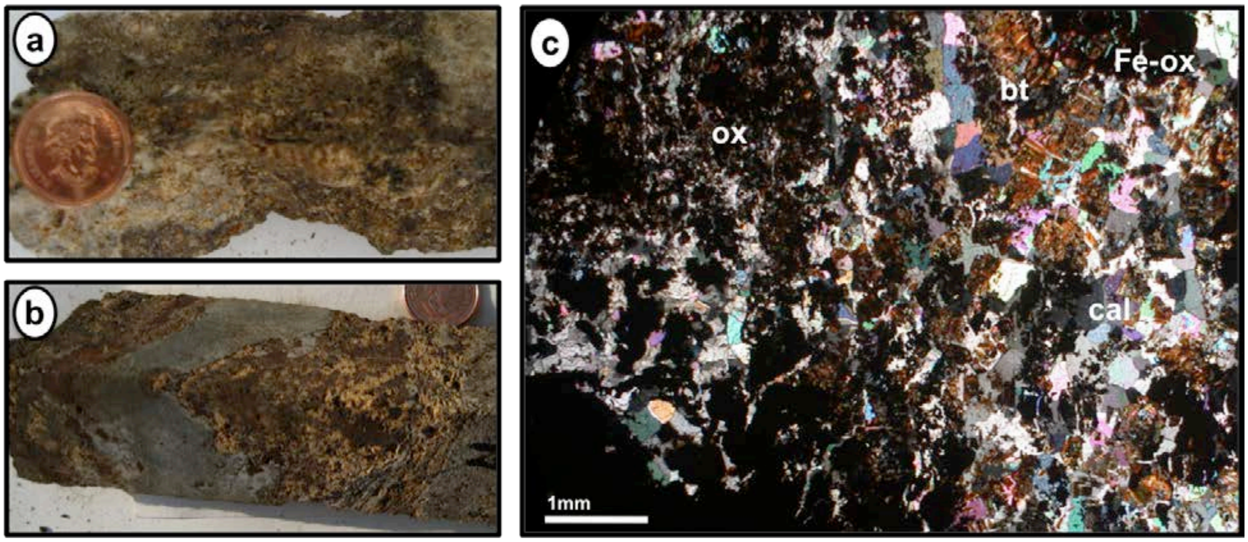

Figure 5.18. Carbonatites from the transitional zone showing incipient oxidation. a) Hand specimen of vuggy oxidized carbonatite (sample BL19). b) Hand specimen showing maroon iron-(hydr)oxide pseudomorphs after pyrite in peach-to brown-colored oxidized carbonatite crosscutting wall-rock trachyte (grey). c) Carbonate groundmass pervasively replaced by Fe-Mn (hydr)oxides (ox) (photomicrograph in XPL), sample BL31. Abbreviations: Fe-ox, iron-(hydr)oxides; cal, calcite; bt, biotite.

The carbonatite groundmass consists of variably Sr- and Mn-enriched heterogranular, allotriomorphic calcite (0.25-5 mm, ~17-75 vol.%) with curved to serrated grain boundaries (Fig. 5.19). Cryptocrystalline inclusions in calcite are common and some calcite is turbid due to the abundance of such inclusions. The mineral shows zoning in CL images (Fig. 5.20). Strontianite is also a groundmass mineral and locally makes up 27 vol.% of the rock; it is commonly zoned with respect to Ca. Other minerals in the groundmass include: subhedral to euhedral biotite (<0.05-0.25 mm, 5-10 vol.%) as discrete crystals and idiomorphic books (~3-8 mm, 12 vol.%), subhedral to euhedral oxidized pyrite (<0.05-0.25 mm, rarely up to 1 mm, 0-7 vol.%) disseminated throughout the groundmass, bladed ilmenite (0.25-0.5 mm in length, < 2 vol.%), and prismatic rutile (< 1 vol.%). Iron and Mn oxides and hydroxides could not be differentiated or identified reliably based on their optical characteristics, and are collectively referred to here as Fe-Mn oxides. These minerals form cryptocrystalline amorphous, crustiform and colloform aggregates up to ~3 cm in their maximum dimension, and locally compose up to 17 vol.% of the rock (Fig. 5.20). The oxides are developed interstitially or replace other minerals. Resorbed xenocrysts of potassium feldspar are also occasionally present (< 2 vol.%).In one sample (BL12), fasciate bundles of REE fluorocarbonates (up to 85 µm in length and ~1 µm in width, ~13 vol.% of the rock) occur in the oxidized groundmass, and potassium feldspar makes up ~27 vol.% of the carbonatite.

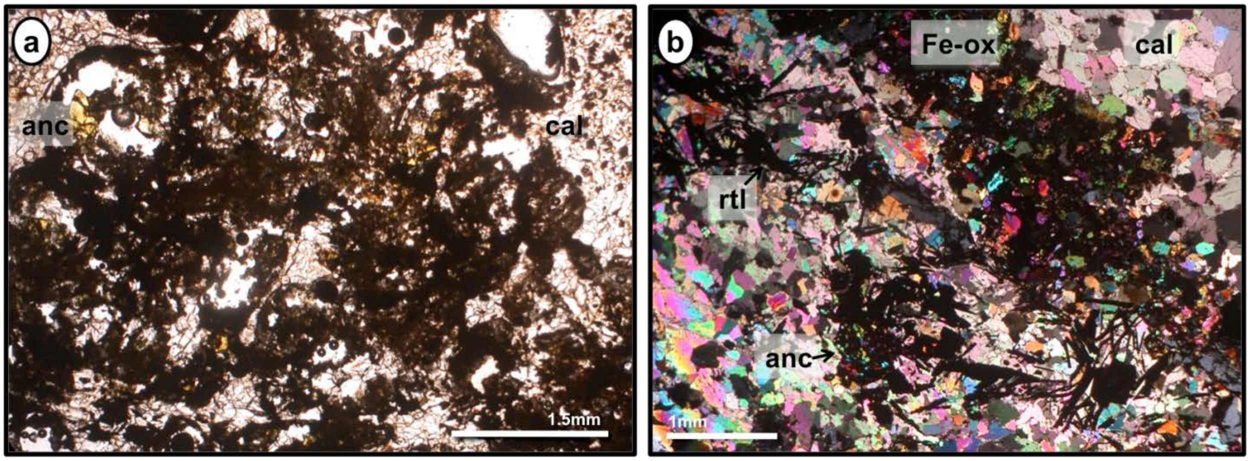

Figure 5.19. Microphotographs of pseudomorphs in carbonatites from the transitional zone. a) Oxidized, vuggy pseudomorphs and ancylite (anc) crystals,sample BL135, plane polarized light (PPL). b) Oxidized pseudomorphs containing highly birefringent ancylite intimately associated with Fe oxides (Fe-ox); rutile (rtl) occurs as acicular opaque crystals in calcite (cal) groundmass (sample BL102B, XPL).

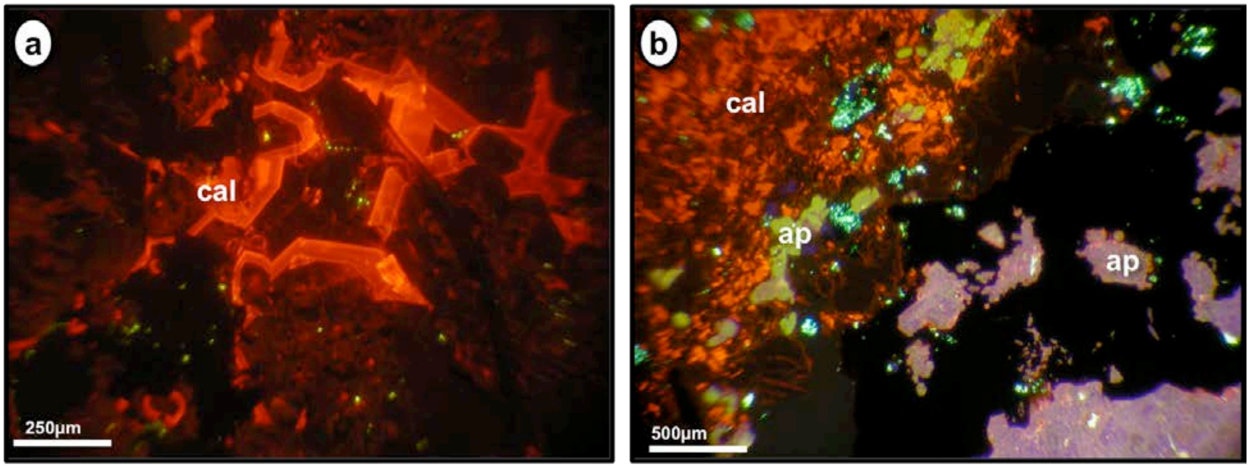

Figure 5.20. CL images of carbonatites from the transitional zone. a) Zoned calcite (cal) in carbonatite vein (sample BL12). b) Orange-luminescent calcite with two generations of apatite (ap): yellow cores with purple rims in the calcite matrix, and purple cores with yellow rims in the Fe-Mn oxide matrix (black). The green-luminescent material is epoxy (sample BL19).

Polymineralic pseudomorphs (1-20 mm, 25-55 vol.%), analogous to those found in the unoxidized carbonatites (see Chapter 5.1), also occur in the transitional zone (Figs. 5.21, 5.22).The pseudomorphs consist of (percent values are relative to the total volume of a pseudomorph): subhedral, commonly “spongy” ancylite (8-400 µm, 16-30 vol.%); anhedral, skeletal strontianite (20 vol.%); interstitial or crustiform Fe-Mn oxides (up to 30 vol.%); subhedral pyrite (~13 vol.%); subhedral to euhedral biotite (up to 10 vol.%); acicular REE fluorocarbonates (< 1µm in width, up to 250 µm in length, ~3 vol.%); subhedral, pitted monazite (~4 vol.%); minor barite and ankerite (< 1 vol.% each). Open space can form up to 20 vol.% of the pseudomorphs.

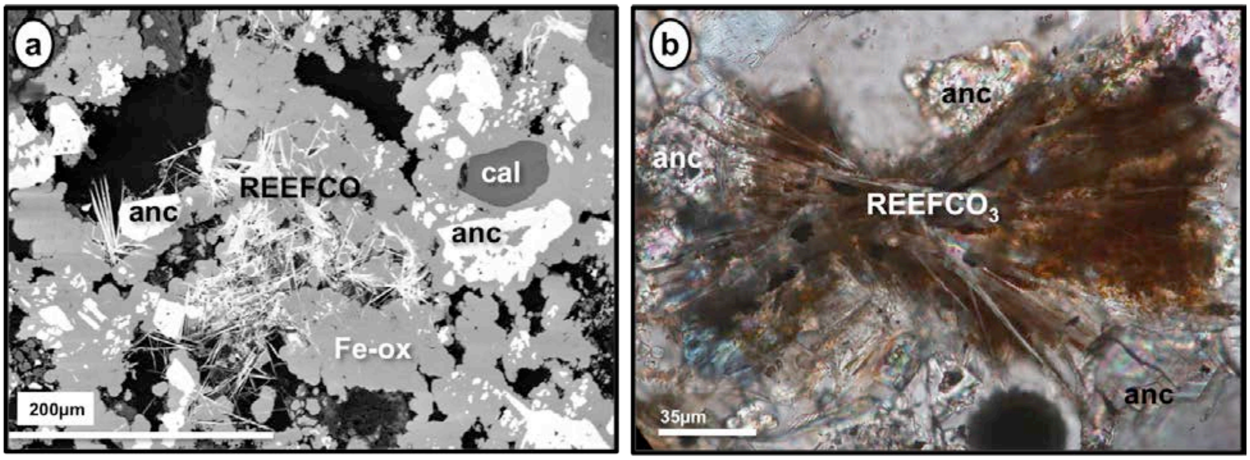

Figure 5.21. Images of sample BL102B from the transitional zone. a) Ancylite (anc) and REE fluorocarbonates (REEFCO$_3$) within crustiform iron-oxide minerals (Fe-ox); cal, calcite. BSE image. b) Textural relationships between ancylite and REE fluorocarbonates (photomicrograph, XPL).

Replacement and pseudomorphization of the precursor mineral was accompanied by removal of material, as indicated by the sub- to euhedral morphology of ancylite and some other minerals, and the large proportion of open space in the pseudomorphs. Some of these minerals were subsequently altered, which is manifested in the commonly observed replacement and “spongy” textures. Ancylite, strontianite, REE fluorocarbonates and monazite clearly developed at the expense of a carbonate precursor phase, whereas ankerite appears to have formed at the expense of pyrite and biotite, which were possibly present as inclusions in that precursor mineral. Many pseudomorphs are disaggregated.

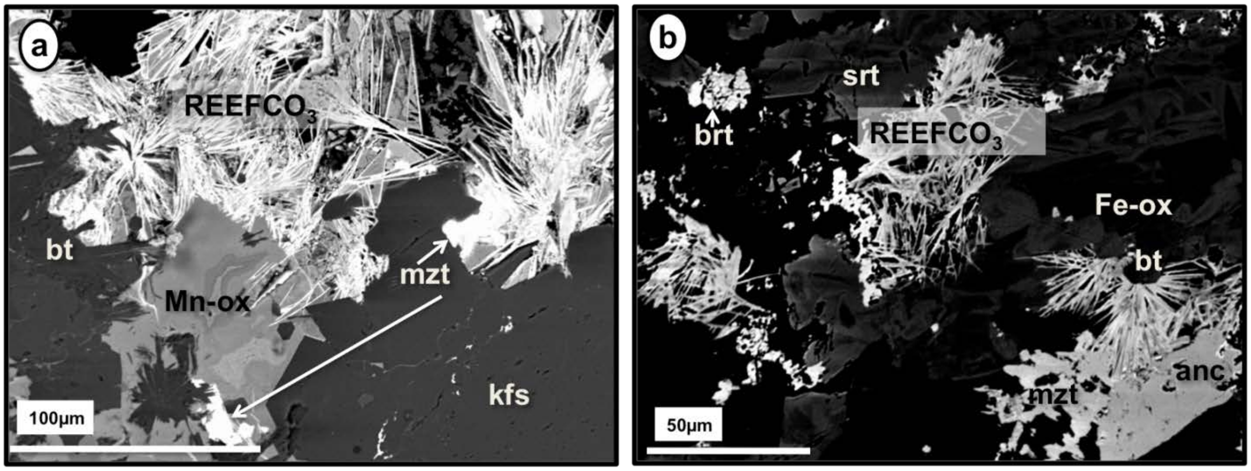

Figure 5.22. Textural relationships among REE minerals in carbonatites from the transitional zone (BSE images). a) Monazite (mzt) crystals perched on fasciate bundles of REE fluorocarbonates (REEFCO$_3$) in association with botryoidal Mn oxide (Mn-ox); biotite (bt) and potassium feldspar (kfs) also present; sample BL12. b) Detail of polymineralic pseudomorph consisting of barite (brt), strontianite (srt), ancylite (anc) and REE fluorocarbonates with interstitially developed Fe oxides (Fe-ox) and monazite; sample BL19.

In samples from the transitional zone, oxidized pyrite and oxide minerals invariably show Si peaks in their EDS spectra. This Si peak undoubtedly stems from submicroscopic silica coprecipitated or adsorbed on the surface of oxide particles (e.g., Vempati and Loeppert, 1989). Manganese oxide minerals typically have a botryoidal habit or are amorphous, whereas Fe-oxides also form pseudomorphs after pyrite. In some samples, Fe-Mn oxides are concentrated dominantly around altered pyrite or in pseudomorphs, whereas they are pervasive throughout the carbonate groundmass in other samples (Fig. 5.18c). Skeletal strontianite crystallized on calcite in some cases, and generally contains numerous minute inclusions of barite. Monazite appears to have formed at the expense of ancylite and REE fluorocarbonates, and occurs as inclusions in oxide minerals in one sample (BL12; Fig. 5.22). Fine-grained apatite forms crudely aligned crystals < 100 μm in length in the selvages of a carbonatite vein in sample BL19 (Fig. 5.23).

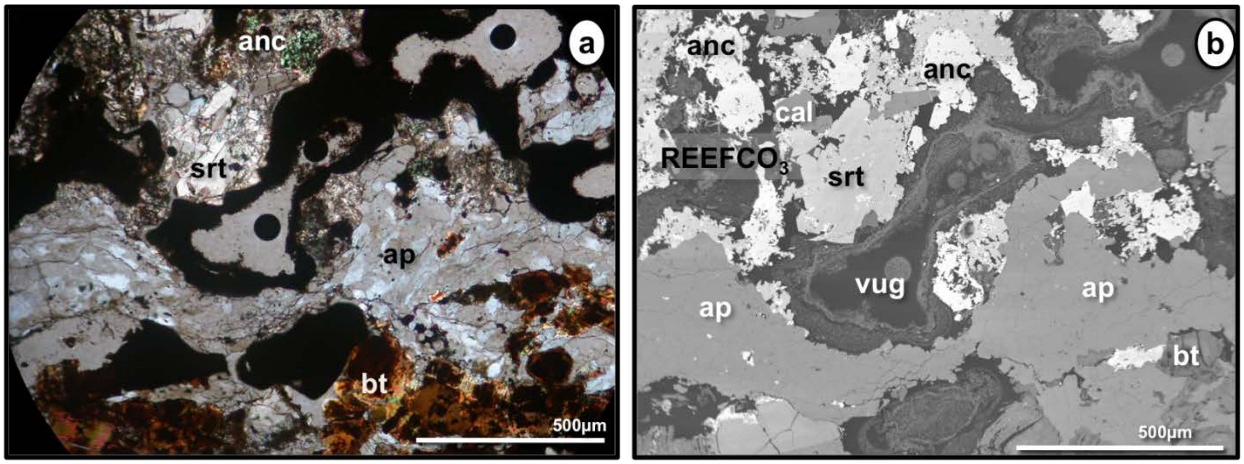

Figure 5.23. Images of sample BL 19 from the transitional zone. a) Apatite (ap) veinlet in the selvage of a strontianite-bearing (srt) calcite carbonatite vein (cal) adjacent to a glimmerite zone composed of biotite (bt) (XPL). b) BSE image of the same area; note abundant REE fluorocarbonates (REEFCO$_3$) confined to open spaces and associated with "spongy" ancylite (anc).

5.3 Oxidized Zone

Thirteen samples from the oxidized zone of the deposit were studied in detail. Based on their modal mineralogy, only one of these samples (BL115) represents the "FMR"-type material characterized by the complete lack of carbonate minerals. The remaining 12 samples come from the "Ox-Ca" subzone, which in addition to secondary oxide mineralization contains relict groundmass carbonates.

The rocks from the oxidized zone are rusty to chocolate brown or black in color and very friable (Figs. 5.24a, b). Samples with a banded or patchy color distribution are common (Fig. 5.24c). In some cases, carbonatites are completely replaced by Fe and Mn oxides, and relict sulfide minerals are not present (Figs. 5.24, 5.25). Some sections of drill core consist entirely of rock fragments. Polycrystalline pseudomorphs containing REE minerals are still recognizable in some samples, but their constituent minerals are more diverse than those observed in either the unoxidized or transitional zones. Rare-earth minerals occur both in the pseudomorphs and in the groundmass. Texturally, the majority of samples from the oxidized zone are very complex because most of their constituent minerals are altered or pseudomorphed. Individual samples described in detail below are placed in the “Ox-Ca” subzone because they do not contain relict sulfide minerals, although they can still be identified as calcite carbonatites.

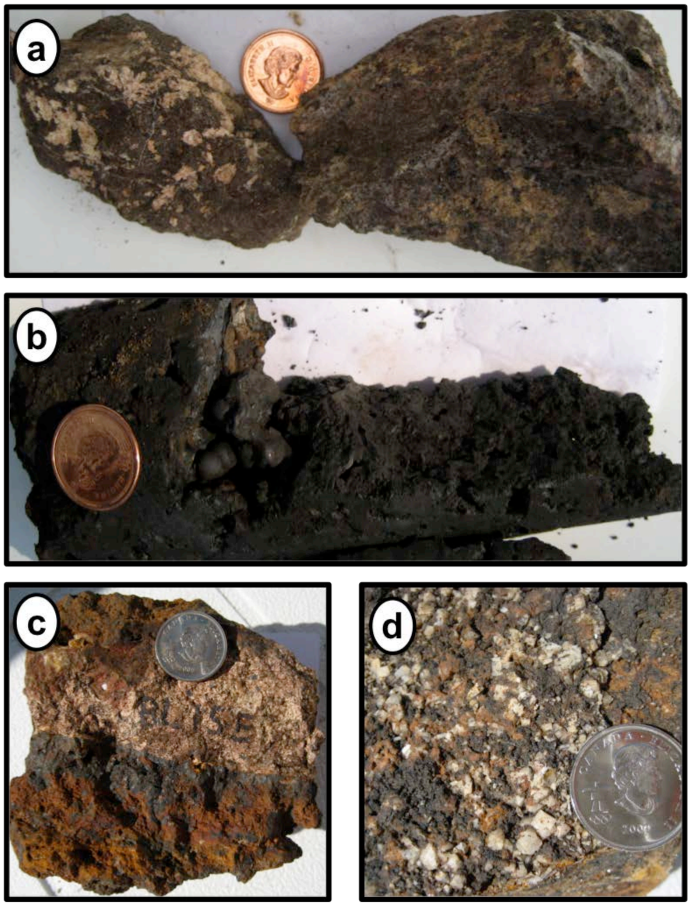

Figure 5.24. Hand specimens from the oxidized zone. a) Peach-colored pseudomorphs in the oxidized dark brown groundmass (sample BL143). b) Botryoidal Mn oxides lining a vug in drill core at a depth of ~30 m (sample BL153). c) Outcrop sample showing pervasive oxidation of carbonatite (rusty brown to black) and much less significant alteration of a feldspar-rich rock in the upper part of the sample. d) Surface sample showing weakly altered euhedral potassium feldspar immersed in a mesostasis of Fe and Mn oxides.

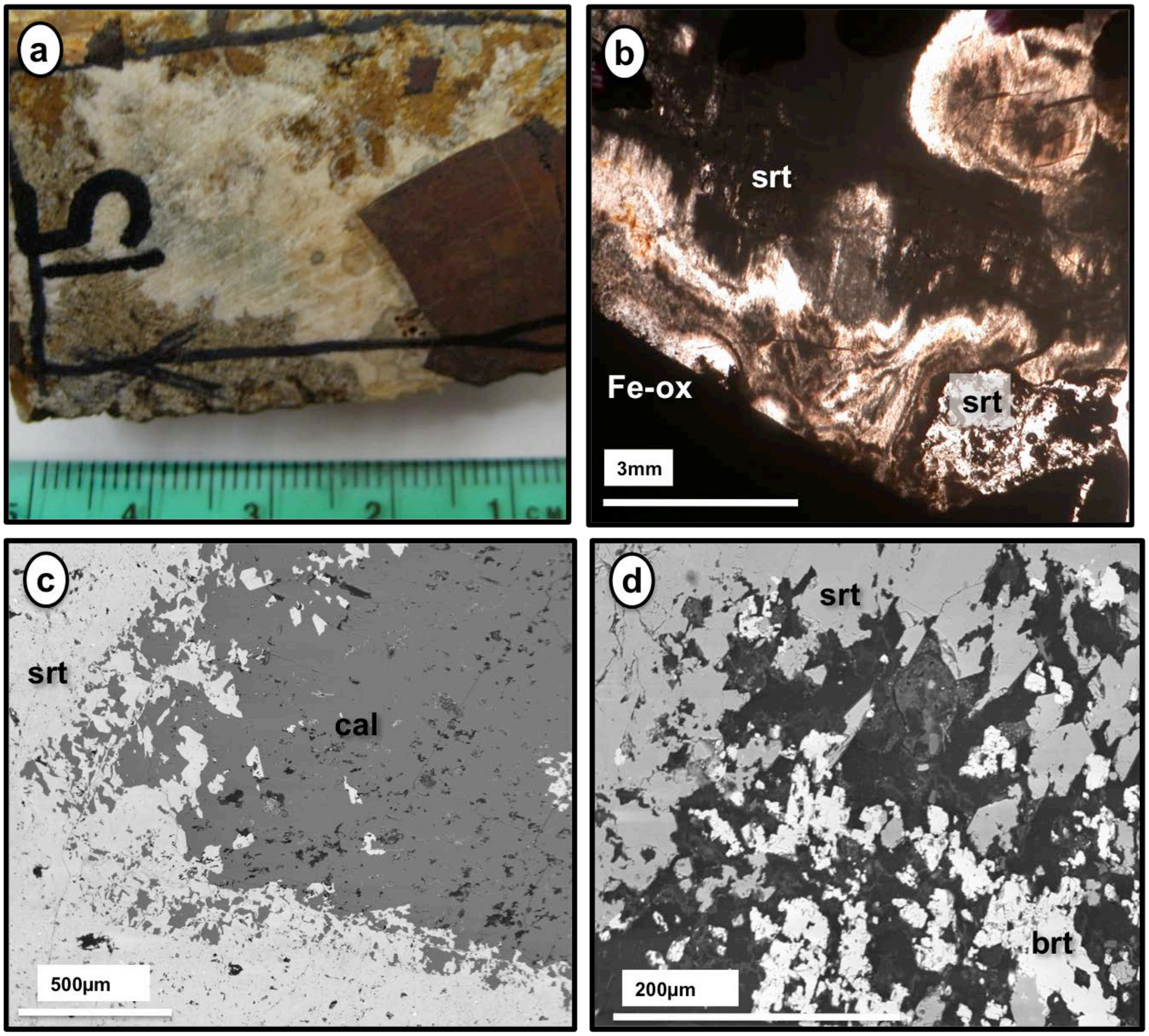

Figure 5.25. Images of unmineralized sample BL15 from the "Ox-Ca"subzone. a) Hand specimen; note pseudomorphs after pyrite. b) Banded, texturally complex intergrowth of brown strontianite (srt) stained by secondary oxides and Fe oxide (Fe-ox) replacing pyrite (XPL). c) Calcite (cal) replaced by strontianite (BSE image). d) Subhedral strontianite and crustiform barite (brt) in a vug (BSE image).

One of the samples (BL15) is not mineralized and consists of strontianite, barite, subordinate residual calcite and large (~3 cm, 10 vol.% of the rock) pseudomorphs of Fe oxides after pyrite (Fig. 5.25). Colloform or spherulitic strontianite with variable proportions of Ca is the dominant groundmass phase (> 50 vol.%). The white strontianite groundmass surrounding the Fe-oxide pseudomorphs fluoresces apple green under the shortwave UV light, whereas other parts of the groundmass fluoresce orange or pink. Barite (~20 vol.%) is also banded and crustiform. Calcite (~10 vol.%) occurs as oxidized rhombohedral grains replaced by strontianite (Fig. 5.25c).

Sample BL25 is unusual because it is composed of oxidized carbonatite crosscut by a vein of unoxidized carbonatite (Fig. 5.26a). The unoxidized material is notably barren of rare-earth minerals and consists of heterogranular, allotriomorphic calcite (85 vol.%), large fragmented crystals of altered biotite (up to 0.8 cm, ~5 vol.%), and a cluster of fine-grained biotite. The calcite hosts multiple micro-inclusions and increases in grain size from the axial zone of the vein toward its contact with the oxidized carbonatite. The oxidized carbonatite consists of Mn-rich zoned, heavily included calcite forming the groundmass (~75 vol.%). Iron and Mn oxides (20-25 vol.%) give the rock its dark color and occur as crustiform aggregates in interstices among calcite grains, around rare-earth minerals, and as partial overprint of the groundmass calcite (Fig. 5.26b). Dark red to maroon-colored Fe-oxide pseudomorphs after pyrite reach up to 0.6 cm across and compose ~10-15 vol.% of the carbonatite. The pseudomorphs are surrounded by halos of Fe oxides confined to interstices in calcite. The remainder of the rock consists of subhedral to euhedral biotite (< 0.05-5 mm, ~15 vol.%), subhedral to euhedral celestine (50-750 µm, ~12 vol.%) with inclusions of anhedral, “spongy” ancylite (~10 µm, <2 vol.%), anhedral masses of parisite and synchysite (10-25 µm, < 2 vol.%) associated with oxide minerals, and small globules of cerianite (< 5 µm, < 1 vol.%) and celestine. The REE fluorocarbonates are depleted in Ce and are represented dominantly by parisite. The REE minerals occur in the carbonatite groundmass, and pseudomorphs are not observed. Aggregates of Ce-poor parisite and celestine associated with cerianite are developed at the expense of ancylite.

Sample BL28 is also unusual enough to warrant a detailed description. It is a bluish-grey to brownish-grey, bleached rock with dark grey carbonatite veins crosscutting heterolithic breccia.The veinlets are only 1 to 2 mm wide and pervasively oxidized, locally containing up to 100 vol.% of Fe and Mn oxides (Fig. 5.27). Elsewhere, the oxide minerals are developed interstitially with respect to xenomorphic calcite (~75 vol.%), bladed strontianite (0.25 mm, 10-30 vol.%), acicular REE fluorocarbonates (< 120 µm in length, 2-10 µm in width, 5-10 vol.%), euhedral biotite (< 1 mm, ~5 vol.%), anhedral to subhedral ancylite (0.25 mm, 2-5 vol.%), amorphous monazite (< 10 µm, < 5 vol.%), and anhedral barite (< 20-30µm, < 5 vol.%).

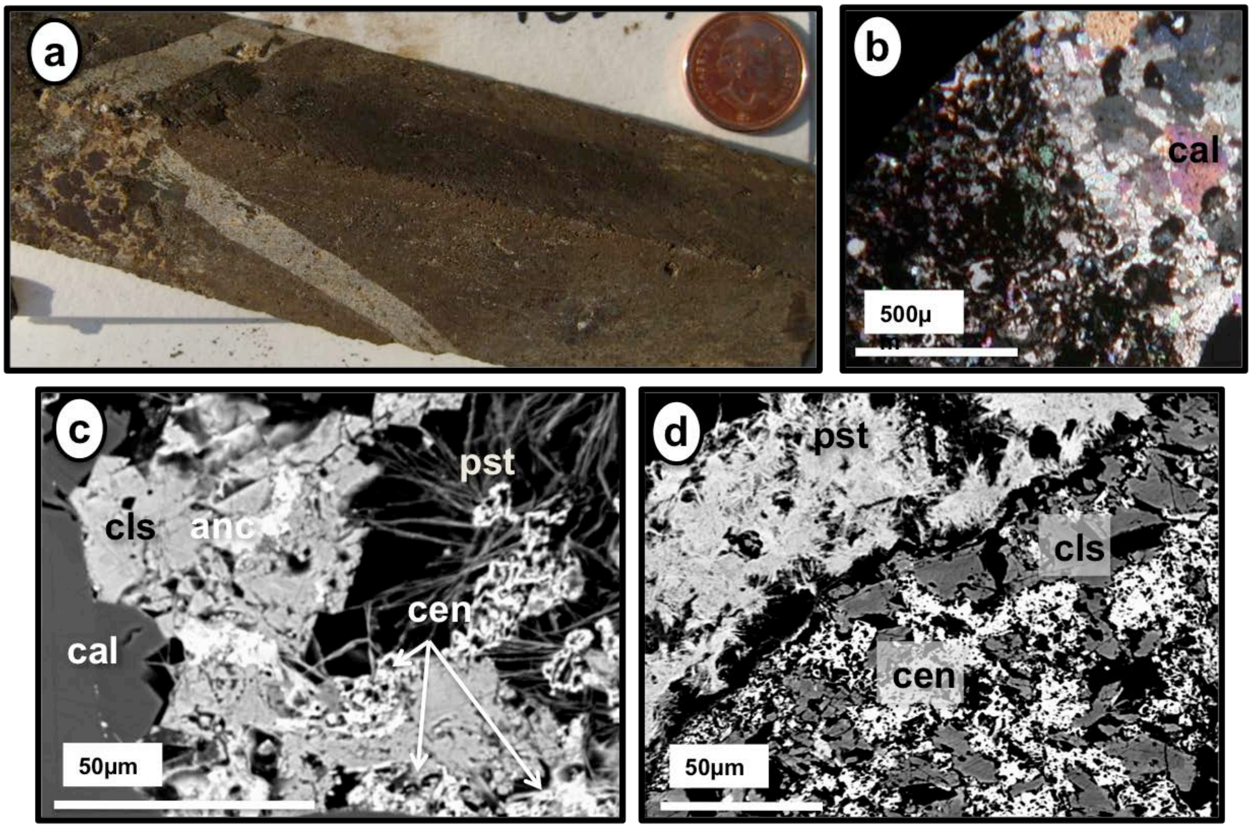

Figure 5.26. Images of sample BL25 from the "Ox-Ca" subzone. a) Unoxidized carbonatite vein crosscutting oxidized groundmass; hand specimen. b) Contact between the oxidized and unoxidized carbonatites (XPL). c) BSE image of minute cerianite crystals (cen) perched on parisite (pst) and ancylite (anc) intergrowths in celestine (cls). d) BSE image of fasciate bundles of parisite segregated from a celestine-cerianite aggregate.

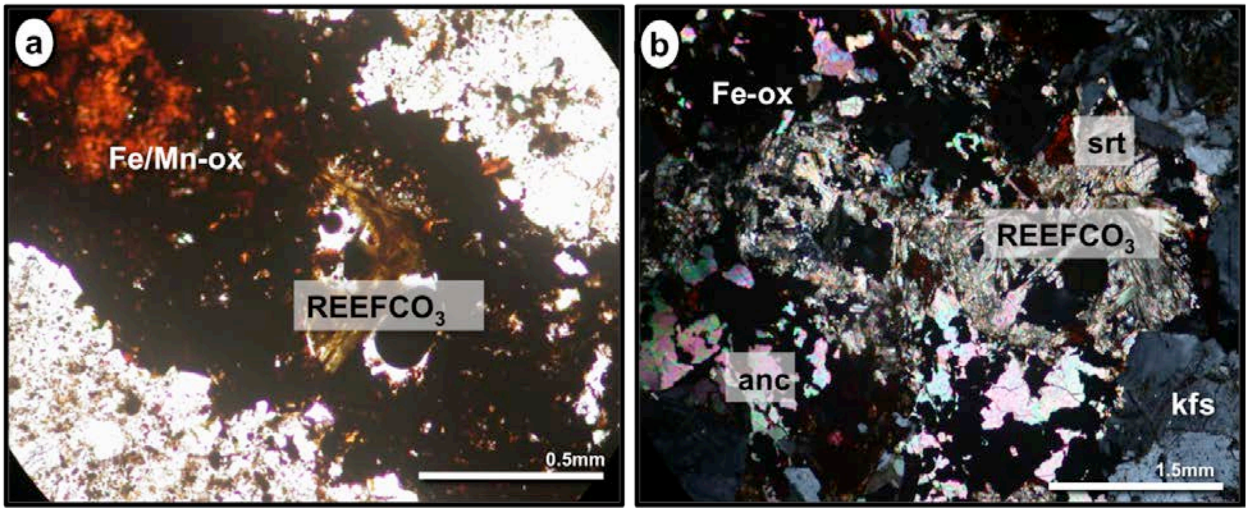

Figure 5.27. Images of sample BL28 from the "Ox-Ca" subzone. a) A vein of oxidized carbonatite (Fe/Mn-ox) crosscutting altered breccia (PPL). b) Carbonatite vein with potassium feldspar (kfs) developed at the contact; REE fluorocarbonates (REEFCO$_3$), ancylite (anc) and strontianite (srt) are surrounded by interstitial Fe oxides (Fe-ox) (XPL).

Glimmerite occurs at the contact of the carbonatite veins with the breccia. In the absence of a glimmerite selvage, potassium feldspar occurs at the contact between the two rock types. A small cluster of fine-grained apatite (~150 µm, 2-5 vol.%) is observed in one of the carbonatite veins. Apatite grains are equant to elongate and locally show a hopper habit. Small vugs in the carbonatite veins contain apatite intimately associated with REE fluorocarbonates. Monazite occurs as pseudomorphs after, or in association with, REE fluorocarbonates. Bastnäsite occurs as overgrowths on earlier-crystallized fluorocarbonates (Fig. 5.28b). Rare-earth minerals locally have a mesh-like texture in the groundmass of the oxidized carbonatite (Fig. 5.28c). Oxide minerals were not analyzed quantitatively or structurally, and their identity is uncertain.

In the remainder of the studied samples, carbonate minerals are minor in abundance and described collectively below. The groundmass consists of subhedral strontianite (10-40 vol.%), subhedral calcite that also occurs as veinlets (microcrystalline, 1.5-3 mm in width, 10-40 vol.%), and equant anhedral barite (10-30 µm, < 20 vol.%); the latter also occurs as inclusions in strontianite. Iron and Mn oxides (limonite, göethite, ramsdellite; Felsman, 2009; Mariano, personal communications; Clark, personal communications) are amorphous to massive or crustiform, and compose up to 70 vol.% of the samples (Fig. 5.24). These minerals were not analyzed quantitatively in the present work. Their EDS spectra show the presence of adsorbed (?) silica similar to the samples from the transitional zone. Where oxide minerals formed in open space, they commonly have a botryoidal habit. In some cases, a mesh-like texture is observed. Subhedral to euhedral Fe-oxide pseudomorphs after pyrite are ubiquitous (≤ 0.25 mm, 5-20 vol.%; Fig. 5.29). Iron and Mn oxides are intimately associated with REE minerals in the oxidized zone (see below). Other minerals, identified in one or more samples, include: subhedral, variably altered biotite (0.02-1.5 mm, 8-16 vol.%); subhedral, commonly turbid potassium feldspar (0.12-5.0 mm, 2-50 vol.%); euhedral to equant anhedral apatite (0.1-0.5 mm, 6-10 vol.%) occurring as veinlets and granular aggregates.

Rare-earth minerals typically found in the groundmass of the oxidized samples include (Fig. 5.29b): cerianite, occurring as “spongy”, crustiform, and interstitial aggregates (microcrystalline to ~0.5 mm across, 5-80 vol.%) and as equant grains associated with Ce-poor REE fluorocarbonates; equant “spongy” monazite (15-160 µm, 7-30 vol.%) intimately associated with oxide minerals and replacing the earlier-formed fluorocarbonates and cerianite in some cases (Fig. 5.30); and fasciate bundles of acicular REE fluorocarbonates (~25 µm in length by 2 µm in width, 25 vol.%). Open space makes up less than 20 vol.% of the groundmass. One sample (BL40) contains phenocrysts of subhedral altered biotite (0.5-1 mm, 5-7 vol.%), and fractured and regenerated potassium feldspar xenocrysts showing turbid cores and clear rims (0.5-3.0 mm, 10-15 vol.%).

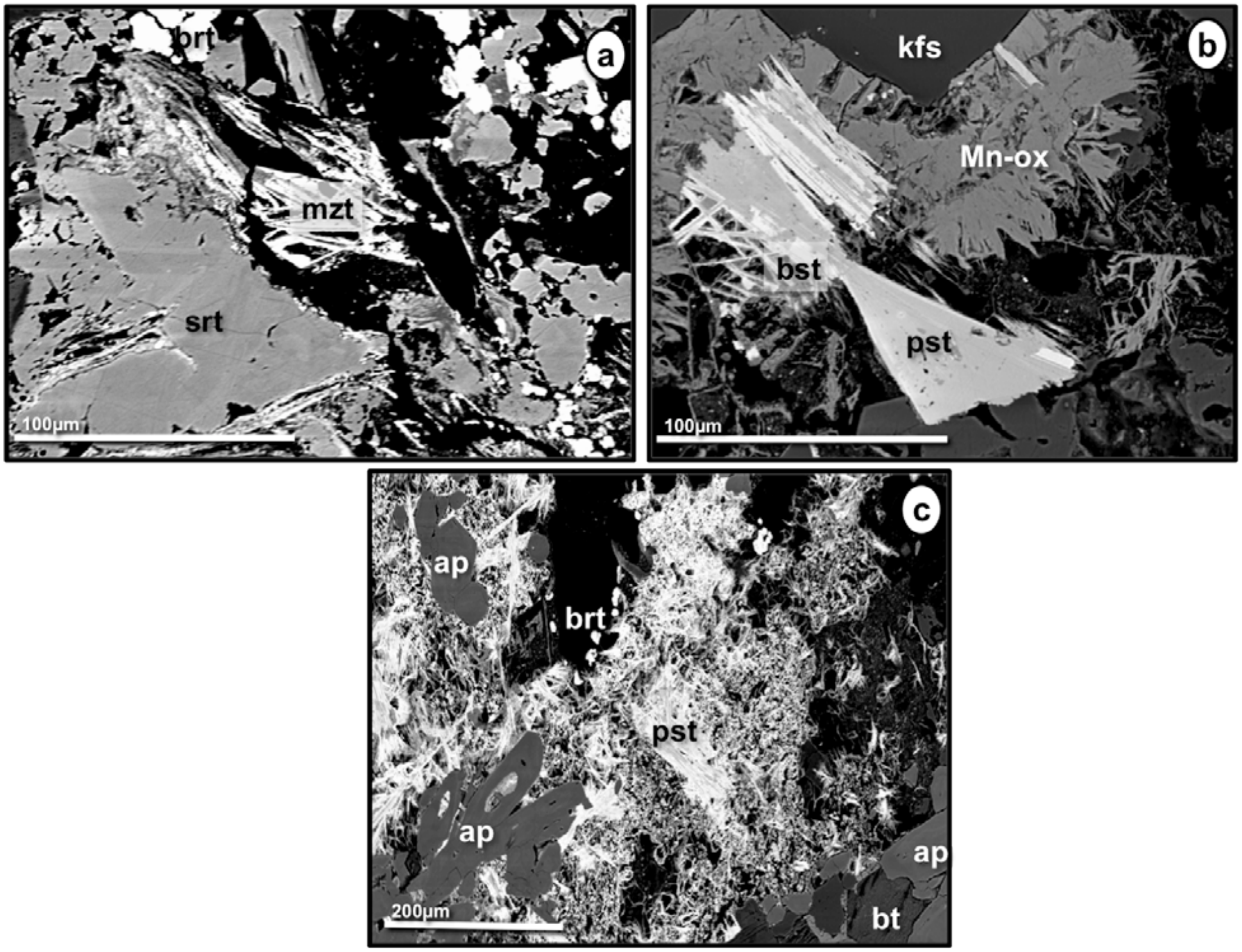

Figure 5.28. Textural characteristics of sample BL28 from the "Ox-Ca" subzone. a) Monazite (mzt) replacing REE fluorocarbonates in association with partially disaggregated strontianite (srt) and crustiform barite (brt). b) Parisite (pst) associated with late-stage bastnäsite (bst) and Mn oxides (Mn-ox) in a vug; kfs, potassium feldspar. c) Mesh-like texture of parisite developed in open space, associated with apatite (ap); note the hopper habit of apatite crystals at lower left. Barite forms thin crustiform aggregates on the parisite.

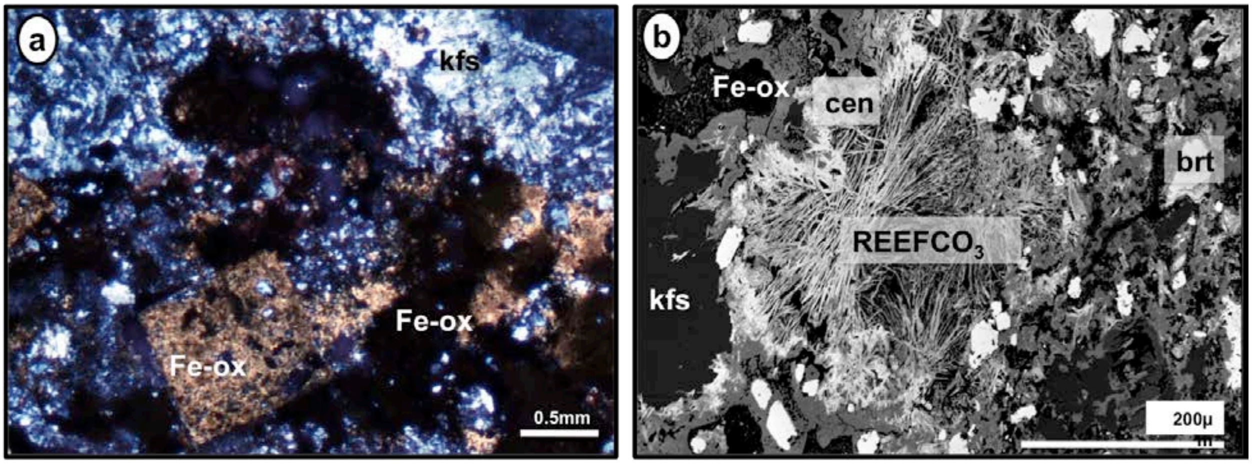

Figure 5.29. Images showing petrographic characteristics of altered rocks from the oxidized zone. a) Undifferentiated Fe-oxide minerals (Fe-ox) occurring throughout trachyte groundmass comprising abundant potassium feldspar (kfs); note a cubic pseudomorph after pyrite in the lower part of the image; thick section, XPL (sample BL44). b) Strongly oxidized sample of "FMR" type (BL115), showing a texturally complex intergrowth of fibrous and fasciate REE fluorocarbonates (REEFCO$_3$) with cerianite (cen), interstitial crustiform Fe-oxide minerals, and barite (brt); also present is relict potassium feldspar (kfs); BSE image.

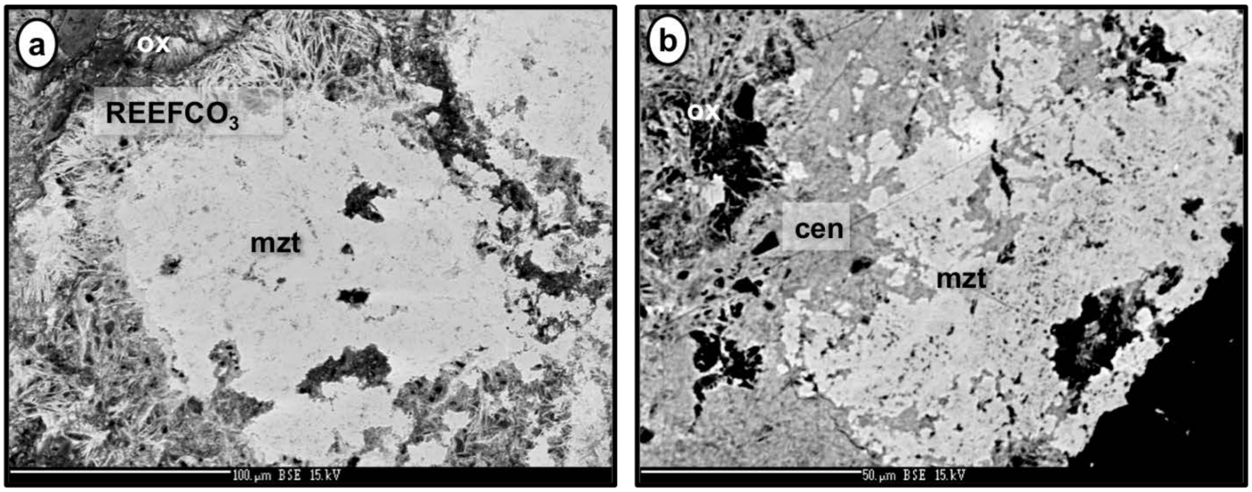

Figure 5.30. BSE images of sample BL115. a) Monazite overprinted by REE fluorocarbonates (REEFCO$_3$) in a vuggy oxidized groundmass (ox).b) Monazite (mzt) associated with cerianite (cen) in a vug (black).

Polymineralic pseudomorphs up to 0.5 cm across make up from 10 to 50 vol.% of the oxidized carbonatites and appear to have undergone multiple episodes of dissolution and crystal growth. Relationships among the individual constituent minerals in these pseudomorphs are quite variable and complex (Figs. 5.31-5.34). The pseudomorphs have a less a distinctive hexagonal morphology than those in the unoxidized and transitional zones, and form aggregates in some cases. A zone of fine-grained biotite or apatite is often developed at the contact between the pseudomorphs and the oxidized groundmass (Fig. 5.31b). Open space makes up to 20 vol.% of the pseudomorphs.

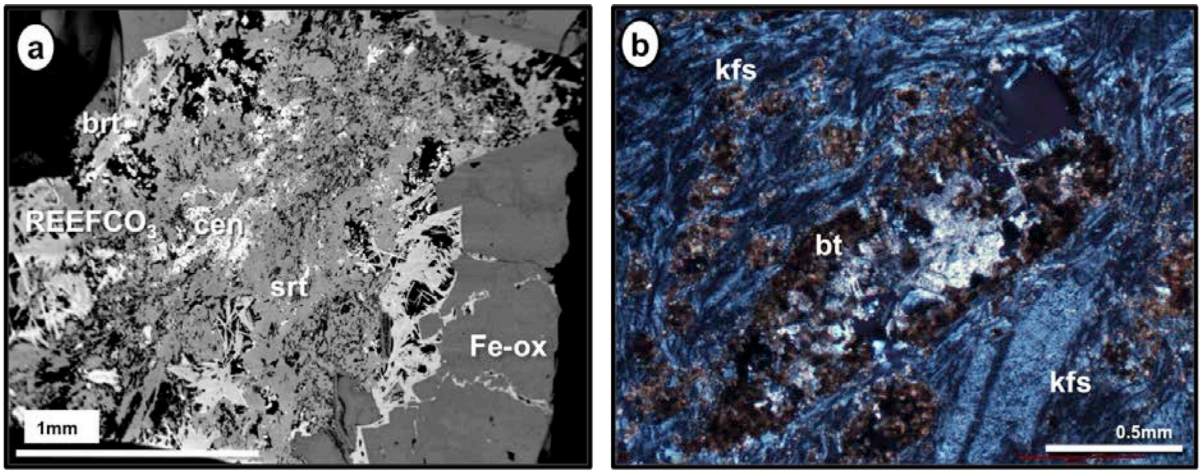

Figure 5.31. REE-bearing pseudomorphs in rocks from the oxidized zone. a) Pseudomorph composedof barite (brt), strontianite (srt), cerianite (cen) and REE fluorocarbonates (REEFCO$_3$) surrounded by Fe oxides (Fe-ox); note lozenge-shaped ancylite replaced by fluorocarbonates at right; sample BL38 (BSE image).b) Pseudomorph rimmed by biotite (bt) at the contact with potassium feldspar (kfs) in the groundmass; the pseudomorph is composed of REE fluorocarbonates and strontianite; sample BL37 (XPL).

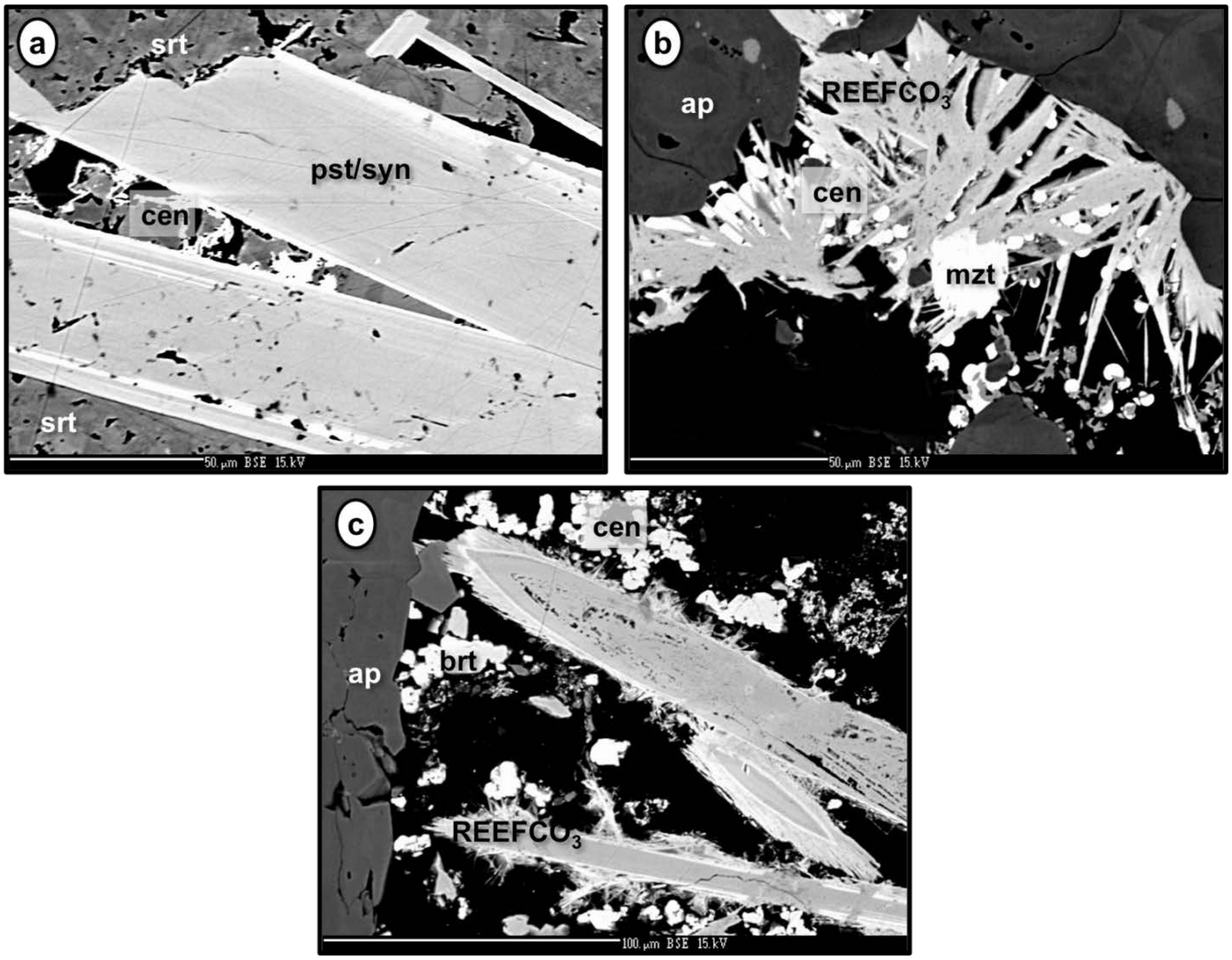

Figure 5.32. BSE images of characteristic rare-earth minerals and textures from the “Ox-Ca”subzone. a) Syntaxial intergrowths of REE fluorocarbonates ($REEFCO_3$), composed principally of parisite (white) and synchysite (grey) associated with strontianite (srt) in a pseudomorph; note minute grains and crusts of cerianite (cen) coating strontianite between the fluorocarbonate laths (sample BL37). b) Equant crystals of cerianite perched on acicular crystals of REE fluorocarbonates associated with monazite (mzt); the aggregate of REE minerals is developed interstitially with respect to apatite (ap) (sample BL38). c) Multiple minute needles of parisite decorating the edges of prismatic synchysite ($REEFCO_3$) in a vuggy pseudomorph; other associated minerals are cerianite, barite (brt), and apatite; note subtle zonation and a mesh texture in the largest synchysite crystal (sample BL38).

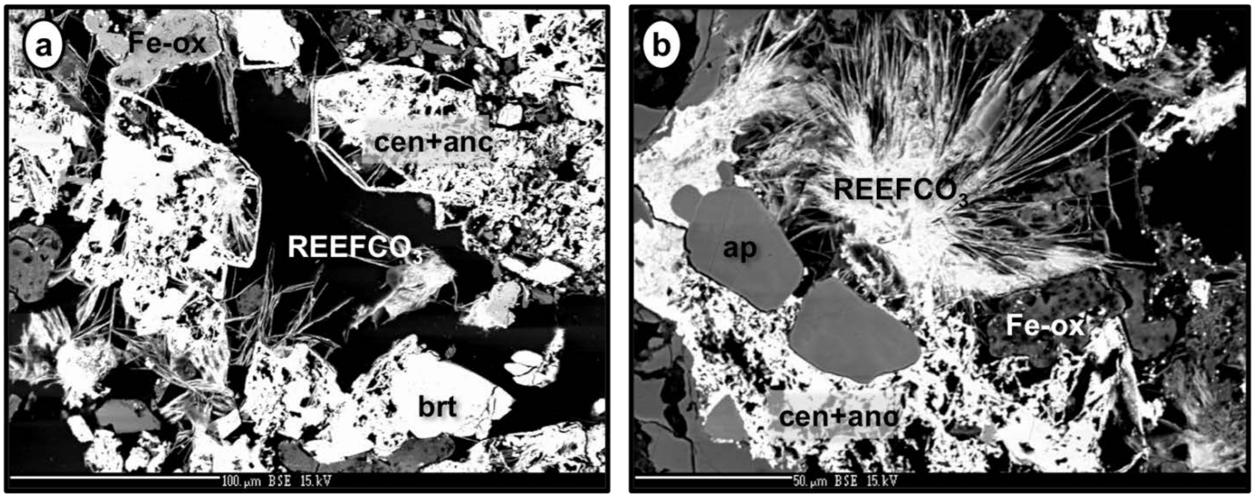

Figure 5.33. BSE images showing characteristic textures of sample BL143. a) Lozenge-shaped "spongy" crystals of ancylite replaced by cerianite (cen+anc) in a pseudomorph; also present are REE fluorocarbonates ($REEFCO_3$) and barite (brt). b) Apatite (ap) overgrown by a "spongy" aggregate of cerianite and ancylite, with acicular REE fluorocarbonates developed in open space in association with Fe oxides (Fe-ox).

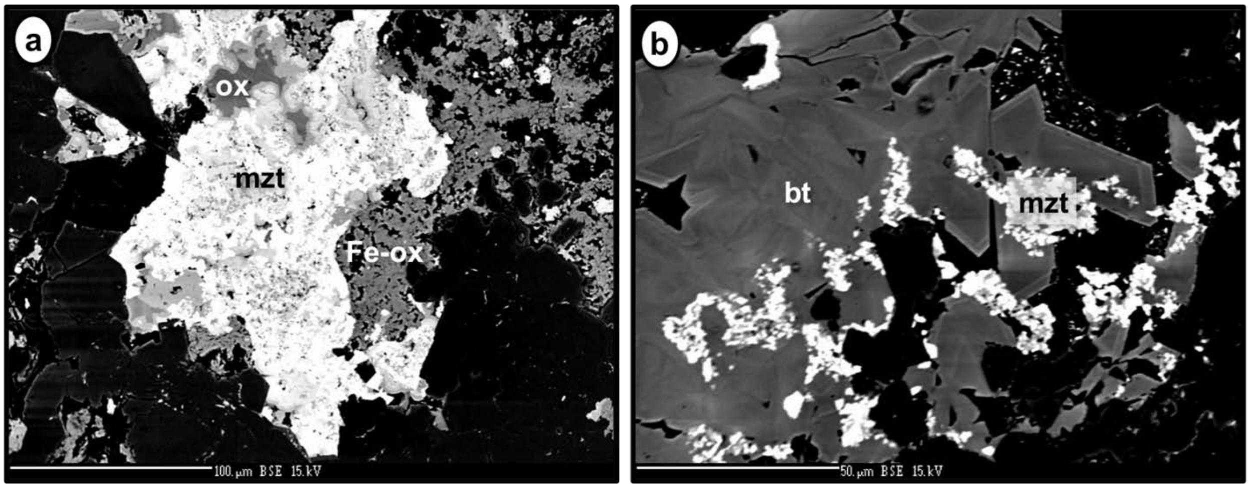

Figure 5.34. BSE images showing characteristic textures of sample BL44. a) Monazite (mzt) intergrown with amorphous oxide minerals (ox, Fe-ox) in oxidized carbonatite; bright spots in the Fe-oxide groundmass are barite. b) Minute equant crystals of monazite developed interstitially with respect to zoned biotite (bt) in a vug.

The pseudomorphs comprise the following constituent minerals (percent values in parentheses refer to the total volume of a pseudomorph):

1) fasciate bundles and isolated crystals of acicular, syntaxially intergrown bastnäsite, parisite and synchysite (up to 1 mm in length and 50 μm in width, 20-50 vol.%);

2) crustiform cerianite (1-15 μm, 10-20 vol.%);

3) "spongy" strontianite (interstitial, < 20 vol.%);

4) interstitial calcite (20-40 vol.%);

5) subhedral equant barite (20-50 μm, 5-12 vol.%);

6) subhedral potassium feldspar altered to sericite or clay (0.1-2.0 mm, ~10 vol.%).

7) scarce monazite (~20 μm, < 5 vol.%; Fig. 5.31) and "spongy" ancylite (< 250 μm, 65 vol.%) partially replaced by Ce-depleted parisite and cerianite (Fig. 5.30b) were identified in one sample each (BL38 and BL143, respectively).

Rare-earth fluorocarbonates are common in the oxidized zone. These minerals tend to show a progressive increase in REE-to-Ca ratio, from the early-crystallizing synchysite to parisite rimming or fringing synchysite crystals (Figs. 5.32a, c), to bastnäsite confined to the edges of synchysite and parisite grains (Fig. 5.28b). In one sample (BL145, described in detail below), bastnäsite is developed interstitially and along cleavage planes in biotite (Fig. 5.35a). In this sample, bastnäsite occurs as two different morphological varieties: acicular syntaxial intergrowths with parisite and synchysite similar to fluorocarbonate intergrowths elsewhere, and amorphous or crustiform aggregates (Fig. 5.35b). The latter variety has distinctive chemical composition (see chapter 6) and is termed here “bastnäsite II”.

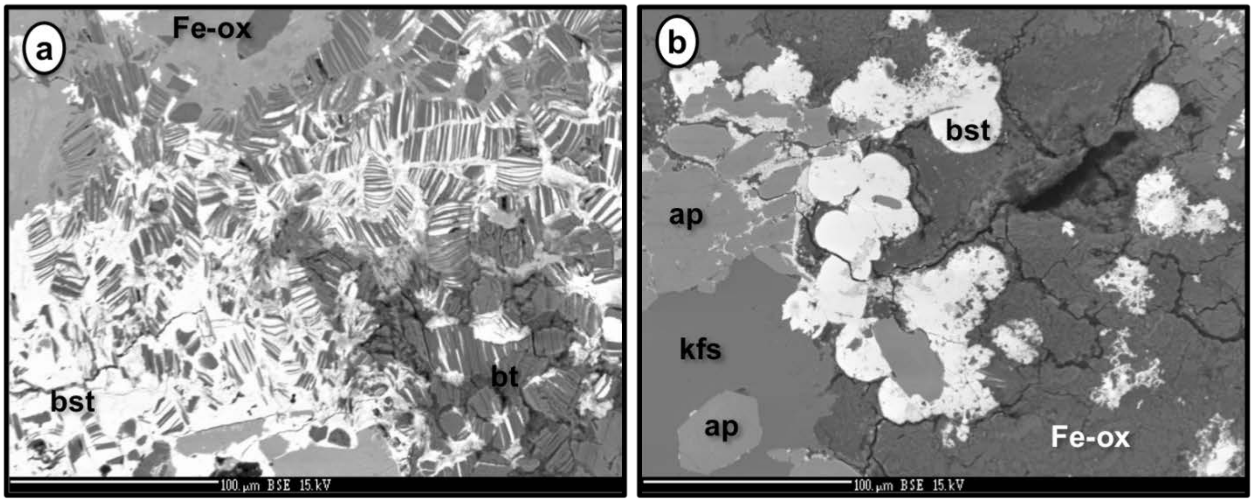

Figure 5.35. BSE images showing characteristic textures of sample BL145. a) Late-stage bastnäsite (bst II) developed interstitially and along biotite (bt) cleavage plains in glimmerite; Fe-ox = Fe oxides. B) Equant crystals or aggregates of late-stage bastnäsite overgrowing relict apatite (ap) and potassium feldspar (kfs) in the Fe-oxide groundmass.

Apatite in the oxidized samples is morphologicallydiverse, ranging from euhedral and hopper crystals to veinlets crosscutting earlier-formedminerals. Several growth episodes are indicated (Fig. 5.28c; 5.32; 5.33c). The Fe and Mn oxides clearly developed via late-stage processes, an interpretation supported by the crustiform and botryoidal morphology of their aggregates, which are either developed interstitially or overprint the earlier-crystallized carbonate minerals (Figs. 5.33-5.36).

Sample BL145 consists of a typical “FMR” material (phase 1) and a very heterogeneous brecciated calcite-bearing material (phase 2). Phase 1 consists of a boxwork of Fe oxides (~30 vol.%) associated with bladed rutile (5-10 vol.%) and late-stage potassium feldspar (~40 vol.%). This sample also contains bastnäsite of two morphological types intergrown with the Fe oxides (Figs. 5.35b, 5.36a). Phase 2 consists of undifferentiated interstitial and amorphous Fe and Mn oxides (~50-70 vol.%), interstitial calcite (~40 vol.%), bladed ilmenite (< 5 vol.%), synchysite (25 µm in length, 2 µm in width, ~5 vol.%), microcrystalline cerianite (< 5 vol.%) and resorbed potassium feldspar (< 5 vol.%). Apatite (< 5 vol.%) occurs as subhedral crystals or aggregates associated with bastnäsite II (~5-10 vol.%). This rock also contains zircon (20 µm, < 5 vol.%), which was not identified in any other samples.

Sample BL138 is notable in lacking rare-earth minerals (Fig. 5.37). In this sample, oxide minerals (dominated by Mn phases) form bands 0.1-3.0 mm in thickness, making up ~60 vol.% of the rock. The oxide material is interlayered with aggregates comprising equal proportions of calcite and strontianite. Calcite is zoned with respect to Sr, Ba and REE (see Chapter 6). All of these minerals appear to be secondary.

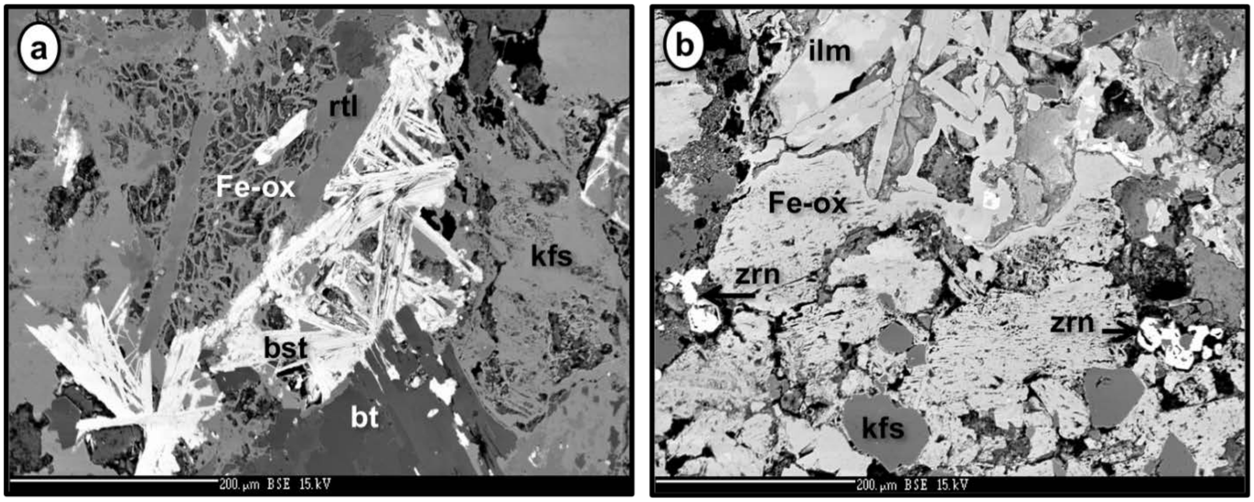

Figure 5.36. BSE images showing the complex mineralogy of sample BL145. a) Phase I; acicular bastnäsite (bst) developed in a boxwork of iron-oxides(Fe-ox); other minerals include biotite (bt), rutile (rtl) and potassium feldspar (kfs). b) Phase II; texturally complex groundmass consisting dominantly of Fe oxides with relict grains of ilmenite (ilm), zircon (zrn) and potassium feldspar.

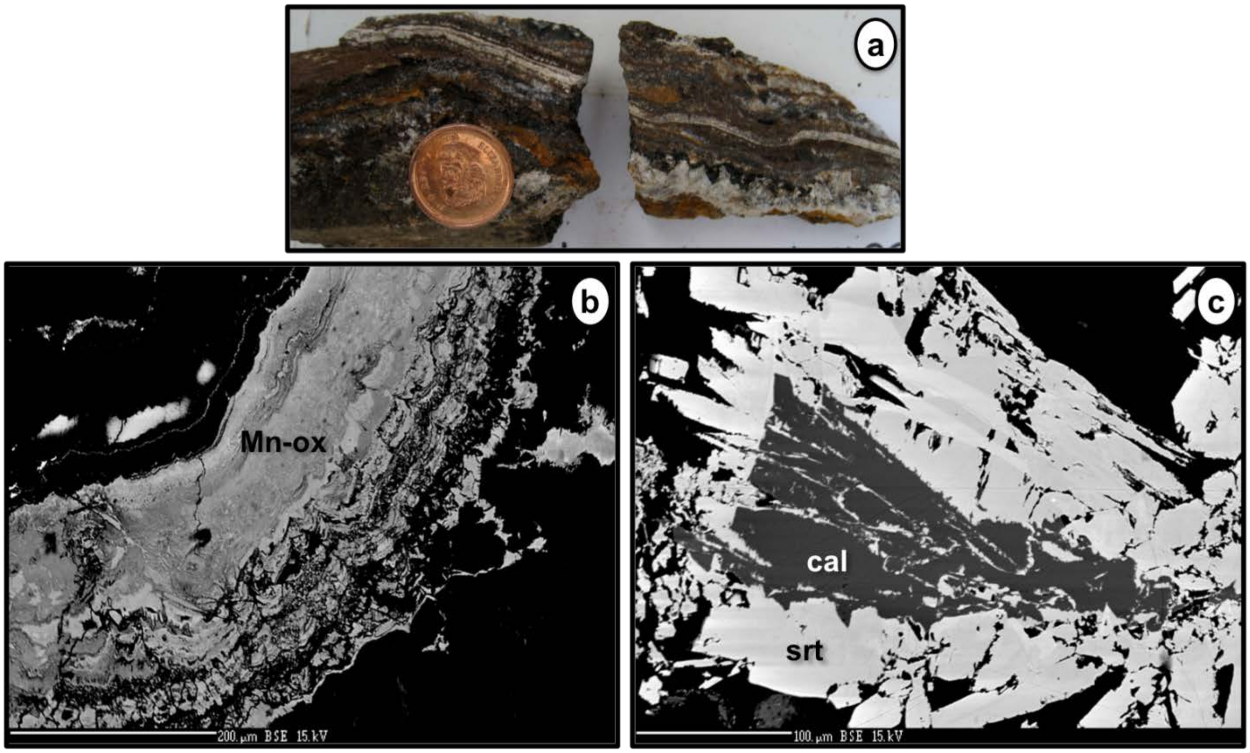

Figure 5.37. Images of sample BL138. a) Hand specimen showing conspicuous banding and variations in color. b) Botryoidal texture and zoning in Mn-oxide aggregates (Mn-ox), BSE image. c) Intergrowth of calcite (cal) and strontianite (srt) in a carbonate layer,BSE image.

Chapter 6. Mineral Chemistry

6.1 Burbankite and Carbocernaite

6.1.1 Introduction to the crystal chemistry of burbankite-group minerals and carbocernaite

Burbankite-group minerals have the general chemical formula $A_3B_3(CO_3)_5$ and include burbankite [$(Na,Ca)_3(Sr,REE,Ba,Ca)_3(CO_3)_5$], khanneshite [$(Na,Ca)_3(Ba,Sr,REE,Ca)_3(CO_3)_5$], calcioburbankite [$(Na,Ca)_3(Ca,REE,Sr)_3(CO_3)_5$], remondite-(Ce) and -(La) [$Na_3(Ce,La,Ca,Na,Sr)_3(CO_3)_5$] and petersenite-(Ce) [$(Na,Ca)_4(Ce,La,Sr)_2(CO_3)_5$]. Burbankite, khanneshite and calcioburbankite are hexagonal, whereas remondite and petersenite are pseudohexagonal (monoclinic). Burbankite-group minerals form a complex isomorphous series involving end-members whose formulae can be generalized as $(Na_2Ca)(Sr,Ca,Ba)(CO_3)_5$ (REE-free components) and $Na_3(REE_2Na)(CO_3)_5$ (Belovitskaya and Pekov, 2004). Note that from the standpoint of mineral nomenclature, burbankite is not an REE mineral because these elements are not essential to its crystal structure. The REE_2O_3 contents reported in the literature range from nil to 23 wt.% in calcioburbankite from the Vuoriyarvi carbonatite, Russia (ibid.).

Carbocernaite is a rare Na-Ca-Sr carbonate mineral known from less than a dozen carbonatite localities worldwide, including its type locality at Vuoriyarvi. This mineral is structurally and compositionally distinct from burbankite. It has lower Na_2O and higher REE_2O_3 contents (< 6 and > 23 wt.%, respectively) and crystallizes with an orthorhombic symmetry (Bulakh et al., 1961; Yakovenchuk et al., 2005). The idealized formula of carbocernaite can be written as $(Ca,Na)(Sr,REE,Ba)(CO_3)_2$.

There is a significant variation in the composition of burbankite and carbocernaite from the unoxidized Bull Hill carbonatites. Compositions of these minerals obtained by WDS are presented in Appendix C. All EMPA data for burbankite were recalculated on the basis of five CO_3 groups, then the Sr-dominant B-site was filled to 3 apfu with REE, Sr, Ba, Th, and then Ca and Na; the remainder of Ca and Na was allocated to the A site. The carbocernaite analyses were recalculated on the basis of two CO_3 groups.

6.1.2 Burbankite

Burbankite in T-684-L is a primary magmatic phase, interpreted as phenocrysts immersed in a calcitic groundmass (Fig. 5.1). High concentrations of BaO (up to 9.7wt.%) in this mineral are consistent with what has been reported previously for primary burbankite from other carbonatites (e.g., Belovitskaya and Pekov, 2004). The burbankite crystals exhibit complex zonation with respect to Ba and Sr. Cerium is the dominant lanthanide in most analyses, but the REE distribution also varies with zonation (Figs. 6.1 and 6.2). Relict crystals of burbankite in polymineralic pseudomorphs in sample BL71 (Fig. 5.3b) have the highest concentrations of BaO, ranging from 24.3 to 27.2wt.%, but some proportion of this Ba is probably an analytical artifact because Pr was consistently below its limit of detection byWDS, implying analytical peak overlap between Ba and Pr. In this sample, the occurrence of relict burbankite in the cores of pseudomorphs composed of ancylite and strontianite but lacking barite (Fig. 5.1) could indicate relatively high mobility of Ba or unavailability of sulfate during the pseudomorphization.

There are clear differences in the distribution of individual LREE in the burbankite from the two samples that are apparent in the plot of chondrite-normalized $(La/Ce)_{cn}$ vs. $(La/Nd)_{cn}$ values in Fig. 6.3. Whereas Fig. 6.2 shows some clustering between the two samples with respect to Na, Ca, Sr and Ba contents, Fig. 6.3 highlights the fact that the crystals in sample T-684-L are zoned, and form a trend of overall positive correlation between $(La/Ce)_{cn}$ and $(La/Nd)_{cn}$ that correlates with that of carbocernaite (described below). Burbankite from sample BL71 plots in a distinct area with high values of $(La/Ce)_{cn}$ and correspondingly low values of $(La/Nd)_{cn}$. Burbankite from sample BL71 has higher REE_2O_3 concentrations (23.9 to 29.0 wt.%) than that from sample T-684-L (13 to 21 wt.%). Samarium, Eu, Gd and Y were all below detection in sample T-684-L, but detectable in sample BL71. In both samples, high REE_2O_3 concentrations correspond to low SrO contents.

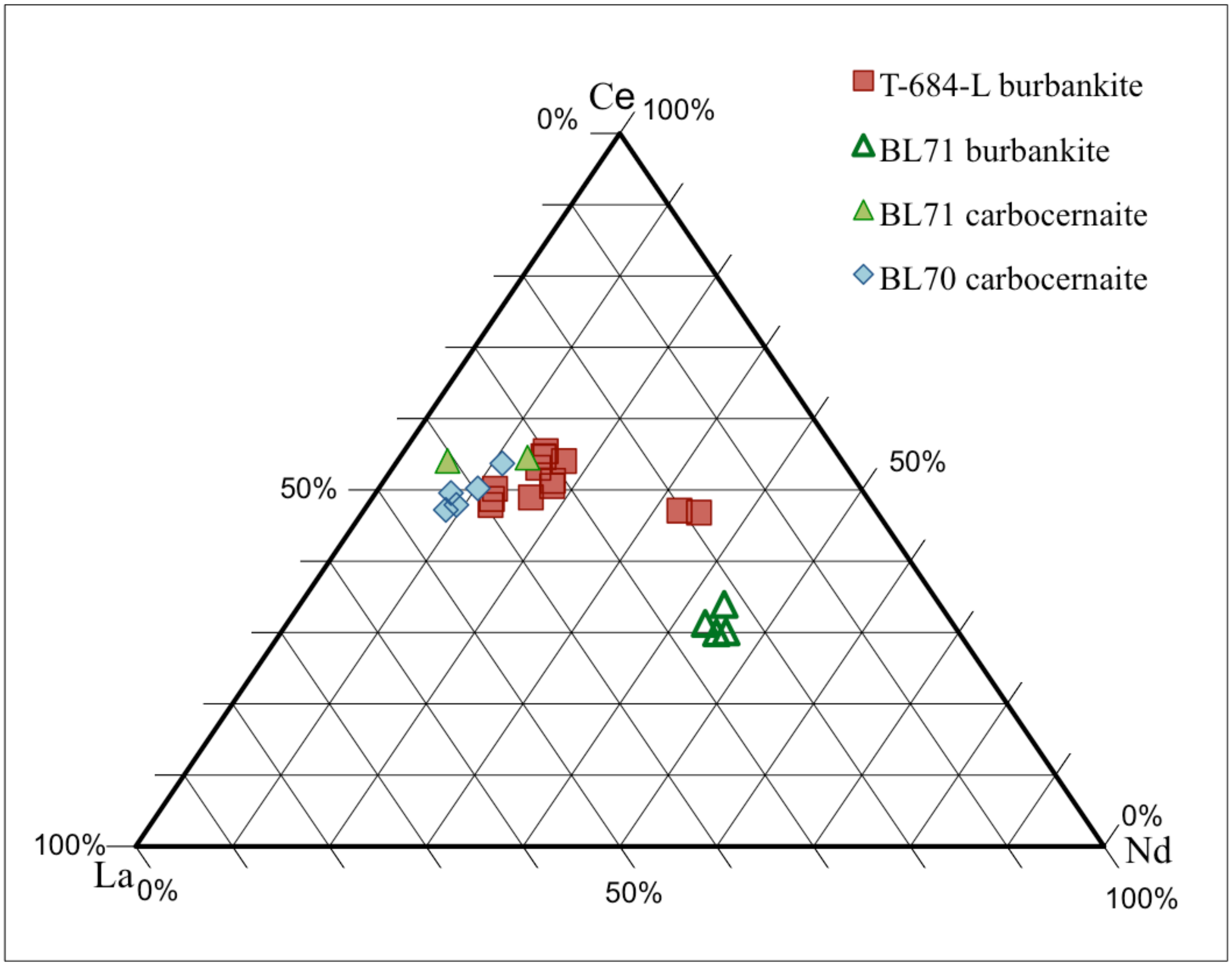

Figure 6.1. Ternary diagram showing burbankite-group REE speciation. WDS data in ppm normalized to 100%. All analyses of carbocernaite are Ce-dominant with La as the second-most abundant lanthanide. The burbankite analyses correspond to Ce- and Nd-dominant compositions.

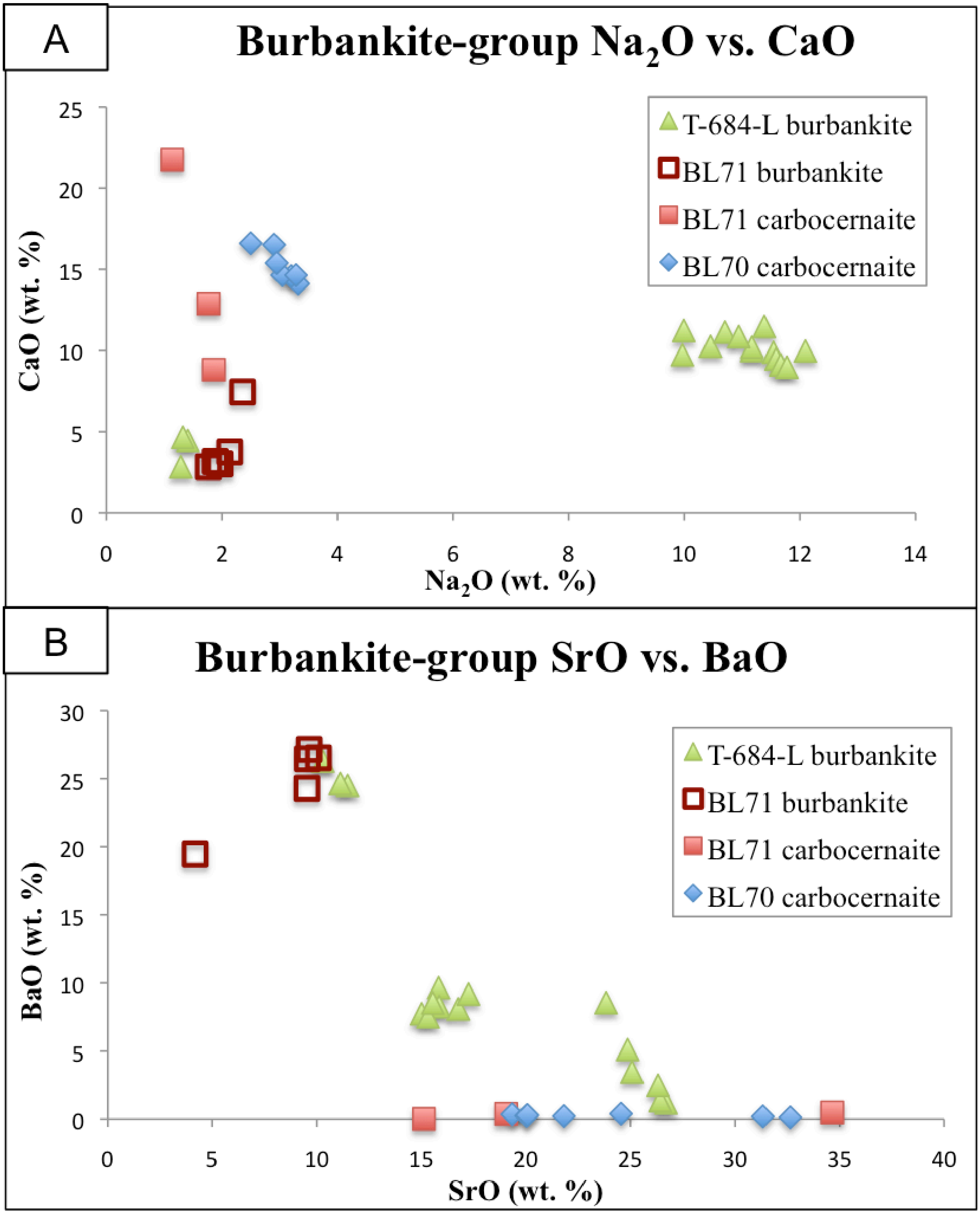

Figure 6.2. Compositional variation (wt.%) of burbankite-group minerals. A) Na_2O vs. CaO; B) SrO vs. BaO, highlighting low Ba concentrations in carbocernaite and zoned distribution of the two elements in burbankite from sample T-684-L.

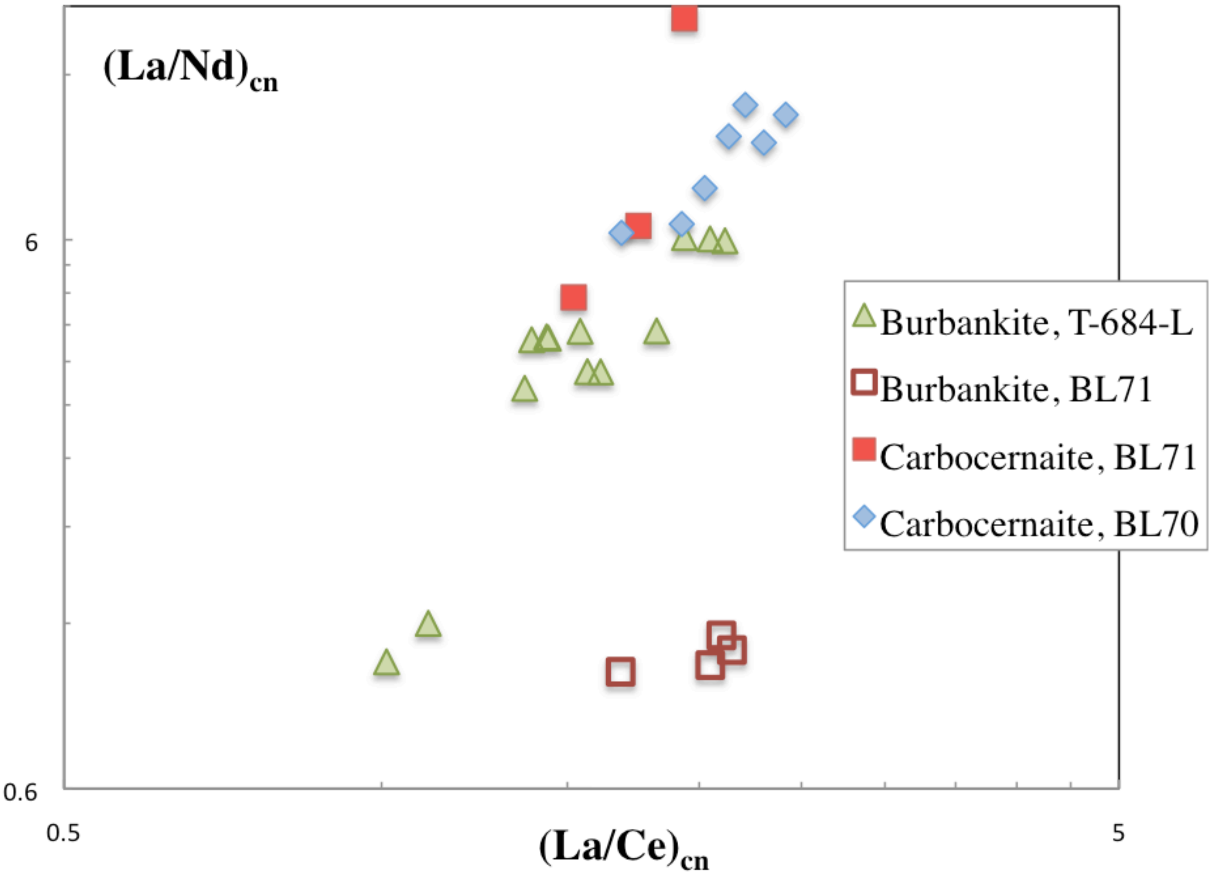

Figure 6.3. Variation in chondrite-normalized (La/Ce)$_{cn}$ *and* (La/Nd)$_{cn}$ *ratios of burbankite-group minerals; Nd-dominant burbankite from BL71 plots in a distinct area. The normalization values are from Anders and Grevesse (1989).*

Chondrite-normalized REE profiles of burbankite and carbocernaite have the same negative, steeply sloping shape in the light-lanthanide part of the series (Fig. 6.4). Although REE with higher atomic numbers than Sm were below their limit of detection by EMPA, it can be inferred that the observed trend would continue with the same slope through the lanthanide series for all samples except BL71, which does not produce a smooth profile and has anomalous Nd and Sm concentrations with respect to the other samples (Fig. 6.4).

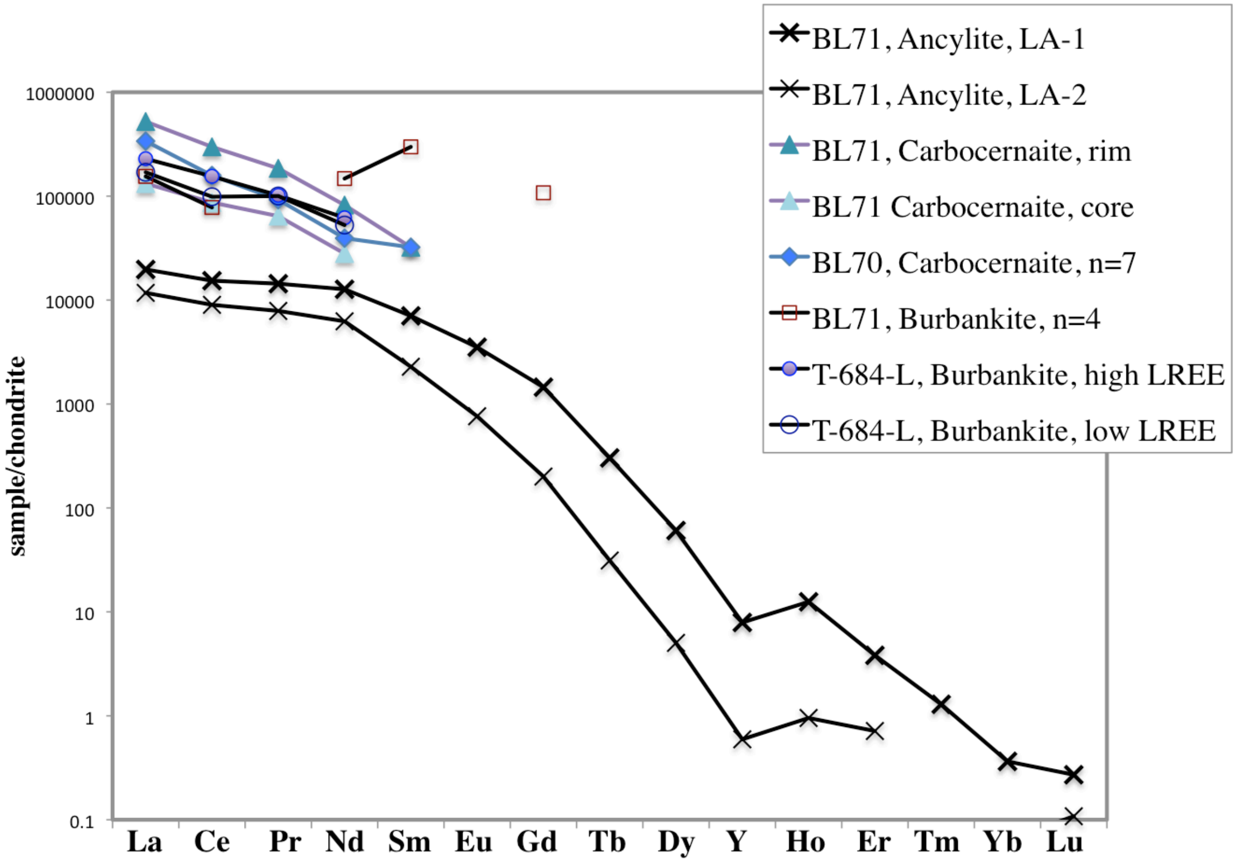

Figure 6.4. Chondrite-normalized REE profiles of burbankite and carbocernaite (WDS data); LA-ICP-MS data for ancylite from the burbankite paragenesis (BL71) are shown for comparison.

6.1.3 Carbocernaite

Considerable variation in carbocernaite chemistry occurs between the two samples in which it was identified. Both have a low BaO content (< 0.4 wt.%), but carbocernaite from sample BL71 has much lower Na_2O contents than that from sample BL70 (1.1-1.9 and 2.5-3.3 wt.%, respectively). Notably, carbocernaite in the two samples occurs with different mineral associations (see Chapter 5). An inverse relationship between CaO and Na_2O, as well as between SrO and BaO contents, is observed in carbocernaite from sample BL70. Crystals from sample BL71 show strong sector zonation and an inverse relationship between the Na_2O and CaO contents. In contrast, the SrO and BaO contents show a positive correlation in these crystals (Fig. 6.2). The highest REE_2O_3 values are associated with the lowest SrO contents in both samples. Carbocernaite has a much greater range of REE_2O_3 values (11.9 wt.% in the core to 42.2 wt.% in the rim of of the sector-zoned crystal from BL71; 13.9-28.3 wt.% in sample BL70) relative to burbankite (13.0-29.0 wt.%), but has much lower BaO and Na_2O contents. Strontium concentrations range from 9.6 to 26.3 wt.% SrO in burbankite and from 15.1 to 32.6 wt.% SrO in carbocernaite. Both carbocernaite-bearing samples show similar chondrite-normalized REE profiles (Fig. 6.4); in the $(La/Ce)_{cn}$ vs. $(La/Nd)_{cn}$ diagram, their compositions plot along the same trend as the burbankite data, but at higher $(La/Nd)_{cn}$ values (Fig. 6.3).

6.2 Rare-Earth Fluorocarbonates

The REE fluorocarbonates include bastnäsite [$REE(CO_3)F$], parisite [$CaREE_2(CO_3)_3F_2$], and synchysite [$CaREE(CO_3)_2F$]. These minerals often occur as syntaxially intergrown aggregates, with the size of individual crystallites approaching several microns (see Chapter 5). All WDS data for rare-earth fluorocarbonates (Appendix C) were recalculated on the basis of a total positive charge (+3 for bastnäsite, +8 for parisite and +5 for synchysite). Accepted analytical totals range from 98.5 to 100 wt.%, and CO_2 contents were recalculated on the basis of charge balance.

All REE fluorocarbonates in the unoxidized zone and the majority in the transitional and oxidized zones are Ce-dominant. Out of a total of 95 EMPA measurements, 19 analyses of bastnäsite and parisite from the transitional and oxidized zones are La-dominant, and one analysis of bastnäsite from the oxidized zone is Nd-dominant (Fig. 6.5). Most analyses plot in a cluster at approximately 50% Ce and between 10% and 35% Nd on the La-Ce-Nd ternary diagram.

Table 6.1 summarizes chemical characteristics of the REE fluorocarbonates. The complete analytical data set is given in Appendix C. While the total rare-earth oxide content detectable by WDS ($La_2O_3 + Ce_2O_3 + Pr_2O_3 + Nd_2O_3 + Sm_2O_3 + Gd_2O_3 + Y_2O_3$) is relatively consistent in the individual REE fluorocarbonates, a slight enrichment trend in each mineral is observed from the unoxidized to the oxidized zone. Fluorocarbonates from the fluorocarbonate paragenesis have the highest REE_2O_3 levels among all samples from the unoxidized zone, and on average, the highest REE_2O_3 content overall. Some overlap of REE content between synchysite and parisite could indicate that some of these data represent analyses of a mixture of these two minerals in various proportions, as suggested by the microscopic nature of syntaxial intergrowths, although care was taken to analyze only areas that appear homogeneous in BSE images and were large enough for the 2 µm electron beam. The wide range of CaO and FeO values attests to the presence of submicroscopic intergrowths of different fluorocarbonates (and also Fe oxides in some cases) on a scale smaller than the spatial resolution of EMPA. Although structural studies of these minerals were not conducted, recalculated data may indicate the occurrence of vacancies in the crystal lattice.

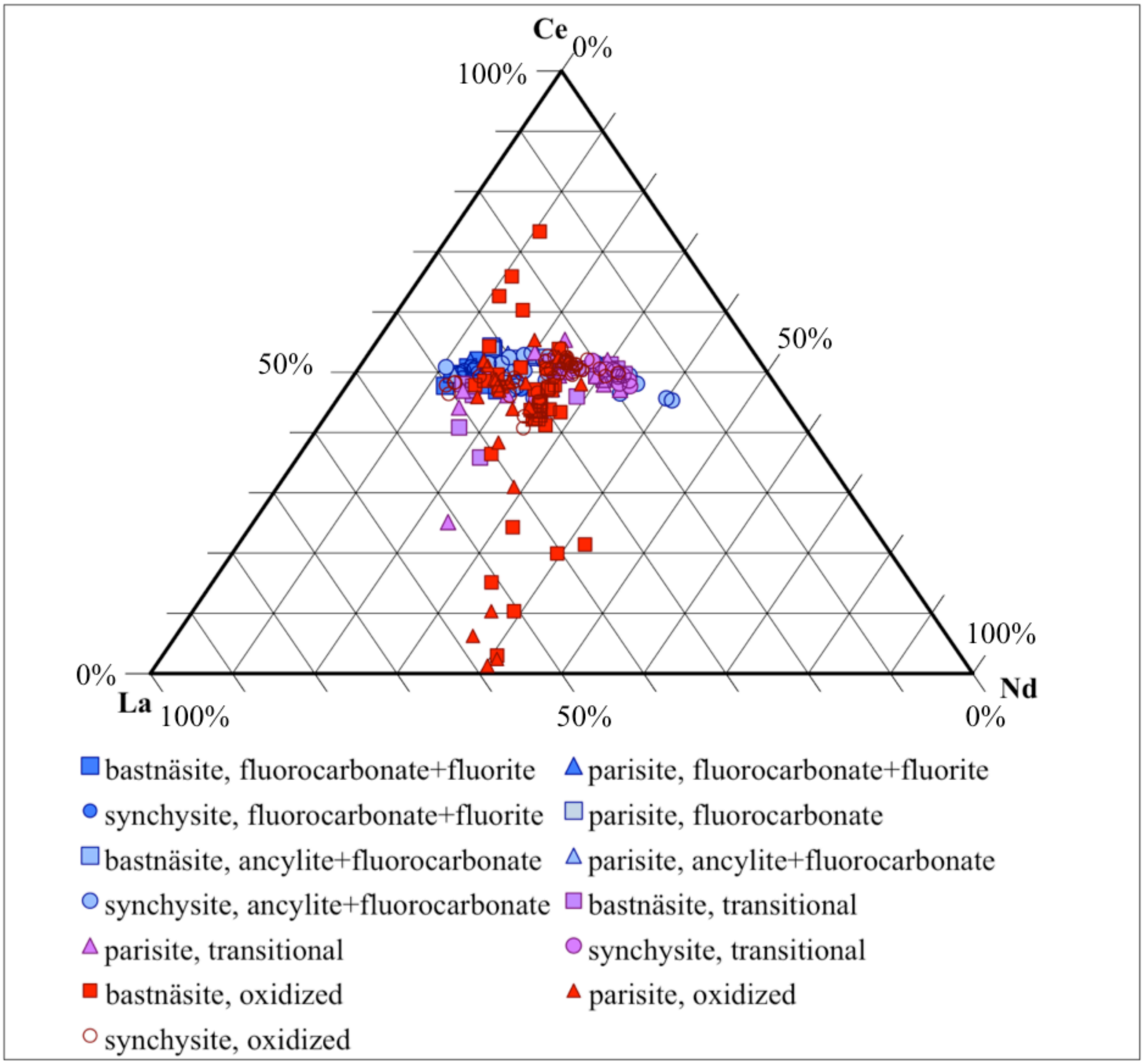

Figure 6.5. Ternary diagram illustrating REE speciation of rare-earth fluorocarbonates by mineral, paragenesis and zone; WDS data in ppm normalized to 100%. Blue symbols are from the unoxidized, purple from the transitional and red from the oxidized zones.

Table 6.1. Selected aspects of REE fluorocarbonate chemistry. Complete analytical data set in Appendix C.

Rare-earth fluorocarbonate chemistry						
zone, paragenesis	***n***	**ΣREE_2O_3 wt%**	**Average ΣREE_2O_3**	**CaO wt%**	**ΣM^{2+}(wt% oxides)**	**ΣREE (apfu)**
			Synchysite			
Unoxidized, fluorocarbonate	13	48-64-56.23	53.18	14.24-20.09	14.70-20.70	0.94-1.04
Unoxidized, fluorocarbonate+fluorite	15	52.19-60.31	56.53	15.10-19.98	15.84-20.75	0.94-1.11
Unoxidized, ancylite+fluorocarbonate	24	38.71-59.23	49.09	4.31-19.95	13.23-21.54	0.89-1.42
Transitional	13	41.45-61.98	55.08	4.32-18.05	9.10-26.74	0.90-1.21
Oxide	50	30.59-62.37	54.67	6.03-19.37	6.82-22.66	0.88-1.26
			Parisite			
Unoxidized, fluorocarbonate	7	51.56-63.41	56.86	7.65-18.90	9.34-18.18	1.57-2.00
Unoxidized, fluorocarbonate+fluorite	4	59.14-65.35	61.85	9.47-15.57	10.03-16.28	1.74-2.04
Unoxidized, ancylite+fluorocarbonate	5	51.53-69.46	60.22	5.26-9.19	6.89-14.29	1.65-2.11
Transitional	25	42.79-61.36	58.88	2.10-18.45	3.74-19.52	1.15-2.15
Oxide	23	53.01-66.63	62.35	3.81-13.31	5.14-17.15	1.59-2.17
			Bastnäsite			
Unoxidized, fluorocarbonate	6	62.78-68.16	65.47	3.28-5.63	4.32-10.71	0.77-0.89
Unoxidized, fluorocarbonate+fluorite	10	66.88-75.01	71.78	0.84-5.02	1.49-6.56	0.84-0.97
Unoxidized, ancylite+fluorocarbonate	4	62.75-71.55	67.03	3.05-4.17	4.77-8.58	0.85-0.90
Transitional	23	71.13-74.82	72.68	1.87-3.86	2.66-5.67	0.75-0.93
Oxide	54	61.25-75.65	69.09	1.81-5.61	2.78-11.77	0.56-0.91

Variations in CaO wt.% are likely due to intimate intergrowths of the fluorocarbonates. Ideal CaO wt.% is ~17 for synchysite, ~10 for parisite and ~0 for bastnäsite. M^{2+} = Ca, Sr, Ba, Fe

Strontium, Mn, Fe, and Ba are present in variable proportions, up to a few wt.% oxide. The highest Fe content occurs in REE fluorocarbonates from the transitional zone and is certainly due to contamination (Table 6.1, Appendix C). It is noteworthy that ThO_2 concentrations are below the limit of detection in most samples. Where detected, the highest ThO_2 contents are observed in fluorocarbonates from the oxidized zone and the lowest in the unoxidized zone (2.5 wt% in bastnäsite II and 0.4 wt % in parisite, respectively). Values of Y/Ho from laser-ablation analyses range from 19.4 to 20.4, and $(La/Yb)_{cn}$ values range from 1203 to 2955 in synchysite and bastnäsite, respectively (Appendix D).

6.2.1 Synchysite

Consistent variation in the content of La, Ce and Nd in synchysite occurs in the different parageneses and zones (Figs. 6.6 and 6.7). Two clusters of synchysite compositions from the transitional zone are evident in the $(La/Ce)_{cn}$ vs. $(La/Nd)_{cn}$ diagram, whereas samples from the oxidized zone plot over a larger area, with considerable overlap between analyses from the unoxidized and transitional zones. An overall positive correlation exists between $(La/Ce)_{cn}$ and $(La/Nd)_{cn}$.

Chondrite-normalized profiles of synchysite from the different zones show slight differences (Fig. 6.8). All profiles show LREE enrichment, with a negative slope from La to Y, and a gradual change from relatively flat from La to Sm in the unoxidized zone to slightly convex in the oxidized zone. One data set from the oxidized zone shows a prominent negative Ce anomaly. One complete set of REE data was obtained by LA-ICP-MS analysis for synchysite from the fluorocarbonate paragenesis in the unoxidized zone (sample BL81); this set shows a prominent negative Y anomaly reflected in a subchondritic Y/Ho ratio in this material (Fig. 6.8).

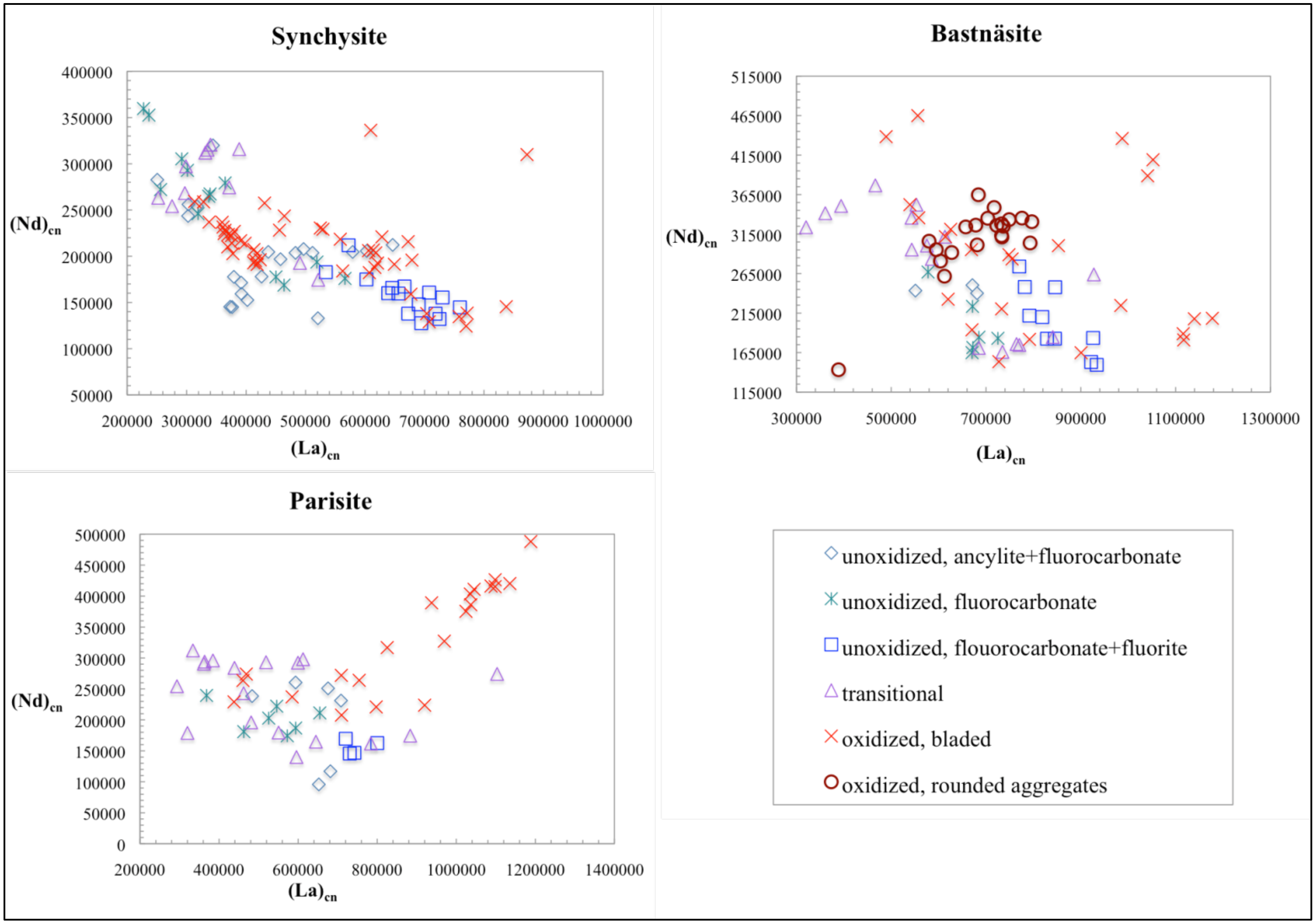

Figure 6.6. Chondrite-normalized plot of La vs. Nd concentrations in rare-earth fluorocarbonates. Note distinct clustering of minerals from the different parageneses in the unoxidized zone and large variations in values in the samples from the transitional and oxidized zones.

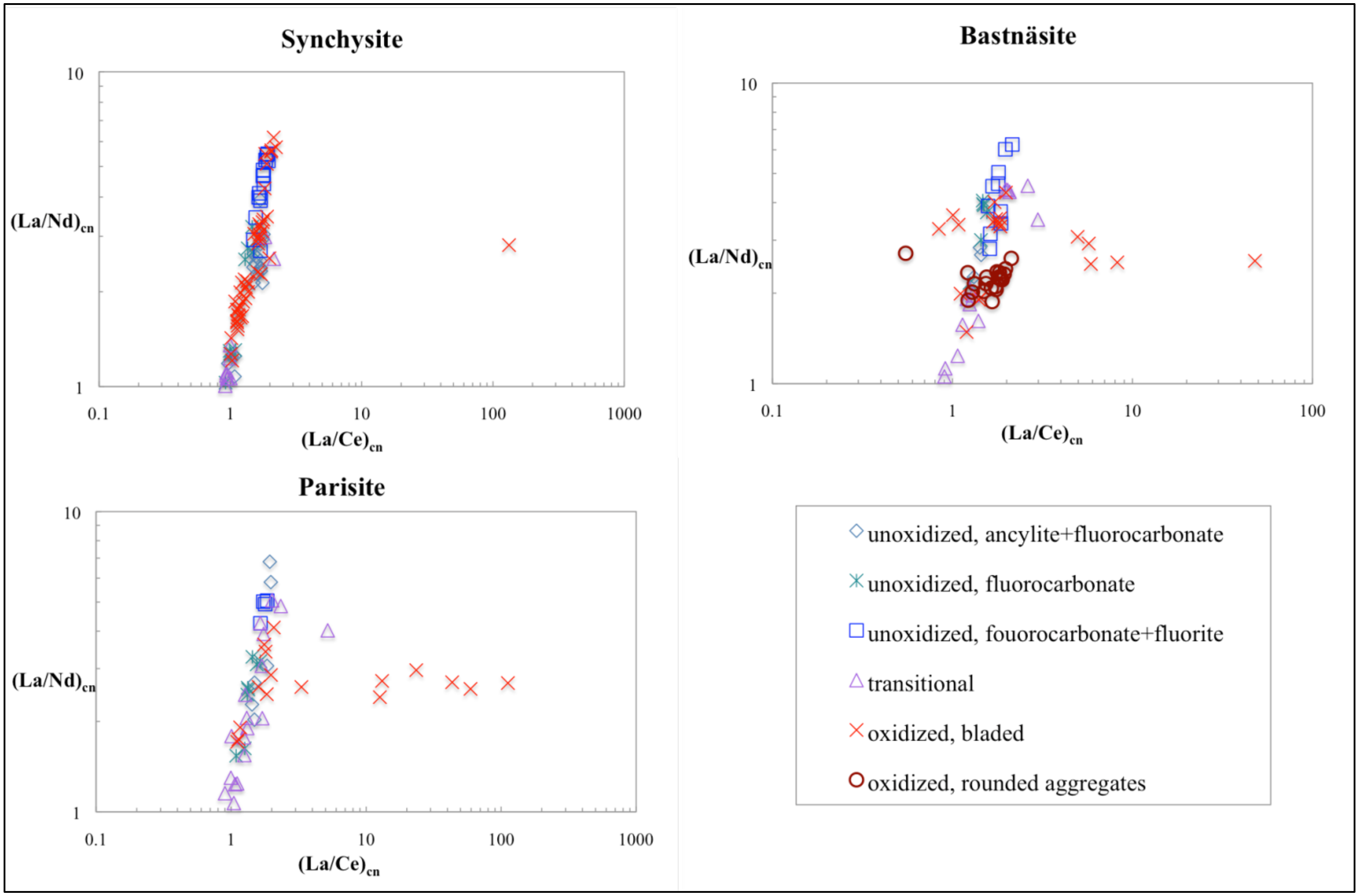

Figure 6.7. Variation in chondrite-normalized element ratios (La/Ce)$_{cn}$ and (La/Nd)$_{cn}$ in REE fluorocarbonates. Note high (La/Ce)$_{cn}$ values in fluorocarbonates from the oxidized zone, clustering of compositions representing the different parageneses in the unoxidized and the transitional zones, and a diffuse range of compositions from the oxidized zone.

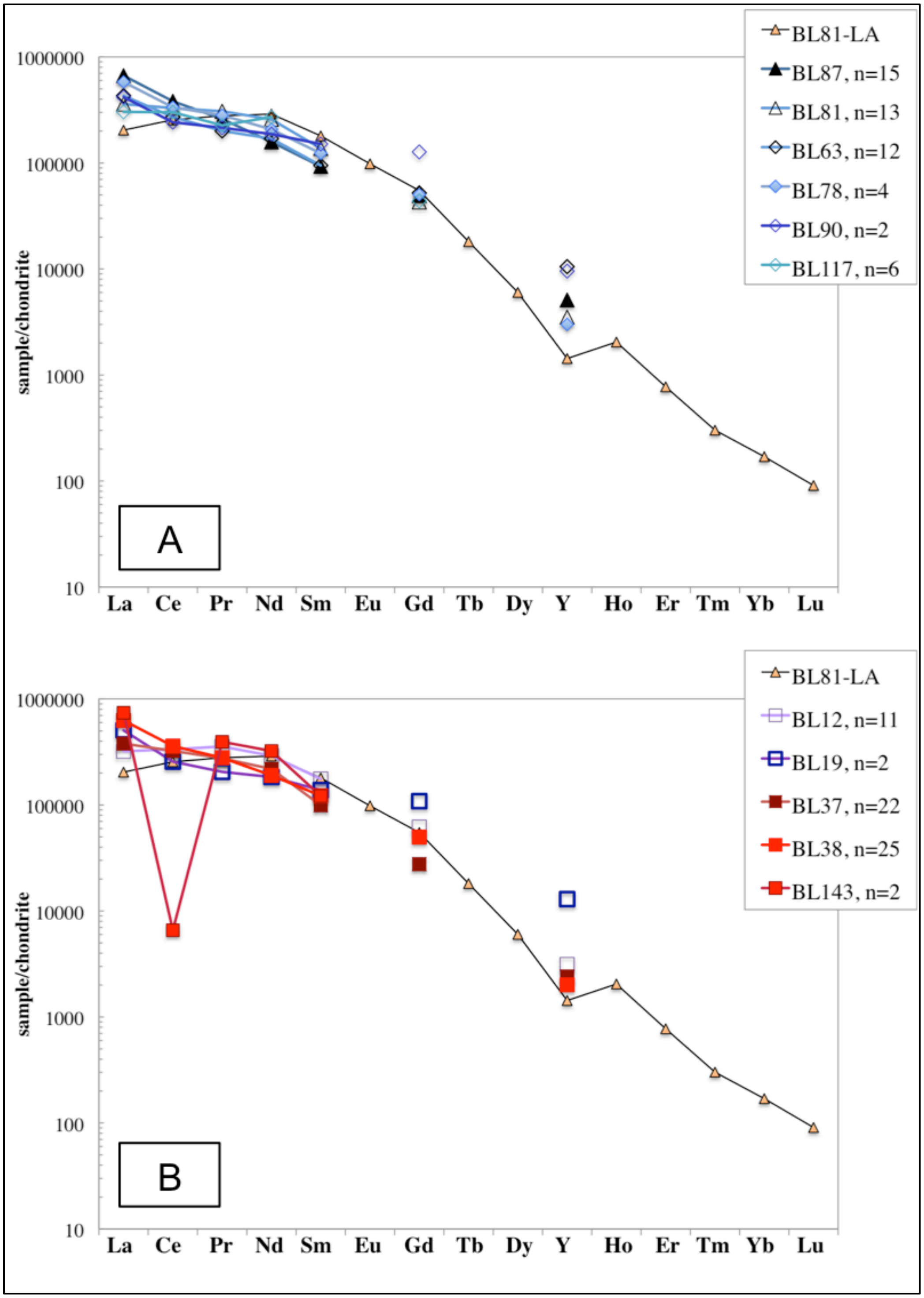

Figure 6.8. Chondrite-normalized profiles of synchysite from the A) unoxidized and B) transitional and oxidized zones. Complete REE profile from sample BL81 was constructed from LA-ICP-MS data, all others are based on EMPA data. The laser-ablation data show negative slope of LREE enrichment typical of REE fluorocarbonates from carbonatites, with a prominent negative Y anomaly.

Laser-ablation data of sample BL81 show slightly lower values in the range from La through Nd with respect to WDS data from the same sample, because these are major elements in the fluorocarbonates, and the resolution of WDS for these elements is better than that of LA-ICP-MS analysis (P. Yang, personal communication). The most horizontal profile from La to Nd is observed in synchysite in comparison with the other fluorocarbonates (see below), and is also observed in the LA-ICP-MS data.

6.2.2 Parisite

Variations similar to those observed in synchysite also occur in parisite. Analyses of parisite from the fluorocarbonate-fluorite paragenesis in the unoxidized zone plot in a distinct field in the $(La)_{cn}$ vs. $(Nd)_{cn}$ and $(La/Ce)_{cn}$ vs. $(La/Nd)_{cn}$ bivariate diagrams, whereas those from the ancylite-fluorocarbonate paragenesis show a wider range of values (Figs. 6.6 and 6.7). Two distinct clusters of parisite from the transitional zone are evident in the $(La/Ce)_{cn}$ vs. $(La/Nd)_{cn}$ diagram. Parisite in the oxidized zone co-crystallized with cerianite and is characterized by high $(La/Ce)_{cn}$ values.

Chondrite-normalized REE discrimination diagrams for parisite show characteristics similar to those described above for synchysite. Samples with the largest negative Ce anomalies also have the highest concentrations of La, Pr, Nd and Sm (Fig. 6.9, Appendix C). Chondrite-normalized profiles from the unoxidized zone have smooth shapes and are relatively flat in the La-Nd range, whereas those from the oxidized zone show curvature (Fig. 6.9). Profiles from the transitional zone range from convex to relatively flat, with a slightly negative slope in the LREE range. Chondrite-normalized profiles constructed on the basis of laser-ablation data for parisite from sample BL81 (fluorocarbonate paragenesis) are convex upward, with a prominent negative Y anomaly (Fig. 6.9).

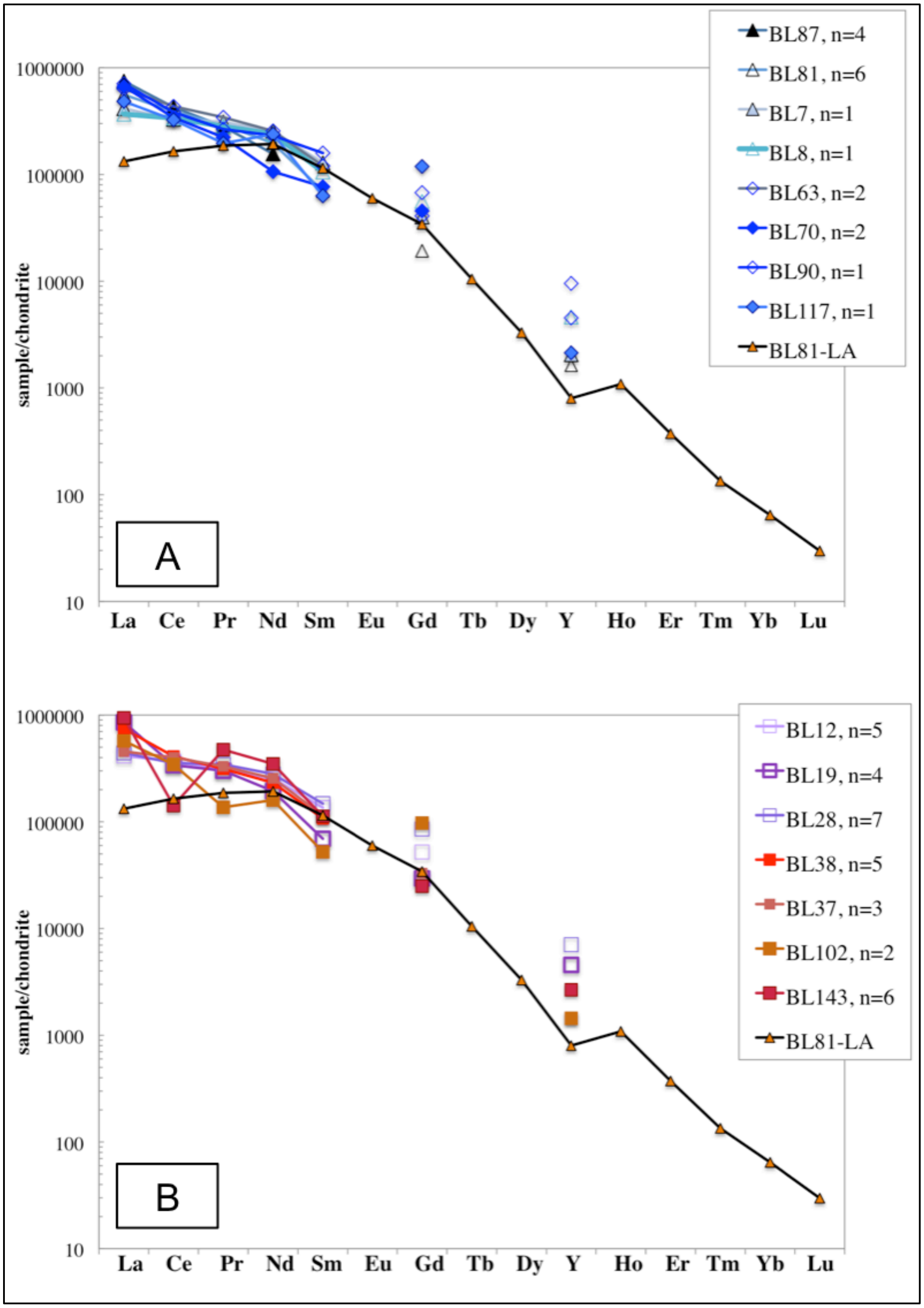

Figure 6.9. Chondrite-normalized profiles of parisite from the A) unoxidized and B) transitional and oxidized zones. Complete REE profile from LA-ICP-MS data, all others from EMPA. Note similarity between the chondrite-normalized profiles of synchysite and parisite from sample BL81 (cf. Fig. 6.8).

6.2.3 Bastnäsite

All bastnäsite analyses from this study contain some Ca (0.8 to 5.6 wt.% CaO; Appendix C). The recalculated data indicate there could be vacancies in the REE site, although the possibility that Ca-rich compositions represent submicroscopic intergrowths with parisite or synchysite cannot be ruled out. It appears that two compositional varieties of bastnäsite are present in the transitional zone and three varieties in the oxidized rocks, as indicated by data clustering in the $(La)_{cn}$ vs. $(Nd)_{cn}$ and $(La/Nd)_{cn}$ vs. $(La/Ce)_{cn}$ diagrams (Figs. 6.6 and 6.7). Bastnäsite and bastnäsite II that are developed in different phases of the pervasively oxidized sample BL145 ("FMR" type and "Ox-Ca" subzone, respectively, discussed in detail in Chapter 5.3) occupy distinct fields in these diagrams. With the exception of one outlier, bastnäsite II plots in a relatively tight cluster in the central area of Fig. 6.6 at average $(La)_{cn}$ and $(Nd)_{cn}$ values of ~681,000 and 309,000, respectively, and at low values of $(La/Nd)_{cn}$ and intermediate values of $(La/Ce)_{cn}$ (on average, 2.22 and 1.62, respectively). A negative Ce anomaly is not observed (Figs. 5.6, 5.7, 5.10). All other bastnäsite analyses from the oxidized zone show a wide range of values, overlapping with the data from the transitional and unoxidized zones. Chondrite-normalized profiles of bastnäsite are similar to those of parisite and synchysite described above (Fig. 6.10). A negative Ce anomaly is present in some samples from the oxidized zone. The LA-ICP-MS data for sample BL81 show a relatively flat pattern between La and Nd and a negative Y anomaly.

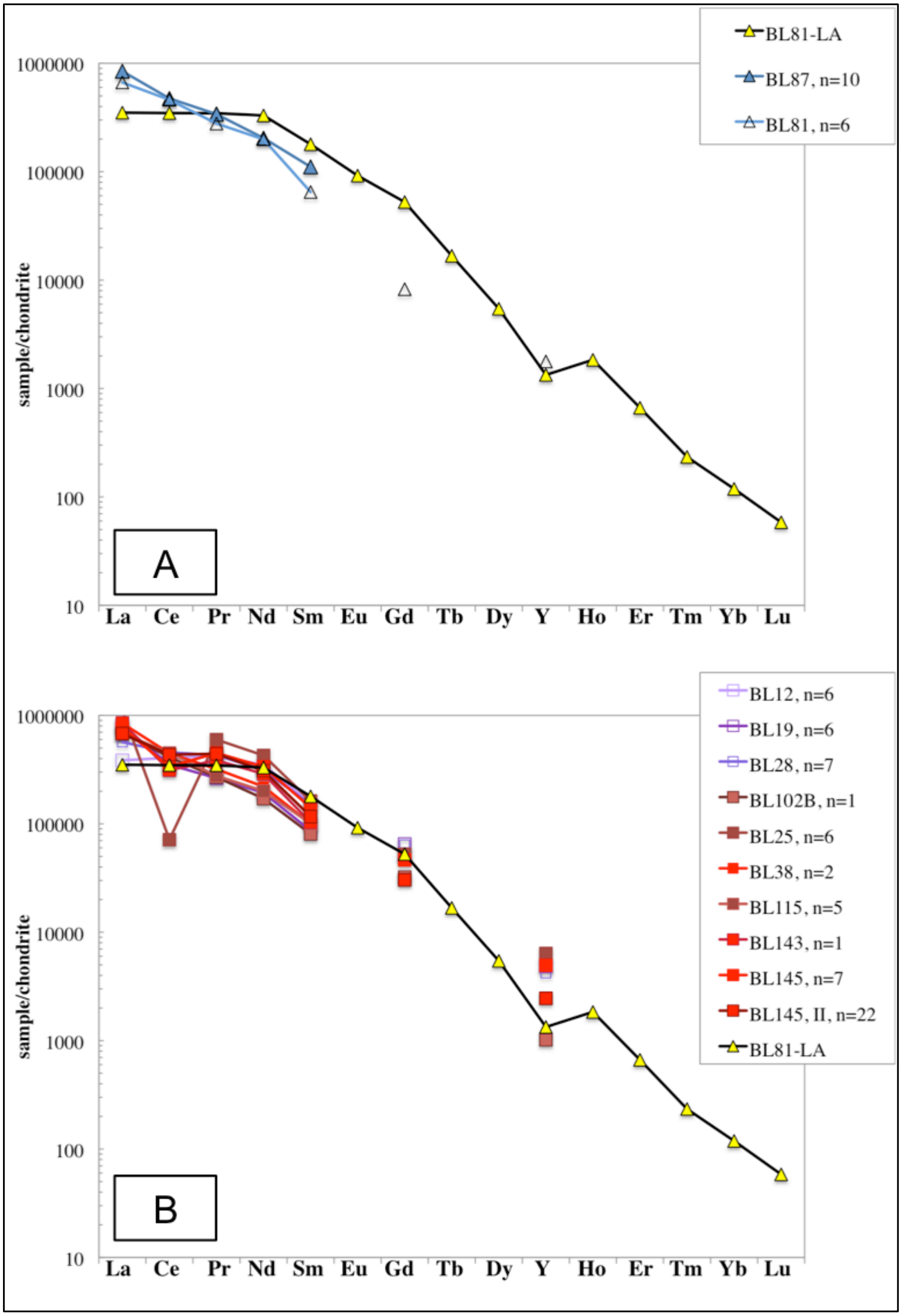

Figure 6.10. Chondrite-normalized profiles of bastnäsite from the A) unoxidized and B) transitional and oxidized zones. Complete REE profile from LA-ICP-MS data, all others from EMPA. See text for discussion.

6.3 Ancylite

Ancylite-group minerals have the general chemical formula $M^{2+}M^{3+}(CO_3)_2(OH)•H_2O$, where M^{2+} is Ca or Sr, and M^{3+} is REE, typically Ce > La > Nd (Dal Negro et al., 1975). The group includes ancylite-(Ce) [$SrCe(CO_3)_2(OH)•2H_2O$], ancylite-(La) [$Sr(La,Ce)(CO_3)_2(OH)•2H_2O$], calcioancylite-(Ce) [$(Ca,Sr)Ce(CO_3)_2(OH)•2H_2O$], and calcioancylite-(Nd) [$(Ca,Sr)(Nd,Ce,La)(CO_3)_2(OH)•2H_2O$]. Ancylite-(Nd)was identified tentatively from the Rocky Boy carbonatite (Bearpaw Mountains, Montana), but is not yet officially recognized as a valid mineral species (Regiur and Mitchell, 2000). Calcioancylite-(La) was tentatively identified in carbonatites from Afrikanda, Russia (Zaitsev and Chakhmouradian, 2002). Fluorine-bearing ancylite-(Ce) with ~0.8-2.5 wt% F was reported from the Khibiny carbonatite, Russia (Zaitsev et al., 1998).

Ancylite WDS data were recalculated on the basis of four cations; H_2O, CO_2 and OH^- were then calculated on the basis of charge balance and stoichiometry (see above). Ancylite-group minerals in the Bull Hill carbonatites are dominantly ancylite-(Ce), although the analyses from the burbankite paragenesis (sample BL70) correspond to ancylite-(La), and one analysis from the ancylite-fluorocarbonate paragenesis is ancylite-(Nd) (Fig. 6.11). All ancylite analyses have some Ca (0.4-3.6 wt.% CaO), which substitutes in the Sr site, but is of insufficient abundance for the mineral to be considered calcioancylite (Table 6.2). Significant compositional variation is observed between ancylite in different samples from the same paragenesis and from different zones (Table 6.2, Appendix C). A distinct enrichment in REE content of ancylite is observed from the burbankite paragenesis to the “Ox-Ca”subzone.

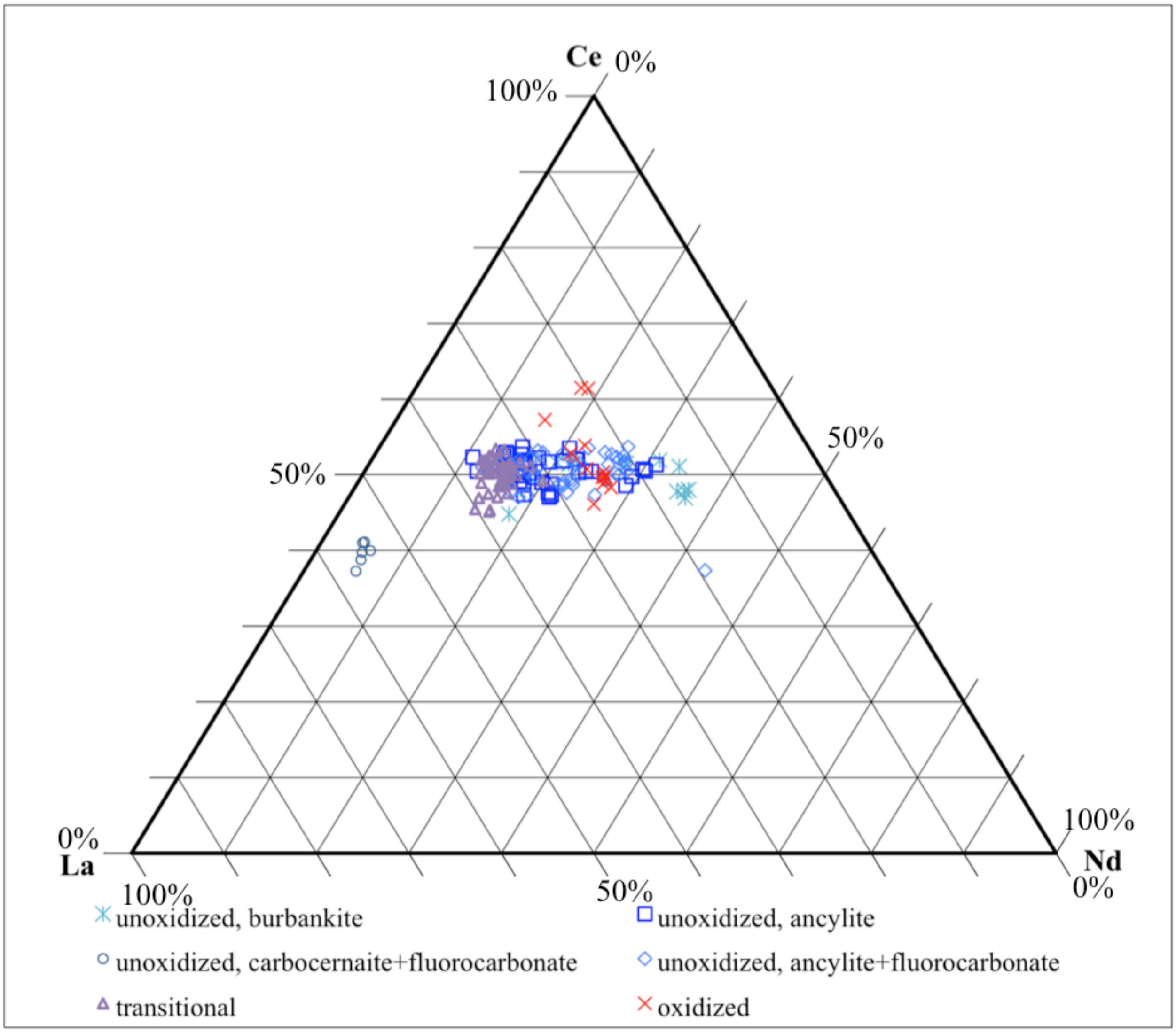

Figure 6.11. Ternary diagram showing rare-earth speciation of ancylite. Data from WDS in ppm; normalized to 100%. Legend lists zone, then paragenesis; the carbocernaite-fluorocarbonate sample (BL70) is from the burbankite paragenesis.

Table 6.2. Selected aspects of ancylite chemistry from different parageneses and zones. Complete data set in Appendix C.

	Ancylite chemistry				
Zone/Paragenesis	**ΣREE (apfu)**	**Ca+Sr (apfu)**	**ΣREE$_2$O$_3$ (wt%)**	**CaO (wt%)**	**SrO (wt%)**
unoxidized, burbankite (n=10)	2.31-2.50	1.43-1.63	48.75-52.94	0.41-2.34	16.02-20.54
unoxidized, ancylite (n=37)	2.09-2.66	1.27-1.76	45.82-58.72	0.43-3.63	9.45-20.31
unoxidized, ancylite+fluorocarbonate (n=44)	1.88-2.66	1.32-1.91	38.74-60.46	0.50-2.89	10.23-22.38
transitional (n=46)	2.10-2.66	1.23-1.79	45.87-57.00	0.48-2.07	13.21-21.12
oxidized (n=12)	2.25-2.72	0.98-2.59	50.74-66.84	0.98-3.50	7.52-18.14

Significant variation is observed in $(La/Nd)_{cn}$ values for ancylite in the unoxidized zone: ~0.8 to 5.7 in the ancylite and ancylite-fluorocarbonate parageneses, respectively. Ancylite from the other parageneses and zones has $(La/Nd)_{cn}$ values within this range (Fig. 6.12). An overall negative correlation between chondrite-normalized La and Nd values is observed. Ancylite compositions from the different parageneses and zones form distinct clusters (Fig. 6.12A). In the $(La/Ce)_{cn}$ vs. $(La/Nd)_{cn}$diagram, there is a positive correlation between $(La/Ce)_{cn}$ and $(La/Nd)_{cn}$ values, with some compositions from the ancylite paragenesis deviating from that general trend (Fig. 6.12B). Two LA-ICP-MS analyses of sample BL71 from the burbankite paragenesis give an Y/Ho ratio of ~17.0, and a Y/Y* value of ~0.2. The range of $(La/Yb)_{cn}$ values are between~54,000 to 183,000, indicating a significant variation in the degree of REE fractionation.

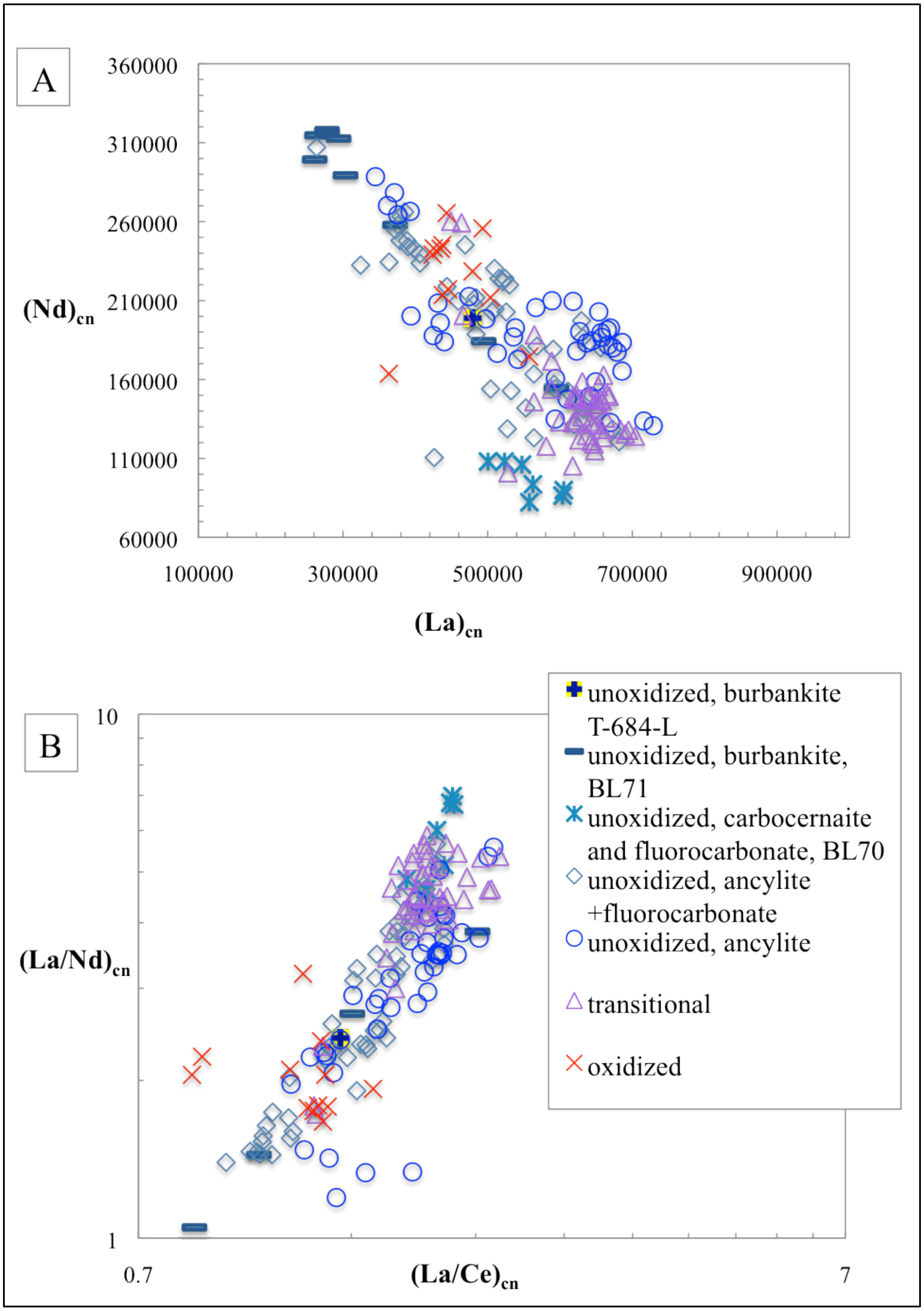

Figure 6.12. Variation in chondrite-normalized element ratios for ancylite. A) $(La)_{cn}$ and $(Nd)_{cn}$; B) $(La/Ce)_{cn}$ and $(La/Nd)_{cn}$. See text for discussion. Legend applies to both figures and lists zone and then paragenesis, separated by a comma; sample BL70 is from the burbankite paragenesis.

In the oxidized zone, the lowest SrO content occurs in ancylite with the highest CaO content. This is not always the case, however, as some low-Sr ancylite from the oxidized zone also contains low Ca. The highest SrO content was observed in the burbankite paragenesis (Table 6.2). Overall, there is no significant correlation between the Ca and Sr contents in the Bear Lodge samples (Fig. 6.13). Chondrite-normalized REE profiles show LREE enrichment typical of ancylite-group minerals (Fig. 6.14). A complete profile available for ancylite from the burbankite paragenesis is slightly convex between La and Sm, which is also observed in the only ancylite-bearing sample from the oxidized zone, as well as in samples from the transitional zone. Partial chondrite-normalized profiles of ancylite from the ancylite-fluorocarbonate (BL97) and ancylite (BL125) parageneses in the unoxidized zone are noticeably flatter in the range from La to Sm, indicating a lesser degree of REE fractionation (Fig. 6.14).

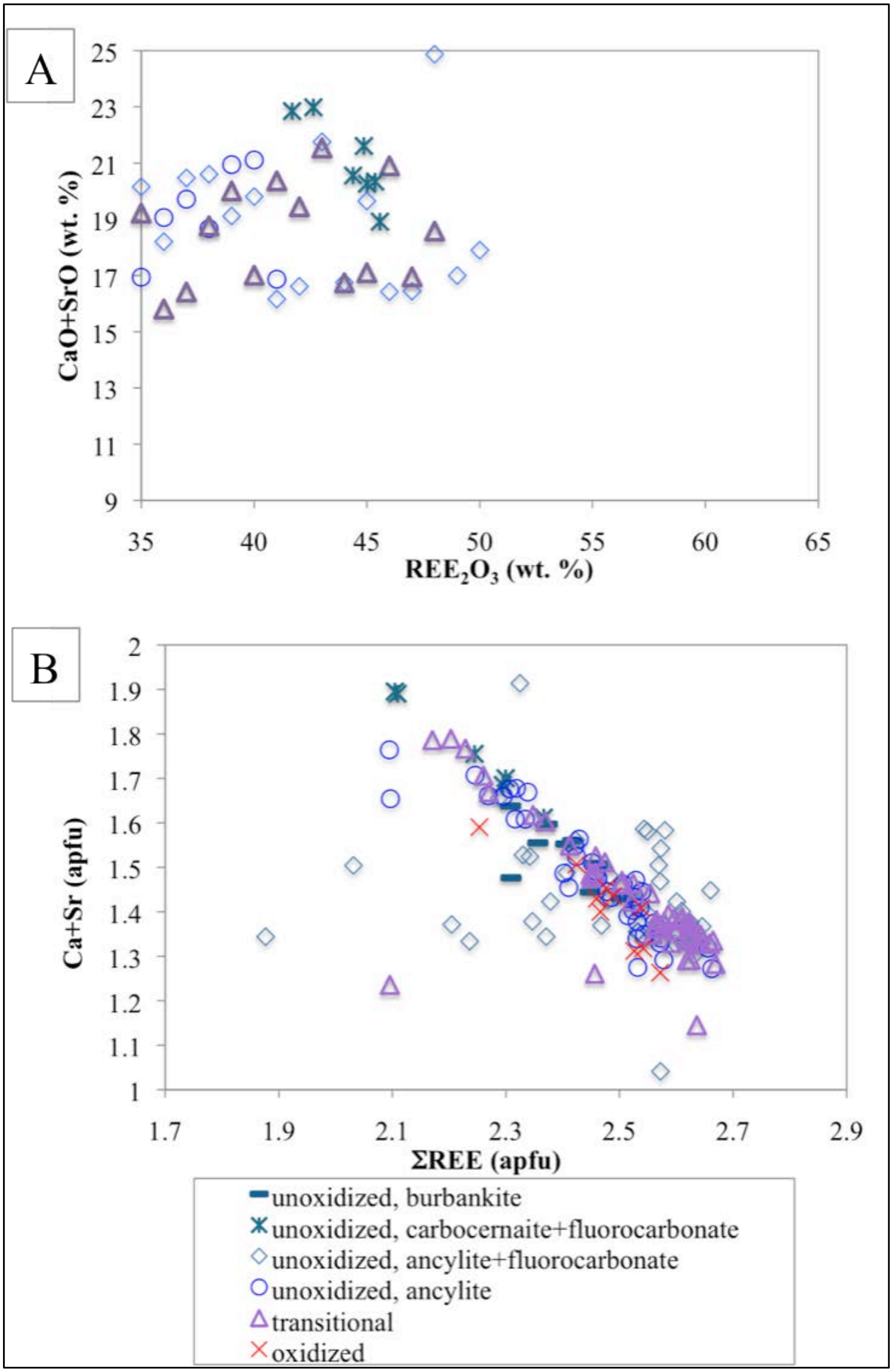

Figure 6.13. Variations in REE and Ca + Sr contents of ancylite. A) in wt%. oxide; B) in apfu. The carbocernaite-fluorocarbonate sample (BL70) is from the burbankite paragenesis.

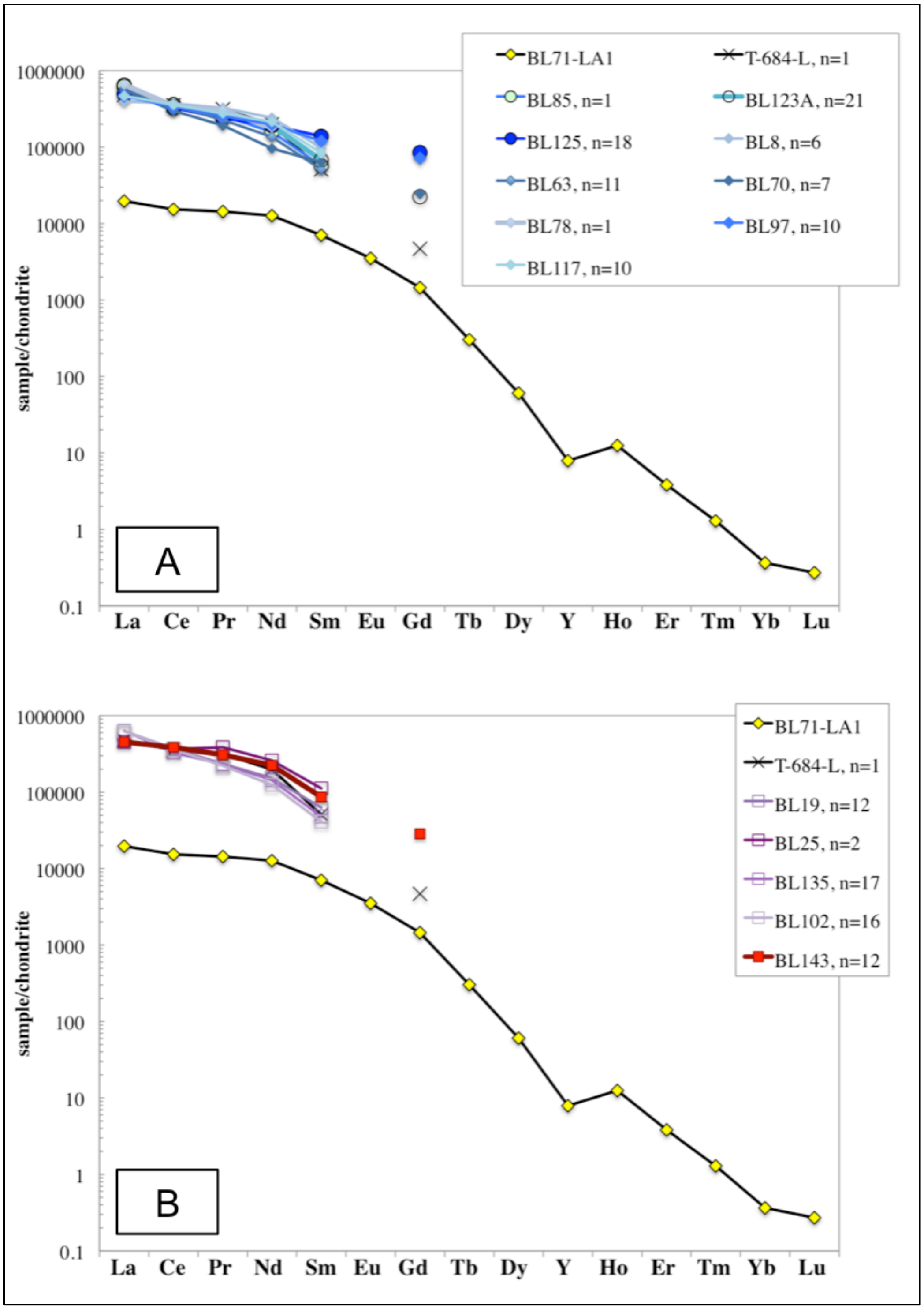

Figure 6.14. Chondrite-normalized profiles of ancylite constructed from WDS and LA-ICP-MS data. A) Unoxidized and B) transitional and oxidized zones. Europium and elements with higher atomic numbers than Gd are below the detection limits of WDS. LA-ICP-MS data for ancylite from sample BL71 (burbankite paragenesis) show the entire REE series.

6.4 Monazite

Monazite [LREE(PO_4)] is a monoclinic orthophosphate that can be dominated by Ce, La, Nd, or Sm. It is structurally distinct from xenotime [Y(PO_4)], which is tetragonal and preferentially incorporates the HREE. Monazite incorporates the lanthanide cations in an $REEO_9$ polyhedron, which is larger than the YO_8 polyhedron in xenotime (Ni et al., 1995), and provides a structural impetus for REE fractionation in phosphate-rich systems like the majority of carbonatites. Note however, that monazite is very common, whereas xenotime is exceedingly rare in these rocks (Wall and Mariano, 1996; Wall et al., 2008). Another related phosphate that is difficult to distinguish from monazite using conventional techniques is rhabdophane [LREE(PO_4)•0.5-2H_2O], which is a hexagonal mineral that commonly also hosts Ca and HREE substituting for LREE (Mooney, 1950; Nagy et al., 2002). In the present work, all WDS data were recalculated on the basis of four O + F atoms to account for possible vacancies in the cation site.

All monazite analyses from the Bull Hill rocks are Ce-dominant, although two of the analyses from the oxidized zone show Ce $\approx$ Nd (Fig. 6.15). Table 6.3 summarizes chemical characteristics of monazite from the different parageneses and zones; the complete analytical data set is located in Appendix C. Only one sample from the ancylite paragenesis contains monazite, which has higher REE and lower Ca, Fe, Si and Th contents than monazite from the ancylite-fluorocarbonate paragenesis (Chapter 5.1.4, Fig. 6.17, Table 6.3, Appendix C). Monazite from the ancylite paragenesis has significantly different $(La/Ce)_{cn}$ and $(La/Nd)_{cn}$ values than that from the ancylite-fluorocarbonate paragenesis (Fig. 6.18).

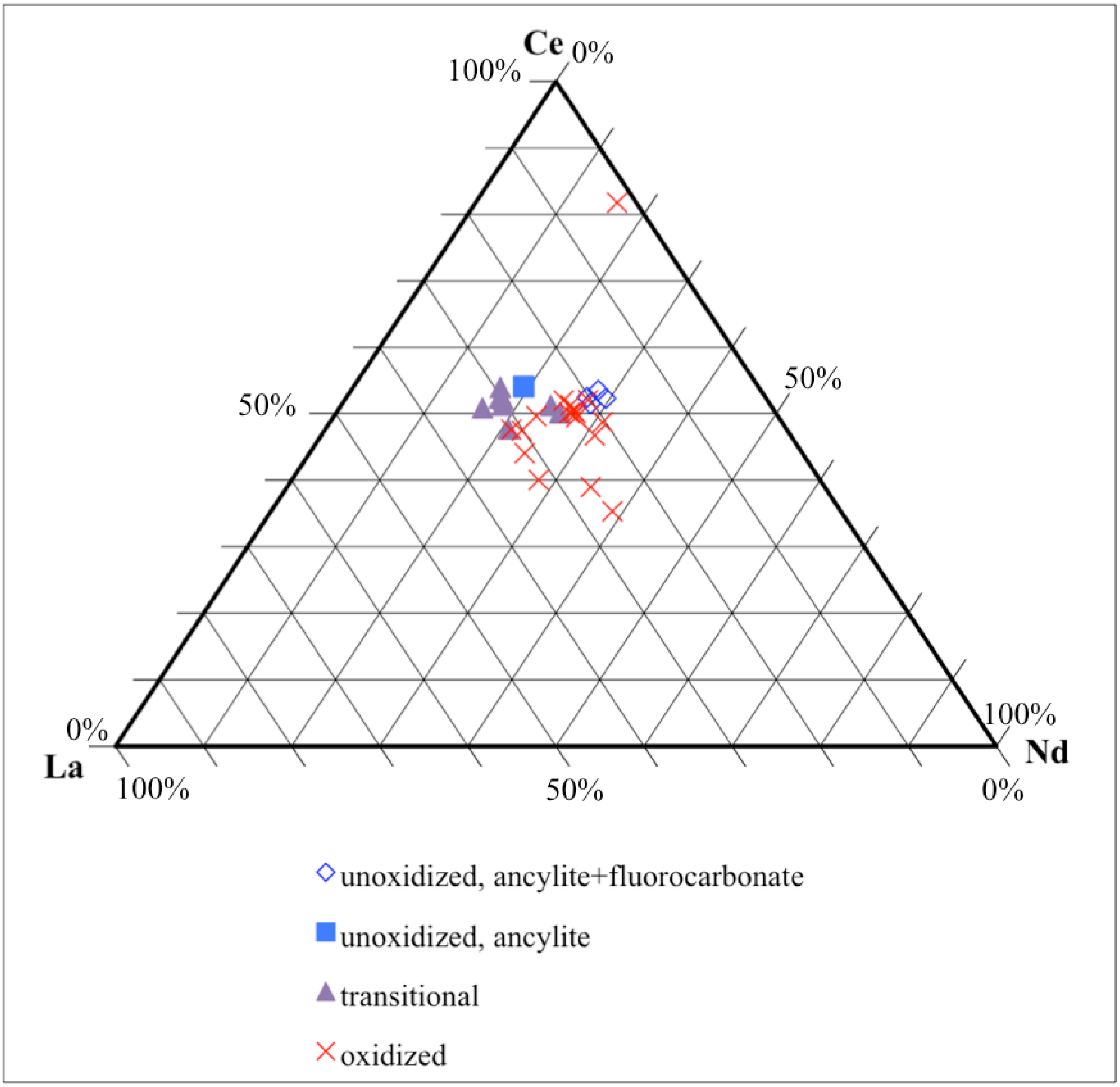

Figure 6.15. Ternary diagram showing REE speciation of monazite from the different parageneses and zones. Data in ppm normalized to 100%.

Monazite from the transitional zone has higher Si and Th contents, but lower values of Ca, Sr, Mn, Fe and Ba than that from the unoxidized zone. The Ca content of monazite from the transitional zone is variable, but is always < 6 wt.% CaO or 0.33 apfu Ca (Table 6.3, Appendix C). The limited analytical data also indicate an increase in Gd and Y (i.e. medium-sized REE^{3+} cations) in monazite from the transitional and oxidized zones relative to that in the unoxidized zone. The compositions of monazite from the transitional zone plot in three clusters in the $(La/Ce)_{cn}$ vs. $(La/Nd)_{cn}$ diagram (compare Figs. 6.17 and 6.7).

Table 6.3. Selected chemical characteristics of monazite from the different parageneses and zones. Complete data set in Appendix C.

Monazite chemistry							
zone, paragenesis	***n***	**ΣREE_2O_3 (wt. %)**	**ΣREE (apfu)**	**ThO_2 (wt. %)**	**SiO_2 (wt. %)**	**CaO (wt. %)**	**ΣM^{2+} (wt. % oxides)**
unoxidized, ancylite+fluorocarbonate	4	50.85-58.70	0.93-1.06	0.32-0.80	0.14-0.79	2.94-5.97	6.20-8.47
unoxidized, ancylite	2	59.26-60.24	0.85-0.88	0.18-0.22	0.04-0.07	2.65-3.29	7.74-9.14
transitional	8	55.60-64.06	0.91-0.96	0.08-1.10	0.07-0.25	1.58-6.15	6.18-9.36
oxidized	17	52.42-60.64	0.77-1.10	0.42-4.07	0.11-0.69	2.65-6.31	6.01-9.12

ΣM^{2+}: Ca+Sr+Ba+Mn+Fe

Monazite is most abundant in samples from the oxidized zone, making up as much as ~30 vol.% of the rock (see Chapter 5.3). This monazite contains consistently high Th levels, with sample BL115 showing higher ThO_2 content than BL44 (1.8-4.0 vs. 0.4-1.7 wt.%, respectively; Fig. 6.16; Table 6.3; Appendix C). Fluorine and Sr are also important substituent elements in the majority of samples (up to 2.1 wt.% F and 5.2 wt.% SrO). Monazite compositions from the oxidized zone plot in two distinct fields in the $(La/Ce)_{cn}$ vs. $(La/Nd)_{cn}$ diagram (Fig. 6.17).

The La-Nd segment of chondrite-normalized profiles, based on WDS data, either has a negative slope or is slightly convex upward, with Ce at the pivoting point; the overall distribution of REE shows a negative slope (Fig. 6.18). Analyses of samples from the ancylite paragenesis by LA-ICP-MS confirm the strong preponderance of LREE over HREE [$(La/Yb)_{cn}$ = 4300-4900] and give subchondritic Y/Ho ratios (19-21) expressed as a negative Y anomaly (Fig. 6.18).

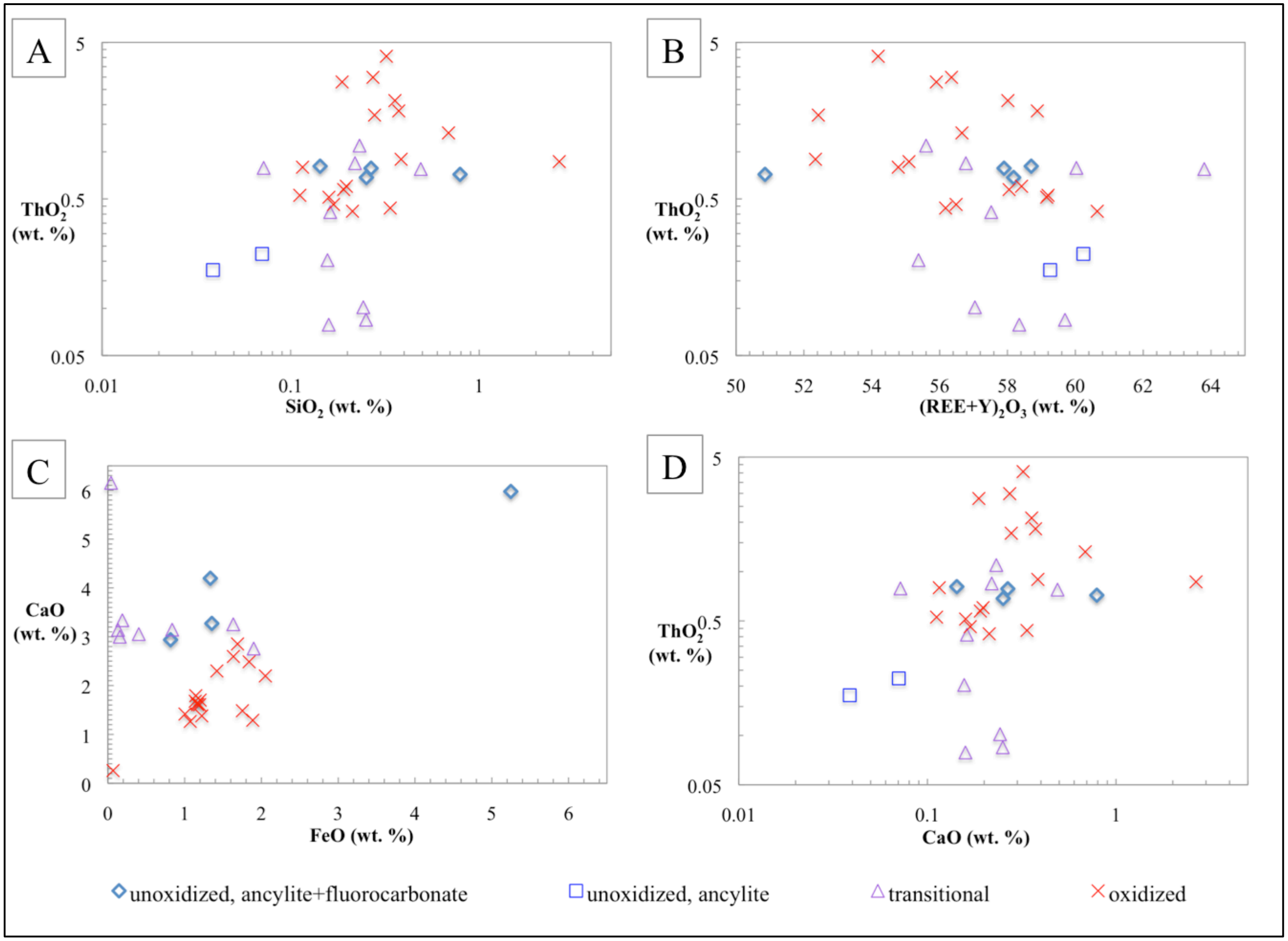

Figure 6.16. Variation in major and minor elements (wt.%) in monazite from the different zones and parageneses. Legend applies to all plots. A) ThO_2 vs. SiO_2. B) ThO_2 vs. REE_2O_3. C) CaO vs. FeO; the ancylite paragenesis is not shown on this diagram because FeO was below detection. D) ThO_2 vs. CaO.

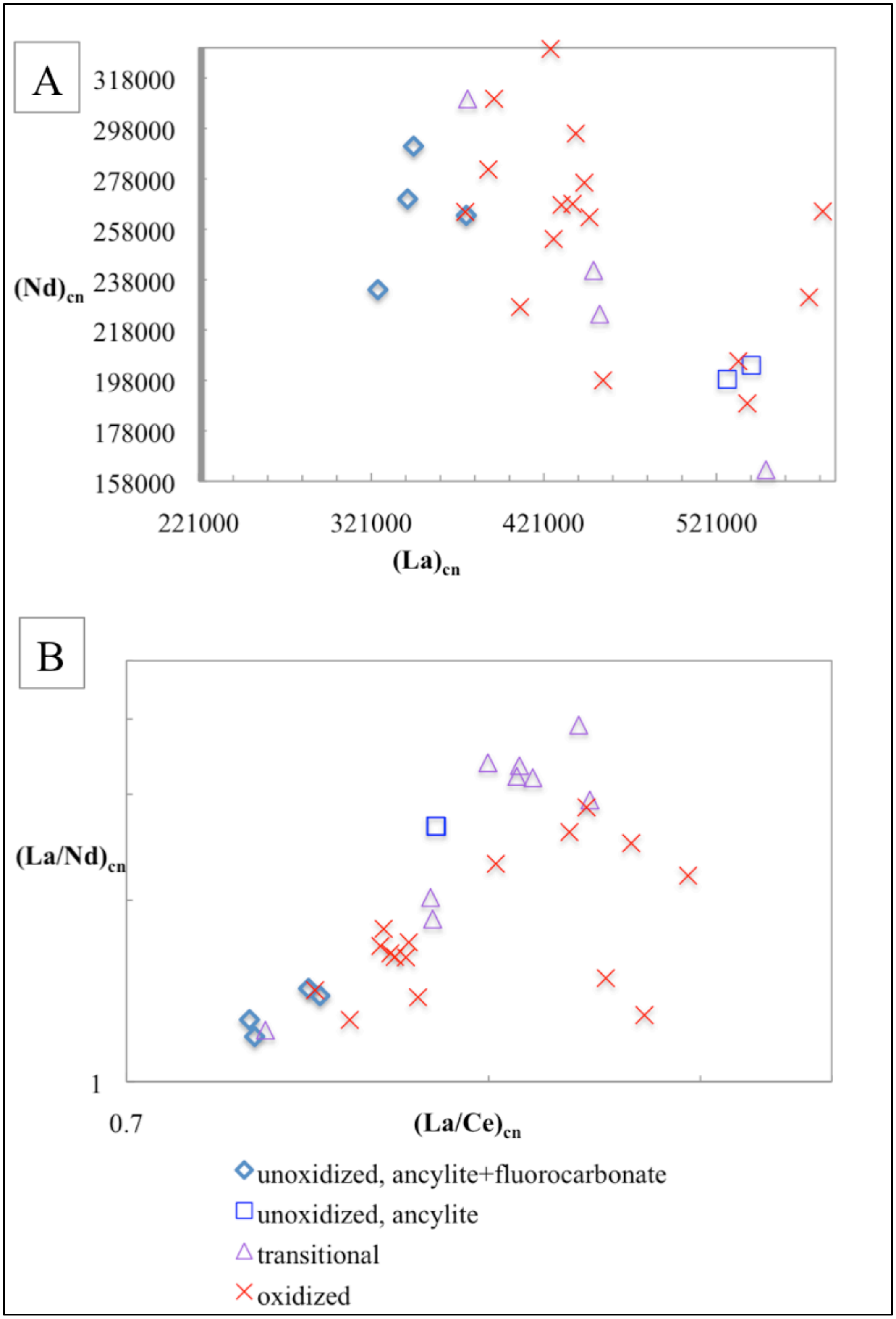

Figure 6.17. Variation in LREE abundances (chondrite-normalized values and ratios) in monazite from the different zones and parageneses. A) $(La)_{cn}$ vs. $(Nd)_{cn}$; B) $(La/Ce)_{cn}$ vs. $(La/Nd)_{cn}$. Legend applies to both plots.

Rare-earth phosphates from the ancylite-fluorocarbonate paragenesis (unoxidized zone) and sample BL44 (oxidized zone) were investigated using Raman micro-spectroscopy to determine if water was present in these minerals, i.e. if the analyzed samples were rhabdophane, rather than monazite. The spectra from the unoxidized carbonatite show the same peaks as well-characterized monazite standards from different localities, and lack any signals in the O-H stretching range (2800-3500 cm^{-1}) expected in hydrous phosphates (e.g., Frost et al., 2013). The spectrum of sample BL44 from the oxidized zone shows slightly different Raman shifts than those recorded for the unoxidized sample, but is still comparable to the known monazite spectra and lacks detectable O-H peaks (Fig. 6.19).

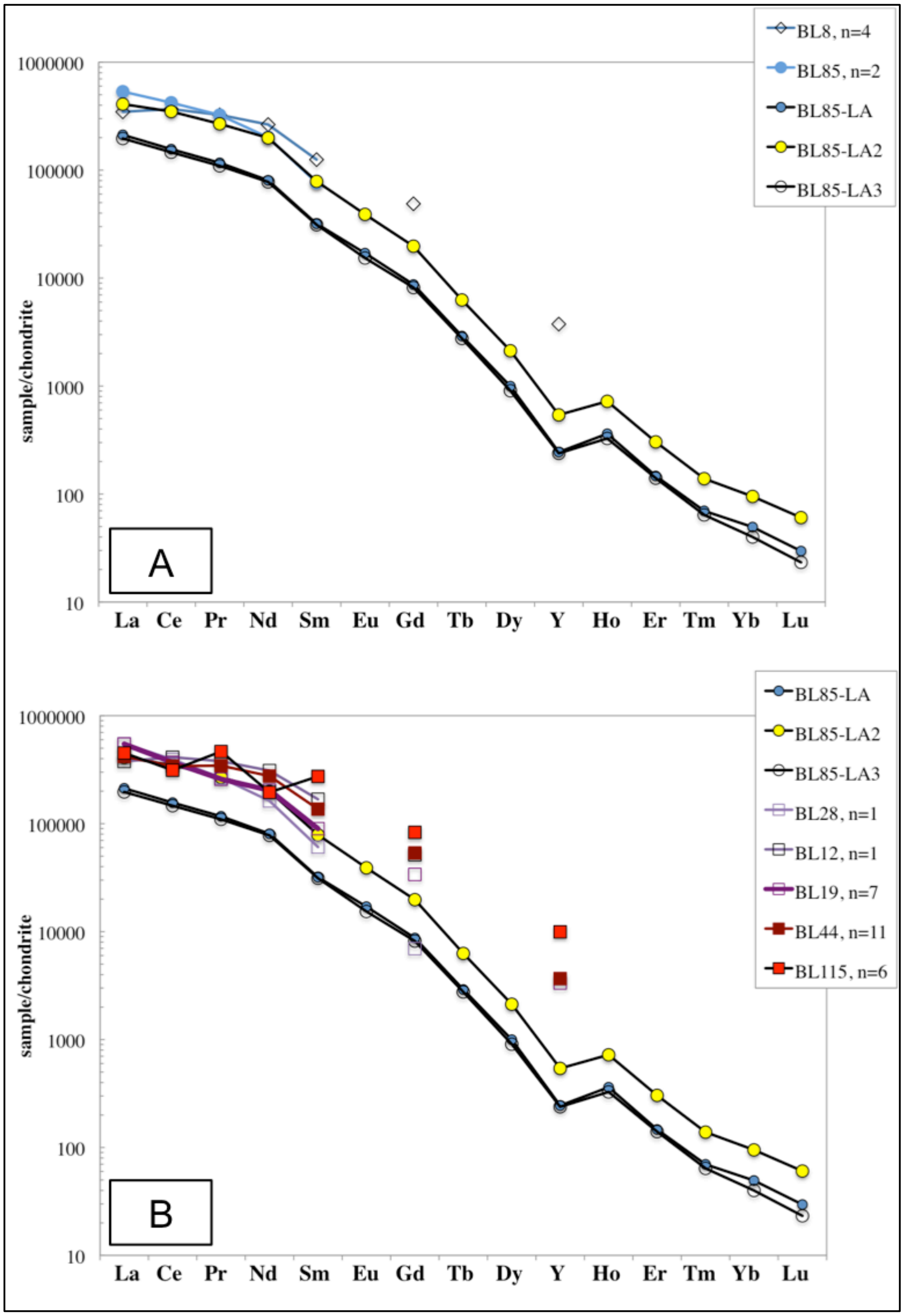

Figure 6.18. Chondrite-normalized REE profiles constructed from WDS and LA-ICP-MS data for monazite from the A) unoxidized and B) transitional and oxidized zones. Complete profiles are for samples from the ancylite paragenesis and were acquired by LA-ICP-MS; the remaining profiles are based on WDS data (Eu, Tb, Dy and Ho-Lu were below their limit of detection by WDS). See text for discussion.

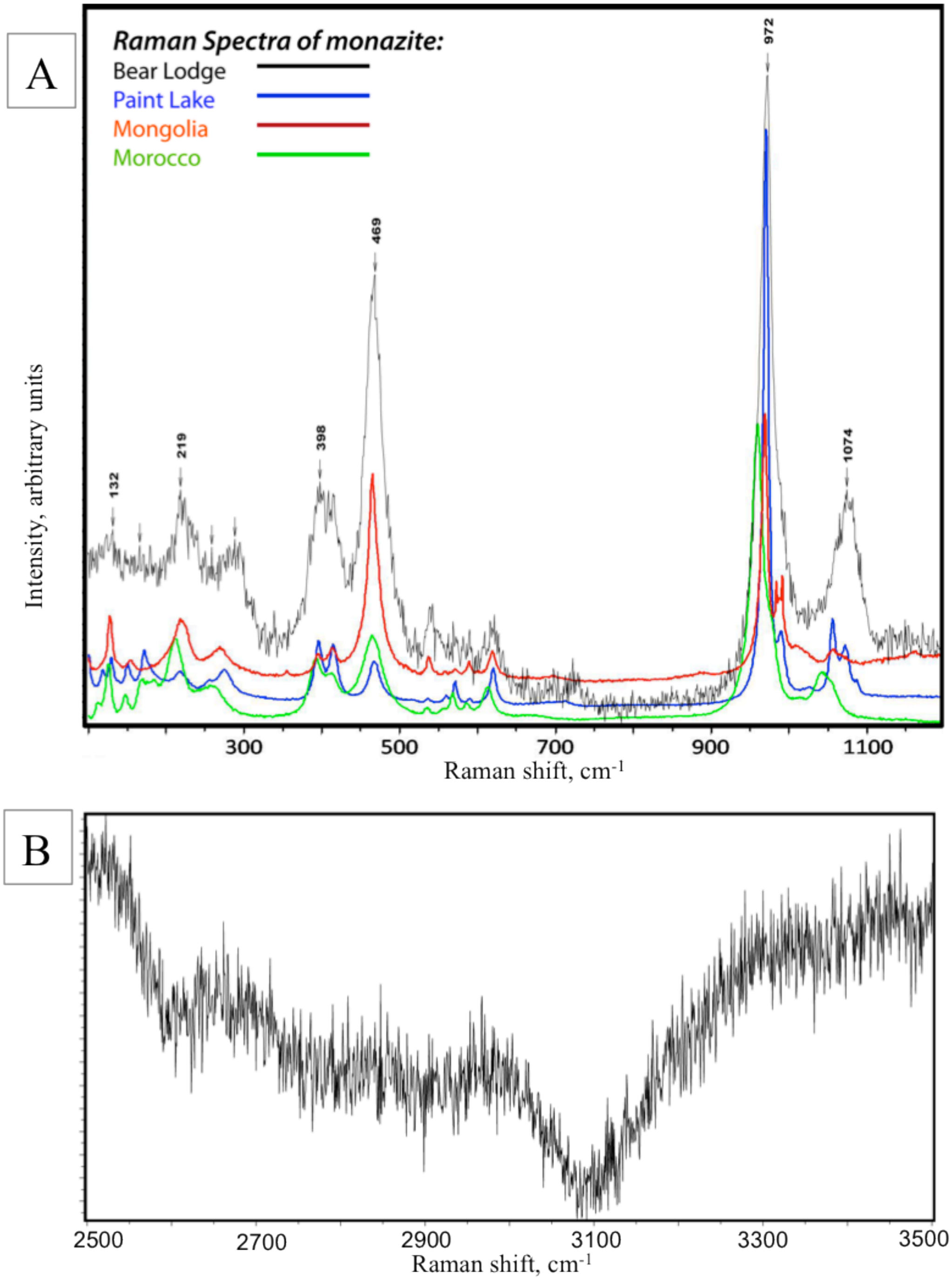

Figure 6.19. Raman spectra of monazite from the oxidized zone of the Bull Hill carbonatites. A) 100-1200 cm^{-1} range showing vibration modes characteristic of monazite standards from different localities; B) 2500-3500 cm^{-1} range (enhanced vertical resolution) showing lack of O-H stretching signals typical of hydrous phosphates (Frost et al., 2013).

6.5 Cerianite

Cerianite (CeO_2) is the most common Ce^{4+} mineral forming under oxidizing conditions. Although it was initially discovered in carbonatites at Lackner Lake, Canada (Graham, 1955), it is relatively more abundant in laterites and other products of weathering of REE-bearing rocks. In this environment, Ce is oxidized from its normal trivalent state to form a tetravalent cation, which is ~15% smaller than Ce^{3+} (see Fig. 1.2). This difference in ionic radius is sufficient to drive separation of Ce^{4+} from the remaining trivalent REE in the oxidized environment. The oxidation is typically facilitated by late-stage hydrothermal or supergene processes, where earlier-formed REE-bearing minerals serve as a source of Ce. Owing to sequestration of Ce in cerianite, its associated co-crystallized REE minerals are invariably depleted in Ce and exhibit a negative Ce anomaly in their chondrite-normalized profiles (e.g., Mariano, 1989b). Analyses of cerianite from this study were recalculated to a total charge of +4.

Due to the small grain size and "spongy" nature of cerianite from the oxidized zone, only three of the acquired WDS analyses were of marginally acceptable quality, but still show low totals (72-86 wt.%). Chemically, this cerianite is relatively uniform; the total content of trivalent REE or other cations is negligible (Table 6.4). Because alkali-earth cations, such as Sr^{2+}, Ba^{2+} and Ca^{2+}, are too large to substitute for Ce^{4+} (Shannon, 1976), their presence in some of the analyses is likely due to contamination by carbonate minerals or barite. Silica is commonly present in the analyses, but as noted in Chapter 5.2, is likely cryptocrystalline SiO_2 inextricably intergrown with cerianite grains or adsorbed on their surfaces. Silica has been observed in cerianite from several other localities (A.N. Mariano, personal communication).

Table 6.4. Selected chemical characteristics of cerianite from the oxidized zone. Complete data set in Appendix C, all data in wt.%. ΣREE_2O_3 only includes La_2O_3 and Nd_2O_3, all the other REE were below the detection limit by WDS, Ce calculated as Ce^{4+}.

Cerianite Chemistry						
n	**CeO_2**	**ΣREE_2O_3**	**SiO_2**	**CaO**	**SrO**	**FeO**
3	63.11-71.78	2.01-2.98	4.78-10.00	2.23-3.35	0.86-3.90	0.50-2.00

6.6 Apatite

Apatite [$Ca_5(PO_4)_3(F,OH)$] is a common accessory constituent in carbonatites (Hornig-Kjarsgaard, 1998; Bühn et al., 2001). Rare-earths are important substituent elements in this mineral and are accommodated via coupled substitutions of REE + Si or REE + Na for Ca + P (Roeder et al., 1987). Mariano (1989a, 1989b) observed that apatite from some igneous rocks may preferentially incorporate the HREE, while other samples are LREE-dominant. The WDS data from the present work (Appendix C) were recalculated to formulae on the basis of eight cations because the proportion of OH in the monovalent anion site could not be analyzed.

Apatite in the Bull Hill carbonatites occurs as an accessory phase in the ancylite-fluorocarbonate and ancylite parageneses, and in the transitional and oxidized zones. Most, but not all, analyzed samples contain detectable LREE, whereas lanthanides between Eu and Lu are consistently below their limit of detection by WDS. In many cases, only Ce was detected. The REE_2O_3 content is highly variable, ranging from nil to 5.0 wt.%; the La-Sm segment in chondrite-normalized patterns based on these WDS data is relatively flat or shows a slightly positive slope (Table 6.5; Fig. 6.20). Complete chondrite-normalized REE profiles constructed from LA-ICP-MS data for apatite from the ancylite-fluorocarbonate paragenesis (BL117) are convex upward in the LREE range, showing pronounced enrichment in the Ce-Eu range and only a very slight negative Y anomaly. In contrast, the profile from the oxidized sample (BL143) shows a prominent negative Ce anomaly and much lower levels of most REE with the exception of La, whose value is comparable to those in the unoxidized samples (Fig. 6.20). Grains analyzed by LA-ICP-MS show a lesser degree of LREE enrichment or Y-Ho decoupling than any of the carbonate minerals or monazite [$(La/Yb)_{cn}$ = 45-72; Y/Ho = 22-28]. Although hydroxyl-apatite has been identified from the oxidized zone (Clark, 2014 personal communication), all apatite analyses acquired in the present work correspond to fluorapatite, with consistently higher F contents relative to the average apatite composition from carbonatites (Table 6.5; Appendix C; cf. Appendix A in Chakhmouradian et al., 2008). The Bull Hill fluorapatite is enriched in Sr and has low Si contents, which are consistent with the average values for carbonatitic apatite worldwide (ibid.). There is a negative correlation between the CaO content and both (SrO + Na_2O) and (SiO_2 + Na_2O); other elements substituting for Ca and P do not show consistent trends, indicating that multiple substitution mechanisms are involved in charge compensation (Figs. 6.21 and 6.22).

Table 6.5. Selected aspects of apatite chemistry from the different zones. Complete data set in Appendix C.

Apatite chemistry								
zone, paragenesis	***n***	**ΣREE_2O_3 wt%**	**Na_2O**	**CaO**	**SiO_2**	**SrO**	**P_2O_5**	**F**
unoxidized, ancylite+fluorocarbonate	13	0.58-5.04	0.33-2.31	45.89-51.96	0.02-0.05	1.25-3.51	35.10-41.76	2.17-4.33
unoxidized, ancylite	8	0-3.57	0.37-0.63	48.45-52.92	0.14-0.25	0.93-1.99	38.63-41.86	3.15-3.83
transitional	5	2.64-3.19	0.53-0.83	49.29-51.22	0.02-0.05	1.52-1.84	38.91-39.84	3.64-4.22
oxidized	14	0-3.29	0.55-1.11	49.39-51.17	0.01-0.11	1.22-2.45	39.13-51.43	3.61-4.21

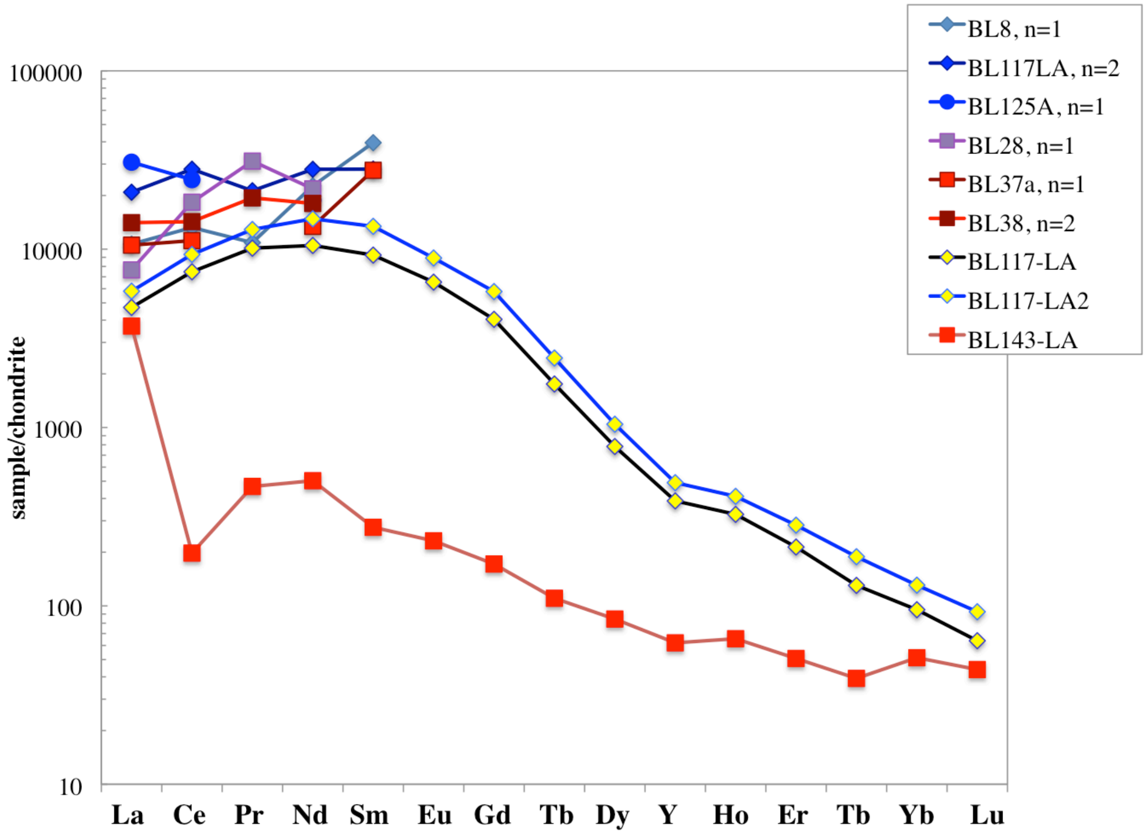

Figure 6.20. Chondrite-normalized REE profiles of apatite from the different parageneses and zones in the Bull Hill diatreme. Blue symbols from the unoxidized, purple from the transitional and red from the oxidized zones. Complete profiles were constructed using LA-ICP-MS data; the remaining profiles are based on WDS data. See text for discussion.

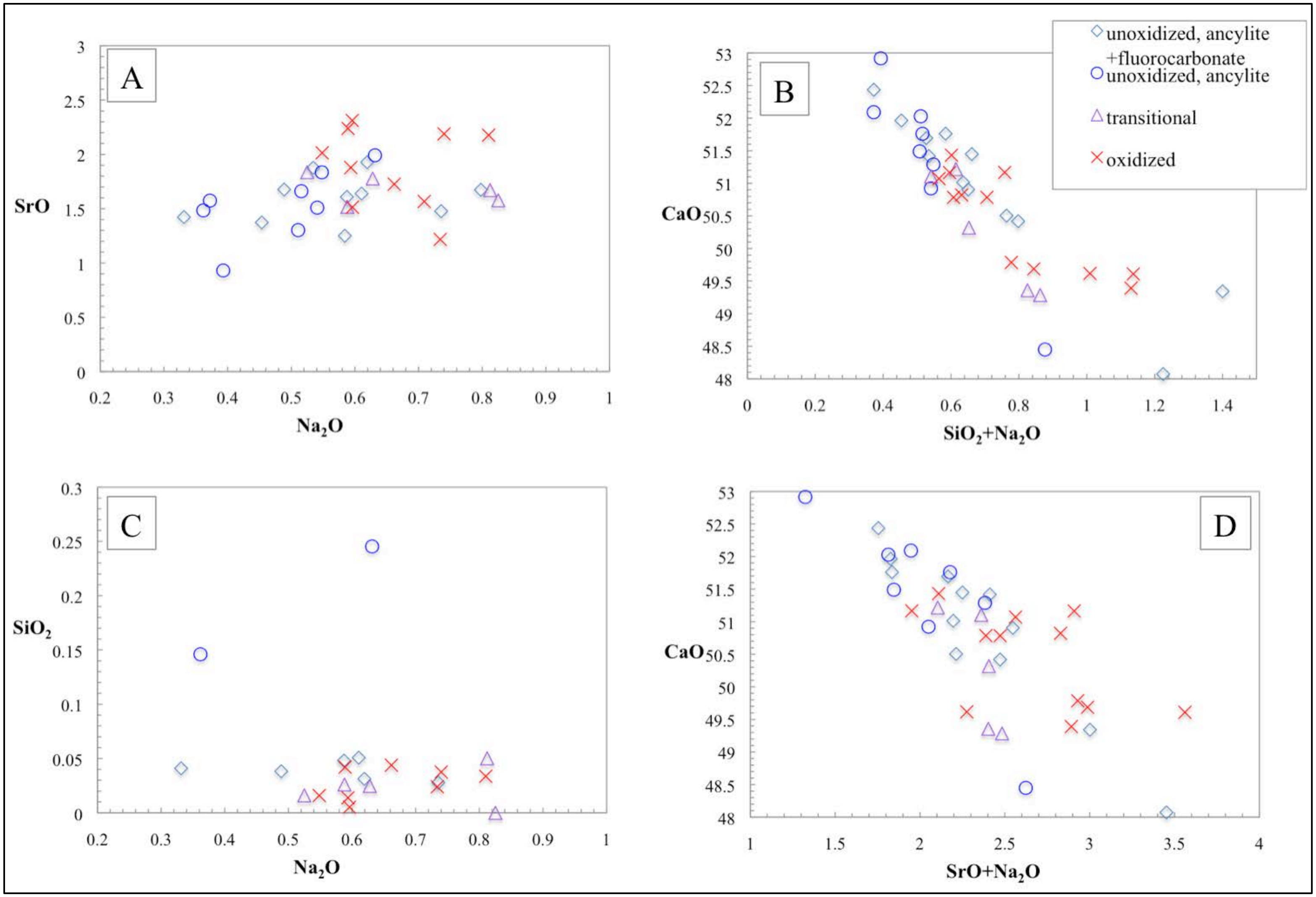

Figure 6.21. Variation in major and substituent elements in fluorapatite (wt.% oxides). A) SrO vs. Na_2O. B) CaO vs. SiO_2+Na_2O. C) SiO_2 vs. Na_2O. D) CaO vs. $SrO+Na_2O$. Legend applies to all plots. See text for discussion.

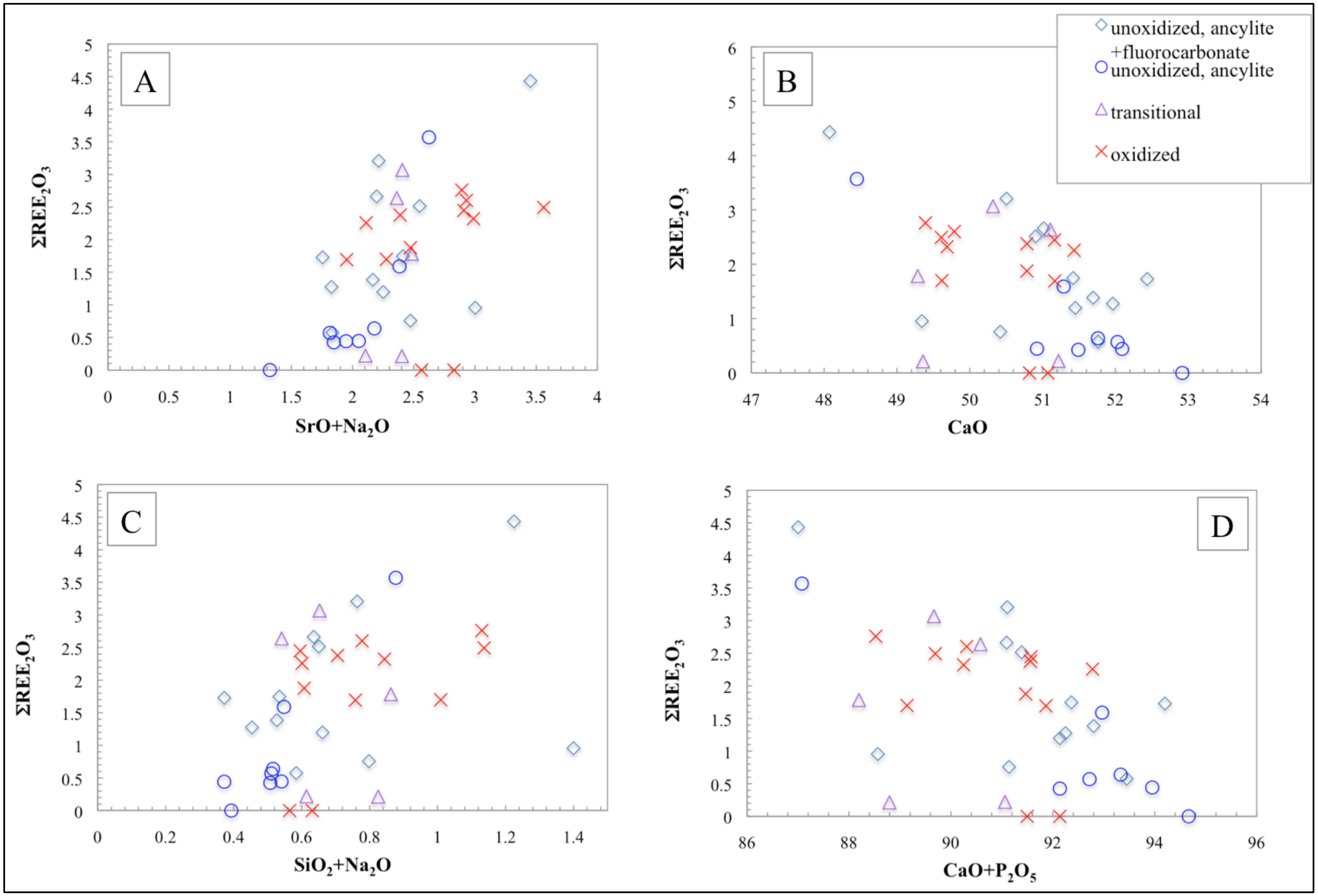

Figure 6.22. Variations in major and trace elements that may facilitate incorporation of REE in fluorapatite. A) ΣREE$_2$O$_3$ vs. SrO+Na$_2$O. B) ΣREE$_2$O$_3$ vs. CaO. C) ΣREE$_2$O$_3$ vs. SiO$_2$+Na$_2$O. D) ΣREE$_2$O$_3$ vs. CaO+P$_2$O$_5$. Legend applies to all plots. See text for discussion.

6.7 Fluorite

Fluorite (CaF_2) is a common accessory mineral in carbonatites, where it could be of igneous or hydrothermal origin (Bühn et al., 2002; Doroshkevich et al., 2008). Due to the low solubility of fluorite in fluids, it is often difficult to determine whether it is primary or secondary in nature, and the timing of its crystallization (Bühn et al., 2003).

Although only one sample from the present study contains fluorite (see Chapter 5.1.3), a small fluorite prospect is located in close proximity to Bull Hill in the BLAC, where multiple layers of yellow and purple fluorite cement hydrothermal breccia developed in trachyte. Other studies of the BLAC rocks also documented fluorite (Olinger, 2012). The fluorite examined in the present study is enriched in Sr (3562-5865 ppm), REE (108-480 ppm), and particularly in Y (260-720 ppm) (Table 6.6; Appendix C). Thorium concentrations are low ($\leq$ 2.3 ppm), and U was not detected by LA-ICP-MS. Values of $(La/Yb)_{cn}$ are low, ranging from 1.2 to 3.4, whereas Y/Ho values are very high (100-137). Chondrite-normalized profiles constructed from LA-ICP-MS data show a convex-upward topology with enrichment in the Nd-Dy range and a prominent positive Y anomaly (Fig. 6.23).

Table 6.6. Selected trace-element ratios of fluorite.

Fluorite					
(La/Nd)$_{cn}$	**(La/Yb)$_{cn}$**	**(Y/Ho)**	**Ce/Ce***	**Eu/Eu***	**Y/Y***
0.19-0.42	1.17-3.89	100.2-136.8	0.84-0.91	0.86-1.05	3.13-4.21

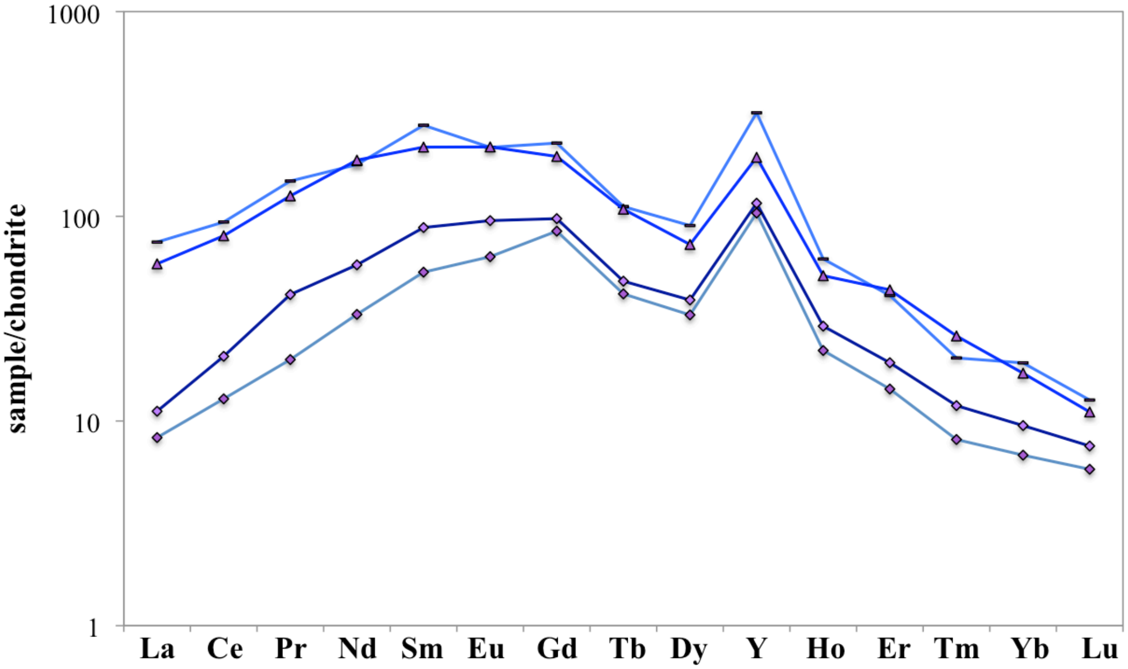

Figure 6.23. Chondrite-normalized profiles constructed from LA-ICP-MS data for fluorite from sample BL87 (fluorocarbonate-fluorite paragenesis).

6.8. Calcite

Calcite is the dominant mineral in the Bull Hill carbonatites from the unoxidized and transitional zones, and is a major to minor phase in the “Ox-Ca” subzone (see Chapter 5.3). Variations in the calcite grain size and morphology are described in Chapter 5. This section focuses on variations in calcite trace-element composition, as determined by LA-ICP-MS.

6.8.1 Unoxidized zone

Most calcite from the unoxidized zone contains significant Sr and/or Mn (Tables 6.7 and 6.8; Appendix D). Three different generations of calcite in the unoxidized parageneses were identified on the basis of key trace-element ratios, particularly $(La/Nd)_{cn}$ (Table 6.7; Fig. 6.24), and differences in chondrite-normalized REE profiles, which show three dominant topologies (Fig. 6.25): (1) negative-sloping, with enrichment in LREE [calcite-1; $(La/Yb)_{cn}$ = 3-412; $(La/Nd)_{cn}$ = 0.8-2.5]; (2) convex-upward, with mid-range REE enrichment [calcite-2; $(La/Yb)_{cn}$ = 0.4-13.1; $(La/Nd)_{cn}$ = 0.4-1.1]; and (3) overall positive-sloping with pronounced depletion in LREE [calcite-3; $(La/Yb)_{cn}$ = 0.2-0.9; $(La/Nd)_{cn}$ = 0.1-0.4]. No Ce or Eu anomalies are observed, and small negative Y anomalies are rare (Fig. 6.25; Tables 6.9 and 6.10). At least two generations of calcite with distinct compositions occur in every sample, which explains the range of overlapping values of elemental concentrations between the different parageneses and zones, as well as distinct ranges of element ratios within the same paragenesis or zone (Fig. 6.24; Tables 6.9 and 6.10). For this reason, the compositional variation of calcite from Bull Hill is best described in terms of its generation based on trace-element ratios and chondrite-normalized profiles, and not on the basis of REE mineral paragenesis where it is found. However, some noteworthy characteristics of calcite from the different parageneses are first highlighted below.

In the burbankite paragenesis, calcite is either homogeneous (sample T-684-L), or zoned with cores containing higher levels of Mn, but lower levels of Sr relative to the rims (BL71). All calcite in BL71 is enriched in Mn, Sr and LREE, with Nd >> Ce and Y/Ho values between 25 and 30 (Table 6.7). Two distinct chondrite-normalized REE patterns are observed, which correspond to calcite-2 and calcite-3 described above (Fig. 6.25A).

Table 6.7. Trace element-compositions of calcite grouped by zone and mineral paragenesis, all data are in ppm (see complete data set in Appendix D).

unoxidized paragenesis	**n**	**Mn**	**Sr**	**LREE + MREE**	**HREE**
burbankite	13	29094-40917	4194-6481	130-711	92-966
fluorocarbonate	12	789-10703	1629-9215	55-3579	3-1240
ancylite	6	10606-29826	4698-11291	205-501	105-385
fluorocarbonate-fluorite	10	26292-31898	9586-17212	46-391	137-222
ancylite-fluorocarbonate	31	2586-42945	3971-9479	131-1597	136-971
transitional zone	12	16967-31654	4444-10835	131-401	137-1220
"Ox-Ca"subzone (sample-early or late calcite):					
BL138-early calcite	1	b.d.l.	1447	18	8
BL143-early calcite	6	29219-35521	5679-9990	192-412	208-341
BL147-early calcite	4	683-767	56-61	18-22	80-89
BL44-late calcite	5	b.d.l.	149-914	b.d.l.-166	8-33
BL138-late calcite	2	b.d.l.&4694	559 & 6092	14 & 153	1-8
BL143-late calcite	4	31499-34699	6843-7117	278-456	217-384
BL147-late calcite	3	b.d.l.	634-811	103-252	8-16

Note: b.d.l. = below detection limit. For the purpose of Tables 6.7 and 6.8 only, LREE = La-Nd; MREE = Sm-Gd; HREE = Tb-Lu + Y.

Table 6.8. Trace element compositions of calcite grouped by zone and interpreted generation.

(sub)zone, calcite generation	**n**	**Mn**	**Sr**	**LREE + MREE**	**HREE**
unoxidized calcite-1	5	789-29398	2010-15275	377-1322	13-242
unoxidized calcite-2	13	2586-38993	3971-13438	43-2972	158-1240
unoxidized calcite-3	11	10380-35064	2640-14314	72-327	214-873
transitional calcite-2	3	16968-28348	9630-10570	165-383	158-207
transitional calcite-3	2	23653-31654	4444-5872	202-317	617-1220
"Ox-Ca" calcite-4	15	b.d.l.-35521	56-9990	14-333	8-341
"Ox-Ca" calcite-5	11	b.d.l.-34699	149-7117	b.d.l.-377	1-384

Note: b.d.l. = below detection limit.

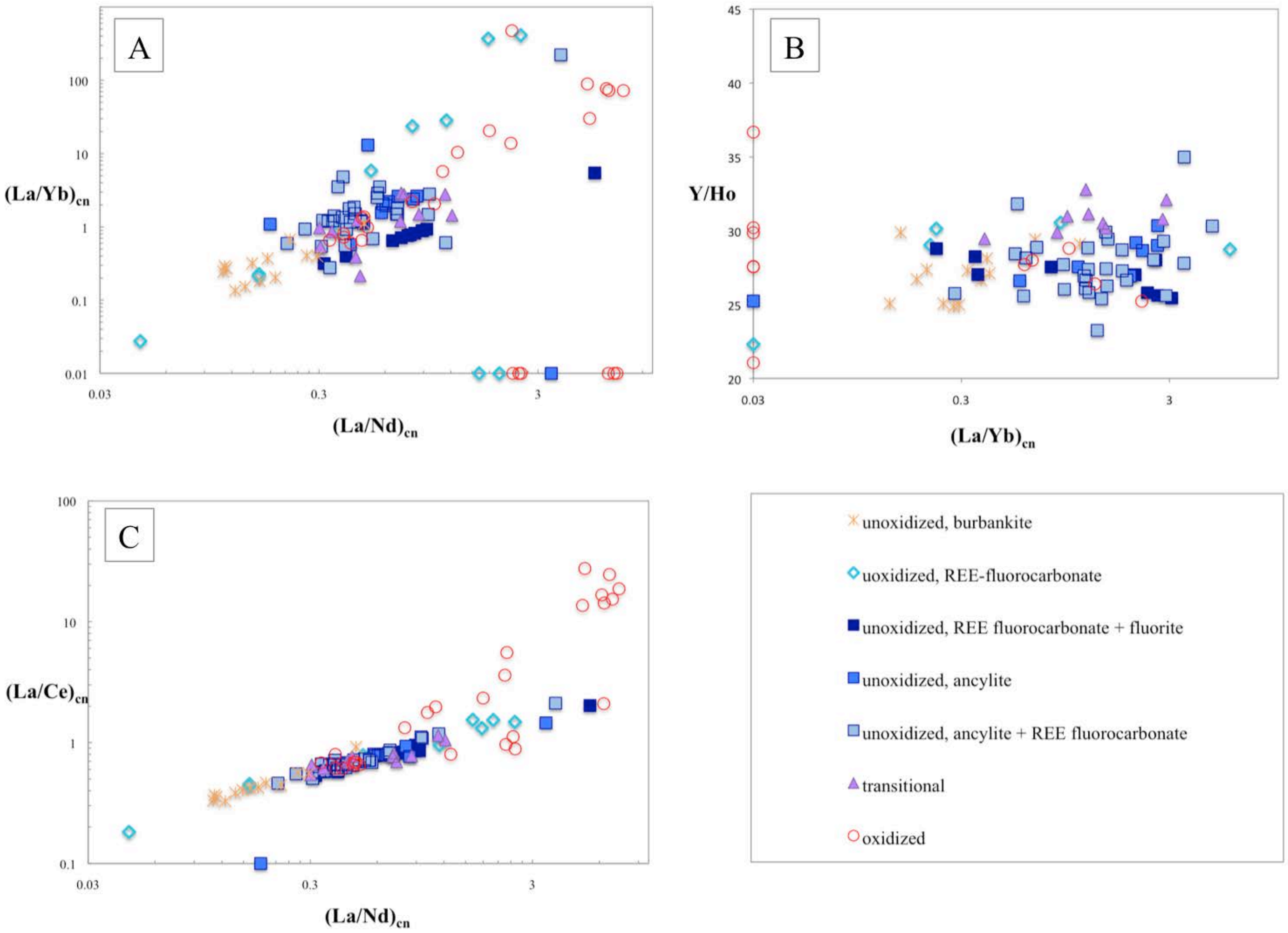

Figure 6.24. Variation in trace-element ratios of calcite. A) $(La/Nd)_{cn}$ vs. $(La/Yb)_{cn}$; analyses that plot on the abscissa have Yb values < 0.01 ppm. B) $(La/Yb)_{cn}$ vs. Y/Ho. C) $(La/Nd)_{cn}$ vs. $(La/Ce)_{cn}$; here, compositions with low Ce values are calcite-5 co-crystallized with cerianite.

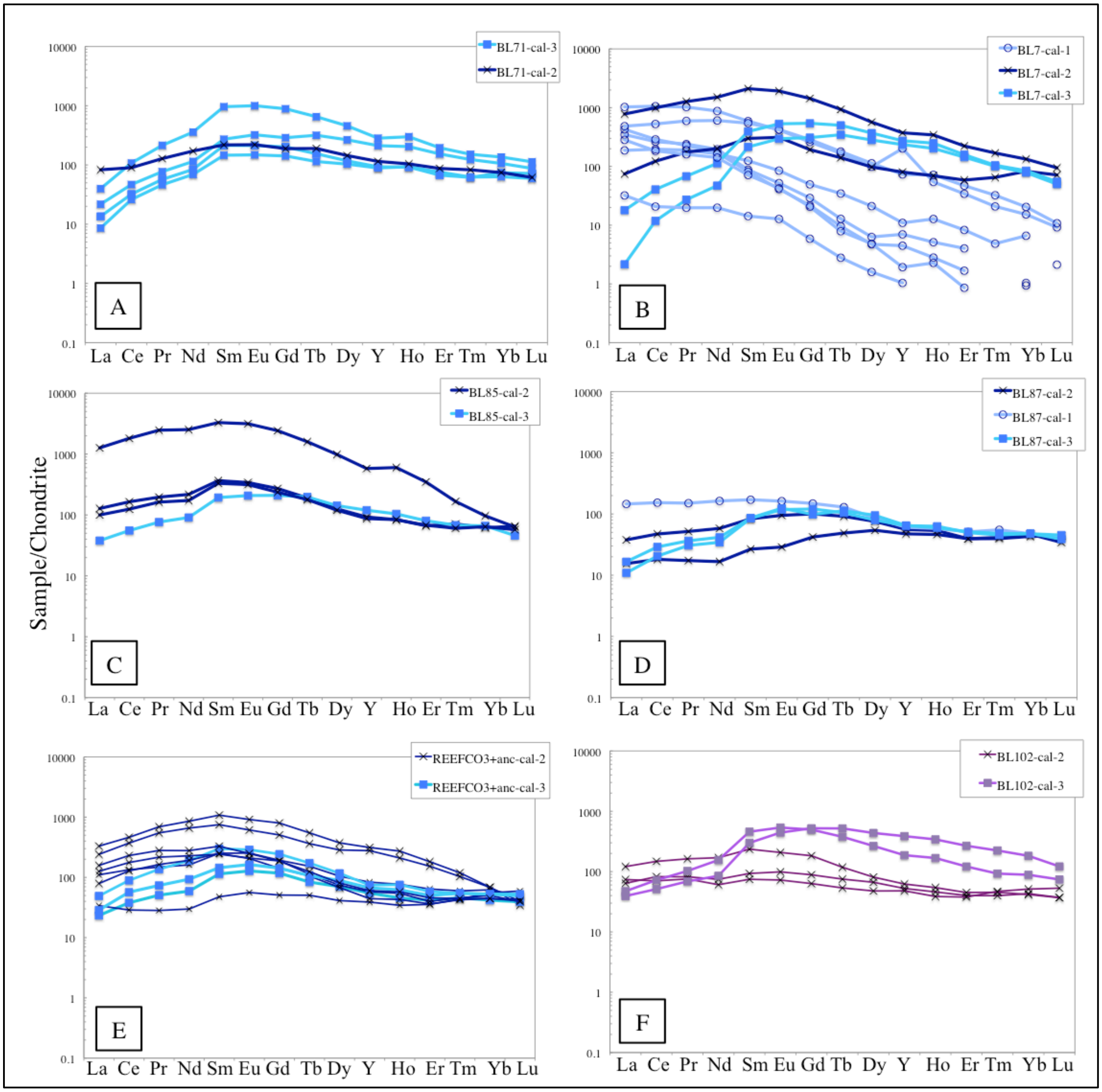

Figure 6.25. Chondrite-normalized REE profiles constructed from LA-ICP-MS data for calcite from the unoxidized (blue, A-E) and transitional (purple, F) zones. A) Burbankite paragenesis. B) Fluorocarbonate paragenesis. C) Ancylite paragenesis. D) Fluorocarbonate-fluorite paragenesis. E) Ancylite-fluorocarbonate paragenesis. Cal-1, cal-2 and cal-3 are interpreted as first-, second- and third-generation calcite, respectively. See text for discussion.

Table 6.9. Trace-element ratios of calcite grouped by zone and mineral paragenesis.

unoxidized paragenesis	**$(La/Nd)_{cn}$**	**$(La/Yb)_{cn}$**	**Y/Ho**	**Ce/Ce***	**Eu/Eu***	**Y/Y***
burbankite	0.11-0.48	0.13-1.11	24.88-29.49	0.85-0.95	0.98-1.16	0.73-0.96
fluorocarbonate	0.04, 0.80, 2.50	0.2, 28, 412	22.32-42.13	0.80-1.04	0.89-1.27	0.65-1.30
ancylite	0.17-0.84	0.57, 1.09-2.63	25.24-30.36	0.93-1.10	0.79-1.21	0.73-0.98
fluorocarbonate-fluorite	0.32-0.93	0.36, 2.05-3.07	25.62-28.80	0.99-1.10	0.84-1.34	0.78-0.94
ancylite-fluorocarbonate	0.25-0.94	0.28-0.93, 1.18-4.80	25.11-34.99	0.70-1.11	0.93-1.18	0.74-1.12
transitional zone	0.30-0.85, 1.13-1.21	0.22-0.97, 1.22-2.90	29.02-32.80	0.94-1.15	0.99-1.12	0.86-1.11
"Ox-Ca"subzone (sample-early or late calcite):						
BL138-early calcite	2.51	Yb b.d.l.	36.68	1.25-1.52	0.74-1.40	3.29
BL143-early calcite	0.33-0.80	0.60-0.99	25.23-29.82	0.81-1.21	0.99-1.25	0.78-0.94
BL147-early calcite	0.49-0.60	0.2	40.1-41.4	0.88-0.96	1.12-1.31	1.64-1.70
BL44-late calcite	5.04-6.88	Yb b.d.l.-0.89	14.4-30.22	0.04-0.09	0.27-0.57	0.75-1.54
BL138-late calcite	6.28	Yb b.d.l.	82.5	0.28-0.69	0.91	0.16-1.32
BL143-late calcite	1.01-1.80	2.06-20.52	27.72-29.88	0.53-0.70	1.05-1.19	0.85-0.92
BL147-late calcite	2.40-3.18	172-235	33.3-35.8	0.04-0.05	0.83-0.89	0.94-1.02

Note: cn = chondrite-normalized; b.d.l. = below detection limit.

Table 6.10. Trace-element ratios of calcite grouped by zone and generation.

(sub)zone, calcite generation	**$(La/Nd)_{cn}$**	**$(La/Yb)_{cn}$**	**Y/Ho**	**Ce/Ce***	**Eu/Eu***	**Y/Y***
unoxidized, calcite-1	0.80-2.50	3.08-411.65	22.70-42.13	0.88-1.04	0.80-1.02	0.65-1.22
unoxidized, calcite-2	0.37-1.13	0.36-13.09	27.05-34.99	0.90-1.10	0.52-1.11	0.73-1.12
unoxidized, calcite-3	0.12-0.41	0.14-0.94	25.07-31.83	0.90-1.11	0.52-1.34	0.77-0.97
transitional, calcite-2	1.71-1.22	1.44-2.90	30.14-32.80	0.94-1.13	0.99-1.08	0.93-1.11
transitional, calcite-3	0.30-0.46	0.22-0.53	29.48-29.89	0.95-0.96	1.08-1.12	0.86-0.99
Ox-Ca, calcite-4	0.33-2.51	Yb b.d.l-0.99	25.23-41.4	0.81-1.52	0.74-1.40	0.78-3.29
Ox-Ca, calcite-5	1.01-6.88	Yb b.d.l-235	14.4-82.5	0.04-0.70	0.27-1.19	0.16-1.32

Note: cn = chondrite normalized; b.d.l. = below detection limit.

Calcite from the fluorocarbonate paragenesis is least enriched in Mn and Sr, but has the highest REE content with respect to the other parageneses from the unoxidized zone (Table 6.9). This calcite does not show any consistent variation in Mn or Sr contents, but in a few samples, there is an inverse correlation between the two elements (Fig. 6.26). All three chondrite-normalized profiles described above are observed in calcite from the fluorocarbonate paragenesis, which explains the wide range of element ratios reported in Table 6.9. Calcite from the fluorocarbonate-fluorite paragenesis has Mn levels similar to those measured in calcite from the other unoxidized parageneses, but is comparatively richer in Sr and poorer in LREE (Table 6.7). Chondrite-normalized REE profiles show the least enrichment in the MREE and least fractionated profile of any paragenesis (Fig. 6.25D). The three dominant chondrite-normalized patterns described above are also observed in the fluorocarbonate-fluorite paragenesis. Chondrite-normalized profiles of calcite from the ancylite paragenesis are only of two types, calcite-2 and calcite-3 (Fig. 6.25C). In terms of their Mn, Sr and REE contents, and trace-element ratios, these samples are within the range delineated by calcite from the other unoxidized parageneses. The largest variation in Mn content occurs in calcite from the ancylite-fluorocarbonate paragenesis. The low-Mn variety has the highest REE (especially LREE) contents among all unoxidized samples (Appendix D). Similar to the ancylite paragenesis, only calcite-2 and calcite-3 were recognized in this paragenesis (Fig. 6.25E).

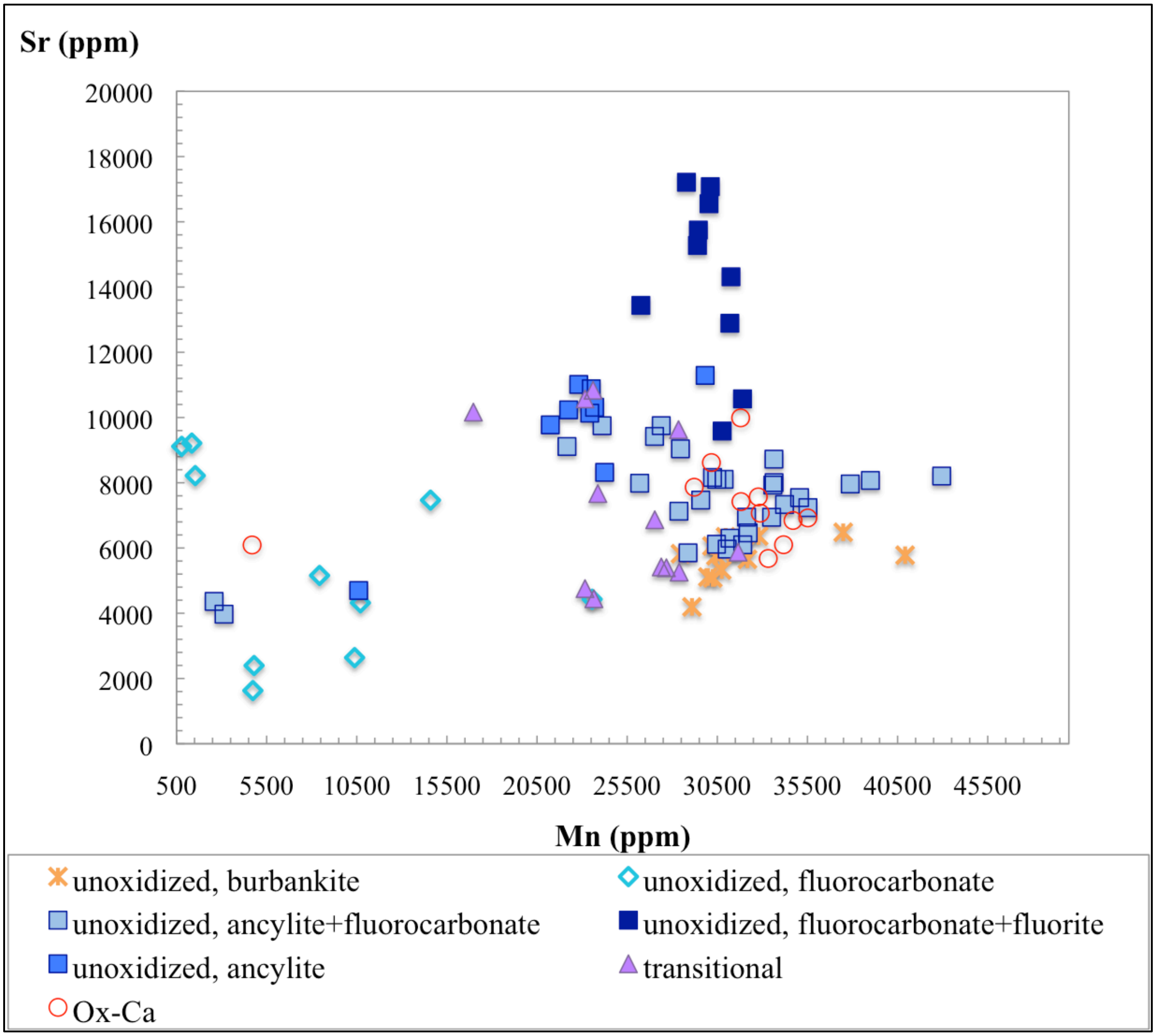

Figure 6.26. Variation in Mn and Sr contents of calcite by zone and paragenesis.

6.8.2 Transitional zone

Chondrite-normalized profiles of calcite from the transitional zone show depletion in LREE (La-Nd) and enrichment in Sm-Ho (Fig. 6.25F). Heavier lanthanides (Dy-Lu) are variably enriched or depleted with respect to the LREE. On the basis of chondrite-normalized profiles, both calcite-2 and calcite-3 can be recognized in this zone. No prominent Ce, Eu, or Y anomalies are observed, and values for element ratios are within the range of those reported above for the unoxidized carbonatites (Table 6.9).

6.8.3 “Ox-Ca” subzone

Several compositionally distinct varieties of calcite were recognized in the “Ox-Ca” subzone. However, only two varieties can also be distinguished based on the relative timing of their crystallization and are termed early and late. The early calcite shows significant variations in the shape of chondrite-normalized REE profiles, undoubtedly because some of this material is represented by relict grains not completely destroyed by oxidation, whereas the late calcite consistently shows a prominent negative Ce-anomaly (Ce/Ce* = 0.04-0.70; Fig. 6.27).

All analyzed calcite grains from sample BL44 are late crystals that show a negative Ce anomaly juxtaposed over a W-type tetrad distribution pattern. The tetrad effect is well known in synthetic systems, where REE abundances are controlled by speciation, and has been described from rocks precipitated from, or affected by, low-temperature fluids (Masuda et al., 1987; Takahashi et al., 2002). Calcite from sample BL44 is Mn- and LREE-poor (Fig. 6.27B; Tables 6.7, 6.9). All the other samples from this subzone comprise at least two varieties: one with normalized profiles similar to those observed in the unoxidized parageneses, and one with a distinct negative Ce anomaly (compare Figs. 6.25 and 6.27). Chondrite-normalized profiles of the early calcite from sample BL143 show REE distributions that are strikingly similar to calcite-1 and -2 in the unoxidized zone. The REE patterns of late calcite crystals from this sample differ in having a distinct negative Ce anomaly. Calcite from the barren sample BL138 is characterized by low REE contents, mostly at or below their limit of detection by LA-ICP-MS (Tables 6.7 and 6.8). In this sample, chondrite-normalized REE patterns of calcite from the unmineralized vein show a negative log-linear distribution with a negative Ce anomaly, whereas calcite grains from the groundmass lack Ce anomalies.

Early- and late-crystallizing calcite from sample BL147 show the most strikingly different normalized patterns (Fig. 6.27A). Here, the early generation shows a positively sloping log-linear profile characterized by depletion in LREE and a slight positive Y anomaly, whereas the late generation is enriched in LREE (with the exception of Ce), lacks an Y anomaly, and is strongly depleted in Ce. It is clear that these chemical differences reflect very different crystallization conditions of calcite in the “Ox-Ca” subzone.

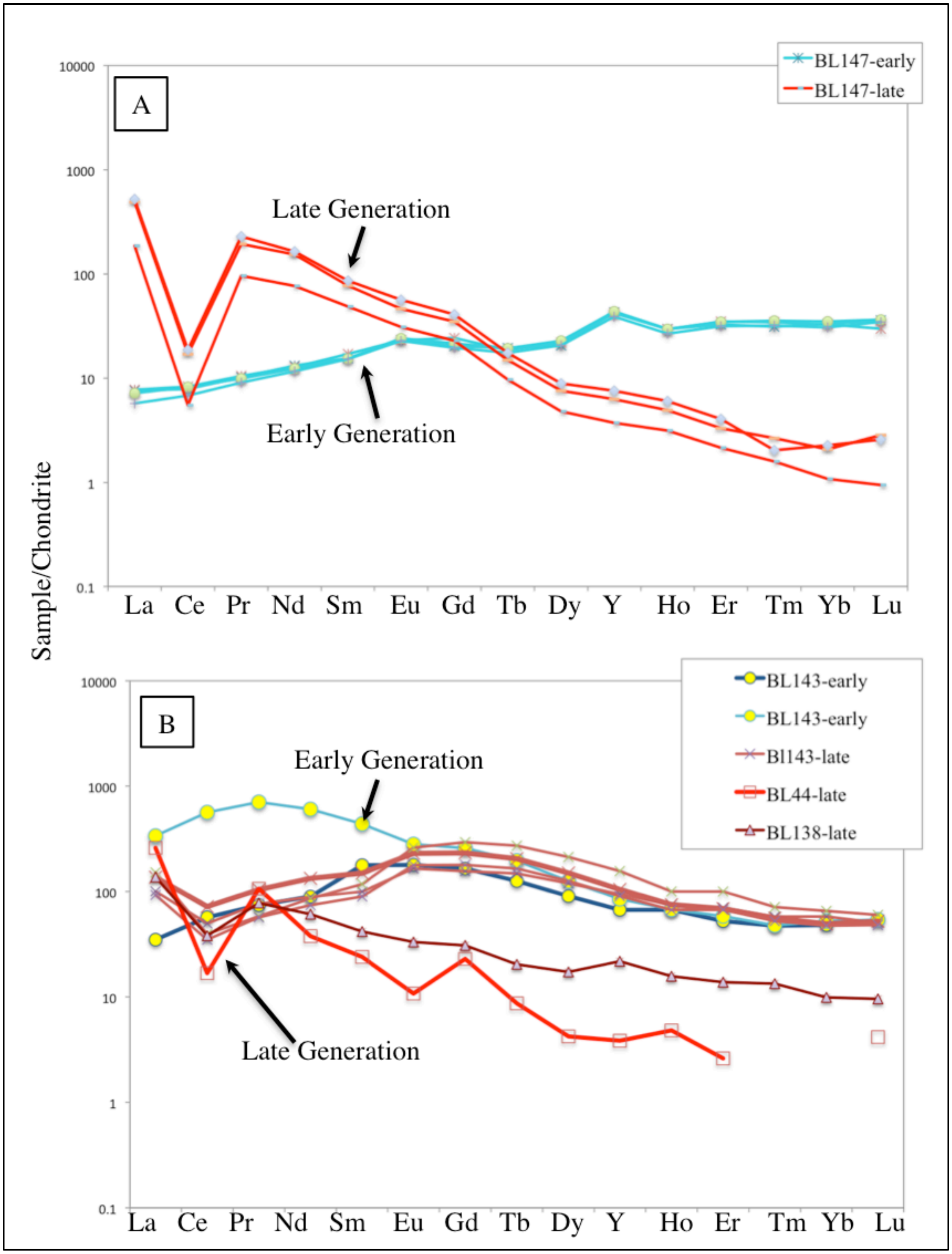

Figure 6.27. Chondrite-normalized REE profiles of calcite from the "Ox-Ca" subzone showing variation in early- and late-stage calcite mineralization. A) Sample BL147. B) Samples BL44, BL138 and BL143. See text for discussion.

6.8.4 Five generations of calcite: comparative analysis

Calcite-1

First-generation calcite is characterized by the negative-sloping chondrite-normalized profiles observed in the fluorocarbonate and fluorocarbonate-fluorite parageneses (Figs. 6.25B and D). This calcite has the lowest Mn and HREE abundances and highest Sr content among all samples from the unoxidized zone (Table 6.8). This calcite also has the highest $(La/Nd)_{cn}$, $(La/Yb)_{cn}$ and Y/Ho values (Table 6.10). A slight negative Y anomaly is observed in chondrite-normalized REE profiles of some grains (Table 6.10).

Calcite-2

Second-generation calcite is variably enriched in Mn and Sr and has the highest REE contents of all samples from the unoxidized zone (Table 6.8). Calcite of similar composition was identified also from the transitional and oxidized zones (Figs. 6.25 and 6.27), where it occurs as relict grains. Chondrite-normalized profiles of calcite-2 show enrichment in MREE. In this calcite, $(La/Nd)_{cn}$, $(La/Yb)_{cn}$ and Y/Ho values fall between those of calcite-1 and calcite-3 (Table 6.10). A slight negative Eu anomaly ($Eu/Eu^* = 0.52$) is observed in some, but not all, chondrite-normalized REE patterns of the analyzed grains. Cerium or Y anomalies were not detected.

Calcite-3

Third-generation calcite is also present in all three zones. In terms of minor substituent elements (Mn and Sr), the compositional ranges of calcite-1, -2, and -3 overlap (Figs. 6.25, 6.26 and 6.27). However, the abundances of HREE are highest in calcite-3, particularly in samples from the transitional zone. Chondrite-normalized profiles of this variety are characterized by pronounced enrichment in Sm relative to Nd and often have an overall positive slope due to greater enrichment of calcite-3 in MREE and HREE relative to calcite-2. Values of $(La/Nd)_{cn}$, $(La/Yb)_{cn}$ and Y/Ho are the lowest in the third generation of calcite (Table 6.10). The chondrite-normalized profiles are smooth and devoid of any anomalies.

Calcite-4

Significant compositional variation is observed in the early-crystallizing calcite from the oxidized zone. Some of this early calcite is chemically indistinguishable from the varieties described above and probably represents relict grains inherited from the precursor carbonatite. However, sample BL147 contains a distinct variety of calcite, which shows a positive-sloping log-linear normalized pattern and a positive Y anomaly (Y/Y* = 1.64-1.70), setting this variety apart from the other early calcite in the “Ox-Ca” subzone. This unique variety, referred to here as calcite-4, has the lowest Mn, Sr and REE values of any calcite from the examined rocks (Tables 6.7 and 6.8). Calcite-4 has $(La/Nd)_{cn}$ values intermediate with respect to those in calcite-2 and -3, whereas its $(La/Yb)_{cn}$ value range overlaps that of calcite-3 (Tables 6.9 and 6.10) . The Y/Ho values of calcite-4 are higher than in any other variety from the unoxidized or transitional zone.

Calcite-5

Fifth-generation calcite occurs exclusively in the “Ox-Ca” subzone and is characterized by a prominent negative Ce anomaly (Ce/Ce* = 0.04-0.70). The timing of its crystallization can be thus constrained to the same oxidation event that produced cerianite and Ce-depleted fluorocarbonates during supergene alteration of carbonatites.

6.8.5 Calcite zonation

Little variation in minor elements was detected in the Bull Hill calcite using WDS (see Chapter 6.8.1). To test for zonation involving trace elements, line profiles were collected using LA-ICP-MS for selected calcite grains that showed zonation in either CL or BSE images (Figs.

6.28-6.30). One transect was in calcite-2 from the carbonatite groundmass of sample BL81, which hosts both the ancylite and fluorocarbonate parageneses in different areas. Two other profiles were obtained for calcite-3 and -5 from the unmineralized oxidized sample BL138. In all three profiles, the REE behave as a coherent suite, i.e. no fractionation between the individual elements is observed. Strontium shows the least amount of variation in all three transects, whereas Ba shows the greatest variation of all trace elements. A slight inverse correlation is observed between Mn and Mg in calcite-2 from sample BL81 (Fig. 6.28). Third-generation calcite from sample BL138 has higher Sr, Ba, U and REE values than calcite-5 from the same sample. Both varieties show an inverse relationship between Mg and the REE, whereas inverse correlations between Mn and Mg, Mg and Fe, and Fe and Mn were also observed locally in calcite-5 (Figs. 6.29 and 6.30).

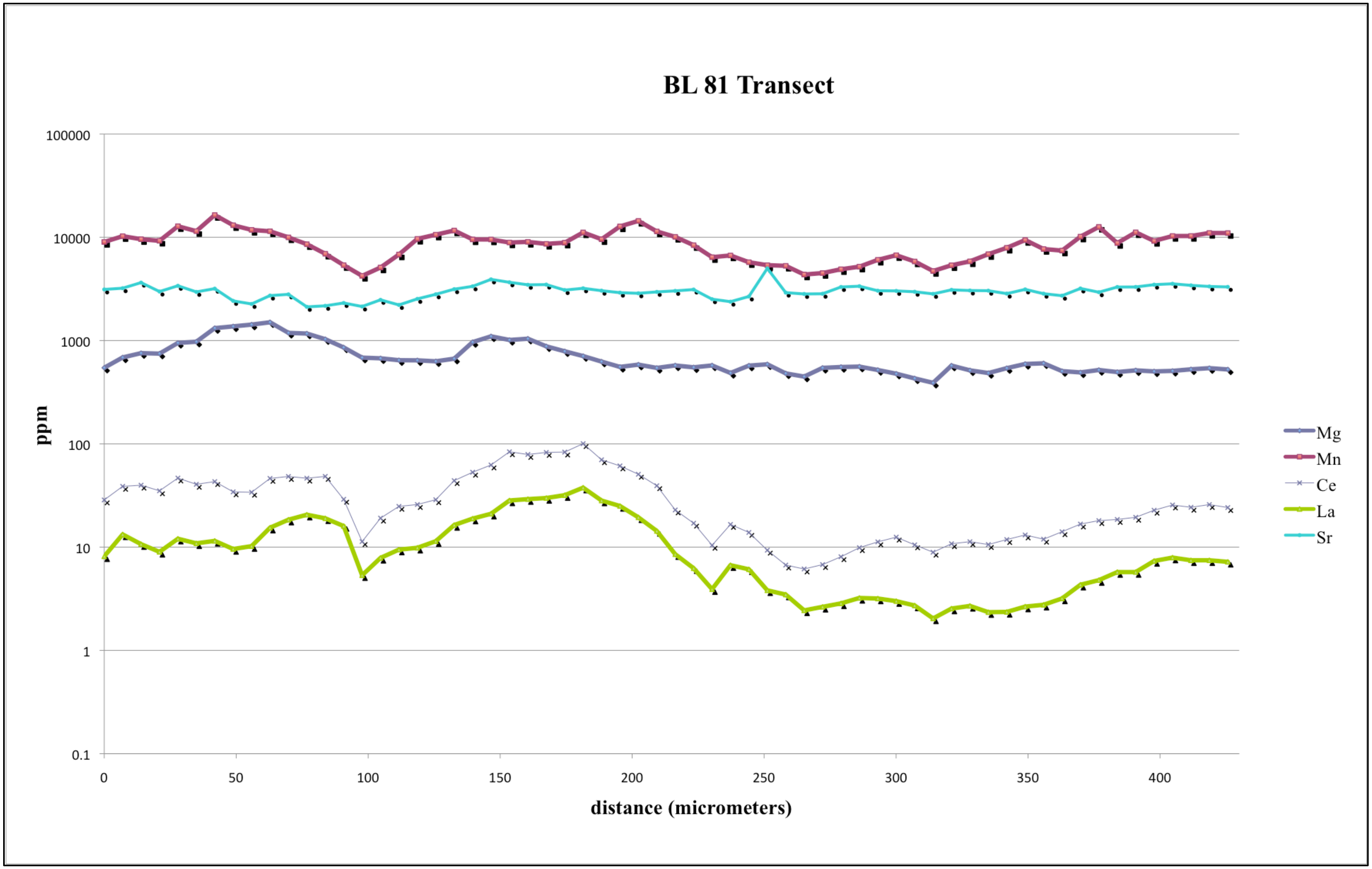

Figure 6.28. Transect profile of calcite-2 from sample BL81 showing element variations with zonation.

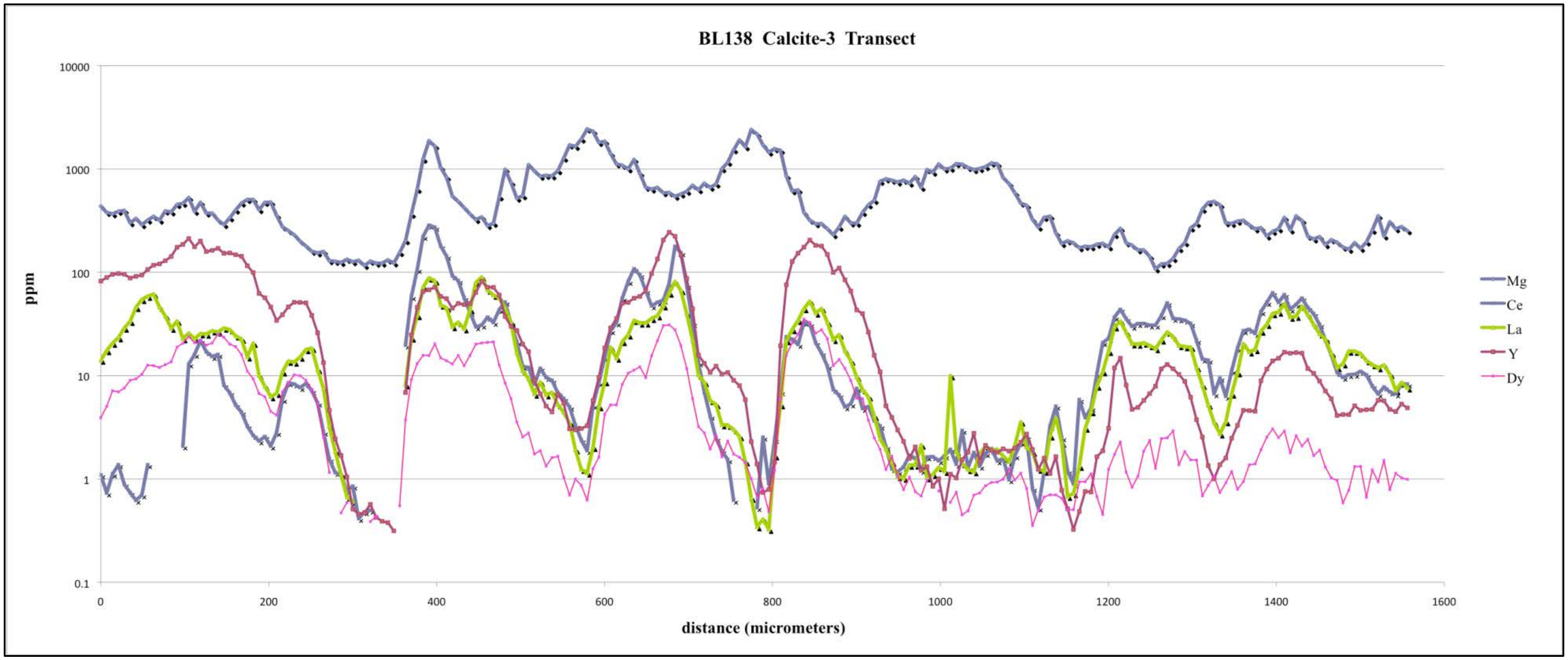

Figure 6.29. Transect profile of calcite-3 from sample BL138.

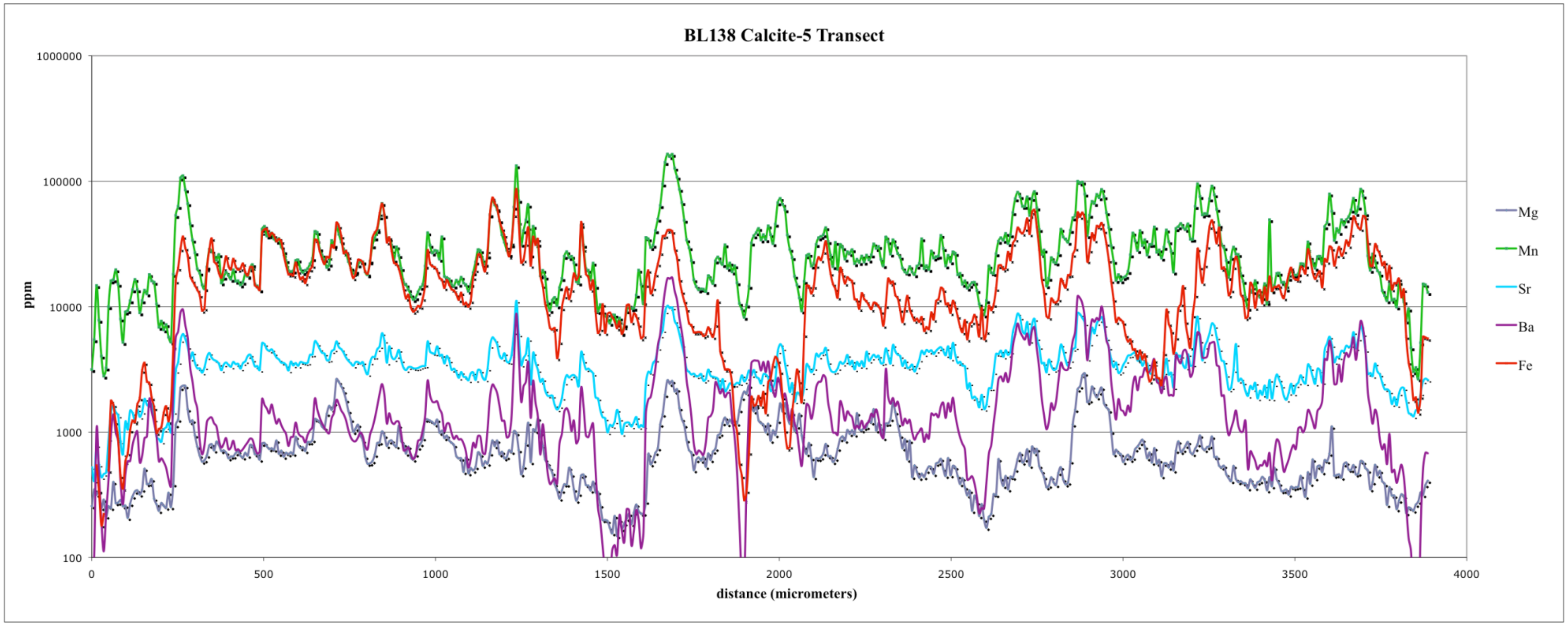

Figure 6.30. Transect profile of calcite-5 from sample BL138.

Chapter 7. Geochemistry

Whole-rock major- and trace-element geochemical data are presented in Table 7.1 and summarized in Figs. 7.1-7.3. Because of the small number of samples selected for analysis, these data should be viewed as complementary to the mineral chemistry data (Chapter 6).

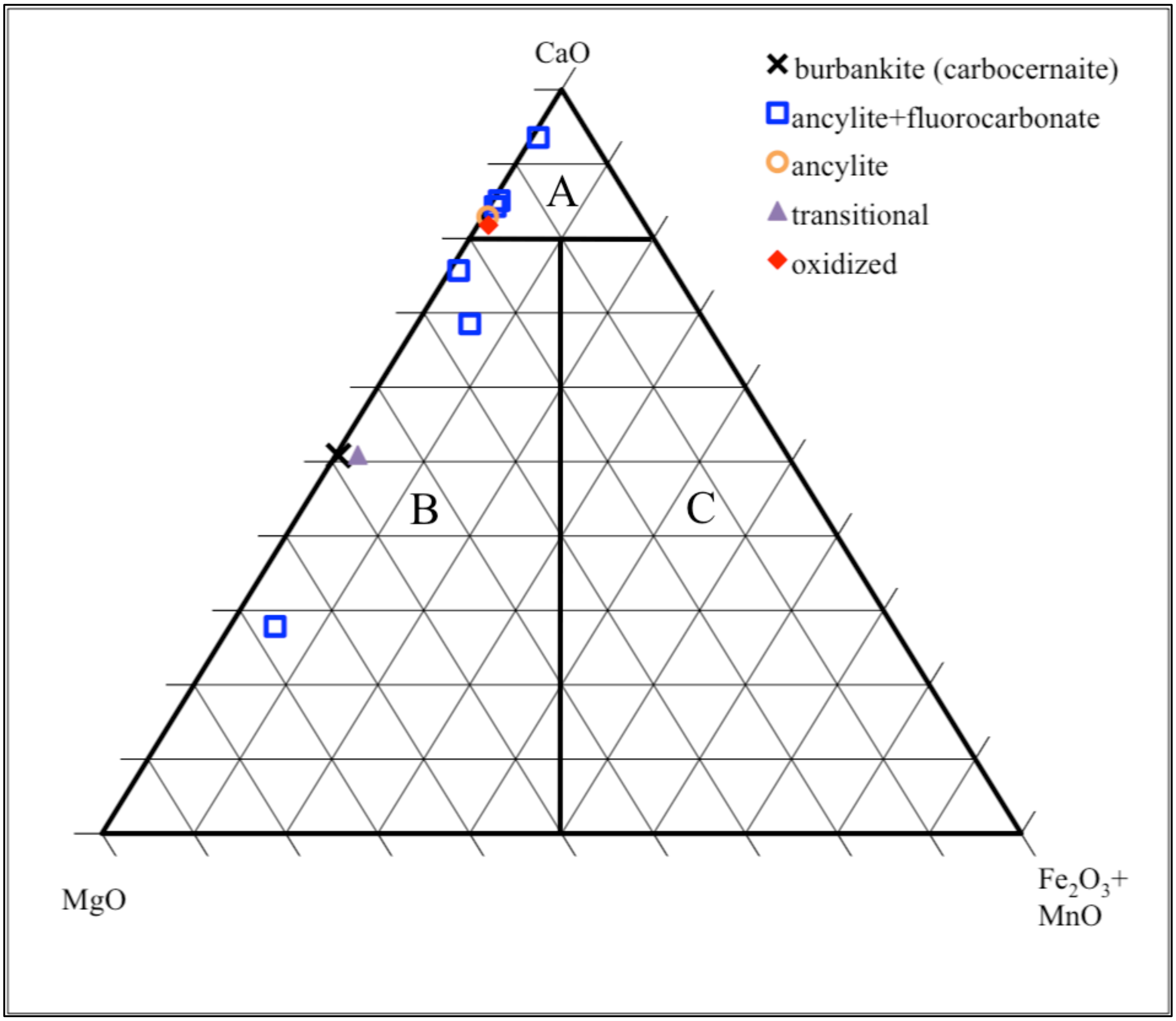

Figure 7.1. Ternary plot showing classification of carbonatites from different parageneses and zones of the Bull Hill area according to the geochemical criteria of Woolley and Kempe (1989) based on weight percentages of the four major oxide components, MgO, CaO, MnO and Fe_2O_3 (total). A: calciocarbonatite field, B: magnesiocarbonatite field, C: ferrocarbonatite field.

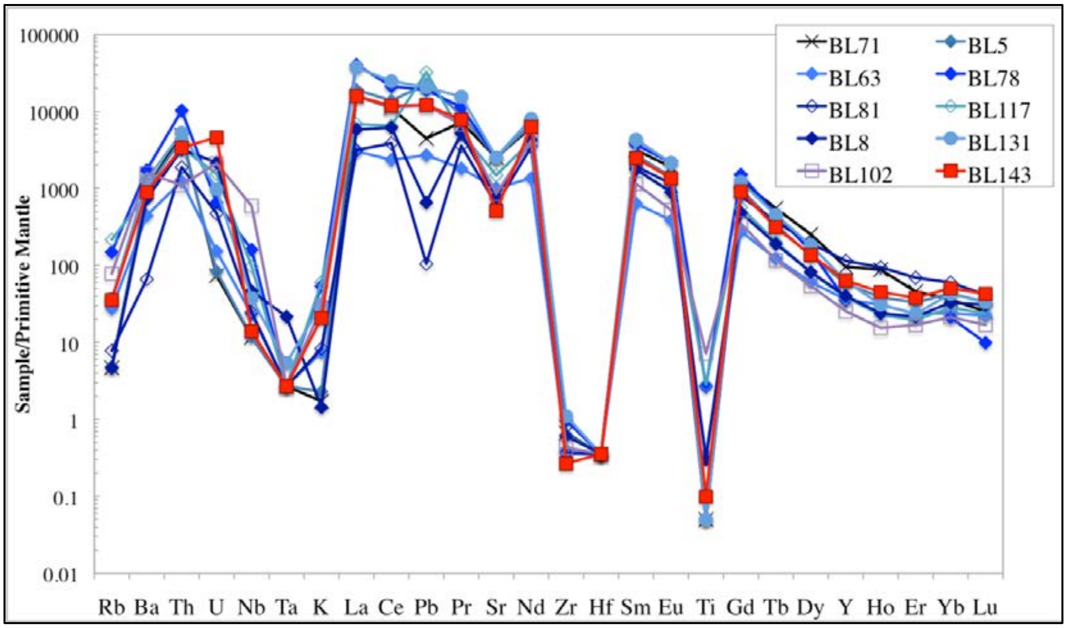

Figure 7.2. Primitive-mantle normalized spider diagram showing distribution of incompatible lithophile elements in carbonatite samples from the Bull Hill diatreme. Normalization values are from Sun and McDonough (1995).

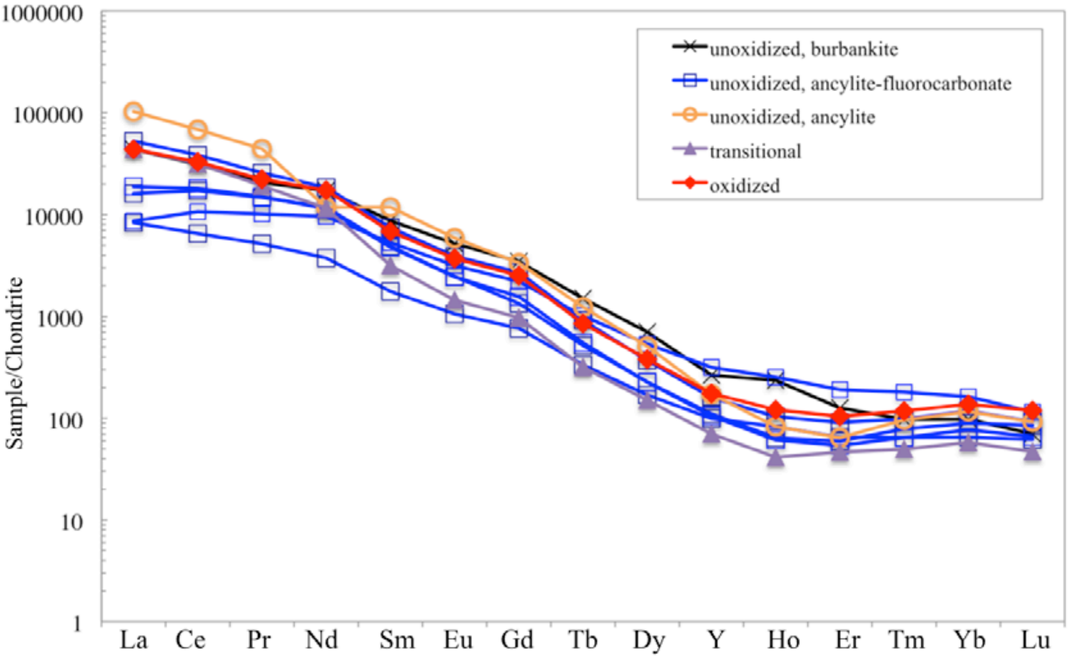

Figure 7.3. Chondrite-normalized REE diagram constructed from whole-rock geochemical data. Normalization values are from Anders and Grevesse (1989).

Five of the ten whole-rock analyses plot in the calciocarbonatite field of Woolley and Kempe (1989), including the single analyzed sample from the oxidized zone. The remaining samples plot along the magnesiocarbonatite side of the ternary plot (Fig. 7.1). These data are in contrast to those of Olinger (2012), whose samples dominantly plot in the ferrocarbonatite field. The coarse-grained sulfide fraction was removed from the samples studied in the present work before analysis, and undoubtedly accounts for the discrepancy in Fe values reported here and by Olinger (2012). The higher whole-rock Fe content in the latter work was imparted by late-stage sulfide minerals (predominantly pyrite). The highest concentrations of MnO are observed in the sample from the oxidized zone. Based on their modal mineralogy, all of the examined fresh rocks should be classified as calcite carbonatites (Woolley and Kempe, 1989)

Table 7.1. Whole-rock composition of carbonatites from different zones and parageneses.

zone	**unoxidized**								**transitional**	**oxidized**
paragenesis	burbankite (carbocernaite)	ancylite + fluorocarbonate						ancylite		
sample #	BL 71	BL5	BL8	BL63	BL78	BL81	BL117	BL131	BL102	BL143
oxide, wt. %										
Na_2O	0.70	0.07	0.08	0.07	0.06	0.06	0.06	0.13	0.03	0.06
K_2O	0.06	0.08	0.05	0.26	1.88	0.29	2.11	1.09	0.81	0.60
MgO	0.16	0.30	0.32	0.53	1.64	0.36	2.86	0.18	1.27	0.56
CaO	24.31	37.93	42.94	41.77	9.29	50.22	34.08	29.70	27.12	39.72
MnO	2.01	3.88	4.79	3.44	0.39	1.61	3.66	2.38	2.55	5.83
SiO_2	0.49	0.36	0.46	1.24	7.37	1.52	8.26	4.80	4.06	2.77
TiO_2	<0.01	0.01	0.06	0.07	0.54	<0.01	0.57	<0.01	1.44	0.02
Al_2O_3	0.13	0.05	0.11	0.31	2.04	0.35	2.11	1.42	0.99	0.80
Cr_2O_3	<0.002	0.01	<0.002	<0.002	0.02	0.01	0.01	<0.002	0.01	0.01
$Fe_2O_3^{**}$	21.37	2.47	2.89	9.45	22.05	1.48	9.14	3.56	22.35	2.46
P_2O_5	0.11	0.02	0.37	<0.01	0.09	0.15	0.55	0.04	0.03	1.35
F	0.04	0.03	0.05	0.10	0.44	0.13	0.26	0.03	0.19	0.08
total	49.38	45.21	52.12	57.24	45.81	56.18	63.67	43.33	60.85	54.26
CO_2 (calc)	26.49	26.49	26.49	26.49	26.49	26.49	26.49	26.49	26.49	26.49
S	17.13	2.30	0.90	5.20	16.40	0.12	1.24	1.50	7.03	<0.02
total	93.00	74.00	79.51	88.93	88.70	82.79	91.40	71.32	94.37	80.75

Table 7.1 (cont'd)

zone	**unoxidized**								**transitional**	**oxidized**
paragenesis	burbankite (carbocernaite)	ancylite + fluorocarbonate						ancylite		
sample #	BL 71	BL5	BL8	BL63	BL78	BL81	BL117	BL131	BL102	BL143
element, ppm										
Be	<1	<1	<1	<1	5.00	<1	3.00	<1	<1	<1
Sc	4.00	3.00	3.00	2.00	5.00	2.00	4.00	4.00	3.00	5.00
V	27.00	38.00	23.00	60.00	254.00	18.00	208.00	16.00	219.00	43.00
Co	8.20	0.80	1.40	10.70	11.90	<0.2	4.90	3.90	1.00	1.10
Ni	1.50	<0.1	1.80	0.40	1.50	4.40	<0.1	2.20	<0.1	<0.1
Cu	2.90	16.20	8.00	122.40	30.00	3.50	14.40	31.70	94.90	4.70
Zn	1455.00	>10000	120.00	447.00	8575.00	13.00	4933.00	2275.00	1062.00	785.00
Ga	5.90	2.90	9.60	6.60	18.60	7.30	33.30	1.50	13.90	13.10
As	47.00	46.40	16.20	15.50	204.60	21.90	20.00	32.90	29.20	31.70
Se	21.80	6.90	<0.5	8.00	24.40	4.10	7.30	1.20	3.90	<0.5
Rb	2.80	2.90	2.80	16.50	89.30	4.70	129.70	22.10	47.00	21.30
Sr	>50000.0	>50000.0	15320.10	20072.30	>50000.0	12226.10	29472.80	>50000.0	16967.30	10189.70
Y	413.00	248.80	172.40	155.00	153.40	492.90	164.00	269.40	109.50	273.20
Zr	7.00	4.20	6.40	4.00	10.20	3.80	6.70	11.60	4.50	2.80
Nb	7.00	7.10	27.90	13.90	96.10	14.80	58.30	22.60	355.70	8.40
Mo	1.40	0.60	0.70	1.10	1.90	0.50	1.30	1.70	5.50	58.70
Ag	19.60	19.00	0.40	4.60	49.10	0.10	18.50	12.40	5.70	2.80
Cd	13.40	3.10	0.20	0.10	4.60	<0.1	2.20	0.60	0.50	0.70
Sn	<1	1.00	<1	<1	9.00	<1	1.00	<1	5.00	<1
Sb	0.10	0.10	<0.1	0.10	<0.1	<0.1	<0.1	0.20	0.20	<0.1
Cs	<0.1	0.10	<0.1	0.30	1.80	<0.1	3.60	0.30	1.30	0.70
Ba	6734.00	6440.00	4833.00	2936.00	11401.00	437.00	5540.00	8530.00	10460.00	5922.00

Table 7.1 (cont'd)

zone	**unoxidized**								**transitional**	**oxidized**
paragenesis	burbankite (carbocernaite)	ancylite + fluorocarbonate						ancylite		
sample #	BL 71	BL5	BL8	BL63	BL78	BL81	BL117	BL131	BL102	BL143
La	10335.10	12398.60	3792.50	1963.30	26284.90	2035.20	4445.40	24218.30	10369.40	10297.00
Ce	18712.80	23254.20	10385.60	3934.60	35614.60	6449.60	10962.80	41446.50	19118.20	19889.10
Pr	1849.50	2296.73	1319.14	461.52	2893.57	905.72	1338.31	3954.99	1715.93	1987.89
Nd	7778.90	8384.40	5336.90	1697.00	>10000	4338.50	5196.70	>10000.0	5221.50	7865.00
Sm	1285.57	1099.93	723.02	259.41	1499.08	783.97	706.09	1742.63	466.10	1006.45
Eu	291.03	218.41	138.53	59.27	330.24	177.07	136.99	331.02	81.08	207.92
Gd	680.79	533.77	263.72	150.60	820.39	433.95	307.93	659.82	191.01	495.90
Tb	54.59	33.24	18.85	12.13	45.94	36.77	20.00	44.85	11.55	30.93
Dy	170.64	89.89	55.19	41.09	103.06	130.26	54.86	123.52	36.50	92.24
Ho	13.11	5.77	3.57	4.60	1.26	14.07	3.40	4.61	2.30	6.73
Er	20.02	14.43	9.47	10.34	0.30	30.35	8.57	10.23	7.38	16.56
Tm	2.36	2.38	1.90	1.57	0.58	4.37	1.56	2.33	1.20	2.85
Yb	15.89	19.12	14.49	10.60	9.26	26.49	12.53	18.87	9.39	22.27
Lu	1.70	2.26	2.07	1.50	0.67	2.80	1.60	2.24	1.14	2.89
Hf	<0.1	<0.1	<0.1	<0.1	<0.1	<0.1	<0.1	<0.1	<0.1	<0.1
Ta	<0.1	<0.1	<0.1	<0.1	0.80	<0.1	0.20	0.10	0.90	0.10
W	<0.5	0.70	0.60	0.70	6.20	<0.5	2.10	<0.5	1.20	<0.5
Au	100.00	<0.5	6.10	5.00	<0.5	<0.5	5.40	31.60	<0.5	8.50
Hg	<0.01	0.06	<0.01	<0.01	0.14	0.02	<0.01	<0.01	<0.01	<0.01
Tl	2.60	3.70	<0.1	1.50	9.20	<0.1	4.70	2.30	1.90	0.70
Pb	668.50	3369.30	98.40	405.00	2851.90	15.70	4858.10	3103.50	1802.10	1830.30
Bi	67.00	138.30	3.80	18.60	325.60	0.50	241.70	148.80	33.20	70.20
Th	389.10	352.30	255.00	98.20	820.90	149.50	267.10	419.90	87.60	268.50
U	1.50	1.70	44.00	3.10	13.30	9.60	31.30	19.80	42.90	93.30

Table 7.1 (cont'd)

zone	**unoxidized**								**transitional**	**oxidized**
paragenesis	burbankite (carbocernaite)	ancylite + fluorocarbonate						ancylite		
sample #	BL 71	BL5	BL8	BL63	BL78	BL81	BL117	BL131	BL102	BL143
SREE	41212.00	48353.13	22064.95	8607.53	67603.85	15369.12	23196.74	72559.91	37232.68	41923.73
Elemental ratios										
(La/Yb)$_{cn}$	450.33	448.98	181.22	128.24	1965.33	53.19	245.64	888.61	764.59	320.13
(La/Nd)$_{cn}$	2.56	2.85	1.37	2.23	5.07	0.90	1.65	8.75	3.83	2.52
Y/Ho	31.50	43.12	48.29	33.70	121.75	35.03	48.24	58.44	47.61	40.59
Th/U	259.40	207.24	5.80	31.68	61.72	15.57	8.53	21.21	2.04	2.88
Eu/Eu*	0.85	0.77	0.79	0.84	0.82	0.84	0.77	0.78	0.70	0.79
Ce/Ce*	0.96	0.98	1.11	0.96	0.82	1.14	1.07	0.93	1.00	1.00
Y/Y*	0.56	0.67	0.76	0.79	0.44	0.80	0.73	0.58	0.73	0.70

Detection limits for those elements which one of the analyses was below detection: TiO_2, 0.01 wt. %: Cr_2O_3, 0.002: Ni, 20 ppm: Be, 1 ppm: Cs, 0.1 ppm, Hf, 0.1: Sn, 1: Ta, 0.1: W, 0.5: Ni, 0.1: Sb, 0.1: Au, 0.5: Hg, 0.01: Tl: 0.1: Se, 0.5. Above detection: Zn, 10000: Nd, 10000: Sr, 50000. b.d.l., below detection limits.

** total Fe expressed as Fe^{3+}

Primitive-mantle normalized trace-element data show elevated levels of Sr, Ba, Th, Pb and REE (particularly, LREE), with consistent depletions in HFSE, including Nb, Ta, Zr, Hf and Ti (Fig. 7.2). Niobium is slightly enriched in carbonatite BL102, which has much higher TiO_2 content (1.4 wt.%) relative to the rest of the samples, unquestionably due to the presence of rutile, which can incorporate significant Nb (e.g., Chakhmouradian et al., 2014). Although other samples contain rutile, these were not included for the whole-rock analysis. Overall, the HFSE are strongly depleted in the Bear Lodge rocks when compared with average calciocarbonatite composition (343 ppm Nb, 9 ppm Ta, 281 ppm Zr, 4.9 ppm Hf and 0.28 wt.% TiO_2; Chakhmouradian, 2006). The Pb content shows the most significant variation of all elements, ranging from 16 to 3,370 ppm, consistent with the range reported by Olinger (2012). Barium and U also show large variations (Table 7.1). The whole-rock geochemical data from the current study also show large variations in the content of other LILE exceeding, in some cases, one order of magnitude (3-130 ppm Rb, 12,226 - > 50,000 ppm Sr, 437-11,401 ppm Ba, 8,315-71,362 ppm LREE), and U (2-93 ppm), but are within the range reported for the same elements by Staatz (1983), Duke (2005) and Olinger (2012). The results presented above are in agreement with those of Olinger (2012), who compared her geochemical data to the world average carbonatite of Woolley and Kempe (1989), and noted that the concentrations of Sr, Ba and LREE in the Bear Lodge samples tend to be higher, whereas the HFSE abundances are lower than in the average carbonatite composition.

In the present study, the highest Th/U ratios are observed in the burbankite (carbocernaite-bearing) and ancylite-fluorocarbonate parageneses from the unoxidized zone, and the lowest Th/U ratios occur in the transitional and oxide zones. The Y/Ho ratios are consistently superchondritic (> 31 and up to 122 in sample BL78). The calculated $(La/Nd)_{cn}$ values are moderately high (0.9-3.8), whereas HREE are invariably depleted with respect to LREE at overall high levels of these elements with respect to the chondrite [i.e. $(La/Yb)_{cn} \geq 53$, $Yb_{cn} \geq 57$]. The highest $(La/Yb)_{cn}$ and Y/Ho values (1965 and 122, respectively) are observed in the least HREE-enriched sample BL78 from the ancylite-fluorocarbonate paragenesis (Fig. 7.3), which also shows one of the highest levels of total REE enrichment within the studied sample suite (> 68,000 ppm; Table 7.1). In contrast, the groundmass of the least fractionated sample BL81, which contains both the ancylite and fluorocarbonate parageneses, [$(La/Yb)_{cn} = 53$] is relatively poor in REE (~16000 ppm), but characterized by one of the lowest measured Y/Ho values (35) and one of the highest levels of HREE enrichment ($Yb_{cn} = 163$). Only ~50% of the analyzed samples show HREE enrichment and overall REE depletion, whereas the remaining half do not show any consistent, meaningful variation. Most chondrite-normalized REE profiles (Fig. 7.3) are negatively-sloping. Europium anomalies are small (Eu/Eu*= 0.77-0.85), whereas Ce anomalies are not statistically significant (average Ce/Ce* = 1.00 ± 0.09).

Chapter 8. Stable Isotopic Compositions

Material selected for the measurement of C and O isotopic compositions includes one sample each from the burbankite (carbocernaite-bearing, BL71), ancylite (BL129), REE fluorocarbonate (BL7) and fluorocarbonate-fluorite parageneses (BL87), and six samples from the ancylite-fluorocarbonate paragenesis. All samples from the unoxidized zone are hand-picked calcite grains extracted from the carbonate groundmass, with the exception of sample BL63, which was extracted from a polymineralic pseudomorph. Four samples were chosen from mineralogically different carbonatites from the transitional zone, including one each from an unoxidized vein and the oxidized groundmass in sample BL25 (25A and 25B, respectively), one sample from an oxidized carbonate groundmass (BL12), and one from an unoxidized carbonatite vein (BL102). Four samples are from the “Ox-Ca” subzone and include the barren carbonatite vein in sample BL138, calcite developed interstitially with respect to oxide minerals in BL40 and BL143, and late-stage calcite from a carbonate vein in REE-mineralized sample BL44.

The C-O isotopic data, expressed in the conventional δ-notation, are presented in Table 8.1 and plotted in Fig. 8.1. The range of values typical for igneous carbonates (Taylor et al., 1967), commonly referred to as the Primary Igneous Carbonate (PIC) box, is also shown for reference. Trends of isotopic variation expected for Rayleigh fractionation, degassing and low-temperature alteration of igneous carbonate, shown as arrows in Fig. 8.1, were adapted from Deines (1989) and Demény et al. (2004). Of the samples in this work, only sample BL7 from the unoxidized REE fluorocarbonate paragenesis plots in the PIC range. The remainder of calcite samples from the unoxidized zone and the altered groundmass from the transitional zone plot in the mantle range of $\delta^{18}O_{V\text{-}SMOW}$ values (+9.5 to +10.7, with an average of 9.9‰), but exhibit somewhat lower $\delta^{13}C_{V\text{-}PDB}$ ratios (-8.1 and -10.2‰, with an average of -9.6‰) relative to the PIC range (Deines, 1989; Fig. 8.1). The calcite from the pseudomorph in the unoxidized zone (BL63) and samples from the transitional zone have higher $\delta^{18}O_{V\text{-}SMOW}$, but a comparable range of $\delta^{13}C_{V\text{-}PDB}$ values with respect to the PIC field. The calcite samples from the “Ox-Ca”subzone show enrichment in both ^{13}C and ^{18}O ($\delta^{13}C_{V\text{-}PDB}$ = -2.7 and $\delta^{18}O_{V\text{-}SMOW}$ ~18‰) relative to samples from the unoxidized and transitional zones. Calcite from the oxidized groundmass of sample BL25 also shows enrichment in both ^{13}C and ^{18}O relative to the unoxidized material in the same sample; the enrichment trend has a shallow positive slope.

Table 8.1. Carbon and oxygen isotopic compositions of calcite from the Bull Hill carbonatites.

Sample #	zone, paragenesis, characteristic accessory phases	δ13C (‰, V-PDB)	δ18O (‰, V-SMOW)
BL71	unoxidized, burbankite (carbocernaite-bearing)	-9.7	9.7
BL 7	unoxidized, fluorocarbonate	-7.3	8.7
BL 87	unoxidized, fluorocarbonate+fluorite	-9.5	10.7
BL 129	unoxidized, ancylite	-10.1	9.4
BL 5	unoxidized, ancylite+fluorocarbonate	-9.6	9.9
BL 8	unoxidized, ancylite+fluorocarbonate, monazite	-9.8	10.1
BL 63	unoxidized, ancylite+fluorocarbonate	-8.3	12.5
BL 81	unoxidized, ancylite+fluorocarbonate	-8.5	10.2
BL 117	unoxidized, ancylite+fluorocarbonate	-9.4	10.0
BL 123	unoxidized, ancylite+fluorocarbonate	-9.8	10.0
BL 102	transitional, anclyite+fluorocarbonate	-10.2	9.5
BL12	transitional, fluorocarbonate, monazite	-8.1	13.6
BL25A	transitional, ancylite+fluorocarbonate, from vein	-9.3	9.6
BL25B	transitional, ancylite+fluorocarbonate, from groundmass	-8.2	12.5
BL40	oxidized, fluorocarbonate, monazite	-2.7	17.3
BL143	oxidized, ancylite+fluorocarbonate, cerianite	-6.9	12.9
BL44	oxidized, monazite	-9.1	17.4
BL138	oxidized, barren	-8.6	18.0

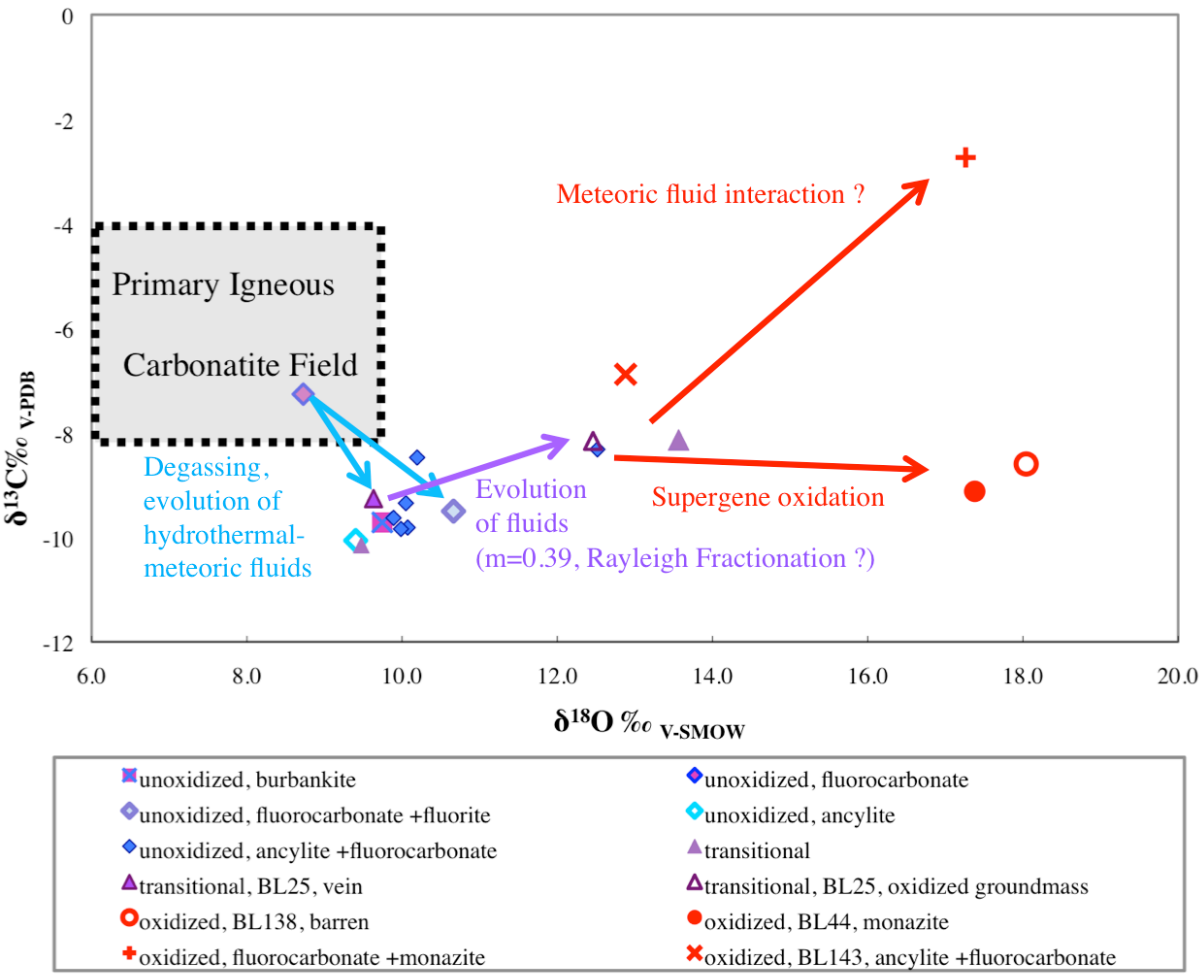

Figure 8.1. Carbon and oxygen isotopic compositions of the Bull Hill carbonatites (relative to V-PDB and V- SMOW reference materials, respectively). Colored arrows indicate various evolutionary processes that affect the isotopic composition of igneous carbonates (according to Deines, 1989; Demény et al., 2004).

Chapter 9. Radiogenic Isotopic Compositions

9.1 Sr, Nd and Pb Isotopic Compositions of the BLAC Carbonatites

Strontium, Nd, and Pb isotopic data are presented in Tables 9.1, 9.2 and 9.3, and in Fig. 9.1. Despite appreciable differences in the mineralogy, trace-element geochemistry, and stable isotopic composition of the seven samples from the unoxidized zone, they have strikingly homogeneous isotopic characteristics. Sample BL102 from the transitional zone is slightly different from the other samples as it has a somewhat lower content of radiogenic Sr and higher content of radiogenic Nd (Tables 9.1 and 9.2). The initial $(^{87}Sr/^{86}Sr)_i$ and εNd values of the carbonatites were calculated assuming an age of 50 Ma (i.e. the carbonatites are coeval with the ~50-Ma silicate rocks in the BLAC dated by Duke et al., 2002). Although more recent age data (Anderson, 2013a) are slightly older, minor corrections (~+6 Ma) to the age value will have a negligible effect on the initial ratios. The calculated ratios [$(^{87}Sr/^{86}Sr)_i$ = 0.70456-0.70462 and εNd = 0.2-0.6] are very close to the bulk-silicate earth (BSE) values of 0.70445 and 0, respectively. It is noteworthy that the data are so homogeneous that three of the four samples from the ancylite-fluorocarbonate paragenesis gave the same measured $(^{143}Nd/^{144}Nd)_i$ ratio to the fifth decimal place (Table 9.2). Whereas the $(^{87}Sr/^{86}Sr)_i$ value is not affected by radiogenic ^{86}Sr due to the small amount of ^{87}Rb in the sample as compared to ^{87}Sr, which is indicated by the $^{87}Rb/^{86}Sr$ values (Table 9.1), the $(^{143}Nd/^{144}Nd)_i$ values are affected by radiogenic ^{143}Nd (produced by the alpha-decay of ^{147}Sm) because there is a large amount of ^{147}Sm in the carbonatites as indicated by $^{147}Sm/^{144}Nd$ values (Table 9.2).

The measured Pb isotopic values are also homogeneous (Table 9.3): $^{208}Pb/^{204}Pb$ = 38.050-38.577, $^{207}Pb/^{204}Pb$ = 0.851527-0.860613 and $^{206}Pb/^{204}Pb$ = 18.069-18.282. Carbonatites hosting the ancylite paragenesis (BL08, BL81, BL131) have the most radiogenic $^{206}Pb/^{204}Pb$ ratios (18.18-18.28), and the sample from the ancylite-fluorocarbonate paragenesis has the least radiogenic $^{206}Pb/^{204}Pb$ ratios (18.07-18.09). The burbankite-carbocernaite sample (BL71) has the most primitive C-O isotopic signature, but a $^{206}Pb/^{204}Pb$ ratio (18.12) intermediate between those of the ancylite and ancylite-fluorocarbonate parageneses.

The Pb, Sr and Nd isotopic values for samples from the different zones and parageneses indicates there was no detectable crustal contamination (e.g., assimilation of basement rocks by the Bull Hill carbonatites). The variations in the radiogenic isotopic data within the sample suite can be explained by mixing of material from three theoretical reservoirs, EM1 (Enriched Mantle 1), EM2 (Enriched Mantle 2) and DMM (depleted MORB mantle; Fig. 9.1). Importantly, the Pb data do not indicate the involvement of the HIMU (high-μ) or FOZO (Focus Zone) mantle components (see below).

Table 9.1. Strontium isotopic data.

Sample #, paragenesis	**Rb (ppm)**	**Sr (ppm)**	**$^{87}Rb/^{86}Sr$**	**2σ**	**$(^{87}Sr/^{86}Sr)_i$**	**εSr**
BL71, burbankite-carbocernaite	2.8	>50000	< 0.000056	0.000009	0.704620	2.47
BL131, ancylite	22.1	>50000	< 0.000442	0.000012	0.704588	2.02
BL08, ancylite+fluorocarbonate	2.8	15320.1	0.000183	0.000010	0.704601	2.20
BL 81, fluorocarbonate and ancylite in different veins	4.7	12226.1	0.000384	0.000010	0.704639	2.74
BL05, ancylite+fluorocarbonate	2.9	>50000	< 0.000058	0.000009	0.704584	1.96
BL 117, ancylite+fluorocarbonate	129.7	29472.8	0.004401	0.000011	0.704622	2.50
BL 102, transitional zone, ancylite+fluorocarbonate	47.0	16967.3	0.002770	0.000010	0.704555	1.55

Initial values are the same as measured

Note: Isotopic ratios are expressed in ε notation, calculated according to the following the formula, where BSE represents Bulk Silicate Earth.

:

$$\varepsilon Sr = [\frac{(^{87}Sr/^{86}Sr)_i}{(^{87}Sr/^{86}Sr)_{BSE}} - 1] * 1000$$

Table 9.2. Neodymium isotopic data.

Sample #, paragenesis	**Sm (ppm)**	**Nd (ppm)**	**^{147}Sm/^{144}Nd**	**^{143}Nd/^{144}Nd**	**2σ**	**(^{143}Nd/^{144}Nd)$_i$**	**εNd**
BL71, burbankite-carbocernaite	1285.6	7778.9	0.099918	0.5126349	0.000009	0.512605	0.5
BL131, ancylite*	1742.6	24678.3	0.174300	0.5126226	0.000009	0.512591	0.2
BL08, ancylite+fluorocarbonate	723.0	5336.9	0.081908	0.5126305	0.000008	0.512606	0.5
BL 81, fluorocarbonate and ancylite in different veins	784.0	4338.5	0.109251	0.5126320	0.000009	0.512599	0.4
BL05, ancylite+fluorocarbonate	1099.9	8384.4	0.079315	0.5126320	0.000009	0.512608	0.6
BL 117, ancylite+fluorocarbonate	706.9	5196.7	0.082148	0.5126320	0.000010	0.512607	0.6
BL 102, transitional zone, ancylite+fluorocarbonate	466.1	5221.5	0.053969	0.5126070	0.000009	0.512591	0.2

* Nd interpolated from the abundances of other lanthanides. Normalized to ^{146}Nd/^{144}Nd = 0.7219. εNd$_{(t)}$ calculated using a value of ^{143}Nd/^{144}Nd = 0.512638 for CHUR to compensate for interlaboratory bias based on La Jolla standard measurements. ^{143}Nd/^{144}Nd CHUR = 0.1966.

Note: Isotopic ratios are expressed in ε notation, calculated according to the following the formula, where CHUR represents the Chondritic Uniform Reservoir.

$$\varepsilon Nd = \left[\frac{(^{143}Nd/^{144}Nd)_i}{(^{143}Nd/^{144}Nd)_{\ CHUR}} - 1\right] * 1000$$

Table 9.3. Lead isotopic data.

Sample #, paragenesis	**Pb (ppm)**	**U (ppm)**	**Th (ppm)**	**^{208}Pb/^{204}Pb**	**2σ**	**^{207}Pb/^{204}Pb**	**2σ**	**^{206}Pb/^{204}Pb**	**2σ**
BL71, burbankite-carbocernaite	668.5	1.5	389.1	38.2548	0.018	15.5741	0.004	18.1203	0.004
BL131(TE), ancylite	3103.5	19.8	419.9	38.0815	0.002	15.5496	0.001	18.1779	0.005
BL08(TE), ancylite+fluorocarbonate	98.4	44.0	255.0	38.6023	0.005	15.5927	0.002	18.2681	0.001
BL 81, fluorocarbonate and ancylite in different veins	15.7	9.6	149.5	39.1649	0.003	15.5686	0.001	18.2822	0.001
BL05, ancylite+fluorocarbonate	3369.3	1.7	352.3	38.0557	0.001	15.5435	0.000	18.0712	0.001
BL 117, ancylite+fluorocarbonate	4858.1	31.3	267.1	38.0576	0.003	15.5512	0.001	18.0691	0.001
BL 102, transitional zone, ancylite+fluorocarbonate	1802.1	42.9	87.6	38.0774	0.004	15.5504	0.001	18.0936	0.001

Table 9.3. (cont.)

Sample #, paragenesis	**^{208}Pb/^{206}Pb**	**2σ**	**^{207}Pb/^{206}Pb**	**2σ**	**^{208}Pb/^{204}Pb$_{(i)}$**	**^{207}Pb/^{204}Pb$_{(i)}$**	**^{206}Pb/^{204}Pb$_{(i)}$**
BL71, burbankite-carbocernaite	2.11108	0.00017	0.859443	0.000034	38.168	15.574	18.119
BL131(TE), ancylite	2.10538	0.00004	0.859865	0.000010	38.061	15.549	18.175
BL08(TE), ancylite+fluorocarbonate	2.11339	0.00015	0.853644	0.000030	38.215	15.583	18.066
BL 81, fluorocarbonate and ancylite in different veins	2.14218	0.00009	0.851527	0.000014	37.731	15.556	18.004
BL05, ancylite+fluorocarbonate	2.10580	0.00003	0.860083	0.000008	38.040	15.543	18.071
BL 117, ancylite+fluorocarbonate	2.10612	0.00009	0.860613	0.000016	38.049	15.551	18.066
BL 102, transitional zone, ancylite+fluorocarbonate	2.10443	0.00009	0.859419	0.000016	38.070	15.550	18.083

TE = total evaporation method, standard deviation values from repeat measurements.

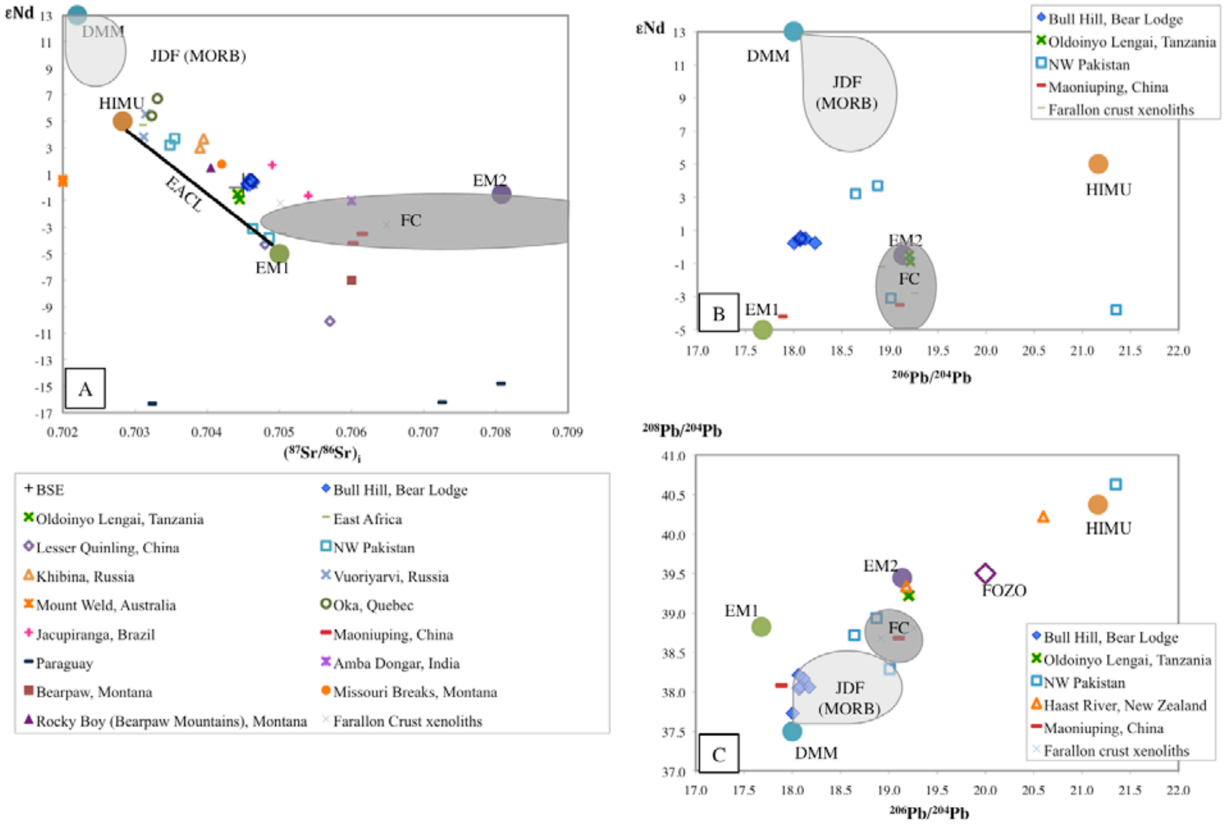

Figure 9.1. Isotopic compositions of the Bull Hill carbonatites. (A) εNd vs. (^{87}Sr/^{86}Sr)$_i$*, (B) εNd vs.* ^{206}Pb/^{204}Pb*and (C)* ^{206}Pb/^{204}Pb *vs.* ^{207}Pb/^{204}Pb*. The mantle components EM1, EM2, DMM, HIMU and FOZO, are shown for reference. BSE = Bulk Silicate Earth reference value shown in (A); EACL = East African Carbonatite Line from Bell and Blenkinsop (1987); JDF, Juan de Fuca MORB field; FC, Farallon Crust field from Usui et al. (2006). Data for selected other carbonatites discussed in this thesis are shown for comparison (Bell and Blenkinsop, 1989; Tilton et al., 1998; Zaitsev et al., 2002; Xu et al., 2003; 2004; 2011; Cooper and Patterson, 2008; Duke, 2009).*

9.2 Isotopic Characteristics of Mantle Reservoirs with Relation to Carbonatites

It is now recognized from the isotopic data gathered from carbonatites in different tectonic settings worldwide (Bell and Blenkinsop, 1989; Tilton et al., 1998; Zaitsev et al., 2002; Xu et al., 2003; 2004; 2011; Cooper and Patterson, 2008) that carbonatite magma generation involves more than one mantle source; in some cases, these magmas tap as many as five mantle reservoirs with distinct isotopic signatures (e.g., Dunworth and Bell, 2001). The published petrogenetic models for carbonatites invoke the same five major reservoirs that were proposed to explain the isotopic diversity of ocean-island magmas. The brief overview presented below and mantle reservoirs shown in Figure 9.1 are based on the work of Hart (1988), Bell and Tilton (2001), and Strake et al. (2005). The previously identified principal mantle reservoirs include, but potentially are not limited to:

(1) HIMU (High-μ), characterized by highly radiogenic ^{206}Pb/^{204}Pb values, found in ocean-island basalts (OIB) and other magmas whose generation involves mantle plumes ascending in extensional tectonic settings, such as the East African Rift. HIMU is the low-^{87}Sr/^{86}Sr end-member of the isotopic mixing line for East African carbonatites (EACL) identified by Bell and Blenkinsop (1987).

(2) FOZO (Focus Zone), characterized by higher ^{208}Pb/^{206}Pb with lower ^{206,207,208}Pb/^{204}Pb and higher ^{87}Sr/^{86}Sr values than HIMU. FOZO is interpreted as the depleted end-member for the Devonian Kola Carbonatite isotopic mixing line (KCL) proposed by Dunworth and Bell (2001) for rift-related carbonatites in the Kola Peninsula, Russia.

(3) EM1 (Enriched Mantle 1), distinguished by lower ^{143}Nd/^{144}Nd and higher ^{87}Sr/^{86}Sr values than the BSE reference, interpreted as a result of lithospheric or SCLM contribution. EM1 is the enriched end-member of the East African Carbonatite Line (EACL; Bell and Blenkinsop,

1987) and is invoked in the generation of most carbonatite magmas from various tectonic environments, such as extensional settings unrelated to plume activity, continental rifts and post-orogenic settings (Bell and Blenkinsop, 1989; Tilton et al., 1998; Zaitsev et al., 2002; Xu et al., 2003; 2004; 2011; Cooper and Patterson, 2008).

(4) EM2 (Enriched Mantle 2), identified by higher $^{143}Nd/^{144}Nd$ and $^{87}Sr/^{86}Sr$ than EM1, and interpreted to involve subducted and recycled oceanic crustal input. According to Xu et al., (2003; 2004), REE-enriched carbonatites in Maoniuping (China), emplaced in a collisional tectonic setting, tapped the EM2 mantle component.

(5) DMM (Depleted MORB Mantle), characterized by higher $^{143}Nd/^{144}Nd$ and lower $^{87}Sr/^{86}Sr$ than the HIMU and FOZO mantle reservoirs. DMM has been depleted by extraction of MORB-type melt and is recognized as being involved in the generation of carbonatites at Maoniuping, China (Xu et al., 2004).

9.3 Isotopic Variations of Carbonatites Worldwide: Key Examples

The isotopic composition of carbonatites is cuitical to understanding the deep mantle and lithospheric processes that lead to their formation in different tectonic settings (e.g., Bell, 1998). Many occurrences situated in continental rifts, such as east Africa, have isotopic compositions similar to OIB that have higher $^{143}Nd/^{144}Nd$ and lower $^{87}Sr/^{86}Sr$ ratios than the BSE reference. These carbonatites generally plot along a line between the HIMU and EM1 mantle reservoirs, defining the EACL (Bell and Tilton, 2001). Isotopic compositions in along the EACL are thought to be associated with extensional tectonic settings. Due to isotopic similarities with OIB, along with geophysical data and the common association with flood basalts, the East African carbonatites are interpreted to originate from EM1-type SCLM modified by mantle plume activity (Bell and Simonetti, 1996; Bell and Tilton, 2001). Positive εNd and negative εSr values in rift carbonatites are taken as evidence for contributions from HIMU and/or DMM sources (Tilton et al., 1998). Other carbonatites that have similar isotopic compositions as the East African carbonatites include those in the Alto Paranaíba igneous province of Brazil (some of which host economic REE and Nb ore deposits), although the Brazilian occurrences show much smaller contribution from a plume (HIMU) source (Gomes and Comin-Chiaramonti, 2005). Many carbonatites confined to rift settings in the Superior and Kola Cratons exhibit positive εNd and negative εSr values but follow trends different from the EACL. Thir petrogenesis was interpreted to indicate long-lived LILE and LREE depletion in their mantle sources, with generation of carbonatitic magmas from multiple sources (Bell and Blenkinsop, 1989; Dunworth and Bell, 2001).

Post-orogenic carbonatites from the Lesser Quinling Mountains (China) have isotopic compositions similar to EM1 and are devoid of any HIMU-type contribution that could be linked to mantle plume activity. This isotopic signature was interpreted to represent re-equilibration of the SCLM with fluids derived from old recycled crust derived from post-collisional delamination of the dense lower lithosphere beneath the Qinling orogen (Xu et al., 2011). Some carbonatites derived by direct melting of metasomatized SCLM exhibit EM1-type Sr-Nd-Pb compositions lacking any evidence for either HIMU or EM2-type contribution (ibid.). In contrast to the Qinling carbonatites, those at Maoniuping (China) host economic REE mineralization and were emplaced in a syn-collisional (transtensional) tectonic regime related to the Himalayan orogeny. The isotopic compositions of the Maoniuping carbonatites are consistent with mixing of the EM1 and EM2 reservoirs with a less significant input from a DMM-type source (Xu et al., 2003). Carbonatites emplaced in pre- and syn-collisional settings in Pakistan have different isotopic signatures. Syn-collisional carbonatites have negative εNd values and plot near EM1, whereas pre-collisional rocks give positive εNd values and plot close to FOZO in the εNd vs. $(^{87}Sr/^{86}Sr)_i$ diagram (Tilton et al., 1998).

The isotopic data obtained in the present work are quite unique in comparison with carbonatites from other areas of continental magmatism (Fig. 9.1). For example, the Bull Hill samples plot near the EACL (Bell and Blenkinsop, 1989) in the εNd vs. $(^{87}Sr/^{86}Sr)_i$ diagram, but are quite different from the African carbonatites in their Pb isotopic composition. The Pb-isotopic signatures of carbonatites from the BLAC and Maoniuping overlap, but the latter have more radiogenic Sr and less radiogenic Nd compositions relative to the samples examined in the present work. The implications of these differences are discussed in Chapter 10.6.

Chapter 10. Discussion

10.1 REE Mineralization: Paragenetic Evolution and Compositional Variation

Calcite, apatite, burbankite and REE fluorocarbonates were the primary REE hosts in magmatitic carbonatites. Subsolidus processes modified the primary parageneses and produced the late-stage hydrothermal and supergene mineralization that is the focus of current exploration efforts. The processes of magmatic crystallization and subsolidus alteration can be tracked using trace-element and isotopic variations, as is shown below. The evolution of REE mineralization is described in approximately paragenetic order, starting with primary magmatic host minerals. An introduction to these minerals based on the literature is presented first, and observations from this study are then discussed in context.

Calcite from carbonatites is often enriched in (L)REE, and, similar to apatite (see below) will release the REE during late-stage hydrothermal or supergene processes to form secondary REE-minerals (Mariano, 1989a, 1989b; Hornig-Kjarsgaard, 1998). Although the REE content of primary calcite is low, because calcite, and to a lesser extent apatite, are the most abundant rock-forming minerals, a significant proportion of the REE is often contained in these minerals (Mariano, personal communications). Primary calcite from carbonatites is typically Sr-rich, whereas late-stage calcite associated with strontianite or ancylite is low in Sr (e.g., Zaitsev and Chakhmouradian, 2002). Compositional variations of calcite in the present study are discussed in detail in the context of carbonatite evolution in Chapter 10.3. Briefly summarized, primary calcite in the BLAC is enriched in LREE (by $n * 10^3$ ppm) Sr and Mn as compared to later calcite generations.

Apatite is referred to as “the most common accessory mineral in early- to intermediate-stage carbonatites and associated alkaline rocks” by Mariano (1989a) in his detailed summary of apatite from various geological settings (p. 161). Fluorapatite is commonly an early cumulus phase in carbonatites (Bühn et al., 2003). This primary apatite often contains appreciable levels of REE (< 0.5 wt.%) in its crystal structure (Mariano, 1989a). Hydrothermal or surficial (weathering) processes can cause the breakdown of apatite and releaseof the REE hosted in this mineral to form secondary mineralization, enhancing the REE grade (Mariano, 1989a, 1989b). Apatite crystals from carbonatites often have a lozenge-shaped habit and show enrichment in REE from core to rim (Wall and Mariano, 1996; Chakhmouradian et al., 2008). The REE budget of primary apatite from carbonatites is invariably LREE-dominant, but apatite from other geological environments can be LREE- or HREE-dominant (Mariano, 1989a).

Apatite is ubiquitous in the BLAC. A study of silicate rocks from Taylor Ridge indicates there were multiple stages of apatite crystallization, with hydrothermal F- and MREE-HREE-enriched varieties replacing or mantling either early LREE-enriched igneous apatite or detrital apatite from surrounding sedimentary rocks in the Deadwood formation (Felsman, 2009; Clark, 2014 personal communications). Felsman (2009) also proposed that enrichment of the hydrothermal apatite in MREE and HREE can be explained by preferential partitioning of these elements into the apatite structure relative to carbonatite-related fenitizing fluids, but does not require that these fluids be MREE- or HREE-dominant. The data from the present study support this observation, showing a slight depletion in La and Ce relative to Pr, Nd and Sm, in analyses from the unoxidized zone. This is consistent with the preferential partitioning of the LREE into the rare-earth fluorocarbonates and ancylite, and apatite showing an affinity for the smaller REE^{3+} cations. This pattern of REE distribution in addition to textural evidence implies that apatite in the ancyite-fluorocarbonate paragenesis is a late-stage mineral precipitated at the hydrothermal, rather than magmatic, stage of carbonatite evolution. In the oxidized zone, apatite is clearly a late-stage hydrothermal mineral, as shown by a negative Ce anomaly in its chondrite-normalized REE profile (Fig. 6.20). In addition to REE, WDS analyses of the Bear Lodge apatite from all zones and parageneses show the predominance of F over other monovalent anions and appreciable levels of Sr substituting for Ca in the structure (Table 6.5). With the exception of the late-stage, Ce-depleted variety (BL143), these samples are compositionally indistinguishable from Sr-REE-bearing fluorapatite from other carbonatite occurrences (Hornig-Kjarsgaard, 1998; Bühn et al., 2003; Chakhmouradian et al., 2008).

Burbankite-group minerals have been documented as an early-crystallizing phase in carbonatites from many localities worldwide (e.g., Pecora and Kerr, 1953; Platt and Wolley, 1990; Zaitsev et al., 1998; Bühn et al., 1999; Zaitsev and Chakhmouradian, 2002; Belovitskaya and Pekov, 2004; Wall and Zaitsev, 2004; Tucker et al., 2012; Chakhmouradian et al., 2014). The burbankite structure is very flexible and allows for a wide range of substitutions involving LILE and REE cations (Belovitskaya and Pekov, 2004). Burbankite-group minerals that precipitate from carbonatite melts have higher Ba content relative to those forming in other environments, such as pegmatites or alkaline hydrothermalites. The Ba-dominant member khanneshite [$(Na,Ca)_3(Ba,Sr,REE)_3(CO_3)_5$] has been so far reported only in primary igneous carbonatites from Afrikanda and Kovdor in the Kola Peninsula, and from Khanneshin in Afghanistan (Zaitsev and Chakhmouradian, 2002; Belovitskaya and Pekov, 2004; Tucker et al., 2012). The large proportion of Ba in this mineral indicates relatively high crystallization temperatures (>500°C) conducive to the incorporation of the large Ba cation in the crystal lattice (Belovitskaya and Pekov, 2004). Strontium concentrations in burbankite-group minerals increase from early- to late-stage crystallization in carbonatites (Zaitsev et al., 1998)

Quartzite affected by carbonatite-derived fluids from the to the Kalkfeld carbonatite complex (Namibia) contains carbonatitic fluid inclusions that include abundant burbankite crystals, providing evidence that orthomagmatic fluids in equilibrium with carbonatite at this locality were saturated with respect to burbankite, i.e. were rich in alkalis, Sr and REE (Bühn et al., 1999). In the absence of large, optically detectable crystals, primary magmatic burbankite is commonly preserved as inclusions in early-crystallizing oxide, phosphate and carbonate minerals (e.g., Platt and Woolley, 1990; Zaitsev et al., 1998; Zaitsev and Chakhmouradian, 2002). Zaitsev et al. (2002) found that C and O isotopic compositions of both burbankite-group minerals and coexisting rock-forming carbonate phases in the Khibiny and Vuoriyarvi complexes (Kola, Russia) plot in the PIC field of Taylor et al. (1967), further supporting the primary igneous nature of burbankite in carbonatites. The REE budget of burbankite-group minerals is generally Ce-dominant, with two orders of magnitude higher chondrite-normalized LREE abundances relative to HREE (Belovitskaya and Pekov, 2004). Lanthanum was shown to become more abundant in burbankite precipitated at lower temperatures, thus providing insight to the degree of REE fractionation in the carbonatite system (Belovitskaya and Pekov, 2004).

With a decrease in alkalinity in an evolving carbonatite system (either magma or rock + fluid), burbankite-group minerals are readily altered and replaced (Belovitskaya and Pekov, 2004; Wall and Zaitsev, 2004). In many carbonatite complexes, including Bear Lodge, burbankite appears to be the primary igneous mineral that gives way to complex polymineralic pseudomorphs, such as those described in Chapter 5 of the present thesis. Burbankite is commonly replaced, partially or completely, with aggregates of ancylite, barite and strontianite, or of synchysite, barite and strontianite. Rare-earth carbonatites at Khibiny and Vuoriyarvi provide the most convincing evidence for pseudomorphic replacement of burbankite because all stages of this process were observed: from small veins of secondary minerals crosscutting large hexagonal burbankite crystals to complete polycrystalline pseudomorphs (Zaitsev et al., 2002). At these localities, the replacement of burbankite and calcioburbankite is interpreted to have taken place in an open system and involved late-stage, water-rich fluids modified by wall-rock interaction. The presence of secondary minerals, such as REE fluorocarbonates or ancylite, can provide clues to the composition of these fluids, degree of fluid evolution, and temperature. In the Kola complexes, Zaitsev et al. (2002) concluded that the secondary minerals that pseudomorphed burbankite crystallized from a carbonatite-derived fluid enriched in REE, Ba, Sr, F and S. Kapustin (1980) suggested that alteration of burbankite involves intermediate precipitation of carbocernaite, which is then replaced with synchysite and barite at relatively high temperatures, and subsequently by ancylite and barite with decreasing temperature. Zaitsev et al. (1998) reported that, at Khibiny, burbankite and carbocernaite crystallized independently, but both underwent replacement by REE carbonates, strontianite and barite.

Textural observations made in the present work (Chapter 5) indicate that burbankite (or a related mineral) was a primary Sr-Ba-REE phase in the Bull Hill carbonatites. This is supported by the compositional data presented in Chapter 6.1. High Ba and Na contents indicate that the burbankite formed at relatively high temperatures prior to fenitization (i.e. loss of Na to wall-rock metasomatism). The two samples containing burbankite show adequate evidence to support the suggestion that this mineral crystallized early in the evolution of carbonatitic magma and was subsequently replaced by a diverse assemblage of minerals. Pseudomorphs after burbankite consist of carbocernaite, rare-earth fluorocarbonates, and/or ancylite, strontianite and barite. An increase in Sr content coupled with a decrease in Na content in carbocernaite relative to the unaltered burbankite indicates that the two minerals precipitated independently at different stages of carbonatite evolution, and that carbocernaite formed later than burbankite. Although there are significant variations in the chemistry of burbankite and carbocernaite from different samples, it is evident that the large burbankite crystals in sample T-684-L represent the first stage of REE mineralization in the Bull Hill carbonatites. This is supported by the very limited occurrence of other REE-bearing minerals and replacement textures in this sample (ancylite developed along fractures in the burbankite).

Burbankite in sample BL71 was clearly pseudomorphed by ancylite, strontianite, and barite in some areas, and occurs only as relict fragments in some of the pseudomorphs. In support of Kapustin's (1980) interpretation, carbocernaite crystals in this sample are part of intermediate- to late-stage mineralization, as indicated by their occurrence in vugs, euhedral morphology, low Ba content, and other compositional characteristics (see below). This sample probably represents early stages of carbonatite alteration by an evolved, carbonatite-derived fluid, as indicated by C and O isotopic evidence (see below). Carbocernaite in sample BL70 co-exists with rare-earth fluorocarbonates that appear to be replacing the carbocernaite, indicating significant variations in the composition of late-stage fluids within the Bull Hill diatreme.

Rare-earth fluorocarbonates in carbonatites are invariably LREE-dominant (Wall and Zaitsev, 2004; and references therein), although synchysite-(Y) has been documented in a few African localities (Verwoerd, 1993; Orris and Grauch, 2002). Cerium is usually the dominant lanthanide, followed by La and Nd (Williams-Jones and Wood, 1992). Hydroxyl anions may substitute for F in bastnäsite, but to the author's knowledge, hydroxyl-bastnäsite [REE(CO_3)(OH)] is not known to occur in carbonatites. Although it may be an important phase in the BLAC (Clark, 2014, personal communications), it was not identified in this study. The bastnäsite structure is composed of hexagonal sheets of REE and F ions with CO_3 groups sandwiched between the sheets (Terada et al., 1993). Parisite and synchysite are monoclinic (pseudohexagonal) and form a polysomatic series with different elemental proportions of divalent cations (dominantly Ca) interlayered with CO_3 and REE-F sheets (Donnay and Donnay, 1953).

The occurrence of rare-earth fluorocarbonates in diverse geological environments, including carbonatites, peralkaline silica-undersaturateed rocks, hydrothermal veins, granites and granitic pegmatites and laterites (Mariano, 1989a; Peishan et al., 1995; Samson and Wood, 2004; Mariano and Mariano, 2012) attests to their stability under a wide range of temperature and pressure conditions. The presence of secondary fluorocarbonates can give insight to the composition of a mineralizing fluid, degree of fluid evolution, and crystallization temperature (Zaitsev et al. 2002). The occurrences of bastnäsite, parisite and synchysite in carbonatites are far too numerous to be listed here. The best-studied examples include: Mountain Pass, USA; Bayan Obo and Maoniuping, China; Barro do Itapurapuã, Brazil; Kangankunde, Malawi; and Vuoriyarvi, Sallanlatvi and Khibina, Russia (Mariano, 1989b; Zaitsev et al., 1998; Smith et al., 2000; Xu et al., 2003; 2004; Castor and Hedrick, 2006; Ruberti et al., 2008). Syntaxial intergrowths of fluorocarbonates are very common and can be explained in terms of chemical changes in the host fluid (Zaitsev et al., 1998). These changes involve dynamic fluid evolution, notably with respect to the activities of Ca^{2+} and F^- relative to that of $(CO_3)^{2-}$, but not singularly to activity of F^- in the fluid (Williams-Jones and Wood, 1992; Williams-Jones et al., 2000). In their study of REE mineralization at Barro do Itapirapuã, Ruberti et al. (2008) concluded that association of all three fluorocarbonate minerals is metastable.

During hydrothermal alteration of the Bull Hill rocks, the primary bastnäsite-parisite-synchysite intergrowths in the carbonatites were dissolved and the released REE re-precipitated as late-stage fluorocarbonates. The changes in fluorocarbonate chemistry in the studied samples reflect at least six different mineralization events. The key rare-earth characteristics (element ratios, chondrite-normalized profiles) of synchysite and parisite are very similar to those of bastnäsite, indicating little change in REE budget of their host fluid during hydrothermal reworking of the carbonatites. This consistency could best be explained by crystallization of all three minerals from the same fluid phase without significant contribution from external sources. The observed mineralogical variations reflect changes in the relative activity of F^-, $(CO_3)^{2-}$ and Ca^{2+}. The vector of these changes is difficult to determine with any degree of accuracy because of the minute size of fluorocarbonate crystals in most samples (e.g., Figs. 5.17, 5.22). Crystals coarse enough for BSE imaging and quantitative analysis by WDS contain less Ca-rich and more REE-F-rich composition along the rim (e.g., Fig. 5.28, 5.32), indicating a decrease in $a(Ca^{2+})$ and an increase in $a(F^-)$ relative to $a(CO_3^{2-})$ toward the waning stages of hydrothermal activity in at least some samples. The opposite trend was reported for hydrothermal REE mineralization at Barro do Itapirapuã, which differs from the Bull Hill diatreme in that it contains abundant fluorite (Ruberti et al., 2008). It appears that $a(F^-)$ values in the fluid were initially high at Barro do Itapirapuã, which led to early precipitation of fluorite and a drop in $a(F^-)$, leading to the formation of F-poor and Ca-rich fluorocarbonates. At Bull Hill, the activity of F^- was only high enough for the deposition of fluorite early in the evolution of the system, during the precipitation of the fluorocarbonate-fluorite paragenesis. Late-stage fluorite mineralization was not documented in the present stydy but has been observed accompanying Au mineralization at Bull Hill (Clark, personal communications).

Both the fluorocarbonate and fluorocarbonate-fluorite parageneses are interpreted to have formed prior to ancylite because the LREE-F complexes are stable at high temperatures and dissociate with decreasing temperature (Williams-Jones et al., 2012), and also because ancylite-group minerals are hydrous and dissociate at T ≥ 300 ^oC (Lu and Wang, 2002). In synthetic Ca-Sr-free hydrothermal systems, bastnäsite-structured REE carbonates crystallize at higher temperatures than ancylite-type phases, and the upper stability limit of bastnäsite-type phases decreases with increasing atomic number from 700-800 ^oC for $La(CO_3)(OH)$ to ~350 ^oC for $Dy(CO_3)(OH)$ (Kutty et al., 1985; Hsu, 1992). The presence of F (common to all samples from carbonatites) expands their stability fields by about 50 ^oC (Hsu, 1992). Fluid inclusions were not investigated in the present work, but the data available for hydrothermal fluorocarbonates from the Mianning-Dechang area in China indicate crystallization temperatures in the range from 150 to 350 ºC (Hou et al., 2009).

Fluorocarbonates from the oxide zone clearly represent a late mineralization event, probably related to oxidation near the paleosurface. Textural and chemical evidence (such as the proportion of Ce relative to other LREE) indicates that there were at least two stages of late fluorocarbonate growth, one preceding the oxidation and development of cerianite (CeO_2), and the other postdating it and characterized by prominent negative Ce anomalies in the fluorocarbonate chondrite-normalized patterns (Figs. 6.8-6.10). This interpretation is supported by the observed variations in C and O isotopic composition (see below). The late-stage mineralization contains a higher proportion of parisite and bastnäsite relative to the unoxidized parageneses, reflecting an overall increase in REE concentrations in the fluid. Also noteworthy is an increase in the relative proportion of Nd in fluorocarbonate minerals from the oxidized and transitional zones relative to in the unoxidized parageneses.

Ancylite-group minerals are orthorhombic or monoclinic hydrous carbonates that have cation substitution between Ca and Sr in the M^{2+} site, and between the different REE in the M^{3+}

site. Because ancylite-group minerals have a flexible crystal structure, their composition is commonly non-stoichiometric, owing to substitution of REE^{3+} for divalent cations, coupled with the incorporation of $(OH)^-$ anions in the structure (Dal Negro et al., 1975; Miyawaki and Nakai, 1996).

Ancylite-group minerals form from low-temperature, late-stage hydrothermal H_2O-CO_2-bearing fluids commonly associated with carbonatites. The interaction of late-stage H_2O-CO_2-rich fluids with primary burbankite often results in pseudomorphs that comprise ancylite-group minerals, barite, strontianite and rare-earth fluorocarbonates (see above). The formation of abundant ancylite (i.e. the Sr-dominant member of the group) in the Bear Lodge carbonatites also resulted from interaction of a primary burbankite-group mineral with fluids, as indicated by its mineral paragenesis and its predominant occurrence in pseudohexagonal pseudomorphs, such as those shown in Figs. 5.10a and 5.15b. Although no published experimental data are available to constrain accurately the stability range of ancylite, limited published data for other carbonatite complexes indicate low temperatures of crystallization (e.g., 200-250 ^{o}C at Afrikanda: Zaitsev and Chakhmouradian, 2002). According to the published experimental data, under isothermal conditions, ancylite-type REE carbonates crystallize as a stable solidus phase at higher CO_2 activities than bastnäsite-type hydroxylcarbonates (e.g., $X_{CO_2} > 0.6$ for $GdCO_3OH$; Kutty et al., 1985). Hence, late-stage precipitation of ancylite in the Bull Hill rocks could also be promoted by an increasing partial pressure of CO_2 in the fluid.

Observations from other carbonatite localities indicate that early-crystallizing ancylite-group minerals are Sr-rich and evolve toward calcio-ancylite with decreasing temperature (Zaitsev et al., 2002). Electron-microprobe data for ancylite from the Bull Hill carbonatites are generally consistent with that interpretation, because ancylite that replaces burbankite in the unoxidized carbonatites does show higher Sr levels, relative to lower-temperature ancylite from the oxidized zone (Table 5.2). However, it is noteworthy that the highest Sr content was measured in the rim of a large ancylite grain from the ancylite-fluorocarbonate paragenesis (22.4 wt.% SrO), whereas its core is Sr-poor (14.7 wt. % SrO). There is a negative correlation between REE+Y and Ca+Sr contents in the Bear Lodge ancylite, indicating that the composition of this mineral was also controlled by the availability of REE in the fluid (Fig. 6.13).

Ancylite from the ancylite-fluorocarbonate and ancylite parageneses has a similar range of compositions, but the latter is generally poorer in Sr. Ancylite from the unoxidized and transitional zones has similar Sr concentrations, whereas that in the oxidized zone has generally lower Sr, but higher REE contents (up to 68 wt.% REE_2O_3; Table 6.2; Appendix C). Crosscutting relationships of unoxidized carbonatites indicate that the ancylite paragenesis developed after the fluorocarbonate and fluorocarbonate-fluorite parageneses, but before the ancylite-fluorocarbonate paragenesis. The latter may, in fact, represent the ancylite paragenesis overprinted by later fluorocarbonate mineralization. The absence of a negative Ce anomaly in chondrite-normalized REE profiles of ancylite from the “Ox-Ca”subzone of the oxidized zone indicates that this mineral crystallized prior to cerianite and Ce-depleted fluorocarbonates or monazite. The textural evidence indicates that the REE were remobilized from ancylite in the oxidized zone, and likely were incorporated into late-stage cerianite, monazite and fluorocarbonates.

Monazite is probably the most common REE mineral in carbonatites, where it can be magmatic (Xu et al., 2011), hydrothermal (Wall and Mariano, 1996), or supergene in origin (Mariano, 1989a). Supergene monazite forms in deeply weathered laterites, where the phosphate from primary apatite combines with LREE. Primary (igneous) monazite is often strongly enriched in LREE relative to HREE, and has a variable, but typically low Th content (< 1 wt.% ThO_2; Wall and Zaitsev, 2004; Mariano and Mariano, 2012). Light REE enrichment decreases with increasing alteration (most often hydrothermal), leading to enrichment of late-stage, hydrothermal monazite in MREE (Wall and Mariano, 1996; Wall and Zaitsev, 2004). Monazite enriched in Th, Ca, Sr, or S was reported by Wall and Mariano (1996), Chakhmouradian and Mitchell (1998), and Bulakh et al. (2000) as hydrothermal in origin. In the supergene environment (laterites developed at the expense of carbonatites), secondary monazite incorporates more Y and HREE in comparison to the primary monazite (Mariano, 1989a). These chemical variations of monazite in carbonatites can be accommodated by coupled substitutions involving entry of divalent cations in the REE site and S^{6+} in the P site, or Th^{4+} + Si^{4+}substituting for REE^{3+} + P^{5+} (Wall and Zaitsev, 2004).

Monazite can be replaced with its hydrous counterpart, rhabdophane, during lateritization. Low EMPA totals can be indicative of the presence of water in the structure (Krenn and Finger, 2007). Berger et al. (2008) found that monazite in altered granite is most soluble in the presence of a low-temperature hydrothermal fluid, where F and OH are present as ligands. This is in accord with the limited occurrence of hydrothermal monazite in carbonatites (Wall and Mariano, 1996; Chakhmouradian and Mitchell, 1998; Wall and Zaitsev, 2004).

In the Bull Hill carbonatites, the elevated SrO and CaO contents of monazite from the unoxidized parageneses and the transitional zone (Table 6.3) are consistent with its crystallization from carbonatite-derived carbo-hydrothermal fluids. Although the total content of divalent cations ranges from 6.2 to 9.4 wt.% oxide, no clear correlation is observed among these components and either Th or REE (Fig. 6.16). Monazite from the oxidized zone has a “spongy” appearance typical of monazite from supergene environments (Mariano, 1989a). The ThO_2

content of this variety is also higher than that observed in the rest of the samples (0.4-4.1 vs. 0.1-1.1 wt.%, respectively). The high levels of F in the examined samples attest to the F-rich nature of the fluids that deposited monazite in the unoxidized zone. The observed micro-textures (Figs. 5.30b, 5.32b) and the absence of a negative Ce anomaly in monazite from the oxidized zone (Fig. 6.18) indicate that it was deposited prior to cerianite.

Chondrite-normalized $(La/Ce)_{cn}$ ratios are lowest in the unoxidized parageneses and highest in the "Ox-Ca"subzone, whereas $(La/Nd)_{cn}$ ratios are highest in the transitional zone. A slight enrichment in MREE is observed in the transitional and oxidized zones relative to the unoxidized parageneses, which supports the textural evidence that these monazites likely formed during late stages of REE mineralization from a carbo-hydrothermal fluid. Monazite grains from all of the zones show two distinct chondrite-normalized patterns, one showing the typical enrichment in LREE, and the other that is comparatively more MREE-enriched. This difference is reflected in the "pivoting" of the chondrite-normalized profiles around Ce, and reflects variations in the availability of La and Ce relative to heavier lanthanides during the hydrothermal evolution of the Bull Hill rocks. Given the diversity of minerals making up the REE mineralization, it is impossible to identify the cause of these variations with certainty, but the most likely explanation is that another mineral phase was competing with monazite for the lightest lanthanides, producing convex-upward patterns of relative MREE enrichment in sample BL44, for example.

Cerianite is an oxide of tetravalent Ce found exclusively in the oxidized zone of the Bear Lodge deposit. It is associated with fluorocarbonates that may or may not show Ce depletion and with Ce-undepleted monazite. This provides evidence for two stages of fluorocarbonate formation in this supergene environment, i.e. prior to and after the oxidizing event that caused the deposition of minute cerianite crystals (Figs. 5.32-5.34). Because cerianite grains are too small for trace-element analysis by LA-ICP-MS, it is impossible to say how their crystallization affected the REE budget of other minerals beyond Ce.

10.2 Compositional Variation of REE Minerals and its Relation to the Evolution of Bull Hill Carbonatites

According to Zaitsev et al. (2002) and Zaitsev and Chakhmouradian (2002), progressive crystallization of REE minerals under hydrothermal conditions is accompanied by a decrease in their $(La/Nd)_{cn}$ ratio. Note that this observation does not necessarily apply to magmatic minerals. At Bull Hill, primary burbankite (sample T-684-L) does not show a consistent variation with respect to $(La/Nd)_{cn}$, whereas carbocernaite from sample BL71 shows an overall increase in $(La/Nd)_{cn}$ from the core rim-ward. In agreement with the interpretation of Zaitsev and Chakhmouradian (2002), hydrothermal ancylite from the burbankite paragenesis at Bull Hill has a lower $(La/Nd)_{cn}$ ratio than its associated primary burbankite, indicating that it crystallized from an evolved high-CO_2 fluid-dominated environment capable of removing Na from the burbankite.

The presence of Sr in a fluid expands the field of stability of ancylite because this element is not compatible in the structure of REE fluorocarbonates; however, the absence of bastnäsite-type hydrocarbonates and overall abundance of ancylite in the BLAC rocks strongly suggest a (carbo)hydrothermal nature of late-stage fluids involved in carbonatite alteration. Calcite from the REE flurocarbonate and REE fluorocarbonate-fluorite parageneses has higher Sr contents than calcite from the ancylite parageneses. The dissolution of earlier-formed burbankite and recrystallization of early calcite may have raised the REE and Sr contents in the fluids sufficiently to precipitate ancylite.

An overall decrease in $(La/Nd)_{cn}$ was documented in REE fluorocarbonates, particularly bastnäsite and parisite, from the fluorocarbonate-fluorite paragenesis to the fluorocarbonate and then ancylite-fluorocarbonate paragenesis, albeit with considerable overlap between the first two (Fig. 10.1). Considering the textural evidence, the range of values and clustering of fluorocarbonate compositions from different parageneses in the $(La/Ce)_{cn}$ vs. $(La/Nd)_{cn}$ diagram can be attributed to discrete phases of fluorocarbonate mineralization in stages that probably reflect chemical evolution of their parental fluid. The first to form were the fluorocarbonates that show $(La/Ce)_{cn}$ and $(La/Nd)_{cn}$ values similar to those in the primary burbankite and its replacement products in the fluorocarbonate paragenesis. Next was the fluorocarbonate-fluorite paragenesis, where the presence of fluorite indicates that its parental fluid reached fluorite-saturated conditions, as excess F in the system will precipitate fluorite with introduction of Ca (Williams-Jones et al., 2012).

Fluorocarbonates in the ancylite-fluorocarbonate paragenesis have lower $(La/Ce)_{cn}$ vs. $(La/Nd)_{cn}$ values than those from the other fluorocarbonate-bearing parageneses and formed simultaneously with, or after, ancylite as LREE fluoride complexes dissociated with decreasing temperatures (Williams-Jones et al., 2012). Fluorocarbonates from the transitional zone consistently plot in two clusters: one that overlaps, and the other with lower $(La/Nd)_{cn}$ values, than fluorocarbonates from the unoxidized zone. These differences clearly reflect co-existence of relict fluorocarbonates with newly formed fluorocarbonates overprinting the earlier mineralization. The lower $(La/Nd)_{cn}$ values in the latter imply lower crystallization temperatures in the transitional zone.

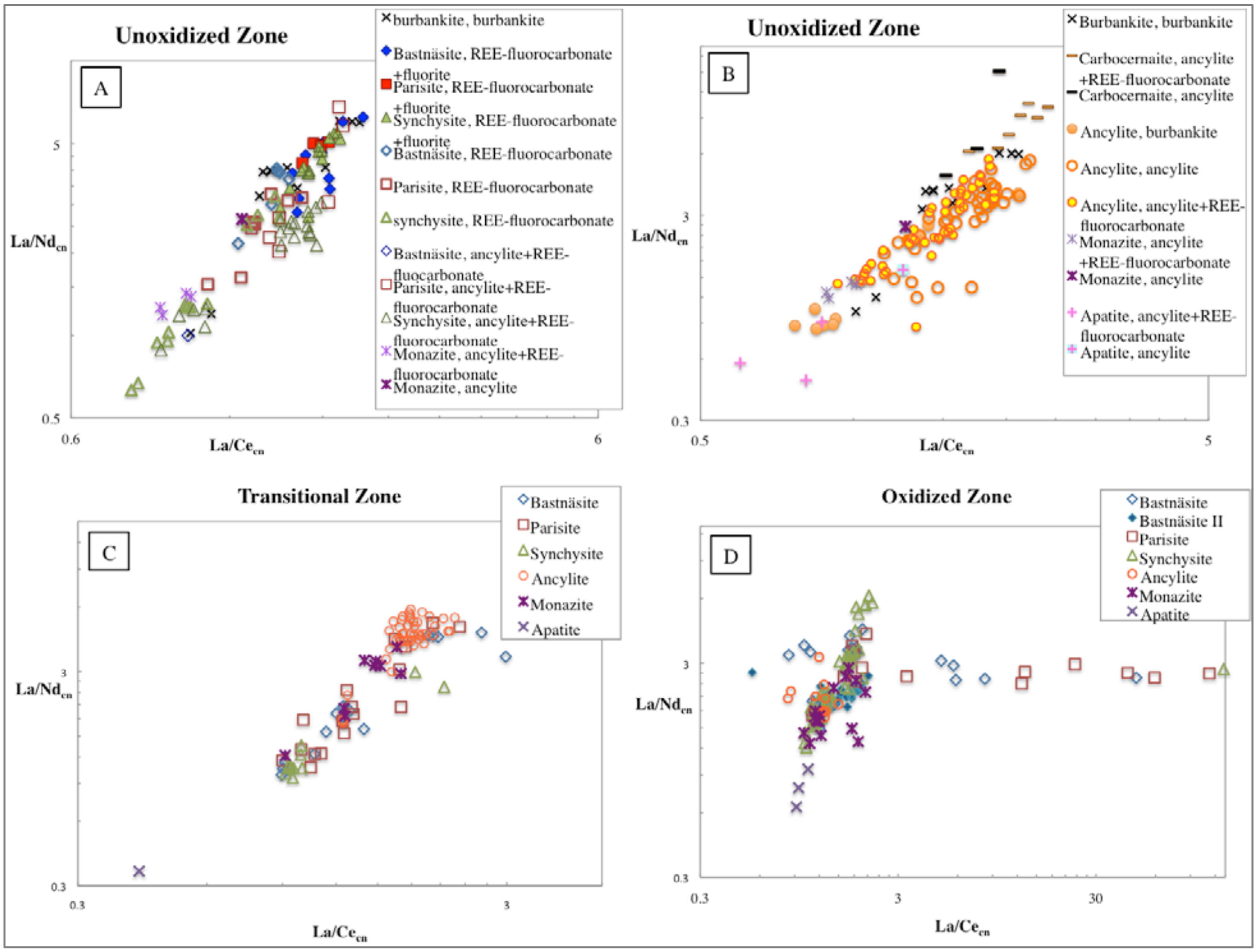

Figure 10.1. Summary (La/Ce)$_{cn}$ vs. (La/Nd)$_{cn}$ diagrams showing the compositional variation of A) fluorocarbonates, burbankite and monazite in the unoxidized zone; B) ancylite, burbankite, monazite and apatite in the unoxidized zone; C) fluorocarbonates, ancylite, monazite and apatite in the transitional zone; D) fluorocarbonates, ancylite, monazite and apatite in the oxidized zone. Minerals are grouped according to their host parageneses; symbols in the legend give the mineral name, then paragenesis, separated by a comma.

Ancylite compositions from the unoxidized zone show appreciable scatter in terms of their (La/Nd)$_{cn}$ and (La/Ce)$_{cn}$ values, with significant overlap among the three principal parageneses (Fig. 10.1). The lowest (La/Nd)$_{cn}$ and (La/Ce)$_{cn}$ ratios were recorded in ancylite replacing burbankite, whereas samples from the ancylite and ancylite-fluorocarbonate parageneses are enriched in La. Most compositions from the ancylite paragenesis cluster below the main trend, possibly indicating three separate crystallization episodes. The observed scatter suggests that fluids precipitating ancylite derived their REE not only from the primary burbankite, but also from other REE carriers, such as early calcite and fluorocarbonates. The compositions of ancylite from the transitional zone tend to plot at relatively high $(La/Nd)_{cn}$ and $(La/Ce)_{cn}$ values, whereas those from the oxidized zone at somewhat lower values, which may indicate preferential partitioning of La into associated minerals, such as the fluorocarbonates (Fig. 6.12).

Relative partitioning of Y and Ho provides insights into fluid compositions because these two elements have the same ionic radius and charge, but exhibit very different complexing characteristics (Bau, 1996). Ratios of Y/Ho give insight to fluid compositions because Y will preferentially form stable complexes with F to a greater extent than Ho; thus, interaction of an REE source with F-rich fluids will decouple Y from Ho and result in high Y/Ho values (e.g., Bühn et al., 2002). Holmium, in contrast, will preferentially complex with carbonate anions. These geochemical differences explain the positive Y anomaly and high Y/Ho values for fluorite, as well as the higher Y/Ho values for fluorocarbonates and fluorapatite in comparison with F-free ancylite (Fig. 10.2). Fluids that precipitated the ancylite had a lower F content than those that precipitated the fluorocarbonates and fluorapatite. This interpretation is supported by elevated Y/Ho values in F-bearing monazite from the Bull Hill diatreme. The genetic implications of Y/Ho variations in rock-forming and secondary calcite are discussed below.

10.3 Compositional Variation of Calcite in Fresh and Oxidized Carbonatites

Calcite from the different parageneses and zones shows significant variation in trace-element composition, and provides insights into the paragenetic sequence and chemical evolution of mineralizing fluids in the Bear Lodge deposit. Based on differences in chondrite-normalized profiles and key element ratios [$(La/Nd)_{cn}$, $(La/Yb)_{cn}$ and Y/Ho], five distinct generations of calcite were recognized in the present work. The analytical results from this study (unoxidized zone) are consistent with those presented by Olinger (2012), who related variations in REE distribution to calcite grain size. In the present work, these variations are interpreted to be controlled exclusively by the chemical evolution of carbonatitic fluids, which likely resulted in (re-)crystallization of calcite with varying grain size.

First generation calcite (calcite-1) shows negative-sloping chondrite-normalized REE patterns, with enrichment in LREE typical of primary carbonatitic calcite (Hornig-Kilsgaard, 1998). This primary calcite is only observed in the fluorocarbonate and fluorocarbonate-fluorite parageneses. Consistently high LREE and Sr contents supports the interpretation of calcite-1, calcite-2 and calcite 3 as early-crystallized phases, and indicates that calcite in the fluorocarbonate and fluorocarbonate-fluorite parageneses did not completely react with evolved carbonatite fluids.

Primary calcite from the BLAC has the highest $(La/Nd)_{cn}$ and $(La/Yb)_{cn}$ values of all five varities, also in agreement with its early crystallization prior to the secondary REE minerals. The high Y/Ho ratios indicate that early carbonatite fluids had high F contents (Bühn et al., 2002). The Sr values are lowest in calcite associated with carbocernaite in the burbankite paragenesis (BL71), likely reflecting multiple stages of alteration, which involved Sr removal from calcite-1 and burbankite, as well as preferential partitioning of this element into late-stage strontianite and ancylite relative to the late-stage calcite. The range of Sr values in the calcite samples is extremely variable, but in general, ancylite-bearing parageneses contain low-Sr calcite due to preferential partitioning of this element in ancylite and associated strontianite, and low affinity of fluorocarbonates for Sr.

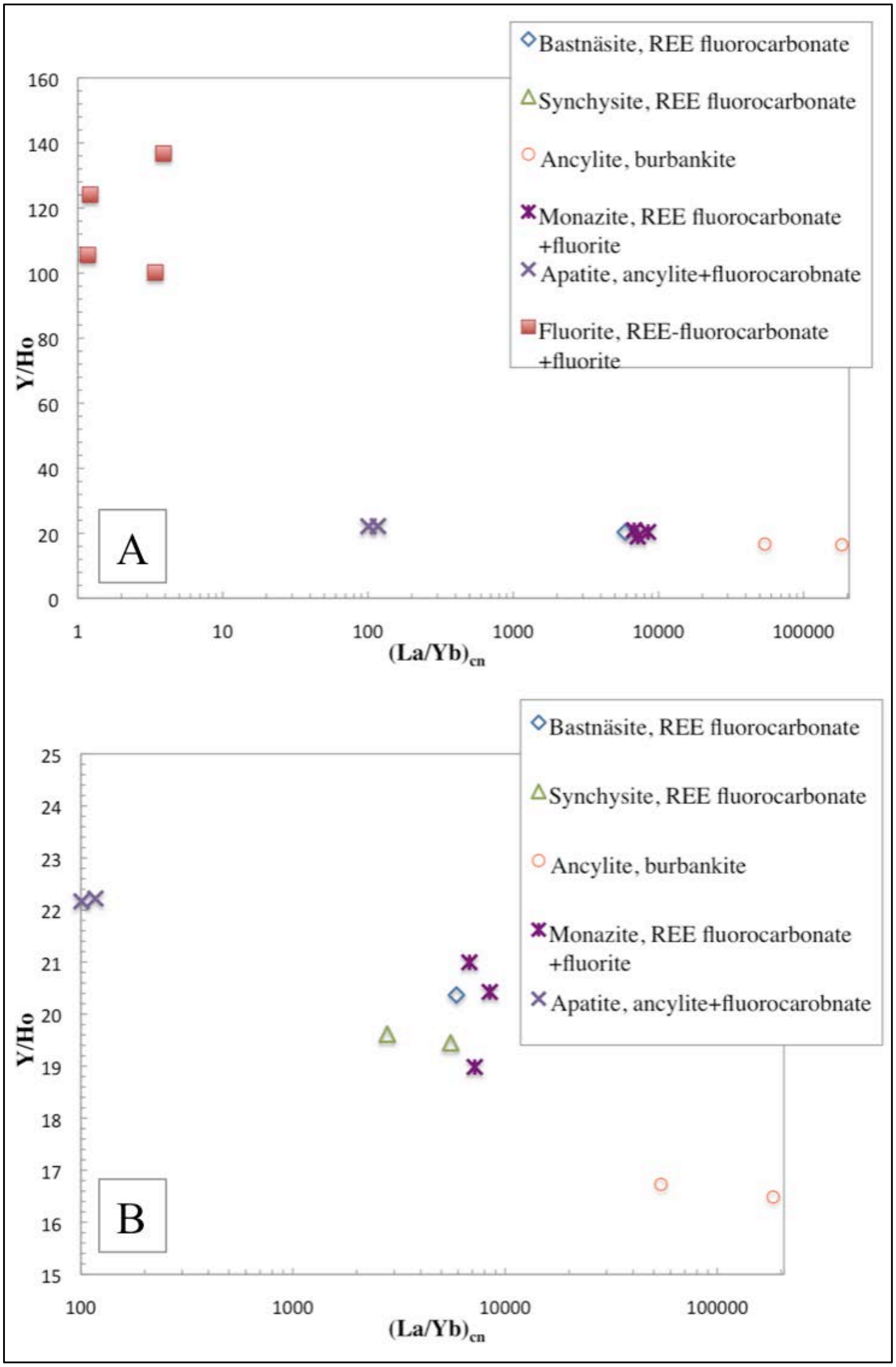

Figure 10.2. Variation in Y/Ho and chondrite-normalized (La/Yb)$_{cn}$ values of minerals from the unoxidized zone. Data from LA-ICP-MS analyses. A) REE minerals and fluorite. B) Detail of A) showing only REE minerals.

Second- and third-generation calcite shows progressive depletion in the LREE and corresponding enrichment in the MREE, and to a lesser extent, HREE. This trend is likely a result of LREE sequestration by ancylite, fluorocarbonates and subordinate monazite prior to the precipitation of second- and third-generation calcite at the expense of first-generation calcite, burbankite, carbocernaite and early fluorocarbonates. These data are in agreement with interpretations made by Olinger (2012). The decreasing $(La/Nd)_{cn}$ and $(La/Yb)_{cn}$ ratios in calcite indicate remobilization of the LREE, whereas the decrease in Y/Ho values possibly reflects a progressive increase in activity of carbonate complexes relative to fluoride species in the evolving fluid (cf. Bühn et al., 2002). Calcite-2 and -3 in the transitional zone are broadly similar in composition to calcite-2 and -3 from the unoxidized zone. The chondrite-normalized profiles of calcite-3 show more pronounced LREE depletion and MREE enrichment at variable HREE concentrations than calcite-3 from the unoxidized zone (Fig. 6.25). Manganese and Sr contents of calcite from the transitional zone are low, but overlap with the range of values of these elements in different calcite generations from the unoxidized zone (Fig. 6.26). Values of $(La/Nd)_{cn}$, $(La/Yb)_{cn}$ and Y/Ho ratios (Tables 6.9 and 6.10) are similar to those from the unoxidized samples.

Early calcite from the “Ox-Ca” subzone (Table 6.7) exhibits a variety of normalized REE profiles, from those similar to the patterns described above for calcite-1, -2 and -3, to LREE-depleted, MREE-enriched convex-upward (variety 4a) and HREE-enriched (4b) patterns not recorded in the unoxidized or transitional zones (Table 6.8; Fig. 6.27b). The HREE-enriched profile was observed in a single sample (BL147 described in section 6.8.7). Calcite grains with REE distributions similar to the earlier generations from the unoxidized and transitional zones are probably relict, whereas the LREE-depleted varieties crystallized after the deposition of

LREE-rich minerals (in particular, ancylite and some fluorocarbonates), but prior to the deposition of cerianite and Ce-depleted fluorocarbonates, as indicated by the lack of a Ce anomaly in the chondrite-normalized REE patterns of calcite-4. High Y/Ho values and the positive Y anomaly in early calcite from sample BL147 indicates that F was re-introduced into the fluid at this late stage of its evolution. The influx of F could be derived either from dissolution of the earlier-formed fluorocarbonates, fluorite and fluorapatite, or from an unknown external source. Because the values of $(La/Nd)_{cn}$ and Y/Ho in calcite-4 are within the range of calcite-1 from the fluorocarbonate paragenesis, and there is convincing textural evidence for the late-stage development of fluorocarbonates at the expense of earlier parisite and synchysite (see sections 5.2, 5.3 and 10.1), the most likely source of F was these latter minerals.

The latest generation of calcite to crystallize (calcite-5, Table 6.8 or late calcite from the "Ox-Ca" subzone, Table 6.7) has extremely low Mn concentrations and a pronounced negative Ce anomaly (Fig. 6.27). This calcite undoubtedly precipitated during the progressive oxidation of the Bull Hill carbonatites, as indicated by conversion of Mn^{2+} to Mn^{4+} and its sequestration in oxides (pyrolusite and ramsdellite), and removal of Ce^{4+} from the fluid as cerianite. This late calcite typically occurs in association with strontianite in barren carbonate veins. Calcite-5 from sample BL143 exhibits a MREE-enriched pattern similar to that in calcite-3, but with a small negative Ce anomaly. These variations imply that the redox processes controlled the trace-element budget of late-stage calcite. The presence of calcite with and without Ce anomalies in the "Ox-Ca" subzone indicates that the oxidation was not pervasive, which is further supported by C and O isotopic evidence presented below.

The $(La/Nd)_{cn}$ values in calcite generally decrease from calcite-1 in the fluorocarbonate-bearing parageneses to calcite-2 and calcite-3 in the other parageneses in the unoxidized and transitional zones, and then increase in the oxidized zone (Fig. 6.24). The $(La/Yb)_{cn}$ value is high (up to 412) for primary LREE-enriched crystals from the fluorocarbonate parageneses, drops to 1-3 in second- and third-generation calcite and then increases to > 170 in the latest generation. This late-stage depletion in HREE can be explained by removal of these elements by fluids into the peripheral parts of the deposit. Although minerals that normally concentrate HREE (e.g., xenotime, YPO_4) were not observed in this work, they have been previously reported at Whitetail Ridge, Carbon Hill and Taylor Ridge by Anderson et al. (2013b) and identified at Bull Hill by other unpublished studies (Clark, 2014 personal communications).

10.4 Trace-element Composition of Fluorite

Radiogenic isotopic data available for carbonatite-hosted fluorite deposits show that precipitation of fluorite in the hydrothermal environment involves the interaction of F-rich magmatic fluids either with Ca-rich wall-rocks or crustal fluids. This process also facilitates the development of late-stage rare-earth mineralization, owing to the breakdown of REE-F complexes as F is sequestered by Ca during fluorite crystallization (Simonetti and Bell, 1995; Bühn et al., 2003; Xu et al., 2012). Williams-Jones et al. (2012) showed that F plays some (probably subordinate to Cl) role in REE transport at high temperatures and low pH values, but acts as a REE-binding ligand facilitating precipitation of bastnäsite and other fluorocarbonates under decreasing temperatures or acidity. In carbonatite systems, fluorite crystallization occurs over a wide temperature range (from < 160 to 350 ºC: Alvin et al., 2004; Hou et al., 2009). The fluorocarbonate-fluorite assemblage is demonstrated to form at lower temperatures than the fluorocarbonate-calcite assemblage (Williams-Jones and Wood, 1992).

Fluorite in the Bull Hill carbonatites has REE levels and a chondrite-normalized profile similar to those in calcite-1 from the same sample, but shows a positive Y-anomaly. The documented variations in REE and Sr contents in the fluorite could indicate protracted crystallization from an evolving carbonatite system, but this is speculative at best because the available petrographic evidence is inconclusive. Values of Y/Ho, Ce/Ce*, and Eu/Eu* are relatively constant, whereas there is a larger spread in the $(La/Yb)_{cn}$ and $(La/Nd)_{cn}$ ratios, possibly arising from co-precipitation of the low-La fluorite with fluorocarbonates (Table 6.6; Appendix D). The four analyses have very similar chondrite-normalized profiles despite a significant difference in the abundances of individual REE.

In the absence of isotopic data for fluorite, the source of F at Bear Lodge remains problematic. Felsman (2009) presented evidence for late-stage replacement of primary LREE-enriched apatite in the silicate rocks by an F- and MREE-HREE-rich variety of apatite. This observation suggests that F and, to a lesser extent, REE may be derived from the dissolution of fluorapatite in silicate (trachytic) rocks in the BLAC, which reacted with carbonatite-derived fluids. It appears that the F complexes became unstable with decreasing alkalinity and loss of Na during the dissolution of primary burbankite to fenitization, as manifested by the precipitation of fluorocarbonates in preference to burbankite in the early stages of carbonatite evolution.

10.5 Stable Isotopic Variations

Stable isotopes are generally used to interpret evolutionary processes in carbonatite systems. Many authors agree that not all mantle-derived carbonatites have C and O isotopic compositions that plot in the PIC field (Taylor et al., 1967). Nevertheless, this box remains an important reference frame for discriminating between carbonatites and other petrographically similar rocks, and for tracking the evolution of individual carbonatite occurrences. The primary magmatic $\delta^{18}O_{V\text{-}SMOW}$ and $\delta^{13}C_{V\text{-}PDB}$ values of igneous carbonates can be affected by the following processes: (i) interaction with a fluid or fluids of different composition and potentially derived from a number of sources; (ii) Rayleigh fractionation due to precipitation of carbonate minerals from the magma; (iii) loss of volatiles; and (iv) assimilation of crustal material by carbonatitic magma (e.g. Deines, 1989; Santos and Clayton, 1995; Horstmann and Verwoerd, 1997; Onuonga et al., 1997; Demény et al., 2004; Nikiforov et al., 2006; Chakhmouradian et al., 2014).

The only Bull Hill sample that plots in the PIC field comes from the unoxidized fluorocarbonate paragenesis and is interpreted to have the least modified isotopic composition approaching that of primary carbonatitic magma. If the evolution of the carbonatite system started with the fluorocarbonate paragenesis, then progressed to the fluorocarbonate-fluorite paragenesis, as indicated by petrographic evidence described in sections 5.1.2 and 5.1.3 and discussed above, the slight enrichment in ^{18}O coupled with enrichment in ^{12}C requires explanation. In their study of Kola carbonatites (Russia), Demény et al. (2004) showed that late-stage carbonatites are invariably enriched in ^{18}O relative to early carbonatites from the same intrusion. Enrichment in both ^{13}C and ^{18}O enrichment is typically explained in terms of Rayleigh fractionation (Demény et al., 2004). In the Afrikanda carbonatite complex (Kola peninsula), enrichment in ^{18}O at nearly constant $\delta^{13}C_{V\text{-}PDB}$ values was interpreted as the result of interaction of a low-T, meteoric-hydrothermal fluid with a low CO_2:H_2O ratio with the carbonatite (e.g., Zaitsev and Chakhmouradian, 2002). Oxygen isotopic compositions in most BLAC samples from the unoxidized and transitional zones are not significantly different from the PIC mantle values. The slight increase in $\delta^{18}O_{V\text{-}SMOW}$ likely results from hydrothermal alteration of the carbonatites at low CO_2:H_2O and fluid-to-rock ratios. The observed variation in isotopic ratios reflects progressive evolution of the fluid during the metasomatic alteration. This interpretation is supported by the documented changes in the mineralogy of polymineralic pseudomorphs (Chapter 5) and the distinctive compositions of multiple generations of calcite (Chapter 6).

Variations in $\delta^{13}C_{V\text{-}PDB}$ values can arise from interaction of carbonatites with non-igneous carbonate rocks such as limestone (typically manifested in increasing $\delta^{13}C_{V\text{-}PDB}$ values), interaction with CO_2-rich vapors or fluids (atmospheric or magmatic), degassing and loss of ^{13}C during decompression, or an increase in F in the evolving carbonatitic system (Santos and Clayton, 1995; Pearce et al., 1997, Demény et al., 2004; Chakhmouradian et al., 2014). Demény et al. (2004) related buildup of ^{12}C (i.e., decreasing $\delta^{13}C_{V\text{-}PDB}$ values) to degassing, which is the process that could also explain the negative shift in the $\delta^{13}C_{V\text{-}PDB}$ values of some Bull Hill carbonatites from the unoxidized and transitional zones. Degassing is supported by the vuggy texture of these samples (locally up to 50 vol. %, particularly in the pseudomorphs). Note that, in the present case, degassing was probably a hydrothermal, rather than magmatic, process related to dissociation of the early-crystallizing carbonate minerals (predominantly, burbankite). Alternatively, Pearce et al. (1997) suggested that a high F content facilitates preferential retention of ^{12}C and ^{18}O in carbonatite melts based on their study of the Grønnedal-Íka complex (Greenland). This process could explain the trend of light-C and heavy-O enrichment ($\delta^{13}C_{V\text{-}PDB} < -8‰$; $\delta^{18}O_{V\text{-}SMOW} > 9‰$) linking the fluorocarbonate and fluorocarbonate-fluorite parageneses (Fig. 8.1). It is impossible to estimate the relative contribution of degassing and F effect to the C-O isotopic budget in the other samples from the unoxidized and transitional zones, because all of them contain mineralogical evidence for both F enrichment and carbonate dissociation.

Low $\delta^{13}C_{V\text{-}PDB}$ values, such as those presented in the present study, may be a primary mantle-derived signature resulting either from incorporation of ^{12}C-rich recycled crustal material in the mantle source of carbonatites, or C-fractionation in that source (Chakhmouradian et al., 2008). These authors noted that many post-orogenic carbonatites situated near ancient subduction zones (e.g., Eden Lake in Canada, Dalucao in China and In'Ouzzal in Algeria) exhibit anomalously low $\delta^{13}C_{V\text{-}PDB}$ values outside the PIC range (≤ -8‰). For example, early carbonatites from In'Ouzzal cover essentially the same range of C-O compositions as the unoxidized Bull Hill rocks studied in the present work (Ouzegane et al., 1988; cf. Fig. 8.1). This alternative interpretation of the relative depletion of the Bear Lodge carbonatites in ^{13}C as a result of a post-orogenic tectonic setting is consistent with very low levels of HFSE in these rocks. In common with arc silicate magmas, HFSE depletion in carbonatites is interpreted as evidence of the presence of a refractory HFSE host in their mantle source (Chakhmouradian et al., 2008; Xu et al., 2011). Notably, other post-orogenic carbonatites also exhibit depletion in HFSE, but are enriched in LREE, sometimes to economic levels (Chakhmouradian and Zaitsev, 2012). The new evidence from radiogenic Sr, Nd and Pb isotopes discussed below lends further support to the post-orogenic model.

In the transitional zone, a positive shift in both $\delta^{18}O_{V\text{-}SMOW}$ and $\delta^{13}C_{V\text{-}PDB}$ values with a slope close to the idealized Rayleigh fractionation trend (~0.4; Deines, 1989) is observed from vein to groundmass calcite in sample BL25, and from the cluster of samples unaffected by oxidation toward calcite from the transitional zone. This shift may indicate progressive enrichment in ^{18}O and, to a lesser extent, ^{13}C due to fractionation of carbonate minerals, or due to isotopic re-equilibration via fluid-rock interaction at advanced stages of carbo-hydrothermal activity. The same trend is observed for calcite from an altered pseudomorph in sample BL63 from the unoxidized zone, providing further evidence that the pseudomorphization of burbankite involved its interaction with evolving carbo-hydrothermal fluids.

Enrichment in $\delta^{18}O_{V\text{-}SMOW}$ without appreciable change in $\delta^{13}C_{V\text{-}PDB}$ is typically related to subsolidus processes, such as a progressive decrease in the CO_2:H_2O ratios via exchange of igneous carbonates with ^{18}O-rich meteoric or low-temperature crustal fluids, or with juvenile fluids that evolved to high^{18}O levels under decreasing temperature (Deines, 1989). The positive shifts in $\delta^{18}O_{V\text{-}SMOW}$ in samples BL138 and BL44 from the oxidized zone, associated with significant changes in mineralogy and mineral chemistry, are interpreted as evidence of supergene oxidation and isotopic exchange with late-stage, low-temperature fluids that likely equilibrated with ^{18}O-enriched meteoric waters near the surface. A different trend is shown by samples BL143 (ancylite-fluorocarbonate-bearing) and BL40 (fluorocarbonate-monazite-bearing) from the oxidized zone, showing enrichment in both ^{18}O and ^{13}C (Fig. 8.1). The absence of intermediate compositions and very high $\delta^{13}C_{V\text{-}PDB}$ and $\delta^{18}O_{V\text{-}SMOW}$ values (ca. –3‰ and 17‰, respectively) are difficult to reconcile with any of the well-known mechanisms that could explain simultaneous enrichment of oxidized material in light C and heavy O. Clearly, simple interaction with a meteoric fluid could not raise the $\delta^{13}C_{V\text{-}PDB}$ value by several per mil, and additional data are required to outline the isotopic exchange trend related to oxidation processes more accurately.

10.6 Sources of Bear Lodge Carbonatites: Evidence from Radiogenic Isotopes

Very few radiogenic isotopic data are available for the BLAC. About a dozen paired Sr-Nd analyses referred to simply as “Black Hills” were plotted in a summary diagram for the Great Plains Alkaline Province by Duke (2009, her Fig. 3), but these data were not grouped by locality or rock type, and the actual isotopic abundances and ratios have not been published in peer-reviewed literature to date. As shown in the previous literature (e.g., Tilton et al., 1998; Bell and Tilton, 2001; Xu et al., 2011), Sr-Nd isotopic ratios are insufficient for discriminating among carbonatites derived from dundamentally different sources and emplaced inn different tectonic settings. For this reason, in the present work, the Pb isotopic compositions were measured in addition to the Sr and Nd measurements to facilitate comparison with the published data for other carbonatites.

As shown in the εNd vs. $(^{87}Sr/^{86}Sr)_i$ diagram (Fig. 9.1), the BLAC data plot close to those from natrocarbonatites derived from Oldoinyo Lengai, a volcano which has recently extruded carbonatite magmas in the East African Rift. Bell and Simonetti (1996) explained the variations in the East African carbonatites to result from the modification of subcontinental lithosphere (EM1 component) by a mantle plume (HIMU component). Evidence for mantle plume activity includes isotopic similarities to OIB and the association of the African carbonatites with continental flood basalts (Bell and Tilton, 2001). Late-Mesozoic carbonatites from Brazil (Jacupiranga) and India (Amba Dongar) also plot along the East African Carbonatite Line (EACL) and are associated with flood basalts, but show the involvement of a mantle component strongly enriched in radiogenic Sr that was interpreted as EM2 (Veena et al., 1998; Gomes and Comin-Chiaramonti, 2005). The sources of Jacupiranga and Amba Dongar carbonatites are interpreted to be less modified by mantle plume activity, based on the relative contribution of the HIMU component to their isotopic budget (Veena et al., 1998; Gomes and Comin-Chiaramonti, 2005).

Although the εNd and $(^{87}Sr/^{86}Sr)_i$ values of the BLAC carbonatites are similar to many other carbonatites (Fig. 9.1A), the εNd vs. $(^{206}Pb/^{204}Pb)$ or the $(^{206}Pb/^{204}Pb)$ vs. $(^{208}Pb/^{204}Pb)$ diagrams (Figs. 9.1B, C) indicate the source had a DMM rather than an HIMU contribution. Importantly, the lack of a HIMU contribution clearly indicates that the source of the Bull Hill carbonatites was not associated with a deep sublithospheric mantle reservoir such as a mantle plume (diaper), as suggested by Duke (2009). The lack of Pb isotopic data for most of the localities mentioned in Chapter 2, including those in close spatial proximity to Bear Lodge (e.g., Missouri Breaks and Bearpaw Mountains in Montana), does not allow for a detailed comparison. The Pb data from carbonatites in the Himalayan collision zone (Pakistan and China) are similar to those presented in this thesis (Xu et al., 2003, 2004; Tilton et al., 1998). Of particular importance is the lack of any evidence for mantle plume contribution and involvement of the DMM reservoir in the generation of carbonatitic magma.

In Pakistan, carbonatites formed in pre- and syn-orogenic settings differ in their isotopic signature. Although both plot close to the EACL in εNd vs. $(^{87}Sr/^{86}Sr)_i$ diagrams, syn-orogenic carbonatites have negative εNd values and plot near EM1, whereas pre-orogenic carbonatites have positive εNd values and plot closer to FOZO (Tilton et al., 1998). The Pb isotopic data for these carbonatites show contributions from both the DMM and EM2 components (Tilton et al., 1998). Postorogenic carbonatites from the Lesser Qinling Mountains in China are isotopically equivalent to EM1 and also lack any HIMU component (Xu et al., 2011). Their unusual composition was explained in terms of re-equilibration of the sublithospheric mantle with lower-crustal material delaminated after the compressional phase of the Qinling orogeny, and with fluids derived from old recycled crust (Xu et al., 2014). The Maoniuping carbonatite (China), also emplaced in a collisional zone, largely follows a trend from EM1 to EM2 (+ minor DMM), which was interpreted to arise from metasomatism of an ill-defined anomalous mantle source (representing EM2) by deep mantle fluids. This mantle source upwelled and metasomatized the EM1-type lithosphere during the transition from a transpressional to transtensional regime, and gave rise to, carbonatite magmatism with the Pb isotopic signatures described above (Xu et al., 2004).

When it comes to comparative analysis and interpretation of the Bear Lodge data in a tectonic context, the major problem is the lack of consensus on what the EM1 and EM2 reservoirs actually represent. For example, previously published interpretations of EM1 range from a near-primary lower-mantle source, to recycled lower crust or lithosphere, to upper-mantle rocks metasomatized by CO_2-rich fluids, to mixtures of HIMU with ancient oceanic crust, to cumulate rocks associated with mantle-plume heads (Hawkesworth et al., 1984; Zindler and Hart, 1986; Chauvel et al., 1992; Roden et al., 1994; Moreira et al., 1999; Gasperini et al., 2000). Xu et al. (2011) proposed that an EM1-type carbonatite reservoir may be generated through the recycling of subducted crust over a long period of time. If the Wyoming cratonic basement crust contains some recycled component with a high carbonate content and EM1-type signature (Chapter 2), it could hypothetically provide the metasomatizing agent to react with previously enriched SCLM beneath this part of the Wyoming craton, and could explain the involvement of both EM1 and EM2-type sources. Alternatively, the Bull Hill carbonatites could be derived from a single, enriched mantle component showing higher $(^{87}Sr/^{86}Sr)_i$, εNd and $^{206}Pb/^{204}Pb$ ratios than the “conventional” EM1 component, but appreciably lower than EM2. This enriched mantle source is most likely to be the subducted and metasomatized Farallon crust, as indicated by the isotopic signature (Sr-Nd-Pb) of eclogite xenoliths recovered from ~30 Ma diatremes on the Colorado Plateau (Fig. 9.1; Usui et al., 2006).

Ultramafic xenoliths from the Montana alkaline province, which represent fragments of mantle-derived rocks generated in a very similar tectonic regime (i.e. in the SCLM affected by subduction of the anomalously thick Farallon plate), are interpreted to originate from ancient, metasomatized subcratonic lithosphere. Given the tectonic and structural framework presented in Chapter 2, which demonstrates that the subcratonic lithosphere in the study area underwent several episodes of LILE enrichment and HFSE depletion, the strong LILE-LREE enrichment of the Bear Lodge carbonatites, coupled with their depletion in HFSE, indicates that their parental magmas were generated by low-degree partial melting of a SCLM source fertilized by subduction-related melts (or fluids). The isotopic evidence from the present study clearly points to a DMM-like mantle source that was modified by contributions from the subducted Farallon slab (Usui et al., 2006; Fig. 9.1). The trace-element geochemistry and C isotopic signature of the examined rocks support this interpretation.

Chapter 11. Conclusions

On the basis of petrographic, mineralogical, geochemical, and isotopic evidence from carbonatites in the BLAC presented above, the following conclusions can be drawn.

The REE enrichment in the Bull Hill deposit is probably derived from partial melting of a fertile metasomatized mantle source related to the low-angle Eocene subduction of the Farallon plate beneath the Wyoming craton (postulated in the earlier-published work). The protracted evolution of the carbonatite system, involving magmatic, hydrothermal, and supergene stages, is responsible for the diversity of mineral parageneses identified in the present work, and for the concentration of LREE to potentially economic levels in minerals amenable to rare earth recovery (e.g., REE fluorocarbonates and monazite).

Geochemical characteristics of the BLAC carbonatites are consistent with a source enriched in LILE and LREE, but strongly depleted in HFSE. This geochemical signature was reported previously for the lithospheric sources of alkaline magmatism in the Great Plains Alkaline Province of the USA and southwestern Canada (Chapter 2). Both LILE enrichment and HFSE depletion are consistent with a metasomatized mantle source modified by subduction-related processes.

The consistent Sr-Nd-Pb isotopic composition of the Bull Hill carbonatites can be explained in terms of metasomatic modification of the Wyoming SCLM by material derived from the subducted Farallon slab. This metasomatized source represents a mixture of the DMM reservoir with an enriched slab component. The Pb isotopic data show no evidence that the source of BLAC magmas was affected by mantle-plume activity.

Variations in the C and O isotopic compositions of the Bull Hill carbonatites show that the development of the Bear Lodge deposit commenced with magmatic crystallization, followed by interaction of the primary carbonate minerals with F-rich hypogene carbo-hydrothermal fluids at decreasing temperature. Prolonged fluid-rock interaction and influx of meteoric water led to lower CO_2:H_2O ratios and enrichment of the system in ^{18}O.

Evolution of the carbonatite system involved at least six mineralization events, which produced distinct parageneses comprising minerals with consistent compositional variations in the unoxidized, transitional and oxidized zones of the Bear Lodge deposit. The early carbonatites crystallized from a magma enriched in alkali elements, Sr, Ba, REE and F, but depleted in Nb and other HFSE. These carbonatites underwent polyphase alteration involving (carbo)hydrothermal fluids derived from the carbonatite magma and meteoric fluids.

Burbankite $[(Ca,Na)_3(Sr,REE,Ca,Ba)_3(CO_3)_5]$, REE fluorocarbonates, LREE-enriched calcite and fluorapatite were early-forming phases that precipitated from the carbonatite magma. These minerals were primary hosts for the REEas indicated by the stable-isotopic and trace-element compositions of these minerals.

The fluorocarbonate-fluorite paragenesis precipitated after the fluorocarbonate paragenesis as polymineralic pseudomorphs after burbankite. The replacement was accompanied by Na loss, as indicated by the vuggy nature and absence of Na minerals in the pseudomorphs. Rare-earth elements and Ca released from the precursor burbankite were sequestered in hydrothermal synchysite and parisite, Sr in strontianite, and Ba in barite. The trace-element composition of fluorite indicates that it co-crystallized with the LREE-enriched fluorocarbonates. Three compositionally distinct varieties of calcite occur in the fluorocarbonate-fluorite paragenesis, providing evidence for multiple stages of hydrothermal REE mineralization.

The ancylite paragenesis also formed at the expense of burbankite prior to the ancylite-fluorocarbonate paragenesis. Ancylite precipitated from fluids that were F-depleted after the early precipitation of fluorocarbonates and fluorite. Ancylite and associated minerals were deposited at lower temperature and CO_2:H_2O fluid ratios than the early fluorocarbonates.

The regular occurrence of Sr- and F-enriched REE minerals with barite and strontianite indicate that Sr, Ba and F were conserved in the system and facilitated development of REE mineralization, dominated by ancylite with lesser REE fluorocarbonates in the unoxidized zone.

Interaction of the hydrothermal fluids circulating in the unoxidized and transitional zones of the deposit with apatite-bearing wall-rock or detrital apatite in sediments of the Deadwood Formation enriched the system in phosphate, facilitating crystallization of monazite at the expense of the earlier-crystallized ancylite at the late stages of hydrothermal activity.

Variations in mineral compositions and complex textural relationships documented in samples from the transitional zone indicate incipient changes in oxygen fugacity and remobilization of REE from the earlier-crystallized minerals (ancylite, in particular) to form parisite, bastnäsite and monazite.

In the latest stages of deposit evolution, pervasive oxidation of the carbonatites was driven initially by hydrothermal, followed by supergene processes, as the relative contribution of meteoric fluid increased. These processes resulted in concentration of REE in the oxidized zone, as manifested by late-stage crystallization of bastnäsite (and, to a lesser extent, other REE fluorocarbonates), monazite and cerianite. The fluorocarbonates are the most abundant REE phases in the oxidized zone, followed by monazite. Cerianite is the principal host for Ce^{4+}.

References

Alvin, M.P., Dunphy, J.M. & Groves, D.I. (2004). Nature and genesis of a carbonatite-associated fluorite deposit at Speewah, East Kimberley region, Western Australia. *Mineralogy and Petrology*, 80, 127-153.

Anders, E. & Grevesse, N. (1989). Abundances of the elements: Meteoric and solar. *Geochimica et Cosmochimica Acta*, 53, 197-214.

Anderson, A.K., Cosca, M.A. & Larson, P.B., (2013a). Timing of carbonatite magmatism in the Bear Lodge alkaline complex. *Geological Society of America Program with Abstracts*, 45, 499.

Anderson, A.K., Van Rythoven, A.D., Clark, J.G. & Larson, P.B. (2013b). Variations in economic REE distribution at the Bear Lodge deposit, Wyoming. *Geological Society of America Program with Abstracts*, 45, 500.

Bau, M. (1996). Controls on the fractionation of isovalent trace elements in magmatic and aqueous systems: Evidence from Y/Ho, Zr/Hf, and lanthanide tetrad effect. *Contributions to Mineralogy and Petrology*, 123, 323-333.

Bell, K. (1998). Radiogenic isotope constraints on relationships between carbonatites and associated silicate rocks—a brief review. *Journal of Petrology*, 39, 1987-1996.

Bell, K. & Blenkinsop, J. (1989). Neodymium and strontium isotope geochemistry of carbonatites. *In* Carbonatites, Genesis and Evolution (K. Bell, ed.) Unwin Hyman, London, U.K., 278-300.

Bell, K., Kjarsgaard, B.A., & Simonetti, A. (1998). Carbonatites—into the twenty-first century. *Journal of Petrology*, 39, 1839-1845.

Bell K., & Simonetti A. (1996). Carbonatite magmatism and plume activity: implications from the Nd, Pb and Sr isotope systematics of Oldoinyo Lengai. *Journal of Petrology*, 37, 1321-1329.

Bell, K. & Tilton, G.R. (2001). Nd, Pb and Sr isotopic compositions of east African carbonatites: Evidence for mantle mixing and plume inhomogeneity. *Journal of Petrology*, 42, 1927-1945.

Belovitskaya, Y.V. & Pekov, I.V. (2004). Genetic mineralogy of the burbankite group. *New Data on Minerals*, 39, 50-64.

Berger, A., Gnos, E., Janots, E., Fernandez, A. & Giese, J. (2008). Formation and composition of rhabdophane, bastnäsite and hydrated thorium minerals during alteration: Implications for geochronology and low-temperature processes. *Chemical Geology*, 254, 238-248.

Bird, P. (1984). Laramide crustal thickening event in the Rocky Mountain foreland and Great Plains. *Tectonics*, 3, 741-758.

Bird, P. (1988). Formation of the Rocky Mountains, Western United States: A continuum computer model. *Science*, 239, 1501-1507.

Bird, P. (1998). Kinematic history of the Laramide orogeny in latitudes 35°-49°N, western United States. *Tectonics*, 17, 780-801.

Blundy, J.D. & Wood, B.J. (2003). Partitioning of trace elements between crystals and melts. *Earth and Planetary Science Letters,* 201, 383-397.

Breitsprecher, K., Thorkelson, D.J., Groome, W.G. & Dostal, J. (2003). Geochemical confirmation for the Kula-Farallon slab window beneath the Pacific Northwest in Eocene time. *Geology*, 31, 351-354.

Buhlmann, A. L., Cavell, P., Burwash, R.A., Creaser, R.A. & Luth, R.W. (2000). Xenoliths from the Milk River area, Southern Alberta: records of a complex history of the northernmost part of the Arechan Wyoming craton. *Canadian Journal of Earth Sciences*, 37, 1629-1650.

Bühn, B., Rankin, A.H., Radtke, M., Haller, M. & Knöchel, A. (1999). Burbankite, a (Sr,REE,Na,Ca)-carbonate in fluid inclusions from carbonatite-derived fluids: Identification and characterization using Laser Raman spectroscopy, SEM-EDX, and synchotron micro-XRF analysis. *American Mineralogist*, 84, 1117-1125.

Bühn, B.,Wall, F., & Le Bas, M.J. (2001). Rare-earth element systematics of carbonatite fluorapatites, and their significance for carbonatite magma evolution. *Contributions to Mineralogy and Petrology*, 141, 572-591.

Bühn, B., Rankin, A. H., Schneider, J. & Dulski, P. (2002). The nature of orthomagmatic, carbonatitic fluids precipitating REE, Sr-rich fluorite: fluid-inclusion evidence from the Okorusu fluorite deposits, Nambia. *Chemical Geology*, 186, 75-98.

Bühn, B., Schneider, J., Dulski, P. & Rankin, A.H. (2003). Fluid-rock interaction during progressive migration of carbonatitic fluids, derived from small-scale trace element and Sr, Pb isotope distribution in hydrothermal fluorite. *Geochimica et Cosmochimica Acta*, 67, 4577-4595.

Bulakh A.G., Nesterov A.R., Zaitsev A.N., Pilipiuk N., Wall F. & Kirillov A.S. (2000). Sulfur-containing monazite-(Ce) from late-stage mineral assemblages at the Kandaguba and Vuoriyarvi carbonatite complexes, Kola peninula, Russia. *Neues Jahrbuch fuer Mineralogie Monatschefte*, 2000, 217-233.

Bunge, H.P. & Grand, S.P. (2000). Mesozoic plate-motion history below the northeast Pacific Ocean from seismic images of the subducted Farallon slab. *Nature*, 405, 337-340.

Burt, D.M. (1989). Compositional and phase relations among rare earth element minerals. *In* Geochemistry and Mineralogy of Rare Earth Elements (B.R. Lipin & G.A. McKay, eds.), Reviews in Mineralogy, Mineralogical Society of America, 21, 259-307.

Castor, S.B. & Hedrick, J.B. (2006). Rare earth elements. *In* Industrial Minerals & Rocks: Commodities, Markets, and Uses (J.E. Kogel, N.C. Trivedi, J.B. Barker & S.T. Krukowski, eds.), Society of Mining, Metallurgy, and Exploration, 769-788.

Chakhmouradian, A.R. (2006). High-field-strength elements in carbonatitic rocks: Geochemistry, crystal chemistry and significance for constraining the sources of carbonatites. *Chemical Geology*, 235, 138-160.

Chakhmouradian, A.R. & Mitchell, R.H. (1998). Lueshite, pyrochlore and monazite-(Ce) from apatite-dolomite carbonatite, Lesnaya Varaka complex, Kola. *Mineralogical Magazine*, 62, 769-782.

Chakhmouradian, A.R., Mumin, A.H., Demény, A. & Elliott, B. (2008). Postorogenic carbonatites ad Eden Lake, Trans-Hudson Orogen (northern Manitoba, Canada): Geological setting, mineralogy, and geochemistry. *Lithos*, 103, 503-526.

Chakhmouradian, A.R., Reguir, E.P., Kressall, R.D., Crozier, J., Pisiak, L.K., Sidhu, R. & Yang, P. (2014). Carbonaitte-hosted niobium deposit at Aley, northern British Columbia (Canada): Mineralogy, geochemistry and petrogenesis. *Ore Geology Reviews, in press.*

Chakhmouradian, A.R. & Wall, F. (2012). Rare Earth Elements: Minerals, mines, magnets (and more). *Elements*, 8, 333-340.

Chakhmouradian, A.R. & Zaitsev, A.N. (2012). Rare earth mineralization in igneous rocks: sources and processes. *Elements*, 8, 347-353.

Chauvel, C., Hofmann, A.W. & Vidal, P. (1992). HIMU-EM: the French Polynesian connection. *Earth and Planetary Science Letters*, 110, 99-119.

Clark, A.M. (1989). Mineralogy of the rare earth elements. *In* Rare earth element geochemistry, (P. Henderson, ed.), Developments in Geochemistry 2. Elsevier, Amsterdam, 33-54.

Clark, J.G. (2009). Geology and exploration of the Bear Lodge REE property, Wyoming. Oral presentation, Technical Session: Rare earths – geology, deposits, and economic assessment. SME Annual Meeting, Denver, Colorado.

Cooper, A.F. & Paterson, L.A. (2008). Carbonatites from a lamprophyric dyke-swarm, South Westland, New Zealand. *Canadian Mineralogist*, 46, 753-757.

Cox, C. (2009). Competing with China in rare earth exploration and production. Oral Presentation, Technical Session: China's impact on industrial minerals. SME Annual Meeting, Denver, Colorado.

Dal Negro, A., Rossi, G.& Tassoli, V. (1975). The crystal structure of ancylite, $(RE)_x(Ca,Sr)_{2-x}(CO_3)_2(OH)_x(2-x)H_2O$. *American Mineralogist*, 60, 280-284.

DeCelles, P.G. & Coogan, J.C. (2004). Regional structure and kinematic history of the Sevier fold-and-thrust belt, central Utah. *Geological Society of America Bulletin*, 118, 841-864.

Deines, P. (1989). Stable isotope variations in carbonatites. *In* Carbonatites, Genesis and Evolution (K. Bell, ed.). Unwin Hyman, London, U.K., 301-359.

Demény, A., Sitnikova, M.A. & Karchevsky, P.I. (2004). Stable C and O isotope compositions of carbonatite complexes of the Kola Alkaline Province: phoscorite-carbonatite relationships and source compositions. *In* Phoscorites and Carbonatites from Mantle to Mine: the Key Example of the Kola Alkaline Province. (F. Wall & A.N. Zaitsev, eds.), Mineralogical Society of Great Britain & Ireland, Cambridge, 407-429.

Donnay, G. & Donnay J.D.H. (1953). The crystallograpyhy of bastnaesite, parisite, roentgeninte, and synchysite. *American Mineralogist*, 38, 932-963.

Doroshkevich, A.G., Ripp, G.S., Viladkar, S.G. & Vladykin, N.V. (2008). The Arshan REE carbonatites, southwestern Transbaikalia, Russia: Mineralogy, paragenesis and evolution. *Canadian Mineralogist*, 46, 807-823.

Dostal, J., Breitsprecher, K., Church, B.N., Thorkelson, D. & Hamilton, T.S. (2003). Eocene melting of Precambrian lithospheric mantle: Analcime-bearing volcanic rocks from the Challis—Kamloops belt of south central British Columbia. *Journal of Volcanology and Geothermal Research*, 126, 303-326.

Dudas, F.Ö. (1991). Geochemistry of igneous rocks from the Crazy Mountains, Montana, and tectonic models for the Montana Alkalic Province. *Journal of Geophysical Research*, 96, 13,261-13,277.

Dudas, F.Ö. & Harlan, S.S. (1999). An ancient depleted mantle sample from a 42-Ma dike in Montana: constraints of persistence of the lithosphere during Eocene magmatism. *Journal of Geology*, 107, 287-299.

Duke, G.I., (2005). Geochemistry and geochronology of Paleocene–Eocene alkalic igneousrocks, northern Black Hills, South Dakota and Wyoming. Ph.D. dissertation, Rapid City, South Dakota School of Mines and Technology, 291 p.

Duke, G.I. (2009). Black Hills-Alberta carbonatite-kimberlite linear trend: Slab edge at depth? *Tectonophysics*, 464, 186-194.

Duke, G.I. and Frost, C.D. (2013). Rattlesnake Hills and Bear Lodge Mountains carbonatite-alkalic igneous complexes, WY: REE's and other trace-element geochemistry. *Geological Society of America Program with Abstracts*, 45, 499.

Duke, G.I., Singer, B.S. & DeWitt, E. (2002). ^{40}Ar/^{39}Ar laser incremental-heating ages of Devil's Tower and Paleocene-Eocene intrusions of the northern Black Hills, South Dakota and Wyoming. Geological Society of America Annual Meeting (Denver, USA). Abstracts, paper 207-7.

Dunworth, A.E. & Bell, K. (2001). The Turiy massif, Kola peninsula, Russia: isotopic and geochemical evidence for multi-source evolution. *Journal of Petrology*, 42, 377-405.

Evensen, N.M., Hamilton, P.J. & O'Nions, R.K. (1978). Rare-earth abundances in chondritic meteorites. *Geochimica et Cosmochimica Acta*, 42, 1199-1212.

Feeley, T.C. (2003). Origin and tectonic implications of across-strike geochemical variations in the Eocene Abaroka Volcanic Province, United States. *Journal of Geology*, 111, 329-346.

Felsman, J.M. (2009). Geology, Hydrothermal Alteration, and Gold – Telluride Mineralization in the vicinity of Carbon Hill and Taylor Ridge, Bear Lodge Mountains, Crook County, Wyoming. M.Sc. Thesis, University of Idaho, 202 p.

Frost, R.L., Xi, Y., Sholz, R. & Tazava, E. (2013). Spectroscopic characterization of the phosphate mineral florencite-La – $LaAl_3(PO_4)_2(OH, H_2O)_6$, a potential tool in the REE mineral prospection. *Journal of Molecular Structure*, 1037, 148-153.

Gasperini, D., Blichert-Toft, J., Bosch, D., Del Moro, A., Macera, P. & Telouk, P. (2000). Evidence from Sardinian basalt geochemistry for recycling of plume heads into the Earth's mantle. *Nature*, 408, 701-704.

Gomes, C.B. & Comin-Chiaramonti, P. (2005). Some notes on the Alto Paranaíba Igneous Province. *In* Mesozoic to Cenozoic Alkaline Magmatism in the Brazilian Platform (P. Comin-Chiaramonti & C.B. Gomes, eds.). Editora da Universidade de São Paulo: Fapesp, São Paulo, Brazil, 318-340.

Goonan, T.G. (2011). Rare earth elements – End use and recyclability: U.S. Geological Survey Scientific Investigations Report 2011–5094, 15 p.; downloadable from http://pubs.usgs.gov/sir/2011/5094/.

Graham, A.R. (1955). Cerianite: a new rare-earth oxide mineral. *American Mineralogist*, 40, 560-564.

Gromet, L.P., Dymek, R.F., Haskin, L.A. & Korotev, R.L. (1984). The "North American shale composite": Its compilation, major and trace element characteristics. *Geochimica et Cosmochimica Acta*, 48, 2469-2482.

Gupta, C.K. & Krishnamurthy, N. (2005). Extractive metallurgy of rare-earths. CRC Press, 450 p.

Habashi, F. (1990). Rare earth metals and their position in the periodic table. *In* Researches on Rare Earths; History and Technology (F. Habashi, ed.). Laval University, 47-52.

Hart, S.R. (1988). Heterogeneous mantle domains – Signatures, genesis, and mixing chronologies. *Earth and Planetary Science Letters*, 90, 273-296.

Hatch, G.P. (2012). Dynamics in the global market for rare earths. *Elements*, 8, 341-346.

Hawkesworth, C.J., Rogers, N.W., van Calsteren, P.W.C. & Menzies, M. (1984). Mantle enrichment processes. *Nature*, 311, 331-335.

Haxel, G.B., Hedrick, J.B. & Orris, G.J. (2002). Rare-earth-elements – critical resources for technology. USGS Fact Sheet 087-02.

Henderson, P. (1984). General Geochemical properties and abundances of the rare earth elements. *In* Rare Earth Element Geochemistry (P. Henderson, ed.), Developments in geochemistry 2. Elsevier, Amsterdam, 1-29.

Henderson, P. (1996). The rare earth elements: introduction and review. *In* Rare Earth Minerals: Chemistry, Origin, and Ore Deposits (F. Wall & T.C. Williams, eds.). Mineralogical Society Series, 1-19.

Hole, M.J., Rogers, G., Saunders, A.D. & Storey, M. (1991). Relation between alkalic volcanism and slab-window formation. *Geology*, 19, 657-660.

Hollings, P. & Wyman, D. (2004). The geochemistry of trace elements in igneous systems: Principles and examples from basaltic systems. *In* Rare-Element Geochemistry and Mineral Deposits (R.L. Linnen & I.M. Samson, eds.). GAC Short Course notes 17, St. Catharines, Ontario, 1-13.

Hornig-Kjarsgaard, I. (1998). Rare earth elements in sövitic carbonatites and their mineral phases. *Journal of Petrology*, 39, 2105-2121.

Horstmann, U.E. & Verwoerd, W.J. (1997). Carbon and oxygen isotope variations in southern African carbonatites. *Journal of African Earth Sciences*, 25, 115-136.

Hou, Z., Tian, S., Xie, Y., Yang, Z., Yuan, Z., Yin, S., Yi, L., Fei, H., Zou, T., Gai, G. & Li, X., (2009). The Himalayan Mianning-Dechang REE belt associated with carbonatite-alkaline complexes, eastern indo-Asian collision zone, SW China. *Ore Geology Reviews*, 36, 65-89.

Hsu, L.C. (1992). Synthesis and stability of bastnaesites in a part of the system (Ce,La)–F–H–C–O. *Mineralogy and Petrology*, 47, 87-101.

ICRE: 6th International Conference on Rare Earth Development and Application (2010). China Rare Earth Industry Policy and Worldwide Rare Earth Economy, Chinese Society of Rare Earths, Aug 2-6, 2010, Beijing, China.

Irving, A.J., O'Brien, H.E. & McCallum, I.S. (1989). Precambrian mantle beneath Montana: Geochemical evidence from Eocene volcanics and their xenoliths. Workshop on the Archean Mantle, LPI Technical Report 89-05, Lunar and Planetary Institute, Houston. 104 p.

Jackson, W.D. & Christiansen, G. (1993). International strategic minerals inventory summary report – rare-earth oxides. U.S. Government Printing Office, Washington, 68 p.

Jacobsen, S.B. (1988). Isotopic and chemical constraints of mantle-crust evolution. *Geochimica et Cosmochimica Acta*, 52, 1341-1350.

Jensen, E. (2003). Magmatic and Hydrothermal Evolution of the Cripple Creek Gold Deposit, Colorado, and Comparisons with Regional and Global Magmatic-Hydrothermal Systems Associated with Alkaline Magmatism. Ph.D. dissertation, Tucson, University of Arizona, 846 p.

Kapustin, Yu.L. (1980). Mineralogy of Carbonatites. Amerind Publishing, New Delhi, 259 p.

Kinicky, J., Smith, M.P. & Xu, C. (2012). Diversity of rare-earth deposits: the key example of China. *Elements*, 8, 361-367.

Kleber, E.V. & Love, B. (1963). Technology of Scandium, Yttrium and the Rare Earth Metals, Elsevier, 230 p.

Krenn, E. & Finger, F. (2007). Formation of monazite and rhabdophane at the expense of allanite during Alpine low temperature retrogression of metapelitic basememt rocks from Crete, Greece: Microprobe data and geochronological implications. *Lithos*, 95, 130-147.

Kutty, T.R.N., Tareen, J.A.K. & Mohammed, I. (1985). Correlation between the stability of carbonates in ternary Ln_2O_3-H_2O-CO_2 hydrothermal systems and lanthanide systematics. *Journal of the Less-Common Metals*, 105, 197-209.

Le Maitre, R.W. (ed.), 2002. Igneous Rocks: A Classification and Glossary of Terms. Cambridge University Press, Cambridge, UK, 236 p.

Lide, D.R. (1997). Abundance of elements in the earths crust and sea. *In* CRC Handbook of Physics and Chemistry, 78th edition. Boca Raton, Florida. CRC Press, 14 p.

Lisenbee, A.L. (1985). Tectonic map of the Black Hills uplift, Montana, Wyoming, and South Dakota, Geological Survey of Wyoming Map Series 13, scale 1:250,000.

Lisenbee, A.L. & DeWitt, E. (1993). Laramide evolution of the Black Hills uplift. Geology of Wyoming: Geological Survey of Wyoming Memoir No. 5, 374-412.

Lu, C.-H., Wang, H.-C. (2002). Formation and microstructural variation of cerium carbonate hydroxide prepared by the hydrothermal process. *Materials Science and Engineering*, B90, 138-141.

Mariano, A.N. (1978a). The application of cathodoluminescence for carbonatite exploration and characterization. *In* Proceedings of the First International Symposium on Carbonatites. Poços de Caldas, Minas Gerais, Brazil, June 1976.

Mariano, A.N. (1978b). A petrographic examination of selected drill core from the Bear Lodge project, Crook County, Wyoming. Confidential report to Molycorp Inc., 34 p.

Mariano, A.N. (1981). Rare Earth Mineralization in the Bear Lodge carbonatite complex Crook County, Wyoming. Confidential report to Molycorp Inc., 38p.

Mariano, A.N. (1988a). Some further geological applications of cathodoluminescence. *In* Cathodoluminescence of Geological Materials (D. J. Marshall, ed.). Unwin Hyman, 94-123.

Mariano, A.N. (1988b). Petrographic examination of three intercepts of core from DDH WP-2 91’, 1175’, and 1240’. Confidential report to Hecla Mining Company, 53 p.

Mariano, A.N. (1989a). Economic Geology of Rare Earth Minerals. *In* Geochemistry and Mineralogy of Rare Earth Elements (B.R. Lipin & G.A. McKay, eds.), Reviews in Mineralogy. Mineralogical Society of America, 21, 309-337.

Mariano, A.N. (1989b). The nature of economic REE and Y minerals on a world level. *In* Proceedings, The global business and technical outlook for NeFeB magnet markets. Monterey, California, 1-10.

Mariano, A.N. (1989c). Nature of economic mineralization in carbonatites and related rocks. *In* Carbonatites: Genesis and Evolution (K. Bell, ed.), Unwin Hyman, London, 149-176.

Mariano, A.N. (1989d). Cathodoluminescence emission spectra of rare earth element activators in minerals. *In* Geochemistry and Mineralogy of Rare Earth Elements (B.R. Lipin & G.A. McKay, eds.), Reviews in Mineralogy. Mineralogical Society of America, 21, 339-348.

Mariano, A.N. & Mariano, A. Jr. (2012). Rare earth mining and exploration in North America. *Elements*, 8, 369-376.

Marshall, D.J. (1988). Cathodoluminescence of Geological Materials. Unwin Hyman, London, 93 p.

Mason, R.A. & Mariano, A.N. (1990). Cathodoluminescence activation in manganese-bearing and rare earth-bearing synthetic calcites. *Chemical Geology*, 88, 191-206.

Masuda, A., Kawakami, O., Dohmoto, Y. & Takenaka, T. (1987). Lanthanide tetrad effects in nature: two mutually opposite types, W and M. *Geochemical Journal*, 21, 119-124.

McDonough, W. F. & Sun, S.-s. (1995). The composition of the Earth. *Chemical Geology*, 120, 223-253.

McGill, I. (1997). Rare earth metals. *In* Handbook of Extractive Metallurgy (F. Habashi, ed.). Weinheim, New York, Wiley-VCH, 3, 1695-1741.

McKay, G.A. (1989). Partitioning of rare earth elements between major silicate minerals and basaltic melts. *In* Geochemistry and Mineralogy of Rare Earth Elements (B.R. Lipin & G.A. McKay, eds.), Reviews in Mineralogy. Mineralogical Society of America, 21, 45-74.

Mirnejad, H. & Bell, K. (2008). Geochemistry of crustal xenoliths from the Hatcher Mesa lamproite, Wyoming, USA: Insights into the composition of the deep crust and upper mantle beneath the Wyoming Craton. *Canadian Mineralogist*, 46, 583-596.

Miyawaki, R. & Nakai, I. (1996). Crystal chemical aspects of rare earth minerals. *In* Rare earth minerals, chemistry, origin, and ore deposits (A.P. Jones, F. Wall & C.T. Williams, eds.) Chapman and Hall, London, 21-37.

Mooney, R.C.L. (1950). X-ray diffraction study of cerous phosphate and related crystals. I. Hexagonal modification. *Acta Crystallografica*, 3, 337-340.

Moreira, M., Doucelance, R., Kurz, M.D., Dupré, B. & Allègre, C.J. (1999). Helium and lead isotope geochemistry of the Azores Archipelago. *Earth and Planetary Science Letters*, 169, 189-205.

Morris, G.A. & Hooper, P.R. (1997). Petrogenesis of the Colville Igneous Complex, northeast Washington: Implications for Eocene tectonics in the northern U.S. Cordillera. *Geology*, 25, 831-834.

Nagy, G., Dragantis, E., Demény, A., Pantó, G. & Arkai, P. (2002). Genesis and transformation of monazite, florencite and rhabdophane during medium grade metamorphism: examples from the Sopron Hills Eastern Alps. *Chemical Geology*, 191, 23-44.

Ni, Y., Hughes, J.M. & Mariano, A.N. (1995). Crystal chemistry of the monazite and xenotime structures. *American Mineralogist*, 80, 21-26.

Nikiforov, A.V., Bolonin, A.V., Pokrovsky, B.G., Sugorakova, A.M., Chugaev, A.V. & Lykhin, D.A. (2006). Isotope geochemistry (O, C, S, Sr) and Rb-Sr age of carbonatites in central Tuva. *Geology of Ore Deposits*, 48, 256-276.

Noble, A. (2013). Technical Report on the Mineral Reserves and Resourcesand Development of the Bull Hill Mine. Compiled for Rare Element Resources, 171p.

Noble, A.C., Clark, J.G. & Ranta, D.E. (2009). NI 43-101 Technical Report on the mineral resources of the Bear Lodge Rare Earths Project. Prepared for Rare Element Resources, Ltd., 163 p.

Norman, M.D. & Mertzman, S.A. (1991). Petrogenesis of Challis volcanics from central and southwestern Idaho: Trace element and Pb isotopic evidence. *Journal of Geophysical Research*, 96, 13,279-13,293.

O'Brien, H.E., Irving, A.J., McCallum, I.S. & Thirlwall, M.F. (1995). Strontium, neodymium, and lead isotopic evidence for the interaction of post-subduction asthenospheric potassic mafic magmas of the Highwood Mountains, Montana, USA, with ancient Wyoming craton lithospheric mantle. *Geochimica et Cosmochimica Acta*, 59, 4539-4556.

Olinger, D. (2012). Characterization and genetic relation of carbonatite and associated alkaline silicate rocks of northwest Bull Hill, Bear Lodge Mountains, northeast Wyoming. M.Sc. Thesis, Texas Tech University, 299 p.

Onuonga, O.I., Fallick, A.E. & Bowden, P. (1997). The recognition of meteoric-hydrothermal and supergene processes in volcanic carbonatites, Nyanza Rift, western Kenya, using carbon and oxygen isotopes. *Journal of African Earth Sciences*, 25, 103-113.

Orris, G.J. & Grauch, R.I. (2002). Rare earth element mines, deposits, and occurrences. USGS Open-File report, 174 p.

Ouzegane, Kh., Fourcade, S., Kienast, J.-R. & Javoy, M. (1988). New carbonatite complexes in the Archean In’Ouzzal nucleus (Ahaggar, Algeria): mineralogical and geochemical data. *Contributions to Mineralogy and Petrology*, 98, 277-292.

Pearce, N.J.G., Leng, M.J., Emeleus, C.H. & Bedford, C.M. (1997). The origins of carbonatites and related rocks from the Grønnedal-Íka nepheline syenite complex, South Greenland: C-O-Sr isotope evidence. *Mineralogical Magazine*, 61, 515-529.

Pecora, W.T. & Kerr, J.H. (1953). Burbankite and calkinsite, two new carbonate minerals from Montana. *American Mineralogist*, 38, 1169-1183.

Peishan, Z., Zhuming, Y., Kejie, T. & Xueming, Y. (1995). Mineralogy and geology of rare earths in China. Science Press, Beijing, 190 p.

Platt, R.G. & Wolley, A.R. (1990). The carbonatites and fenites of Chipman Lake, Ontario. *Canadian Mineralogist*, 28, 241-250.

Ray, J. (2013). Exploration for REE and gold at the Tertiary Bear Lodge Alkaline Complex, Crook County, Wyoming. Oral presentation, Technical Session: Entering the realm of the rare-earths. SME Annual Meeting, Denver, Colorado.

Reguir, E. & Mitchell, R.H. (2000). The mineralogy of carbonatites and related potassic syenites from the Rocky Boy stock, Bearpaw Mountains, north-central Montana. Geological Association of Canada – Mineralogical Association of Canada, GeoCanada 2000 Conference CD (extended abstracts), file 374.pdf.

Roden, M.F., Trull, T., Hart, S.R.& Frey, F.A. (1994). New He, Nd, Pb, and Sr isotope constraints on the constitution of the Hawaiian plume: results from Koolau Volcano, Oahu, Hawaii, USA. *Geochimica et Cosmochimica Acta,* 58, 1431–1440.

Roeder, P.L., MacArthur, D., Ma, Xin-Pei, Palmer, G.R. & Mariano, A.N. (1987). Cathodoluminescence and microprobe study of rare-earth elements in apatite. *American Mineralogist,* 72, 801-811.

Ruberti, E., Enrich, G.E.R., Gomes, C.B.& Comin-Chiramonti, P. (2008). Hydrothermal REE fluorocarbonate mineralization at Barra do Itapirapuã, a multiple stockwork carbonatite, southern Brazil. *Canadian Mineralogist,* 46, 901-914.

Russo, R.M., VanDecar, J.C., Comte, D., Mocanu, V.I., Gallego, A.& Murdie, R.E. (2010). Subduction of the Chile Ridge: Upper mantle structure and flow. *GSA Today,* 20, 4-10.

Sabot, J.-L. &Maestro, P. (1995). Lanthanides. *In* Kirk-0thmer Encyclopedia of Chemical Technology, Vol.14, (J.I. Kroschwitz, & M.H. Grant, eds.) Wiley-Interscience, New York, 1091-1115.

Samson, I.M. & Wood, S.A. (2004). The rare earth elements: behavior in hydrothermal fluids and concentration in hydrothermal mineral deposits, exclusive of alkaline settings. *In* Rare-Element Geochemistry and Mineral Deposits (R.L. Linnen, R.L. & I.M. Samson, eds.) GAC Short Course notes 17. St. Catherine's, Ontario, 269-291.

Santos, R.V.& Clayton, R.N. (1995). Variations of oxygen and carbon isotopes in carbonatites: A study of Brazilian alkaline complexes. *Geochimica et Cosmochimica Acta,* 59, 1339-1352.

Shannon, R.D. (1976). Revised effective ionic radii and systematic studies of interatomic distances in halides and chalcogenides. *Acta Crysta*, 32, 751-767.

Sheard, E.R., Williams-Jones, A.E., Heiligmann, M., Peterson, C. & Trueman, D.L. (2012). Controls on the concentration of zirconium, niobium, and the rare earth elements in the Thor Lake rare metal deposit, Northwest Territories, Canada. *Economic Geology,* 107, 81-104.

Simonetti A. & Bell, K. (1995). Nd, Pb and Sr isotope systematics of fluorite at the Amba Dongar carbonatite complex, India; evidence for hydrothermal and crustal fluid missing. *Economic Geology,* 90, 2018-2027.

Smith, M.P., Campbell, L.S. & Kinicky, J. (2014). A review of the genesis of the world class Bayan Obo Fe-REE-Nb deposits, Inner Mongolia, China: Multistage processes and outstanding questions. *Ore Geology Reviews* (in press).

Smith, M.P., Henderson, P.& Campbell, L.S. (2000). Fractionation of the REE during hydrothermal processes: Constraints from the Bayan Obo Fe-REE-Nb deposit, Inner Mongolia, China. *Geochimica et Cosmochimica Acta*, 64. 3141-3160.

Snoke, A.W. (1993). Geologic history of Wyoming within the tectonic framework of the North American Cordillera. *In* Geology of Wyoming: Geological Survey of Wyoming Memoir No. 5 (A.W. Snoke, J.R. Steidtmann & S.M. Roberts, eds.). Geological Survey of Wyoming, Laramie, 2-56.

Staatz, M.H. (1983). Geology and description of thorium and rare-earth deposits in the southern Bear Lodge Mountains, northeastern Wyoming. USGS Professional Paper 1049-D, 52 p.

Strake, A., Hofmann, A.W. & Hart, S.R. (2005). FOZO, HIMU, and the rest of the mantle zoo. *Geochemistry, Geophysics, Geosystems*, 6, 1-20.

Sun, S.-s. & McDonough, W.F. (1989). Chemical and isotopic systematics of oceanic basalts: implications for mantle composition and processes. *Geological Society, London, Special Publications,* 42, 313-345.

Takahashi, Y., Yoshida, H., Sato, N., Hama, K., Yusa, Y. & Shimizu, H. (2002). W- and M-type tetrad effects in REE patterns for water-rock systems in the Tono uranium deposit, central Japan. *Chemical Geology*, 184, 311-335.

Taylor, H.P., Frechen, J. & Degens, E.T. (1967). Oxygen and carbon isotope studies of carbonatites from the Laacher See District, West Germany and the Alnö District, Sweden. *Geochimica et Cosmochimica Acta*, 31, 407-430.

Taylor, S.R. & McLennan, S.M., (1985). The Continental Crust: Its Composition and Evolution, Blackwell, Oxford, 312 p.

Terada,Y., Nakai, I. & Kawashima, T. (1993). Crystal structure of bastnaesite (Ce, La, Nd, Sm, Gd)CO_3F. *Analytical Sciences*, 9, 561-562.

Thorkelson, D.J. & Taylor, R.P. (1989). Cordilleran slab windows. *Geology*, 17, 833-836.

Tilton, G.R., Bryce, J.G. & Mateen, A. (1998). Pb-Sr-Nd isotope data from 30 and 300 Ma collision zone carbonatites in northwest Pakistan. *Journal of Petrology,* 39, 1865-1874.

Tucker, R.D., Belkin, H.E., Schulz, K.J., Peters, S.G., Horton, F., Buttleman, K. & Scott, E.R. (2012). A major light rare-earth element (LREE) resource in the Khanneshin carbonatite complex, southern Afghanistan. *Economic Geology*, 107, 197-208.

Turekian, K.K. (1971). Rivers, Tributaries, and Estuaries. *In* Impingement of Man on the Ocean. Wiley Inter-Sci, New York, 1-9.

Usui, T., Nakamura, E. & Helmstaedt, H. (2006). Petrology and geochemistry of eclogite xenoliths from the Colorado Plateau: Implications of the evolution of subducted oceanic crust. *Journal of Petrology,* 47, 929-964.

van Achterbergh, E., Ryan, C.G., Jackson, S.E. & Griffin, W.L. (2001). Data reduction software for LA–ICP–MS. *In* Laser-Ablation – ICPMS in the Earth Sciences, Principles and Applications (P. Sylvester, ed.). Mineralogical Association of Canada Short Course Notes, 29, 239-242.

Veena, K., Pandey, B.K., Krishnamurthy, P. & Gupta, J.N. (1998). Pb, Sr and Nd isotopic systematics of the carbonatites of Sung Valley, Meghalaya, Northeast India: implications for contemporary plume-related mantle source characteristics. *Journal of Petrology*, 39, 1875-1884.

Vempati, R.K. & Loeppert, R.H. (1989). Influence of structural and adsorbed Si on the transformation of synthetic ferrihydrite. *Clays and Clay Minerals*, 37, 273-279.

Verwoerd, W.J. (1993). Update on carbonatites of South Africa and Nimibia. *South African Journal of Geology,* 96, 75-95.

Wakita H., Rey P. & Schmitt R.A. (1971). Elemental abundances of major, minor, and trace elements in Apollo 11 lunar rocks, soil and core samples. *Proceedings of the Apollo 11 Lunar Science Conference,* 1685-1717.

Wall, F. & Mariano, A.N. (1996). Rare earth minerals in carbonatites: a discussion centred aon the Kangankunde Carbonatite, Malawi. *In* Rare Earth Minerals: Chemistry, Origin, and Ore Deposits (A.P. Jones, F. Wall & C.T. Williams, eds.). Chapman and Hall, London, 193-225.

Wall, F., Niku-Paavola, V.N., Storey, C., Müller, A. & Jeffries, T. (2008). Xenotime-(Y) from carbonatite dykes at Lodfal, Namibia: unusually low LREE:HREE ratio in carbonatite, and the first dating of xenotime overgrowths on zircon. *Canadian Mineralogist*, 46, 861-877.

Wall, F. & Zaitsev, A.N. (2004). Rare earth minerals in Kola carbonatites. *In* Phoscorites and Carbonatites from Mantle to Mine: the Key Example of the Kola Alkaline Province (F. Wall & A.N. Zaitsev, eds.). Mineralogical Society, London, 341-373.

Wells, M.L. & Hoisch, T.D. (2008). The role of mantle delamination in widespread Late Cretaceous extension and magmatism in the Cordilleran orogen, western United States. *Geological Society of America Bulletin*, 120, 515-530.

Williams-Jones, A.E., Migdisov, A.A. & Samson, I.A. (2012). Hydrothermal mobilization of the rare earth elements: A tale of “ceria” and “yttria”. *Elements*, 8, 355-360.

Williams-Jones, A.E., Samson, I.M. & Olivo, G.R. (2000). The genesis of hydrothermal fluorite-REE deposits in the Gallinas Mountains, New Mexico. *Economic Geology*, 95, 327-342.

Williams-Jones, A.E. & Wood, S.A. (1992). A preliminary petrogenetic grid for REE fluorocarbonates and associated minerals. *Geochimica et Cosmochimica Acta*, 56, 725-738.

Wood, B.J. & Blundy, J.D. (2002). The effect of H_2O on crystal-melt partitioning of trace elements. *Geochimica et Cosmochimica Acta*, 66, 3647-3656.

Woolley, A.R. & Kempe, D.R.C. (1989). Carbonatites: nomenclature, average chemical compositions, and element distribution. *In* Carbonatites: Genesis and Evolution (K. Bell, ed.). Unwin Hyman, London, 1-14.

Workman, R. K., Hart, S.R., Jackson, M. Regelous, M., Farley, K.A., Blusztajn, J., Kurz, M. & Staudigel, H. (2004). Recycled metasomatized lithosphere as the origin of the Enriched Mantle II (EM2) end-member: Evidence from the Samoan Volcanic Chain, *Geochemistry, Geophysics, Geosystems*, 5, Q04008, doi:10.1029/2003GC000623.

Xu C., Chakhmouradian A.R., Taylor R.N., Kynicky J., Li W., Song W. & Fletcher I.R. (2014). Origin of carbonatites in the South Qinling orogen: Implications for crustal recycling and timing of collision between the South and North China Blocks. *Geochimica et Cosmochimica Acta* (in press).

Xu, C., Huang, Z.-L., Liu, C.-L., Qi, L., Li, W.-B. & Guan, T. (2003). Sources of ore-forming fluids in the Maoniuoing REE deposit, Sichuan Orovince, China: Evidence from REE, radiogenic Sr, Nd, and stable-isotope studies. *International Geology Review*, 45, 635-645.

Xu, C., Taylor, R.N., Kynicky, J., Chakhmouradian, A.R., Song, W.& Wang, L. (2011). The origin of enriched mantle beneath North China Block: Evidence from young carbonatites. *Lithos,* 127, 1-9.

Xu, C., Zhang, H., Huang, Z., Liu, C., Qi, L., Li, W. & Guan, T. (2004). Genesis of the carbonatite-syenite complex and REE deposit at Maoniuping, Sichuan Province, China: Evidence from Pb isotope geochemistry. *Geochemical Journal*, 38, 67-76.

Yakovenchuck, V., Ivanyuk, G., Pakhomovsky, Ya & Men'shikov, Yu (2005). Khibiny, (F. Wall, ed.), Laplandia Minerals, Apatity, 468 p.

Zaitsev, A.N. & Chakhmouradian, A.R. (2002). Calcite-amphibole-clinopyroxene rock from the Afrikanda complex, Kola Peninsula, Russia: Mineralogy and a possible link to carbonatites. II. Oxysalt minerals. *Canadian Mineralogist*, 40, 103-120.

Zaitsev, A.N., Demény, A., Sindern, S. & Wall, F. (2002). Burbankite-group minerals and their alteration in rare earth carbonatites – source of elements and fluids (evidence from C–O and Sr–Nd isotopic data). *Lithos,* 62, 15-33.

Zaitsev, A.N., Wall, F.& LeBas, M.J. (1998). REE-Sr-Ba minerals from the Khibina carbonatites, Kola Peninsula, Russia: their mineralogy, paragenesis, and evolution. *Mineralogical Magazine*, 62, 225-250.

Zindler, A. & Hart, S.R. (1986). Chemical dynamics. Annual Review. *Earth Planetary Science Letters*, 14, 493-571.

Appendix A

Samples and Sample Analyses

Table A.1. Summary table of samples and analyses for each sample.

sample	paragenesis or REE mineral phases*	hole #	drill depth (feet)	Thin Section	Thick section	microphotographs	CL	SEM/EDS	BSE	EPMA/WDS	Raman	LA-ICP-MS	Whole rk	stable isotopes	radio isotopes
T-684-L	burbankite			X		X				X	X				
BL4	anc	04--2	1114.3'	X		X	X								
BL5	anc+minor REFCO3	04--2	1111.5'	X	X	X	X	X	X				X	X	X
BL6		04--2	1092'	X		X									
BL7	REFCO3	04--2	864.5'	X	X	X	X			X	X	x		X	
BL8	anc+REFCO3 in distinct areas	04--2	704'	X		X	X	X	X	X	X		X	X	X
BL9	anc	04--2	686'	X		X					X				
BL62	Anc + REFCO3	08--4	1783'	A&B		X									
BL63	Anc + REFCO3	08--4	1772.5'	X		X	X	X	X	X			X	X	
BL68		08--4	1575'	X											
BL69		08--4	1529.3'	X											
BL70	Anc + REFCO3+cbcn	08--4	1501.5'	X		X		X	X	X					
BL71	Bkt	08--4	1505.5'	X	X	X		X	X	X	X	X	X	X	X
BL75		08--4	1345.5'	X		X									
BL76	Anc	08--4	1278.5'	X		X	X				X				
BL78	Anc + REFCO3	08--4	1161.3'	X	X					X		X	X		
BL81	anc and REEFCO3 in diff veins	08--4	1108.5'	X	X	X	X	X	X	X		X	X	X	X
BL83	anc-very little	08--4	1042.5'	X											
BL85	anc-very little	08--4	971.5'	X	X	X				x		X			
BL87	REFCO3+fluorite	08--4	884.3'	X	X	X	X	X	X	X		X		X	
BL90	Anc + REFCO3	08--4	867.5'	X		X		X	X	X					
BL97	Anc + REFCO3	08--4	620.5'	X		X		X	X	X					
BL117	Anc + REFCO3	07--2	964.5'	X	X	X	X	X	X	X		X	X	X	X
BL119	Anc	07--2	943'	X											

sample	paragenesis or REE mineral phases*	hole #	drill depth (feet)	Thin Section	Thick section	microphoto graphs	CL	SEM/ EDS	BSE	EPMA/ WDS	Raman	LA-ICP-MS	Whole rk	stable isotopes	radio isotopes
BL120	Anc+REFCO3	07--2	950'	X											
BL123 A	Anc	07--2	912'	X		X	X	X	X	X				X	
BL123 B				X											
BL123 C				X	X					X		X			
BL125	Anc	07--2	842.5'	X		X		X	X	X					
BL127	Anc, agn	07--2	738.5'	X		X		X	X						
BL128	Anc+REFCO3	07--2	725'	X											
BL129	dom Anc, maybe REFCO3 in gm	07--2	688'	X		X								X	
BL131	Anc?	07--2	606.5'	X	X	X		X	X			X	X		X
BL12	trans, REFCO3	04--2	604.5'	X	X	X	X	X	X	X				X	
BL15	barren	04--2	552.5'	X	X	X	X	X	X	X		X		X--srt no D18O correction	
BL19	Anc+REFCO3	04--2	525.5'	X	X	X	X	X	X	X					
BL23		04--2	466.6'	X											
BL25	Anc+REFCO3	04--2	462.7'	X		X	X	X	X	X				X--two samples one vein and one groundmass	
BL28	REEFCO3+mzt	04--2	429'	X		X	X	X	X	X					
BL31		04--2	424.5'	X		X									
BL33		04--2	412'		X										
BL99		08--4	602.5	A&B											
BL102	Anc + REFCO3	08--4	567.5	A&B	A	B		B	B	X		x A	X	X	X
BL135	Anc	07--2	548'	X	X			X	X	X					
BL37		04--2	396.5'	X	X	X		X	X	X					
BL38	REEFCO3+mzt+cen	04--2	384'	X		X	X	X	X	X					
BL40		04--2	371.5'	X		X	X	X	X					X	
BL44		04--2	319.5'	X	X	X	X	X	X	X	X	X		X	
BL49		04--2	135'	X											

sample	paragenesis or REE mineral phases*	hole #	drill depth (feet)	Thin Section	Thick section	microphotographs	CL	SEM/EDS	BSE	EPMA/WDS	Raman	LA-ICP-MS	Whole rk	stable isotopes	radio isotopes
BL104		08--4	474.5'	X	X										
BL113		08--4	122.5'	X											
BL115		08--4	101'		X			X	X	X					
BL138		07--2	531'		X	X		X	X	X		X		X	
BL143		07--2	455'		X	X		X	X	X		X	X	X	
BL145	cerianite	07--2	373'		X	X		X	X	X					
BL150		07--2	210'		X										
BL152		07--2	104'		X										

* abbreviations for minerals: anc, ancylite; REFCO3, REE fluorocarbonates; mzt, monazite; agn, aegirine; cbcn, carbocernaite; bkt, burbankite; cen, cerianite

- Blue represents samples from the 'unoxidixed zone'.

- Purple represents samples from the 'transitional zone'.

- Red represents samples from the oxidized zone'.

Appendix B

Analytical Instrumentation Parameters

Table B.1. Analytical conditions used in EMPA calibration and acquisition of REE mineral data. Standard=standard used in calibration; Line = element line for counting; Xtal = detection crystal; Peak = wavelength at which counts were detected; Pk Time and Bg Time= count time on peak and background positions, respectively (s); Bg Off1 and Bg Off2 = background positions that were manually set during calibration; Slope/IBg = slope calculated to correct for background when offsets could not be placed due to overlaps.

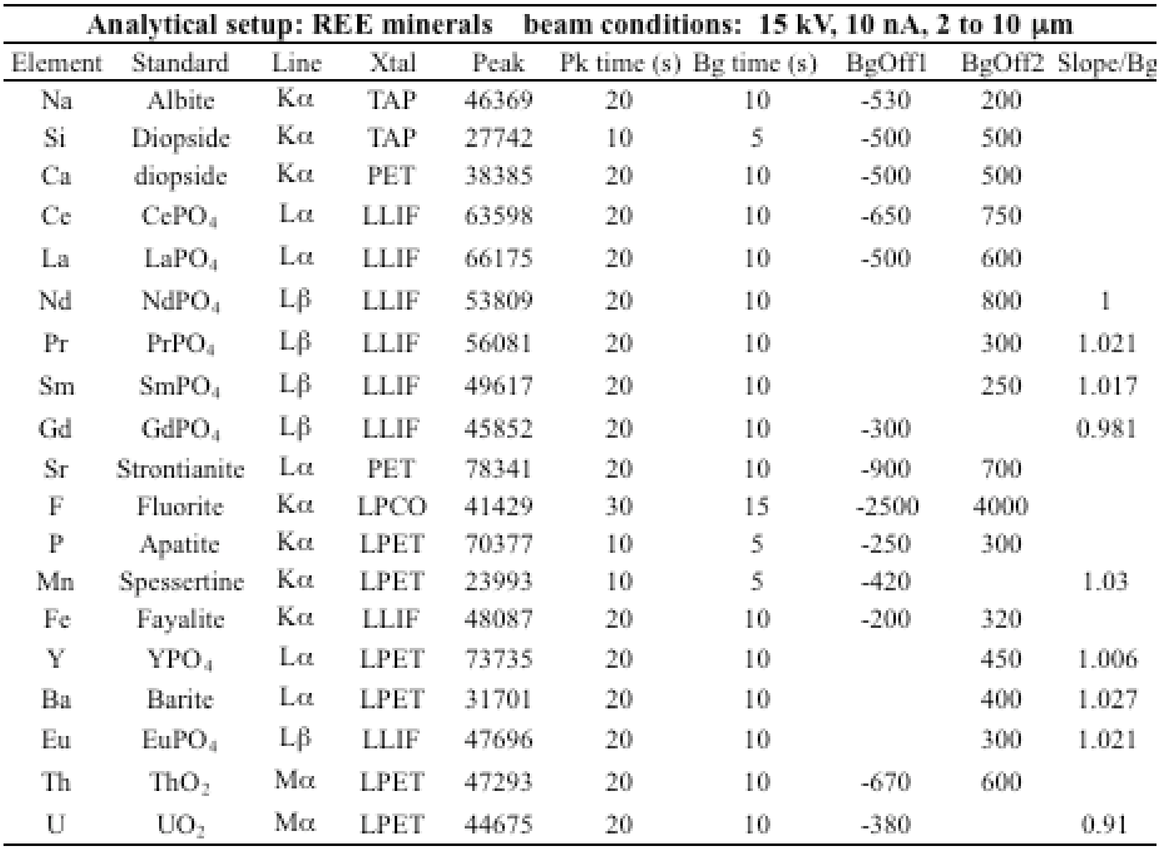

Analytical setup: REE minerals beam conditions: 15 kV, 10 nA, 2 to 10 µm

Element	Standard	Line	Xtal	Peak	Pk time (s)	Bg time (s)	BgOff1	BgOff2	Slope/Bg
Na	Albite	Kα	TAP	46369	20	10	-530	200	
Si	Diopside	Kα	TAP	27742	10	5	-500	500	
Ca	diopside	Kα	PET	38385	20	10	-500	500	
Ce	$CePO_4$	Lα	LLIF	63598	20	10	-650	750	
La	$LaPO_4$	Lα	LLIF	66175	20	10	-500	600	
Nd	$NdPO_4$	Lβ	LLIF	53809	20	10		800	1
Pr	$PrPO_4$	Lβ	LLIF	56081	20	10		300	1.021
Sm	$SmPO_4$	Lβ	LLIF	49617	20	10		250	1.017
Gd	$GdPO_4$	Lβ	LLIF	45852	20	10	-300		0.981
Sr	Strontianite	Lα	PET	78341	20	10	-900	700	
F	Fluorite	Kα	LPCO	41429	30	15	-2500	4000	
P	Apatite	Kα	LPET	70377	10	5	-250	300	
Mn	Spessertine	Kα	LPET	23993	10	5	-420		1.03
Fe	Fayalite	Kα	LLIF	48087	20	10	-200	320	
Y	YPO_4	Lα	LPET	73735	20	10		450	1.006
Ba	Barite	Lα	LPET	31701	20	10		400	1.027
Eu	$EuPO_4$	Lβ	LLIF	47696	20	10		300	1.021
Th	ThO_2	Mα	LPET	47293	20	10	-670	600	
U	UO_2	Mα	LPET	44675	20	10	-380		0.91

Table B.2. Analytical conditions and setups for carbonate minerals calcite and strontianite, and apatite used for quantitative data acquisition in the present work.

Analytical setup: carbonate minerals		
beam conditions: 15kV, 10nA, 10 μm		
Element	Standard	Line
Mg	Olivine	Kα
Ca	Diopside	Kα
Mn	Spessartine	Kα
Fe	Fayalite	Kα
Sr	$SrTiO_3$	Lα
Ba	Barite	Lα

Analytical setup: apatite		
beam condtions: 15kV, 10nA, 10μm		
Element	Standard	Line
F	Topaz	Kα
Na	Albite	Kα
Al	Andalusite	Kα
Si	Diopside	Kα
P	Apatite	Kα
Ca	Diopside	Kα
Sr	$SrTiO_3$	Lα
Ba	Barite	Lα
Cl	Tugtupite	Kα
S	Pyrite	Kα
La	$LaPO_4$	Lα
Ce	$CePO_4$	Lα
Nd	$NdPO_4$	Lα
Pr	$PrPO_4$	Lα
Sm	$SmPO_4$	Lα
Fe	Fayalite	Kα
Mn	Spessartine	Kα

Table B.3. Quantitative compositions of standards used for instrumental calibration in this study. All analyses are in wt%.

Rare-earth orthophosphate standard compositions

grain in mount	formula	O	P	REE		total
1	ScPO4	45.74	22.13	Sc	32.12	99.99
2	YPO4	34.8	16.84	Y	48.35	99.99
3	ZrSiO4	34.92	15.32	Zr	49.76	100.00
4	LaPO4	27.36	13.24	La	59.39	99.99
5	HfSiO4	23.65	10.38	Hf	65.97	100.00
6	CePO4	27.22	13.17	Ce	59.6	100.00
7	PrPO4	27.13	13.13	Pr	59.73	99.99
8	NdPO4	26.75	12.95	Nd	60.3	100.00
9	SmPO4	26.08	12.62	Sm	61.29	99.99
10	EuPO4	25.92	12.54	Eu	61.54	100.00
11	GdPO4	25.37	12.28	Gd	62.35	100.00
12	TbPO4	25.21	12.2	Tb	62.59	100.00
13	DyPO4	24.86	12.03	Dy	63.11	100.00
14	HoPO4	24.62	11.92	Ho	63.46	100.00
15	ErPO4	24.41	11.81	Er	63.78	100.00
16	TmPO4	24.25	11.74	Tm	64.01	100.00
17	YbPO4	23.88	11.55	Yb	64.56	99.99
18	LuPO4	23.71	11.47	Lu	64.81	99.99

Table B.4. Comparison of mass spectrometry techniques used in this work.

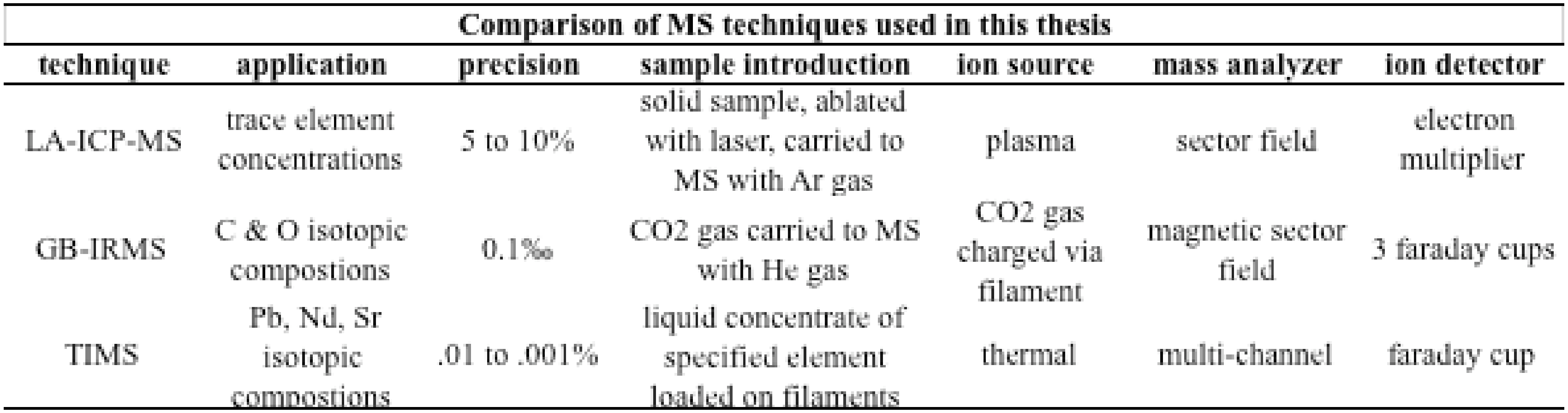

Comparison of MS techniques used in this thesis						
technique	**application**	**precision**	**sample introduction**	**ion source**	**mass analyzer**	**ion detector**
LA-ICP-MS	trace element concentrations	5 to 10%	solid sample, ablated with laser, carried to MS with Ar gas	plasma	sector field	electron multiplier
GB-IRMS	C & O isotopic compostions	0.1‰	CO2 gas carried to MS with He gas	CO2 gas charged via filament	magnetic sector field	3 faraday cups
TIMS	Pb, Nd, Sr isotopic compostions	.01 to .001%	liquid concentrate of specified element loaded on filaments	thermal	multi-channel	faraday cup

Table B.5. Analytical setup for LA-ICP-MS trace-element analyses. See text for instrumental conditions.

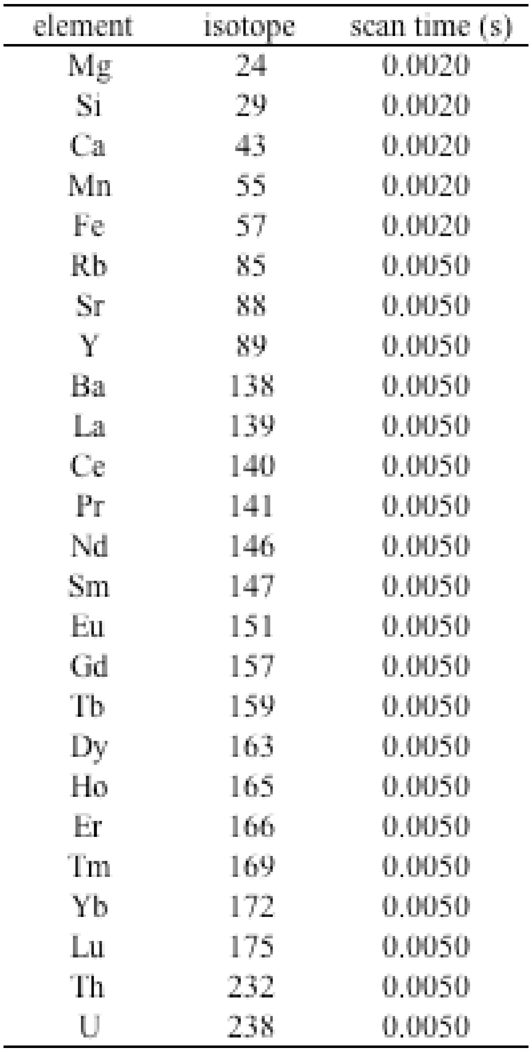

element	isotope	scan time (s)
Mg	24	0.0020
Si	29	0.0020
Ca	43	0.0020
Mn	55	0.0020
Fe	57	0.0020
Rb	85	0.0050
Sr	88	0.0050
Y	89	0.0050
Ba	138	0.0050
La	139	0.0050
Ce	140	0.0050
Pr	141	0.0050
Nd	146	0.0050
Sm	147	0.0050
Eu	151	0.0050
Gd	157	0.0050
Tb	159	0.0050
Dy	163	0.0050
Ho	165	0.0050
Er	166	0.0050
Tm	169	0.0050
Yb	172	0.0050
Lu	175	0.0050
Th	232	0.0050
U	238	0.0050

Table B.6. Instrumental conditions for Pb, Sr, and Nd isotopic analyses.

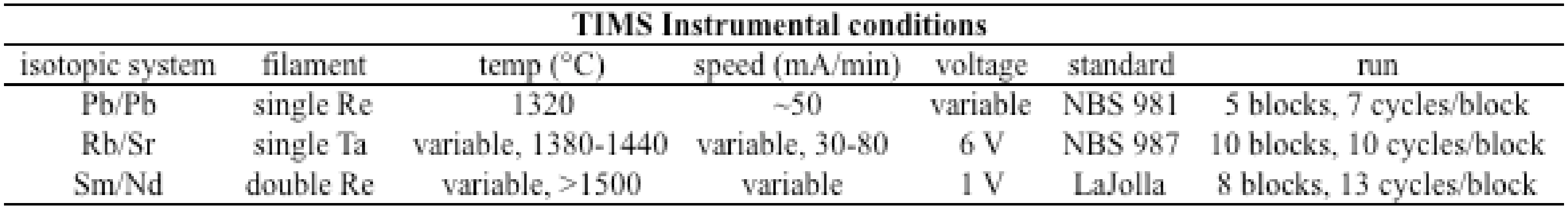

TIMS Instrumental conditions						
isotopic system	filament	temp (°C)	speed (mA/min)	voltage	standard	run
Pb/Pb	single Re	1320	~50	variable	NBS 981	5 blocks, 7 cycles/block
Rb/Sr	single Ta	variable, 1380-1440	variable, 30-80	6 V	NBS 987	10 blocks, 10 cycles/block
Sm/Nd	double Re	variable, >1500	variable	1 V	LaJolla	8 blocks, 13 cycles/block

Appendix C

Electron Microprobe WDS Data

See attached Excel file online/CD

Appendix D

LA-ICP-MS Data

See attached Excel file online/CD